AN ABSTRACT OF THE THESIS OF

Thomas Nickel for the degree of Doctor of Philosophy in Mechanical Engineering presented on April 28, 1999. Title: Estimation of Physical Parameters in Mechanical Systems for Predictive Monitoring and Diagnosis.

Abstract approved: Redacted for privacy

Swavik A. Spiewak

Monitoring, diagnosis and prediction of failures play key roles in automatic supervision of machine tools. They have received much attention because of the potential for reduced maintenance expenses, down time, and an increase in the equipment utilization level. At present, signal analysis techniques are predominantly used. But methods involving *system* analysis are capable of providing more reliable information, especially for predictive applications of supervision. System analysis involves comprehensive analytical models combined with techniques developed in control theory, and experimental modal analysis.

The primary objective of this research is to develop a methodology to monitor critical physical parameters of mechanical systems, which are difficult to measure directly. These parameters are inherent features of constitutive rigid body models. A method for computer aided model generation developed in this thesis leads to a gray box model structure by which physical parameters can be estimated from experimental data. Lagrange's energy formalism, linear algebra and homogenous transformations are used to promote parsimonious three-dimensional model building. A software environment allowing symbolic and arbitrary precision computations facilitates efficient mapping of physical properties of the actual system into specific quantities of the analytical model.

Six different methods are postulated and analyzed in this thesis to estimate physical parameters such as masses, stiffnesses and damping coefficients. Implementation of this methodology is a prerequisite for the design of an on-line monitoring and diagnosis system, which can detect and predict process faults. Two mechanical systems are used to validate the proposed methods: (1) A simple multi degree-of-freedom (MDOF) system and (2) a machine tool spindle assembly.

A practical application of physical parameter estimation is proposed for preload monitoring in high-speed spindles. Preload variations in the bearing can lead to thermal instability and bearing seizure. The feasibility of using accelerometers located on the spindle housing to estimate bearing preload is evaluated.

The optimal environment for continuation of this research is collaboration with machine tool companies to incorporate the proposed methodology (or parts of it) into current design practices.

Estimation of Physical Parameters in Mechanical Systems for Predictive Monitoring and Diagnosis

by

Thomas Nickel

A THESIS

submitted to

Oregon State University

in partial fulfillment of
the requirements for the
degree of

Doctor of Philosophy

Presented April 28, 1999
Commencement June 1999

Doctor of Philosophy thesis of Thomas Nickel presented on April 28, 1999

APPROVED:

Redacted for privacy

Major Professor, representing Mechanical Engineering

Redacted for privacy

Head of Department of Mechanical Engineering

Redacted for privacy

Dean of Graduate School

I understand that my thesis will become part of the permanent collection of Oregon State University libraries. My signature below authorizes release of my thesis to any reader upon request.

Redacted for privacy

Thomas Nickel, Author

ACKNOWLEDGEMENTS

I would like to express my sincere gratitude to Professor Swavik A. Spiewak, for his guidance during my graduate study at the University of Wisconsin-Madison and at Oregon State University. I would like to thank Professor Mario Magaña for his advice and suggestions in the area of modern control theory and Professor William Reiter for sharing his expertise on machine tool design and performance evaluation.

Special thanks to my fellow students in Mechanical Engineering Thanat Jitpraphai and Brian Brisbine for their support and assistance in many difficulties.

I deeply thank my parents for their loving support without which my graduate work in the United States would not have been possible.

TABLE OF CONTENTS

TABLE OF CONTENTS (Continued)

Page

TABLE OF CONTENTS (Continued)

LIST OF FIGURES

LIST OF FIGURES (Continued)

LIST OF FIGURES (Continued)

LIST OF FIGURES (Continued)

LIST OF FIGURES (Continued)

LIST OF TABLES

LIST OF APPENDICES

LIST OF APPENDIX FIGURES

LIST OF APPENDIX TABLES

NOMENCLATURE

$\mathbf{A}$	= evolution matrix of the state-space representation in continuous time-domain
a_i	= analytical transfer function coefficients in the denominator
$\hat{a}_i$	= experimental transfer function coefficients in the denominator
$\mathbf{B}$	= control matrix of the state-space representation in continuous time-domain
b_i	= analytical transfer function coefficients in the numerator
$\hat{b}_j$	= experimental transfer function coefficients in the numerator
$\mathbf{C}$	= output matrix of the state-space representation in continuous time-domain
c_i	= damping of SDE # i
$\mathbf{c_{ij}}$	= damping matrix of all spring-damper elements between mass i and j
$\mathbf{D}$	= direct transmission matrix of the state-space representation in continuous time-domain
D_{ij}	= damping energy between body i and j
F_p	= bearing preload
G_a	= analytical transfer function
G_e	= experimentally identified transfer function
g	= gain
$\mathbf{H}$	= vector of functions of geometric dimensions
$H(j\omega)$	= frequency response function
$h(\tau)$	= impulse response function
$\mathbf{I}$	= identity matrix
J_{ir}	= mass moment of inertia of body i around some axis r
k_i	= stiffness of SDE # I
$\mathbf{k_{ij}}$	= stiffness matrix of all spring-damper elements between mass i and j
L	= Lagrangian
$\mathbf{M_{FE}}$	= finite element mass matrix
$\mathbf{m}$	= global mass matrix
m_i	= mass of SDE # i
$n(t)$	= disturbance
n_{sp}	= rotational speed of the spindle
p_i	= value of pole
$p(y_i \mid \bullet)$	= probability density function
$\mathbf{Q}(t)$	= vector of generalized forces
$Q(\mathbf{\Lambda_p})$	= merrit function of $\mathbf{\Lambda_p}$
$\mathbf{q}(t)$	= vector of generalized coordinates with respect to the inertial reference coordinate system

NOMENCLATURE (Continued)

R_{xx} = auto-correlation of $x(t)$ with $x(t)$
R_{xy} = cross-correlation of $x(t)$ with $y(t)$
S_{xx} = auto-spectrum of $x(t)$ with $x(t)$
S_{xy} = auto-spectrum of $x(t)$ with $y(t)$
s = Laplace variable
T = total kinetic energy
T_i = kinetic energy of body i
$\mathbf{TM}(\mathbf{q}_i^L)$ = transformation matrix for rigid body #i
U = total potential energy
U_{ij} = potential energy between body i and j
$u(t)$ = input signals
$x(t)$ = state variables
$y(t)$ = output signals recorded from sensors during the performance evaluation procedure
$\hat{y}(t)$ = estimated output
$\mathbf{y}^Z$ = matrix of output signals recorded from Z
z_i = value of zero
α = angular acceleration of point P in $(XYZ)_I$
θ, ϕ, ψ = rotations of C.S. $(XYZ)_G$ around X, Y and Z axes, respectively
Γ = linear portion of evolution matrix
$\mathbf{\Delta M_{Bergmann}}$ = mass modification matrix according to Bergmann
Θ = vector of physical parameters
ξ = damping ratio
$\mathbf{\Lambda_g}$ = global vector of coefficients for parametric identification
$\mathbf{\Lambda_p}$ = vector of TF coefficients a_i and b_j
$\hat{\mathbf{\Lambda}}_\mathbf{p}$ = vector of estimated TF coefficients $\hat{a}_i$ and $\hat{b}_j$
Ξ = matrix of experimentally measured mode shapes
σ = standard deviation
$\mathbf{\Phi}$ = column vector of functions
Ψ = discrete state matrix
Ω = discrete input matrix
ω_d = damped natural frequency
ω_i = natural frequency
$*$ = convolution

ABBREVIATIONS

AR	= Auto-Regressive
ASM	= Automatic Supervision in Manufacturing
BJ	= Box-Jenkins
CAFD	= Computer Assisted Fault Diagnosis System
CAPPE	= Computer Aided Physical Parameter Estimation
DOF	= Degree-Of-Freedom
EOM	= Equation Of Motion
FEA	= Finite Element Analysis
FFT	= Fast Fourier Transform
FIR	= Finite Impulse Response
I/O	= Input/Output
IV	= Instrumental Variable
LLS	= Linear Least Squares
MA	= Moving-Average
MDOF	= Multi Degree-Of-Freedom
MIMO	=Multi-Input Multi-Output
PDF	= Probability Density Function
RB	= Rigid Body
SDE	= Stiffness-Damping Element
SISO	= Single-Input Single-Output
TF	= Transfer Function
ZOH	= Zero Order Hold
ZP	= Zero-Pole

ESTIMATION OF PHYSICAL PARAMETERS IN MECHANICAL SYSTEMS FOR PREDICTIVE MONITORING AND DIAGNOSIS

1. INTRODUCTION

1.1 General Context

The supervision of technical processes has become more important in the course of progressive automation. The need for minimizing plant machinery downtime has prompted the development of computer based conditioning, monitoring and diagnosis systems to observe machine-operating behavior and predict malfunction or failure before that condition is reached. Thus, undesirable behavior can be avoided and machine repair can be scheduled without unexpected interruption to plant production. For the general understanding the following definitions have to be made:

Monitoring - According to Szafarczyk (1990), monitoring means to watch over chosen features of the process as an aid to ensure the continuing achievement of the required level of product quality, and where appropriate, to measure significant parameters and to record them if required.

Diagnosis - Diagnosis means identification, classification and correction of malfunctions. It is the proceeding step after monitoring, and is based on the relationship between the observed condition of the system and a reference model.

With diagnosis one expects to assess the place, the kind and the cause of a functional disturbance.

According to Takata & Sata (1986) and Mitchell (1981) monitoring and diagnosis holds a promise of great reduction in lost production time and a decrease in maintenance costs. For example, if a failure can be predicted, maintenance can be scheduled in non-productive periods and the necessary spare parts can be ordered in advance. A detection of failures in their early stages would give the possibility of forecasting and eventually avoiding major breakdowns.

In general, a monitoring system for automatic supervision consists of six cascaded operations represented in Fig. 1.1 (Spiewak, 1994). Functions of these blocks are described below:

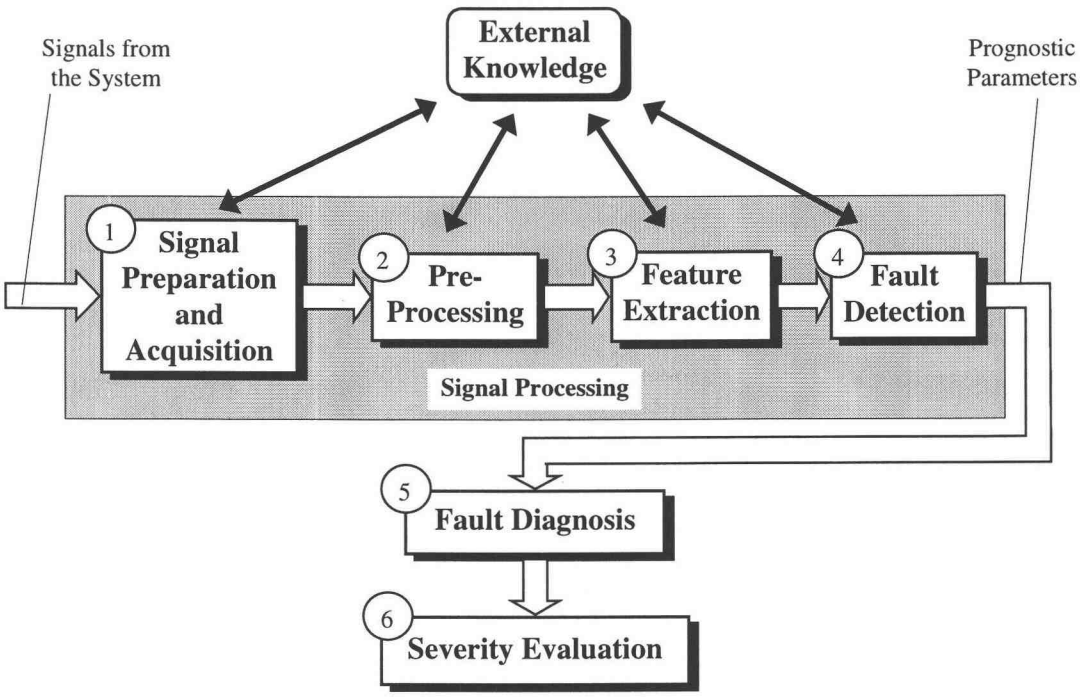

Fig. 1.1: A block diagram of the monitoring chain (Spiewak, 1994).

(1) Signal Preparation and Data Acquisition:

This block has the function of acquiring all the signals, digitizing and storing them in the computer. Advanced systems can also adjust the gain and sampling frequency to maximize the signal-to-noise ratio and minimize quantization errors. Research is also underway on self-tuning sensors, which automatically adapt to a changing working environment (Spiewak and Di Corpo, 1991; Chung, 1993), and fault tolerant sensors, which indicate and compensate sensor malfunctions automatically. These sensors continue to work with acceptable performance even after a sensor malfunction has occurred.

(2) Pre-Processing:

The pre-processing block represents all signal processing techniques to emphasize important features, which are contained in the signal. The functions range from suppression of noise, Fast Fourier Transformation (FFT) and spectrum analysis, to time-series based parametric identification of structures. These functions involve processing of huge amounts of data in a short period of time.

(3) Feature Extraction:

This block converts the more or less abstract data obtained from pre-processing into physical properties or phenomena in the monitored object. The extraction of features representing different failures can be extremely difficult, in part because there are no generic feature extraction algorithms readily available. Instead, there is a broad spectrum of techniques, which need to be adapted to each particular type of monitored object.

(4) Fault Detection:

A fault is to be understood as a non-permitted deviation of a characteristic property, which leads to the inability to fulfil the intended purpose. The features extracted by the previous block are used in the fault detection block to determine whether any

abnormal condition exists. This is done by comparing the current and a past healthy state of the machine.

(5) Fault Diagnosis:

If a fault is detected in the Fault Detection Block, then the location and type of fault should be determined. A database of past failures can aid in such a diagnosis and help to establish the cause of the fault.

(6) Severity Evaluation:

The next step is a severity evaluation that means assessing how the fault affects the process. After the effect of the fault is known a decision on the action to be taken can be made. If the fault is evaluated to be tolerable, the operation may continue and if it is conditionally tolerable a change of operation has to be performed. However, if the fault is intolerable, the operation must be stopped immediately and the fault must be eliminated.

Traditionally signal based methods were used for monitoring and failure prevention. However system analysis, which involves building and analyzing a model instead of signal analysis can provide much deeper insight into the dynamic behavior of the machine.

Until recently process supervision and monitoring was mainly performed by limit value checking of some important and measurable process variables. While this approach is straightforward, it does not take into account how those limits vary according to the state of the system. Disturbances can easily set off an alarm, even if no fault is present. Also, process faults are only detected at a rather late stage after the fault finally affects the measured output, assuming the supervision is based on this simple method. This method of limit observation is not sufficient to allow the operation of machinery without human supervision. Human operators are still required for the supervision of processes. They use their own "sensors" (e.g., noise,

vibrations, temperature, visual inspection), data records and long term experience to obtain the required information on process changes. If the process is going to be automated, a natural first step consists of adding further sensors and a second step is to transfer the operator's knowledge into computers as much as possible. It is usually desirable to add sensors which directly indicate faults. Because the number of sensors, transmitters and cables increases, the overall reliability is not necessarily improved. The probability of miss-alarm increases and fault detection as well as diagnosis might even become more difficult due to contradicting features in many different signals from the machine. Also, many faults cannot be detected directly by available sensors.

Digital computers and microprocessors enable the use of sophisticated methods, which can detect faults in the process earlier and locate them better. Efforts have been made (Szafarczyk, 1994; Isermann, 1984; Willsky, 1976) to trace process changes by using process models and fewer sensors, which don't necessarily detect faults directly, but which provide information about the process through system identification. Such model-based methods utilize information of an analytical model to evaluate the measured signals. Data generated from the analytical model is compared with sensor signals from the actual machine and the results further analyzed (usually involving statistical testing) to arrive at a diagnostic decision.

1.2 Problem Statement

This research is concerned with predictive supervision of manufacturing equipment in general, and metal cutting machine tools in particular. Their dynamic behavior is determined by the values of physical parameters such as masses, stiffnesses and damping coefficients. If critical physical parameters of machine tools are monitored on-line, changes in their values can be used to indicate process changes or

system faults. In addition this facilitates diagnosis and prediction of machine breakdowns.

A systematic approach is sought on how to monitor physical parameters of mechanical systems. Physical parameters are inherent features of analytical models, which are referred to in this thesis as "*gray box*" models. In particular three techniques of modeling structures in the area of mechanics are relevant in this thesis and therefore described below.

Class 1: Constitutive, analytical models - Building models from first principles using Newton's method is a well-established approach. The resulting equation of motion (EOM) for linear lumped parameter systems is a set of second order differential equation shown below in vector-matrix form

$$\mathbf{m}\ \ddot{\mathbf{d}}(t) + \mathbf{c}\ \dot{\mathbf{d}}(t) + \mathbf{k}\ \mathbf{d}(t) = \mathbf{F}(t) \tag{1.1}$$

Other methods such as Lagrange's or Kane's method derive this model efficiently using the concept of energies or generalized forces respectively. Even being the oldest modeling technique available, this class is not as popular as the other classes described below. The main reason is that until recently no efficient software tool was available to build these models with the aid of a computer.

Class 2: Constitutive, numerical models - The most common way of modeling machine tools at present is by Finite Element Analysis (FEA). With FEA complex structures can be modeled with controlled accuracy. This is accomplished by varying the degree of mesh of elements. This method is widely accepted in industry and aids machine tool designers in predicting the behavior of machines. However FE modeling is not suited well for the objective set forth in this research. First, FE models are of numeric nature, and as a result, there is no clear mapping between physical parameters

in the actual system and their representation in the model. Second, if the FE model does not agree with experimental results, on-line adjustment of parameters is difficult. The entire model needs to be recalculated resulting in time consuming computations. It is difficult to build cause-effect relationships, which indicate the type and degree of modification needed by designers to improve the FE model.

Class 3: Empirical, numerical models - It is also possible to build models entirely from experimental data. No physical insight is necessary to determine the structure of these models. They are therefore referred to as "*black box*" models. Such a system usually has multiple inputs **u**(t) and outputs **y**(t) and also disturbances **n**(t) as shown in Fig. 1.2 (Franklin and Powell, 1994).

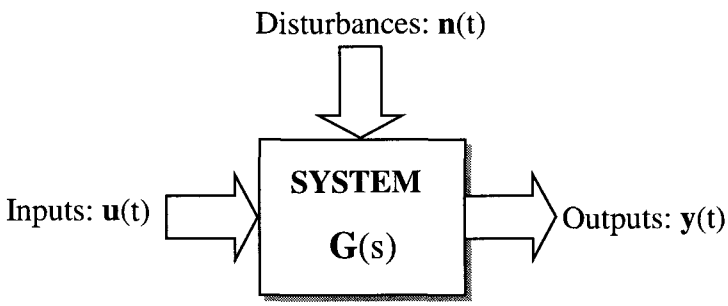

Fig. 1.2: A multi-input multi-output (MIMO) system

The relationship between individual inputs $u_i(t)$ and outputs $y_j(t)$ can be described by an arbitrary equation in time or frequency domain. Commonly a rational polynomial in the *s*-domain is used as follows

$$G_{ij}(s) = \frac{Y_i(s)}{U_j(s)} = \frac{b_p s^p + b_{p-1} s^{p-1} + \ldots + b_2 s^2 + b_1 s + b_0}{s^q + a_{q-1} s^{q-1} + \ldots + a_2 s^2 + a_1 s + a_0} \qquad (1.2)$$

The constants a_i and b_j in Eq. (1.2) are referred to as model coefficients. They don't have any physical meaning and have to be distinguished clearly from constants in Eq. (1.1) which are actual physical parameters in the system. A mapping exists between the black box model coefficients and physical parameters. However without a constitutive, analytical model (gray box) this relationship can not be explored. There are many efficient methods available to estimate the model coefficients very accurately (see Section 2.1.3) and therefore the behavior of those models resembles the actual systems very closely.

Despite extensive research on experimental identification as well as analytical modeling, none of the above models is particularly suited for the goal of physical parameter estimation set forth in this thesis. A framework needs to be established to integrate the existing methods to accomplish the objective of predictive monitoring through physical parameter estimation.

1.3 Proposed Solution

The objective of this research is to develop a methodology for physical parameter estimation facilitating predictive monitoring and diagnosis of mechanical systems. This integrates computer aided model derivation, validation and estimation. The focus is on rigid body models since they are well suited for the task of parameter estimation. These models apply to lumped parameter structures and are expandable to include flexible modes of machines as well. This can be accomplished through "rigid body approximation" or through component mode synthesis. Monitoring physical parameters of such a model is based on estimating their values using experimental data. Three estimation techniques are of particular interest in this thesis:

(1) A "two step" identification procedure. The first step is parametric identification of model coefficients in Eq. (1.2). The second step is comparison of these model coefficients with their respective analytical counterparts. An appropriate performance index is built which can be minimized with respect to the unknown physical parameters.

(2) Minimization of prediction error in time-domain. This is based on the comparison between the response of the actual system and the response of the model excited by the same input signal.

(3) Estimation by training of neural networks. This is predicated on the network's ability to recognize physical parameters based on selected features of the signal.

In this research the first two methods are applied since they involve gray box models. Successful application of one of these methods leads to improved monitoring of machine tools and facilitates diagnosis of faults and prediction of machine breakdowns. In addition there are further benefits:

a) Means of achieving high quality of machined parts;
b) Performance assessment of machine tools;
c) Means to improve design of machine controllers;
d) Assistance for designers to analyze and predict the dynamic behavior of machines.

Accurate computer implementation of features such as arbitrary precision calculations and robust algorithms for finding global minima of complex shaped performance indices is critical. Two systems described below are used to investigated and validate various methods of modeling and parameter estimation.

Simple multi degree-of-freedom (MDOF) system - An experimental set-up comprises two lumped masses supported by a vertical plate through two I-beams, as shown in

Fig. 1.3. Details can be found in Chapter 5.3. Because of its simplicity this set-up allows straightforward mapping between the physical system and its symbolic representation in the constitutive model.

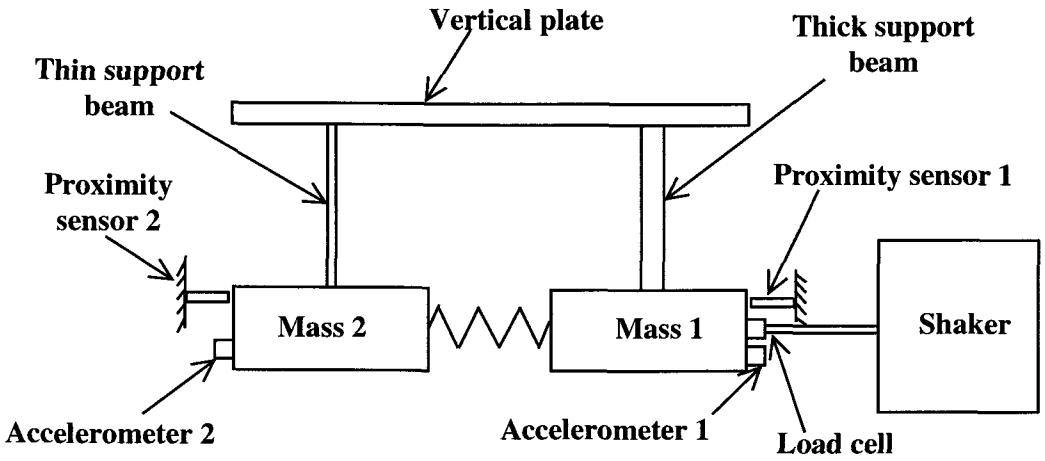

Fig. 1.3: Component top view of the experimental set-up of a simple MDOF system.

Rotor-bearing system - An experimental set-up comprising a small size, medium speed machine tool spindle is investigated.[1] A simplified view of the system is shown in Fig. 1.4. Building a constitutive model of such a system is impossible by hand. Therefore a methodology of computer aided model derivation is developed and applied to this set-up. It uses Lagrange's energy method, linear algebra, homogeous transformations to facilitate efficient model building. The derived model contains physical parameters (e. g. masses, stiffnesses and dampings) of the system in symbolic form which then can be estimated using experimental data.

[1] This spindle was formerly installed on a transfer line in an automotive plant and is therefore well suited for the proposed concept of physical parameter estimation.

Bearings of the machine tool are modeled by linear springs. The bearing stiffnesses are physical parameters of the system and can be estimated with the proposed method. Changes in these stiffnesses indicate a preload change in the bearing caused by temperature variations (Tu, 1991). Excessive preload leads to thermal instability and bearing seizure. The methodology developed in this research can be used to monitor bearing preload and predict bearing failure.

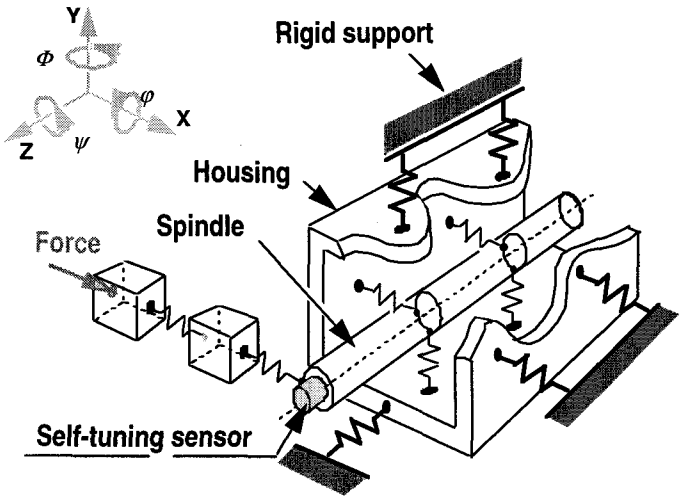

Fig. 1.4: A 'rigid body' model of the spindle.

1.4 Chapter Outline

In Chapter 2 a review of selected literature relevant to the concept of physical parameter estimation is presented. This includes a description of methods pertaining to experimental system identification as well as spindle modeling. In Chapter 3 a methodology for computer aided model derivation of complex mechanical systems is presented. Cases of increasing complexity are used to illustrate important features of

incremental model building. Various methods of estimating physical parameters are then proposed.

Successful application of the theory derived in the previous chapter hinges on accurate implementation of computations. Arbitrary precision calculations and global minimization are important aspects of that. This is presented in Chapter 4. Also additional issues such as model validation and simulations are discussed. Chapter 5 describes the experimental investigation of two representative systems mentioned in the preceding section and presents estimation results. Conclusions and recommendations for future research are presented in Chapter 6.

2. LITERATURE REVIEW

Successful identification of parameters in mechanical systems hinges upon key concepts of *System Identification*, (Young, 1981) developed in various disciplines of science (e.g. estimation theory, time series analysis) and engineering (e.g. control, vibrations). Physical parameter estimation depends heavily on advancements in the areas of experimental identification and analytical modeling, as discussed in Section 1.2. The review presented below is, therefore, focused on these two important fields of control theory. Due to the lack of consistent nomenclature in the reviewed research an attempt has been made to establish some common definition, terminology and notation.

2.1 System Identification

Experimental system identification deals with the problem of building mathematical models of dynamic systems based on observed data from those systems. It is an attempt to link multiple and often loosely related observations into a coherent and informative pattern.

Literature on system identification is extensive. Vast research in this area has been done since the seventies and many of the methods developed then are still used today. Important survey papers include Billings (1980), Unbehauen (1990) and Wellstead (1981). Main references, which cover the whole subject comprehensively, include Ljung (1987), Eykhoff (1974) and Norton (1986). In general, system identification involves four entities:

(1) The data record;

This should be maximally informative by the choice of when or where to measure signals and/or the type of input signals. There are four types of experimental data which can be used for system identification:

a. **Transient response**, such as obtained in the impulse or step test;

b. **Frequency response** which results from exciting the system with sinusoidal inputs;

c. **Response to ambient excitation**, as might come from steady state observation of a process which has natural sources of randomness. An example would be data from an aircraft flying through turbulent air;

d. **Well defined response to random or pseudo-random signal applied to one or more inputs**, as may be generated by a digital computer and used as an input to a process, the output of which is then recorded and analyzed.

(2) A set of candidate models;

A priori knowledge about the system and engineering intuition needs to be used to choose a suitable model. Based upon whether the physical background is involved or not, the selected model can be classified as a *black-box* or *gray-box* model as discussed in the following section.

(3) Determining the best model in the set;

This phase involves model order estimation and subsequent model coefficient estimation. A higher model order usually allows a better fit between the model and the experimental data.

(4) Model validation;

After the three previous tasks have been performed one has arrived at one particular model which best describes the data according to the chosen criterion. Model validation is the following step to test whether the chosen model is "good enough" for its purpose.

None of the identification techniques that are discussed in this thesis is universal in the sense of being capable to identify any system. Each of the techniques presented has its own range of applicability, but all are designed based on one general problem, which is to find the best fit of a model to experimental data. To find the characteristics of the system without knowing its input is referred to as *blind identification.*

2.1.1 Classification of Identification Techniques

Identification can be classified in several different ways. A major distinction can be made between (1) non-parametric identification methods, (Wellstead, 1981) and (2) parametric identification methods, (Astrom, 1980). Non-parametric methods aim at determining transfer functions or corresponding impulse responses by direct techniques, without first selecting a confined set of possible models. Those methods include time-domain techniques such as transient response analysis and correlation analysis as well as frequency-domain techniques such as Fourier analysis and Spectral analysis. Parametric identification techniques are, for example, the Least-Squares method or the Maximum-Likelihood method. They usually require discrete transfer function models of identified systems or difference equations. Those methods will be described in more detail in Section 2.1.3.

Another classification is based upon the amount of information available at the beginning of the identification process and discerns the following chores (Ljung, 1994):

1. **Complete Identification:** No basic a priori knowledge about the system such as its linearity or stationarity is available. Assumptions have to be made about the system's behavior. Standard linear models may be employed without

reference to the physical background. Such models, who's coefficients are basically viewed as means for adjusting the fit to the data and do not necessarily reflect physical considerations in the system, are called "*black-box*" models.

2. **Partial Identification:** When *a priori* knowledge about the system leads to the model structure, then only the values of the model coefficients need to be determined. Therefore, the problem becomes easier. Since some features of the system are known, it is therefore referred to as a "*gray-box*" problem.

With regard to physical parameter estimation, the available methods have to be assessed as to whether actual physical properties of the system can be recovered. Table 2.1 shows a comparison of different models and how various quantities characterizing the modeled system can be computed.

Table 2.1: Assessment of features characterizing dynamic systems based on different models.

Type of Model / Identified Features	Empirical Non-Parametric	Parametric	
		Empirical (Black Box)	Constitutive (Gray Box)
Shape of Response	Time-Domain Methods Frequency-Domain Methods	Readily Available	Readily Available
Model Coefficients	No Direct Assessment *	Direct Identification Possible **	Direct Identification Possible
Physical Parameters	N/A	N/A	Explicit Relationship

* Indirect assessment possible through curve fitting (see Section 2.1.2)

** Many methods available (see Section 2.1.3)

Subject of this research

The identification techniques can also be divided according to the time when they are performed. Identification can be done on-line or off-line. According to Isermann (1981), on-line identification means the identification with computers in on-line operation with the process. In this mode the estimation of model parameters is performed at the same time the experimental data is taken. On-line processing is most frequently implemented recursively, meaning signals are processed and parameters updated after each new data value is recorded. On-line algorithms are desirable in time-critical applications. However, the actual real-time applicability of algorithms strongly depends upon their hardware implementations and the process dynamics. Due to time constraints, the accuracy and the flexibility of on-line identification methods are lower compared to off-line methods.

If the measured signals are first stored in a block or in arrays, this is called batch processing or off-line operation. Off-line usually allows applying suitable input signals, which do not act on the identified system during their normal operation. Off-line processing generally yields more accurate parameters and more flexibility in the selection of the model structure, its order and type of the input signal acting on the process.

2.1.2 Non-Parametric Identification Methods

Non-parametric methods assess features of unstructured system models. Those methods relay only on operational data and evaluate their statistical properties. The result is a time-series of data points, which can be displayed graphically but not in a form of an analytical equation.

The theoretical evolution of the most basic techniques, the impulse and frequency response methods, can be traced to the pair of relations

$$R_{xy}(\tau) = h(\tau) * R_{xx}(\tau) \tag{2.1a}$$

$$S_{xy}(j\omega) = H(j\omega) * S_{xx}(\omega) \tag{2.1b}$$

where $R_{xx}(\tau)$, and $R_{xy}(\tau)$ are the auto-correlation of $x(t)$ and the cross-correlation of $x(t)$ with $y(t)$, respectively, and "*" denotes convolution (Stark et al, 1994). $h(\tau)$ and $H(j\omega)$ are the impulse response and the frequency response of a linear system respectively. Likewise $S_{xx}(\omega)$ and $S_{xy}(\omega)$ are the auto-spectrum of $x(t)$ and the cross-spectrum (also called cross-power spectral density) of $x(t)$ with $y(t)$ respectively, defined by the Fourier transform (Stark et al, 1994)

$$S_{xx}(\omega) = \int_{-\infty}^{+\infty} e^{-j\omega\tau} R_{xx}(\tau)\, d\tau \tag{2.2a}$$

$$S_{xy}(\omega) = \int_{-\infty}^{+\infty} e^{-j\omega\tau} R_{xy}(\tau)\, d\tau . \tag{2.2b}$$

Once $S_{xx}(\omega)$ and $S_{xy}(\omega)$ have been computed, the impulse response $h(\tau)$ and frequency response $H(j\omega)$ can be calculated.

$$h(\tau) = \mathcal{F}^{-1}\left[H(j\omega)\right] = \mathcal{F}^{-1}\left[\frac{S_{xy}(j\omega)}{S_{xx}(j\omega)}\right] \tag{2.3}$$

where $\mathcal{F}^{-1}$ is the inverse Fourier transform. This result is a quantitative but unstructured description of the investigated system. Critical features of the system can be identified, but the result is not useful for further analytical analysis.

Curve fitting of the frequency response can be used to overcome this disadvantage. A parametric model is used to approximate unstructured result. Once the frequency response is obtained from measurements one can derive a linear system model by calculating the least square fit of the frequency response data to a rational polynomial of a chosen order. After this curve fit is complete, the numerator and denominator of the polynomial are factored to obtain zeros and poles. Currently there

are systems available (e.g. Spectrum Analyzer (Hewlett Packard, 1997)), which do this type of curve fitting automatically. However proper engineering judgement needs to be used in evaluating the results. For example repeated root and heavily dampened poles can "hide" behind lightly damped poles. Also data errors in the frequency response measurements such as non-linearity, noise or quantization errors can prevent any curve fit algorithm from easily finding a linear model.

Most of these non-parametric techniques apply only to time-invariant linear systems. Nonlinear systems can be identified by non-parametric means if these systems can be linearized about some working point and the inputs can be kept about this point. These methods often require the employment of special input signals, such as an impulse, a step, a sine wave with variable frequency or white noise. Both, the time- and frequency-domain response methods are well documented (Wellstead, 1981; Rake, 1980). However they are rarely suitable for on-line applications, so data must be collected as part of special tests. The transient response method is quick, but the data does not come in a form immediately suitable for physical parameter estimation, which is the topic of this research. Additional computations are needed to obtain for example poles and zeros of the model (Ziegler and Nichols, 1942). In contrast, the frequency response method is more time consuming, but it provides results in a form, which is more convenient for the assessment of physical parameters. The derivation of dynamic models from operational records or from the response to a pseudo-random input can be based on the concept of cross-correlation (Bendat and Piersol, 1986; Press et al., 1994).

Parametric identification techniques, on the other hand, can handle almost any type of input signal, but at the expense of increased computational burden. In this research, parametric methods are more suitable to physical parameter estimation since they can be put into relation to gray box models. Model coefficients of parametric models are functions of physical parameters and this relationship is essential in this research.

2.1.3 Parametric Identification Methods Based on Black Box Models

In the field of parametric identification there are numerous methods documented in the literature (Astrom, 1971; Billings, 1980; Young, 1984). For single-input single-output (SISO) systems Ljung (1987) proposes a general family of model structures

$$A(q)y(t) = \frac{B(q)}{F(q)}u(t) + \frac{C(q)}{D(q)}n(t) \tag{2.4}$$

where A, B, C, D and F are polynomial functions in the forward time shift operator q such as

$$A(q) = 1 + a_1 q^{-1} + a_2 q^{-2} + \ldots + a_n q^{-k} \tag{2.5}$$

A block diagram of this model is presented below.

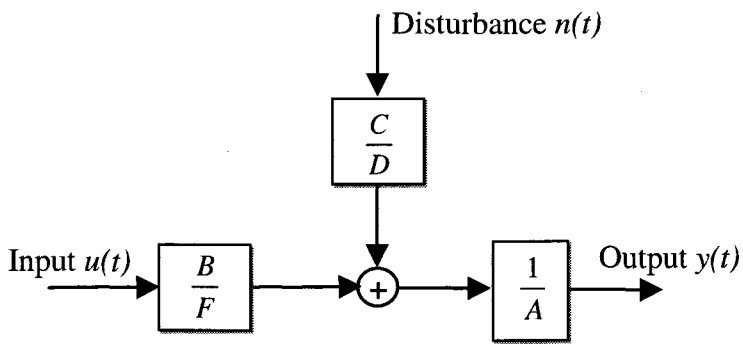

Fig. 2.1: Block diagram of a general model described by Eq. 2.4.

In most practical applications this structure (Eq. 2.4 and Fig 2.1) is too general. Therefore, depending on the information available about the system, only selected

polynomials are used. Several of the most common used model sets are listed in Table 2.2 below.

Table 2.2: Some common black-box SISO models as special cases of Eq. (2.4).

Model Structure	Equation
FIR (Finite Impulse Response)	$y(t) = B(q)\ u(t)$
ARX & Equation Error (EE)	$y(t) = \frac{B(q)}{A(q)}\ u(t) + \frac{1}{A(q)}\ n(t)$
Output Error (OE)	$y(t) = \frac{B(q)}{F(q)}\ u(t) + n(t)$
ARMA	$y(t) = \frac{C(q)}{A(q)}\ n(t)$
ARMAX	$y(t) = \frac{B(q)}{A(q)}\ u(t) + \frac{C(q)}{A(q)}\ n(t)$
BJ (Box-Jenkins)	$y(t) = \frac{B(q)}{F(q)}\ u(t) + \frac{C(q)}{D(q)}\ n(t)$

In this research the ARMAX model is used, where AR refers to the auto-regressive part $A(q)\ y(t)$, MA refers to the moving-average part $C(q)\ n(t)$, and X refers to the extra input $B(q)\ u(t)$ (Pandit and Wu, 1983). This model has become a standard tool in control design. A block diagram is shown below.

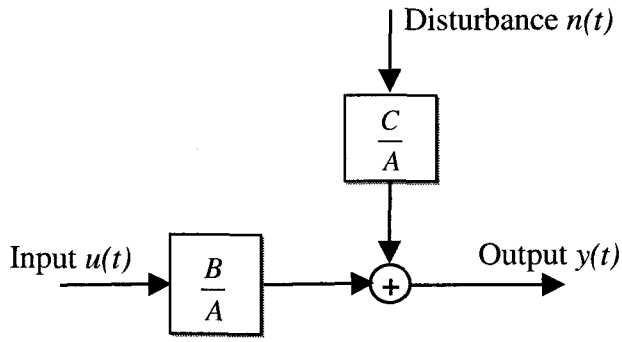

Fig. 2.2: ARMAX model.

Once a model structure is chosen, parametric identification reduces to the problem of determining model coefficients. A general set of coefficients Λ_g is selected where the members of the set are the coefficients a_k, b_l, c_m, d_n and f_o of the polynomials *A(q)*, *B(q)*, *C(q)*, *D(q)* and *F(q)* from Eq. (2.4) respectively.

$$\Lambda_g = \{a_0, a_1, a_2, ..., b_0, b_1, b_2, ..., c_0, c_1, c_2, ..., d_0, d_1, d_2, ..., f_0, f_1, f_2, ...\} \tag{2.6}$$

For simple linear cases there is an analytical closed form solution and thus the model coefficients can be determined uniquely. Using *Linear Least Squares* (LLS) is the method of choice in these cases. Conceptual simplicity makes it applicable to a wide variety of situations. The method is based on the minimization of a merit function representing the sum of squared residuals (Hsia, 1977):

$$Q(\Lambda_g) = \sum_{i=1}^{N} [e_i(\Lambda_g)]^2 \tag{2.7}$$

The variable $e_i(\Lambda_g) = y_i - \hat{y}_i(\Lambda_g)$ is the prediction error, where y_i is the observed output and $\hat{y}_i$ the output predicted on the basis of the model and is a function of parameters Λ_g. An advantage of this method is that the global minimum of the merit function $Q(\Lambda_g)$ is found efficiently and unambiguously by analytical minimization if $e(\Lambda_g)$ is linear in Λ_g, (Ljung, 1987).

In general however, the error is nonlinear in Λ_g and thus a closed form solution does not exist. Iterative methods are needed to optimally estimate the model coefficients. Figure 2.3 illustrates the general approach.

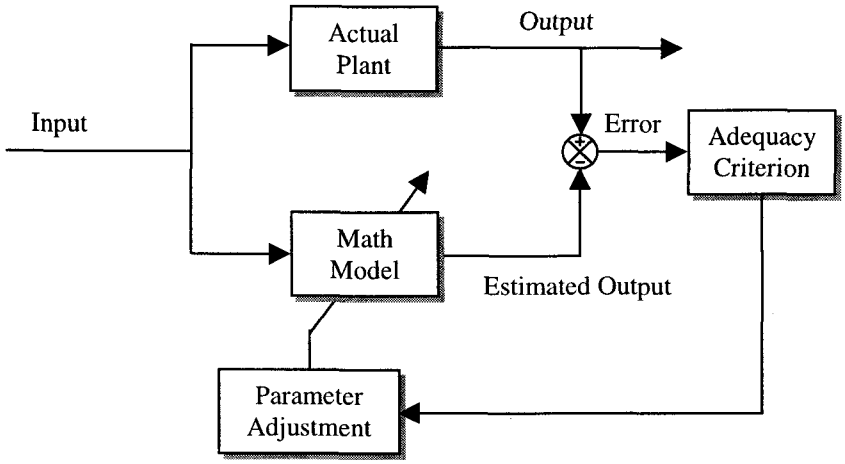

Fig. 2.3: Plant-model comparison in parametric system identification.

Out of the numerous techniques available to adjust the model parameters for an optimal fit, only the Non-Linear Least Squares method (Hsia, 1977) and the Maximum-Likelihood method (Box, 1976; Astrom, 1980) are described, since they are suitable for computer applications and representative of the other methods.

Non-Linear Least-Squares Method - This is an extension of the LLS method described above. If the minimization of Eq. (2.7) can not be found analytically numerical minimization techniques are applied. The merit function $Q(\Lambda_g)$ is minimized with respect to Λ_g until the global minimum is found. This usually consists of two steps, the initial guess and the final guess routine. The purpose of the initial guess is the determination of optimal starting values for the final minimization procedure. Since

the shape of the merit function usually is very complex an uncorrect initial guess can lead to wrong final estimates of model coefficients.

The Maximum-Likelihood Method - The Maximum-Likelihood Method (Astrom, 1980) is derived from the probability density function (PDF) of the output y_i. $\mathbf{\Lambda_g}$ is an unknown parameter vector of the system to be identified and σ is the known standard deviation of the residuals $e(\mathbf{\Lambda_g})$. Assuming independent observations and a gaussian probability density of the individual observations, the PDF for y_i is

$$p\left(y_i\middle|\mathbf{\Lambda_g}\right)=\frac{1}{\sigma\sqrt{2\pi}}\ \exp\left[-\frac{\left(y_i-\hat{y}_i\left(\mathbf{\Lambda_g}\right)\right)^2}{2\sigma^2}\right] \tag{2.8}$$

The output y_i is a function of the parameter vector $\mathbf{\Lambda_g}$. For the case of an N sample long output record the likelihood function $L\left(y\middle|\mathbf{\Lambda_g}\right)$ is written as a product of the individual PDFs.

$$L\left(y\middle|\mathbf{\Lambda_g}\right)=\left(\sigma\sqrt{2\pi}\right)^{-N}\ \exp\left[-\frac{1}{2\sigma^2}\sum_{i=1}^{N}\left(y_i-\hat{y}_i\left(\mathbf{\Lambda_g}\right)\right)^2\right] \tag{2.9}$$

This function is usually expressed in the logarithmic form as

$$\ln L\left(y\middle|\mathbf{\Lambda_g}\right)=-N\ln\sigma-\frac{N}{2}\ln(2\pi)-\frac{1}{2\sigma^2}\sum_{i=1}^{N}\left(y_i-\hat{y}_i\left(\mathbf{\Lambda_g}\right)\right)^2 \tag{2.10}$$

The above equation shows that when σ is known, the maximization of $L\left(y\middle|\mathbf{\Lambda_g}\right)$ simplifies to the minimization of

$$V\left(y\middle|\mathbf{\Lambda_g}\middle|\right)=\sum_{i=1}^{N}\left(y_i-\hat{y}_i\left(\mathbf{\Lambda_g}\right)\right)^2 \tag{2.11}$$

This is equivalent to the criterion of the linear least squares method (compare Eq. (2.7)). If σ is unknown, the optimization of $L\left(y\middle|\mathbf{\Lambda_g}\right)$ with respect to $\mathbf{\Lambda_g}$ and σ has to be performed iteratively. The Maximum Likelihood method yields unbiased, efficient

and gaussian distributed estimators. Its major drawback is the heavy computational load.

Recently, new minimization methods have been developed (e.g. genetic algorithms and simulated annealing) which hold the promise of better and faster convergence than standard gradient based methods. Since they are based on statistical features, they can deal with functions where gradients can not be calculated. In addition, they can handle functions with multiple local minima. Selected successful solutions of difficult cases are documented in the literature, however no generally accepted algorithm exists at present (Gelb, 1988; Ingber, 1992).

2.2 Physical Parameter Estimation

The problem of physical parameter estimation has many features similar as discussed above. However there are unique characteristics, which limit the applicability of methods developed in the area of system identification. The estimation of physical quantities requires the availability of gray box models. No comprehensive methodology can be found in the literature, which integrates model building, validation and estimation. Some research has been done to cover selected aspects of the proposed approach and is documented here.

Estimation in time-domain - One conceptual straightforward method (Link, 1985; Leuridian, 1981) involves the differential EOM given by Eq. (1.1) in vector-matrix form.

$$\mathbf{m}\,\ddot{\mathbf{d}} + \mathbf{c}\,\dot{\mathbf{d}} + \mathbf{k}\,\mathbf{d} = \mathbf{F} \tag{2.12}$$

This method of physical parameter estimation is referred to in this thesis as the *direct* method, since it consists of estimating the mass, damping and stiffness matrix **m**, **c** and **k** from measured system responses $\ddot{\mathbf{d}}$, $\dot{\mathbf{d}}$, **d** and the force input **F**. Measured accelerations, velocities, displacements and forces can be presented in vector form as follows

$$\mathbf{x} = \begin{pmatrix} \ddot{d}_1 \\ \ddot{d}_2 \\ \vdots \end{pmatrix}, \quad \mathbf{y} = \begin{pmatrix} \dot{d}_1 \\ \dot{d}_2 \\ \vdots \end{pmatrix}, \quad \mathbf{z} = \begin{pmatrix} d_1 \\ d_2 \\ \vdots \end{pmatrix}, \text{ and } \mathbf{F} = \begin{pmatrix} F_1 \\ F_2 \\ \vdots \end{pmatrix} \tag{2.13}$$

Then the dynamic model can be written as:

$$[\mathbf{m} \quad \mathbf{c} \quad \mathbf{k}] \cdot \begin{pmatrix} \mathbf{x} \\ \mathbf{y} \\ \mathbf{z} \end{pmatrix} = \mathbf{F} \tag{2.14}$$

If multiple measurements are taken, Eq (2.14) can be reformulated as a least square problem.

$$\mathbf{A} \cdot \mathbf{X} = \mathbf{B} \tag{2.15}$$

where **A** is a matrix of acceleration, velocity and displacement measurements, **X** is a vector of unknown physical parameters and **B** is a matrix of force measurements. If one can find the inverse of the measurement matrix **A**, there is a closed form solution in the form of[2]

$$\mathbf{X} = \mathbf{A}^{-1} \cdot \mathbf{B} \tag{2.16}$$

Depending on the presence of noise in these signals, special care needs to be taken when solving the above least square problem, e. g. using instrumental variables.

---

[2] If the matrix of measurements is not square a pseudo inverse can be found (see Appendix A3).

The instrumental variable method reduces the bias problem (Eq. (2.19)) when noise is present in the signals. It is based on a matrix referred to as the IV matrix, built from undisturbed output signals. These signals don't exist in the actual system, but they can be approximated from an auxiliary model. Fig. 2.4 illustrates the procedure. More details can be found in Fritzen (1986).

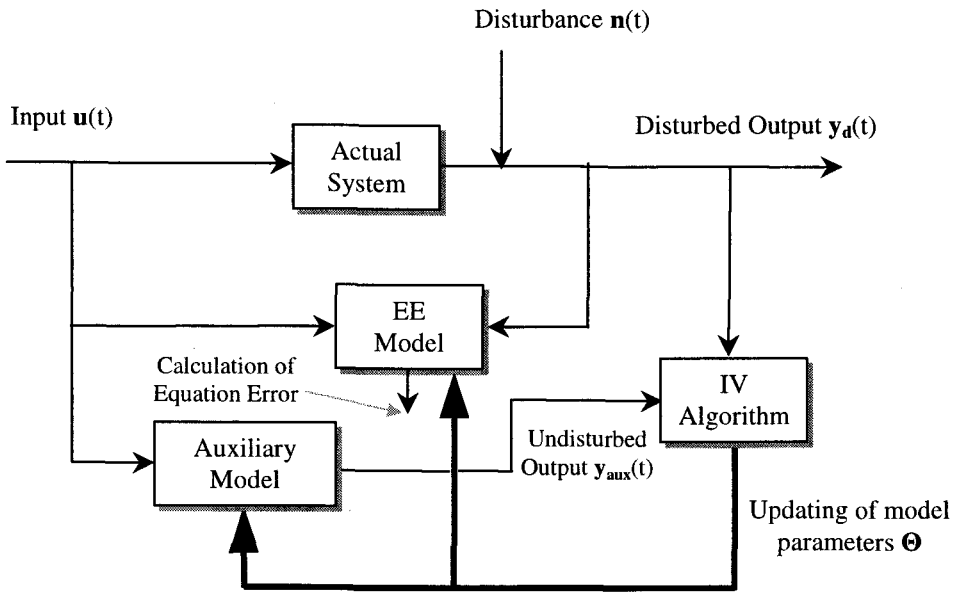

Fig. 2.4: Instrumental variable method.

The number of sensors necessary to use the direct method for higher order systems like the spindle assembly is extensive. Therefore this method has limited practical applicability for industrial monitoring problems.

Estimation in frequency-domain - A similar method can be used in the frequency domain where the Frequency Response Function (FRF) matrix, $\mathbf{H}(j\omega)$, is calculated, using the Fourier transformation

$$\mathbf{H}(j\omega) = \frac{1}{-\omega^2\mathbf{m} + j\omega\,\mathbf{c} + \mathbf{k}} \tag{2.17}$$

If the experimentally measured FRF is denoted by $\mathbf{H}_e(j\omega)$, then the error, $\Delta\mathbf{H}(j\omega)$, between the theoretical and measured FRF can be written as

$$\Delta\mathbf{H}(j\omega) = \mathbf{H}_e(j\omega) - \mathbf{H}(j\omega) = \mathbf{H}_e(j\omega) - \frac{1}{-\omega^2\mathbf{m} + j\omega\,\mathbf{c} + \mathbf{k}} \tag{2.18}$$

The aim is to find the characteristic matrices **m**, **c** and **k** that minimize the error between the experimental and the analytical FRF. Theoretically the direct method is straightforward, but it suffers from several practical problems (Leuridian, 1981). One of them is numerical instability arising when solving usually non-linear equations represented by the vector matrix Eq. (2.18). Also, if the number of unknown physical parameters is too large, the task becomes unmanageable for currently available minimization algorithms. Additional problems are due to the measurement noise in the transfer functions $\mathbf{H}_e(j\omega)$. Results in Eckert et al. (1984), in which the Least Square (LS) method was used to estimate parameters from a noisy FRF, showed that a 2% noise level could result in characteristic matrices with errors more than 200%. The effect of noise on the results as estimated by the LS method is referred to as the bias problem in system identification. The bias $\Delta\mathbf{p}$ denotes the systematic error of an estimator

$$\Delta\mathbf{p} = E\{\hat{\mathbf{p}} - \mathbf{p}_k\} = E\{\hat{\mathbf{p}}\} - \mathbf{p}_0 \neq 0 \tag{2.19}$$

where $\hat{\mathbf{p}}$ are the estimated and $\mathbf{p_0}$ are the true parameters and $E\{\bullet\}$ is the Expectation operator. For an unbiased estimation $E\{\hat{\mathbf{p}}\} = \mathbf{p}_0$. To obtain an unbiased estimation from a noisy process, the Instrumental Variable (IV) method (see Fig. 2.4) is widely applied (Wong and Polak, 1976; Young, 1970). In most of the work using the IV method, however it has been used to estimate parameters from discrete data in the time domain. In the work of Fritzen (1986), the IV method was used to reduce the bias problem from noisy data obtained in the frequency domain. The results in Fritzen

showed that the IV method was less sensitive to noise than the LS method. However, there are disadvantages of the IV method as compared with LS. Generally the IV method needs the FRF data in a broad frequency bandwidth, which results in a high computational burden.

"Two step" identification - Another class of methods, sometimes referred to as *indirect* are based on exploiting the relationship between coefficients, $\mathbf{\Lambda_p}$, of transfer function models from measured I/O signals and physical parameters $\mathbf{\Theta}$ from constitutive models (Isermann, 1991; Isermann, 1992; Dasgupta et al., 1988; Bohlin, 1994). $\mathbf{\Lambda_p}$ refers to a list of analytically obtained TF model coefficients a_i and b_j from Eq. (1.2).

$$\mathbf{\Lambda_p} = \{a_0, a_1, a_2, ..., b_0, b_1, b_2, ...\} \tag{2.20}$$

$\mathbf{\Theta}$ is a list of physical parameters, which are elements of the matrices **m**, **c** and **k** in Eq. (2.12).

$$\mathbf{\Theta} = \{m_1, m_2, m_3, ..., c_1, c_2, c_3, ..., k_1, k_2, k_3, ...\} \tag{2.21}$$

If the physical parameters, $\mathbf{\Theta}$, which indicate process faults are not directly measurable, an attempt can be made to determine their values via the changes in the experimental model coefficients, $\mathbf{\Lambda_p}$. The following procedure illustrated in Fig. 2.5 can be applied:

(a) Establishment of the analytical relationships for the measurable input and output variables.

$$y(t, \mathbf{\Theta}) = f\{u(t), \mathbf{\Theta}\} \tag{2.22}$$

(b) Determination of the relationship between the TF model coefficients $\mathbf{\Lambda_p}$ and the relevant elements of the physical parameter list $\mathbf{\Theta}$:

$$\Lambda_p = \Phi(\Theta) \tag{2.23}$$

where Φ is a column vector of functions.

(c) Estimation of the model coefficients Λ_p as a result of measurements $y(t)$ and $u(t)$[3].

(d) Calculation of the physical parameters through the inverse relationship

$$\Theta = \Phi^{-1}(\Lambda_p) \tag{2.24}$$

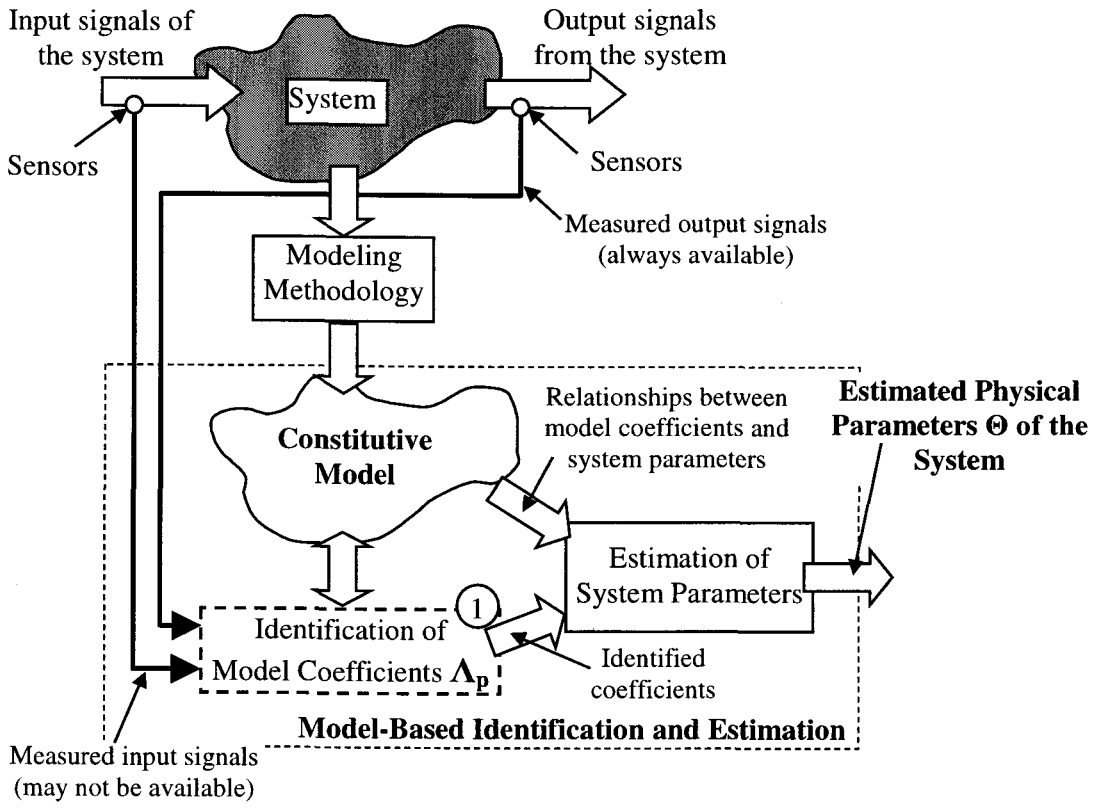

Fig. 2.5: A block diagram of the generic algorithm for parameter estimation (Spiewak, 1994).

[3] Common case in control theory.

A necessary condition for this procedure is the existence of a unique inverse relationship, Eq. (2.24); otherwise the physical parameters cannot be determined uniquely. Therefore it may be restricted to well-behaved processes which are invertible. Also, the estimated model coefficients need to be very accurate.

One step identification - Instead of applying the two step method, in which the estimation of physical parameters is very sensitive to errors introduced by inaccurate experimental identification, it is possible to estimate physical parameters using output signals from the actual system. The error between the response of the actual system and the response of the model excited by the same input signal is minimized with respect to the unknown physical parameters. This method is also illustrated in Fig 2.5 if step of identification of model coefficients (dashed block labeled ①) is not performed.

Other methods - Extensive research on estimation has also been done in the area of optimal filtering. Especially, Kalman filtering is a method of signal processing which gives optimal estimates of the current state of a dynamic system. This method has been originally developed by Kalman (1960) and can be applied to state-space models, which are linear in the parameters. In practice many time-series models are non-linear. Then it may be possible to apply an extended Kalman filter, by making a locally linear approximation to the model. This approach will be closer investigated in Section 3.6.3.

Another possible method is model updating, which is concerned with the correction of finite element models by processing records of dynamic response from test structures (Weaver and Johnston, 1987; Cheung and Leung, 1991; Fagan, 1992). FE modeling is usually considered to be inaccurate because of the idealization involved in structural modeling, while experimentally derived modal data are considered closer to the true representation of the structure. Bergman (1979) for example has proposed to update the mass matrix of the FE model such that it

reproduces the measured mode shape matrix. But since FE models generally are of high order they need to be condensed first to the size of the measured mode shape matrix. The mass modification matrix can then be defined as

$$\Delta \mathbf{M}_{\text{Bergman}} = \mathbf{M}_{FE}\Xi \left(\Xi^T \mathbf{M}_{FE}\Xi\right)^{-1} x \left(\mathbf{I} - \Xi^T \mathbf{M}_{FE}\Xi\right) \left(\Xi^T \mathbf{M}_{FE}\Xi\right)^{-1} \Xi^T \mathbf{M}_{FE} \tag{2.25}$$

where M_{FE} is the mass matrix of the condensed FE model and Ξ is the matrix of experimentally measured mode shapes. No equivalent method for updating the stiffness and damping matrix has been found. These matrices however are more critical in the context of monitoring than the mass matrix.

Despite the research over the past years in the area of model updating (Friswell and Mottershead, 1993; Ziaei-Rad, 1996; He and Ewins, 1991) no reliable and generally applicable procedures have been formulated so far. A review of the case studies reported in the literature (Natke, 1988; Impegrun and Visser, 1991) pinpoints the fundamental problem, namely non-uniqueness of a particular solution. Through the condensation of large FE matrices the relationship between physical parameters in the actual system and their representation in the model is lost. As a consequence, generated solutions do not necessarily represent true physical quantities. For the above reasons model updating is not suited for monitoring of physical parameters.

2.3 Spindle-Bearing Modeling

In this research analytical multi degrees-of-freedom (MDOF) models of machine tools are needed. Theoretically infinite order models are necessary to represent such distributed parameter systems accurately, but practically finite order models which account for a sufficient number of lower resonances are adequate. There is ample literature available on modeling of rotating machinery. The predominant approach involves finite element modeling (Isermann, 1992; Weaver and

Johnston, 1987; Carne et al., 1988; Reddy and Sharan, 1987). An accurate finite element model of the spindle-bearing system dealt with in this research has been derived by Comparin, (1983). Flexible modes have been identified and are listed in Table 5.9.

As mentioned in Chapter 1 those models are not suitable for physical parameter estimation, due to their computational burden and numerical[4] global nature. Desired models have lumped parameters, are modular and contain a clear mapping between physical quantities in the actual system and their representations in the model. In such models bearings are described as linear translating springs with constant stiffness coefficients in the radial and axial directions (Matsubara et al., 1988; Aini, 1990), (see Fig. 2.6).

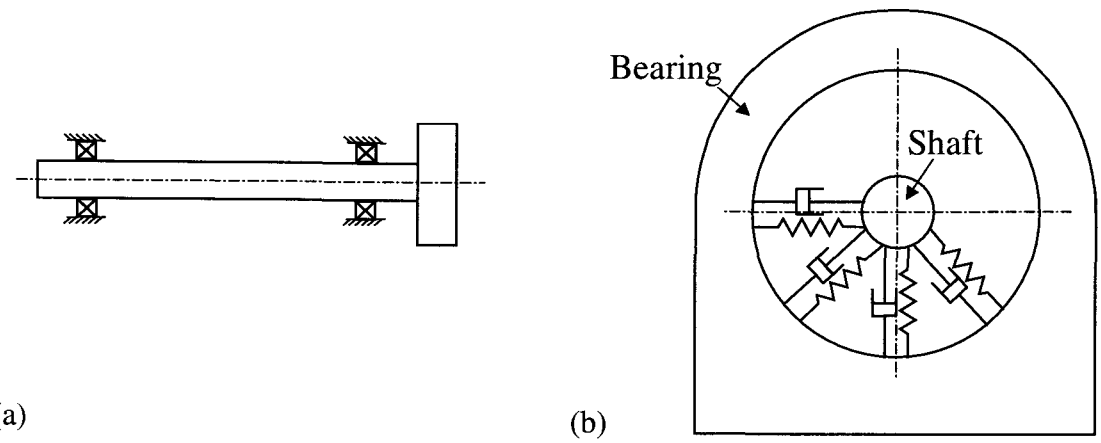

Fig. 2.6: (a) Machine tool spindle and (b) enlarged front view of modeling bearing characteristics with linear spring and damper elements.

[4] As opposed to analytical

Aini (1990) considers a five DOF model of a rigid shaft supported by a pair of angular contact bearings. The equations of motions (EOM) are derived (by hand) and then solved by the linear acceleration method (Timoshenko et al., 1974). The EOMs are non-linear and have many parameters. Other contributions (Shin et al., 1990; Segalman and Dohrmann, 1996) also show very accurate models of spindle-bearing arrangements, even considering elastic shafts, however the equations are derived by hand and thus only simple systems (consisting of one mass connected by springs to a rigid base) are considered.

In this research a lumped-parameter model for machine tools is sought which includes shaft, housing and base. Commercial packages capable of symbolic modeling exist (AUTOLEV, 1988; TSI, 1998) but they have cumbersome user interfaces and are not optimized for applications to machine tools. Therefore in this thesis a specialized software package of computer aided model derivation is developed.

2.4 Preload Monitoring

One application of physical parameter monitoring, closer investigated in this thesis, is the tracking of bearing preload. Therefore current techniques of preload monitoring are briefly reviewed here. Preload is defined as the amount of internally applied force, be it radial, axial or both to a bearing system (Harris, 1991). This internal force causes a initial deformation of the rolling elements and the raceways. Spindle bearings with a conventional lock nut are still the design of choice in modern machine tools to obtain the desired preload. Observation of the space between the inner races in the upper half of the spindle in Fig. 2.7 shows the case before preloading. This space is machined into the bearings to provide a known deflection of the rolling elements when the lock nut is tightened (see Fig. 2.7).

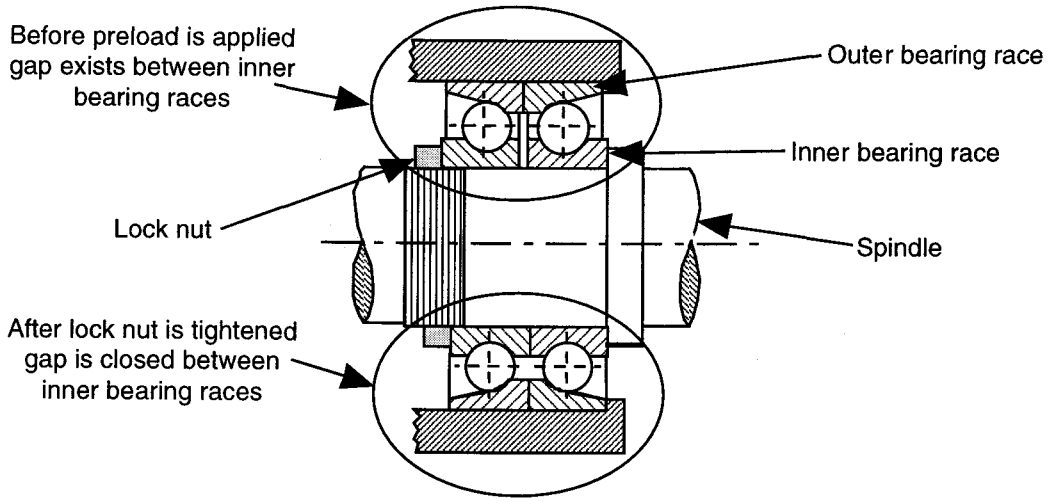

Fig. 2.7: Preloading by compressing the bearings.

Preloading is used to satisfy one or more of the following requirements: 1.) Eliminate all radial and axial play, 2.) Increase system rigidity, 3.) Reduce non-repetitive run-out, 4.) Limit the difference in contact angle between inner and outer rings at high speed and 5.) Prevent ball skidding under very high acceleration. Bearings should not be preloaded more than necessary to obtain the desired rigidity. Excessive preloads generate heat reduce speed capability and shorten bearing life (Harris, 1991; Tlusty, 1986; Weck, 1984). To avoid bearing seizure and possible bearing failure with a resulting machine break down, it is possible to monitor instantaneous bearing preload on-line. Changes could be detected and machining conditions adjusted to control the heat build-up. Direct preload monitoring involves custom equipped bearings, which are expensive and not feasible for off the shelf machine tools.

Following the same objective as presented in this thesis Tu (1991) developed an alternative method to monitor bearing preload. The method employs a thermo-mechanical model, which is partitioned into two components as shown in Fig. 2.8.

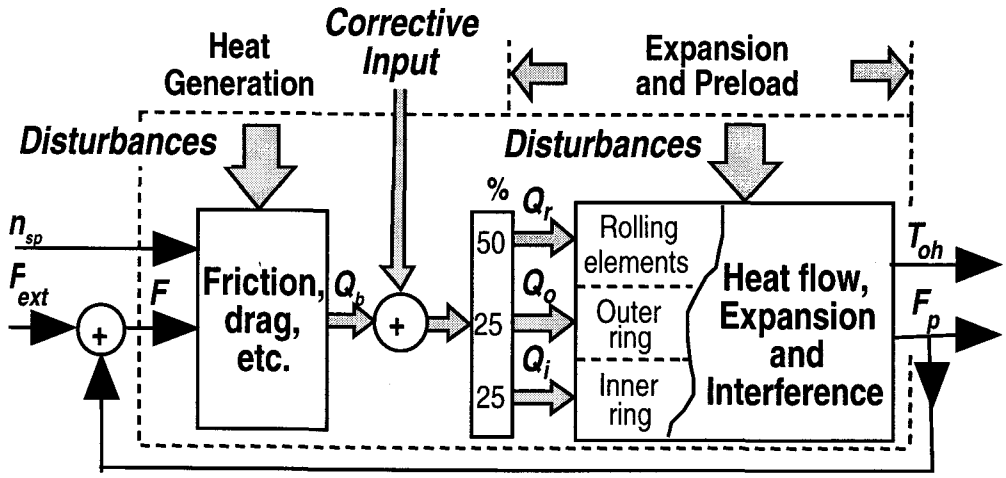

Fig. 2.8: A block diagram of the preload model.

The first component, denoted *Heat Generation*, is of empirical nature. It has two inputs, which are the rotational speed of the spindle, n_{sp} , and the total force, F. Only the former input is measurable and controllable. The output quantity is the total generated heat. There are strong non-measurable disturbances, which are generally related to the lubrication, wear and friction in the bearings. Due to these disturbances and structural uncertainty the accuracy of this part of the model is poor. The second component of the model, referred to as *Expansion & Preload,* utilizes analytical relationships. Its output signals of interest in this analysis are the preload, F_p, and the temperature T_{oh} at the bearing-housing interface. According to Tu (1991), this part is sufficiently accurate and linear for building a state observer.

The proposed preload observer is based on the extended Kalman fiter and uses only one easily measurable signal from the monitored spindle, the temperature T_{oh}. To attenuate the impact of disturbances not accounted for and model uncertainties, a 'servo loop' is introduced from the measured temperature, T_{oh}, to the point marked

Corrective Input in the model of Fig. 2.8. The suitability of the preload observer is limited, in particular during rapid changes of the spindle operating conditions.

To cope with this disadvantage a new method of preload monitoring is explored in this research. It is based on a purely mechanical MDOF model of a spindle assembly (see Fig. 1.4). Physical parameter estimation is used to assess the bearing stiffness on-line. A change in the bearing stiffness indicates a bearing preload variation, and can therefore be used for the detection of bearing seizure.

System identification has been extensively studied and broadly applied in engineering. Substantial amount of knowledge has been acquired in the area of analytical modeling of mechanical systems. Despite of efforts well documented, the problem of physical parameter estimation has not been solved yet. In particular, the available methods have not been integrated, for predictive monitoring and diagnosis of machine tools. Areas that warrant special attention are arbitrary precision calculations and robust minimization methods.

3. MODEL BUILDING AND ESTIMATION METHODOLOGY

3.1 Introduction

As described in Chapter 2, estimation of physical parameters for predictive supervision of machine tools has not yet been sufficiently studied. This is mainly due to the lack of suitable accurate analytical models for multi-degree-of-freedom systems. Therefore, in this chapter an efficient and accurate computer aided method of analytical model building is described. Also, the principle of physical parameter estimation is introduced and discussed. Some estimation techniques for physical parameters already exist (Isermann, 1991) and they are illustrated here. Other techniques, which have not been used for physical parameter estimation directly, but can also be adapted for this purpose. Still others are newly developed in this research. The comparison shows advantages and disadvantages of the different approaches. Guidelines are developed to help the user in the application of different techniques, and to show where potential difficulties can arise. The machine tool monitoring method proposed here combines conventional signal-based techniques with model-based performance indicators. It is referred to as 'gray box' identification (Ljung, 1984), because some form of prior knowledge about the system is used to build an analytical model containing physical parameters, and then these physical parameters are estimated using operational and/or test data. Therefore, in order to carry out parameter estimation, two tasks have to be accomplished first: Analytical modeling and experimental identification.

3.2 Analytical Modeling

Derivation of a generic dynamic model of a machine tool exactly accounting for distributed mass-stiffness-damping properties of its various mechanical components and for their interactions with other components of the machine tool is a task exceeding the capabilities of currently available methods. Because of this, the modeling attempts documented in the literature resort to approximations. Out of many available methods, two deserve particular attention, namely 1) the finite element analysis (Chen, 1996; Bianchi et al., 1996), and 2) 'rigid body' approximation (Ewins, 1984; Spiewak, 1995). In the presented research the latter method has been adopted due to its suitability for on-line estimation of physical parameters. To assure the required accuracy, a methodology has been developed for an incremental, orderly and algorithmic development of the rigid body models of the required fidelity. This methodology, which can be enhanced by 'rigid body' approximation or 'component mode synthesis', is delineated below.

In general, models are defined by their structures (form of equations) and coefficients. While structures can be considered constant for specific machine tools, coefficients usually vary in a broad range. Since numerous factors affect these variations, the only realistic approach to obtaining accurate models requires parameter estimation based on operational and/or test data. If this estimation of critical process parameters is done continuously, it can lead to an on-line monitoring system, which can detect and predict process faults as well as diagnose them. The physical parameters emerge only when the system is modeled analytically. Therefore, an analytical model of the system has to be developed from first principles, by stating the equilibrium equations for mass, energy and momentum. The developed model needs to be an explicit function of the physical parameters to be estimated. To avoid excessively large number of parameters, which would make the estimation very difficult, appropriate simplifications have to be made. The selection of model structure is very important. The desirable features of this structure are as follows:

- Efficient 'mapping' between physical parameters of the actual modeled system and their representations in the model,
- Scalability and accuracy of the model,
- Model parsimony to guarantee good computational efficiency,
- Unambiguous order selection and parameter estimation.

All these features are readily assured by lumped parameter approximation. Therefore, a dynamic model of the machine tool consisting of rigid bodies (RB) with concentrated mass parameters, connected by weightless "*stiffness-damping elements*" (SDE) is used as shown in Fig. 3.1.

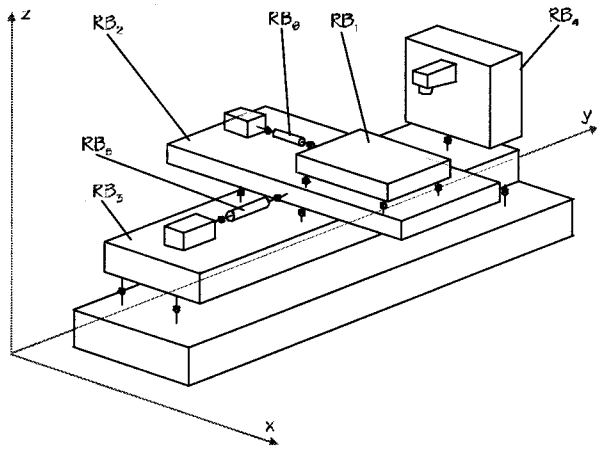

Fig. 3.1: Rigid body model of a serial machine tool.

Such a model is also particularly suited for parallel kinematics machines. An example of such a parallel structure machine tool is the HEXAGLIDE, designed and built at ETH, Zurich, (Hebsacker, 1995) and shown in Fig. 3.2. Those structures are ideal to be modeled by rigid bodies, in which the impact of bending moments can be made negligible by suitable design. In comparison with traditional serial-structure designs parallel machine tools are usually characterized by high stiffness and superior dynamic performance.

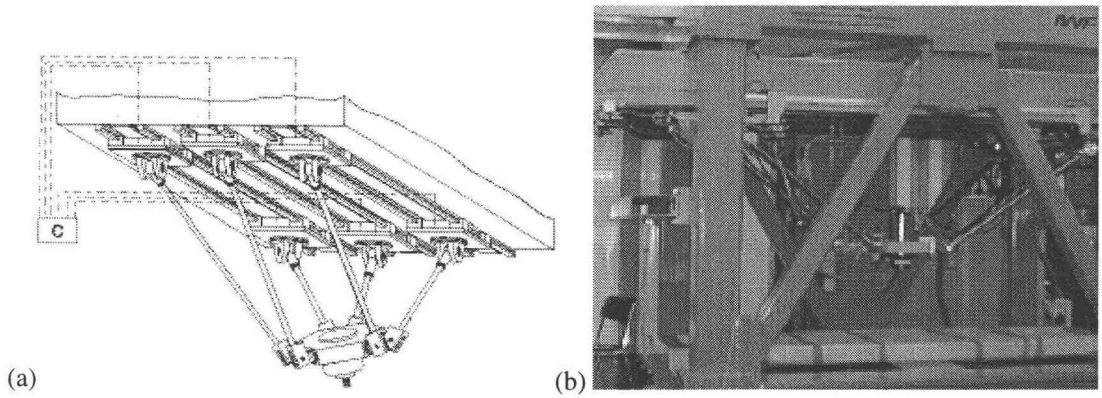

Fig. 3.2: HEXAGLIDE - schematic diagram (a), and the prototype built at ETH(b) (Weikert et al., 1996).

The first step of model development is the separation of objects that act as energy accumulators or dissipators (mass, springs and dampings). The forces acting between these objects are internal forces of the entire system. Driving forces/torques of electric motors, forces of gravity and cutting forces are considered external. This basic rigid body model is then completed with the addition of elements representing the drives and the control. Since the elasticities in a machine tool structure caused by the guideways and the sliders are meant to remain undeformed, the use of rigid bodies for this purpose is sufficiently accurate. Especially for stocky tools and shafts such a rigid body model is acceptable. Additionally, in high speed machining the forces due to acceleration are much greater than the process forces. This can be seen in practice.

Such a discretization of the real system may be called 'natural' discretization because of the natural division of the real structure into its constitutive parts (or rigid bodies). Continuous distribution of flexibility in the real system is replaced by stiffness elements in the model. Damping in the joints of the system is usually assumed to be structural damping, and is dealt with in the same manner as the stiffness elements. For illustrating general considerations in model building a generic MDOF 'rigid body' system is shown in Fig. 3.3.

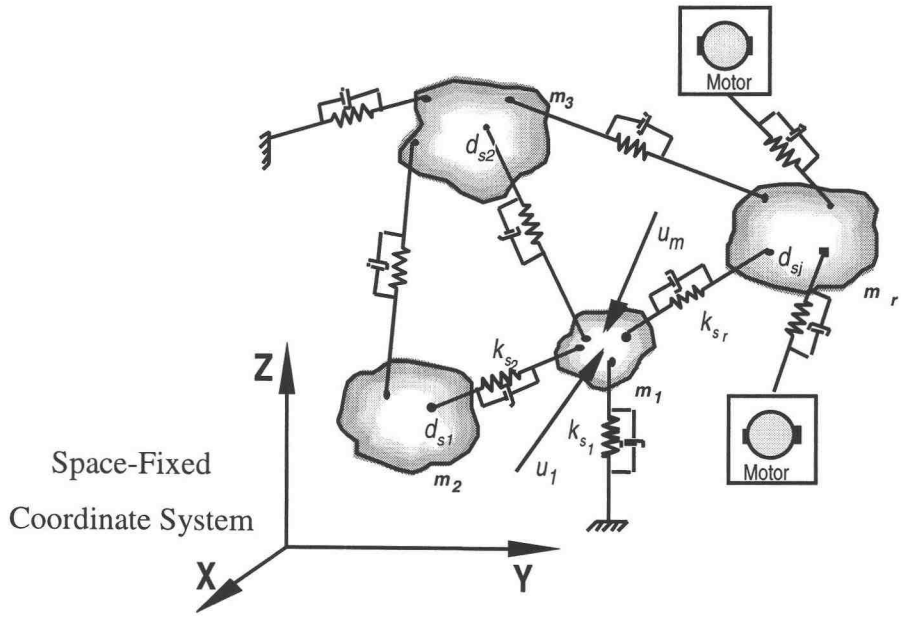

Fig. 3.3: A generic MDOF system.

Each rigid body has a mass m_i, $i=1, 2, \ldots r$, and in general can have forces and torques acting on it, denoted $u_k(t)$, $k=1, 2, \ldots n$. These forces and torques are generated by actuators such as spindle drives or by the cutting process. The generalized displacements (translation and rotation) of the bodies are defined in a space-fixed coordinate system (X, Y, Z), and they or some other parameters of interest such as elongations of the 'spring' elements can be chosen as the output signals. These later signals are denoted $y_j(t)$, $j=1, 2, \ldots m$.

The model shown in Fig. 3.3 is qualitative and mainly involves heuristic knowledge of the system. When modeling systems mathematically, different representations exist as illustrated in Fig. 3.4. Models derived from basic principles (e.g. Newton's law or Lagrange's method) result in differential equations of motion. This continuous model can be transformed into an I/O model or state-space model. For computer implementation discrete models are necessary as outlined on the right side of Fig. 3.4.

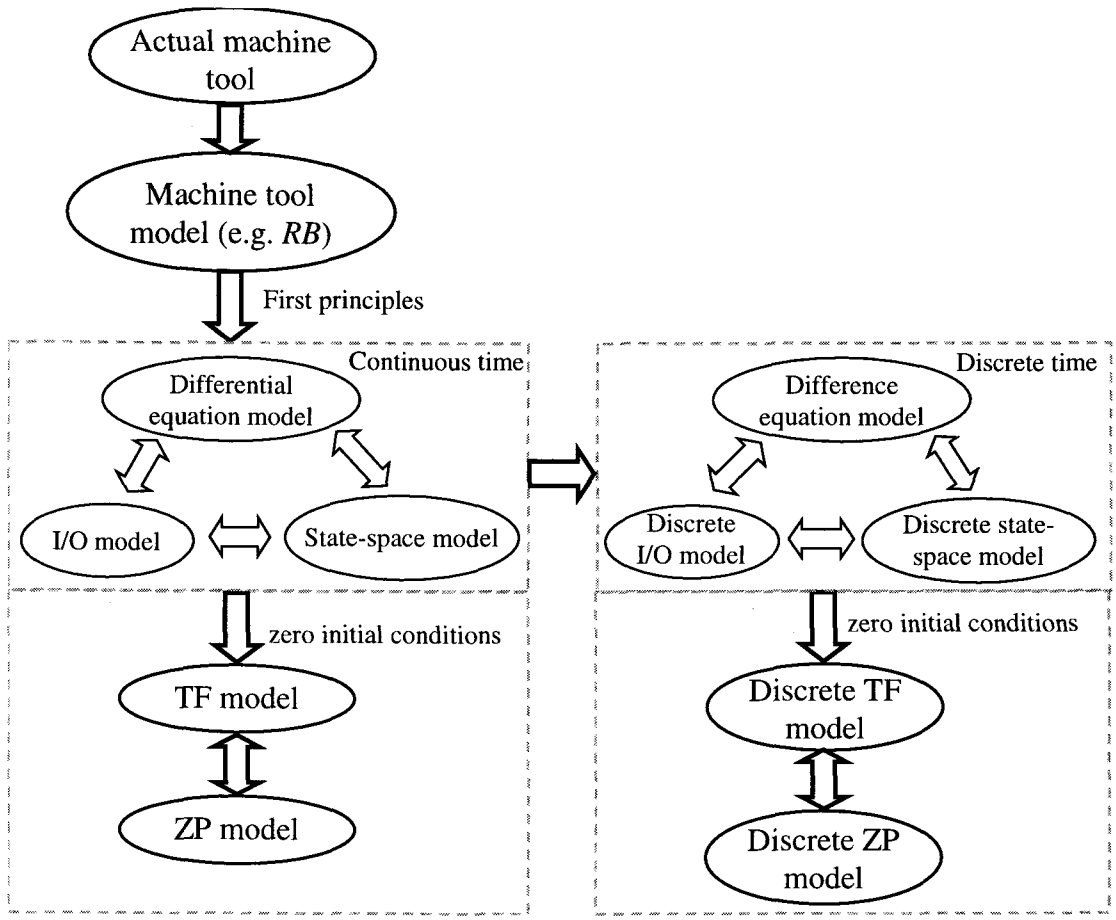

Fig. 3.4: Different types of models considered in this research.

The differential equation model, the state-space model, the transfer function model and the zero-pole model in time-domain are explained in detail below, since they are critical for the research presented in this thesis.

3.2.1 Differential Equation Model

For the dynamics of rigid bodies there are several approaches to obtain the differential equations of motion. One method is based on a direct use of equations

representing relevant first principles, (e.g. Newton's law of motion), other methods use Lagrange-Hamilton equations or Kane's principle (Meriam, 1980). The dynamics of the entire system, shown in Fig. 3.3, is concisely encapsulated in Eq. (3.1) as a set of ordinary differential equations. Eq. (3.1a) accounts for all mechanical phenomena, where as Eq. (3.1b) represents electrical effects.

$$\mathbf{m}\ \ddot{\mathbf{d}}_s(t) + F_1\ [\dot{\mathbf{d}}_s(t), \mathbf{d}_s(t), \mathbf{d}_f(t)] = \mathbf{b}_1\ \mathbf{F}_1(t) \tag{3.1a}$$

$$\mathbf{g}\ \dot{\mathbf{d}}_f(t) + F_2\ [\dot{\mathbf{d}}_s(t), \mathbf{d}_s(t), \mathbf{d}_f(t)] = \mathbf{b}_2\ \mathbf{v}(t) \tag{3.1b}$$

where

m, **g** - matrices depending upon the physical parameters of the modeled machines, such as masses of their components, inductances of electric motors, etc.,

$\mathbf{d}_f(t)$, $\mathbf{d}_S(t)$ - vectors of generalized coordinates which appear in the above model up to their first and second derivatives, respectively,

$F_i\ [\cdot]$ - nonlinear functions of the generalized coordinates (i = 1,2), and

$\mathbf{F}(t)$, $\mathbf{v}(t)$ - vectors of external excitations; example components of these vectors are, respectively, forces/moments acting on the masses and voltage signals applied to servomotors.

For linear systems most frequently dealt with in automatic supervision in manufacturing (ASM) the above set of equations becomes

$$\mathbf{m}\ \ddot{\mathbf{d}}_s(t) + \mathbf{c}\ \dot{\mathbf{d}}_s(t) + \mathbf{k}\ \mathbf{d}_s(t) + \mathbf{e}\ \mathbf{d}_f(t) = \mathbf{b}_1\ \mathbf{F}_1(t) \tag{3.2a}$$

$$\mathbf{g}\ \dot{\mathbf{d}}_f(t) + \mathbf{h}\ \dot{\mathbf{d}}_s(t) + \mathbf{p}\ \mathbf{d}_s(t) + \mathbf{q}\ \mathbf{d}_f(t) = \mathbf{b}_2\ \mathbf{v}(t) \tag{3.2b}$$

If the generalized coordinate vectors $\mathbf{d}_f(t)$ and $\mathbf{d}_s(t)$ comprise f and s elements respectively, then the matrices in the above equations have the following dimensions denoted by the subscripts: $\mathbf{c}_{sxs}$, $\mathbf{k}_{sxs}$, $\mathbf{e}_{sxf}$, $\mathbf{g}_{fxf}$, $\mathbf{h}_{fxs}$, $\mathbf{p}_{fxs}$, $\mathbf{q}_{fxf}$.

Once such a differential equation model is available, it can be transformed into other forms developed in control theory. The main model representations relevant in this context are (1) state-space model, (2) transfer function model and (3) zero-pole model. They are described below in more detail.

3.2.2 State Space Model

The state-space model can be represented in continuous or in discrete time-domain. Both, are briefly explained below.

Continuous Time-Domain: The continuous state-space model can be obtained by transforming the equations of motion of a system into a set of simultaneous first-order differential equations

$$\text{State equation:} \qquad \dot{\mathbf{x}}(t) = \mathbf{f}\big(\mathbf{x}(t), \mathbf{u}(t)\big) \tag{3.3a}$$

$$\text{Output equation:} \qquad \mathbf{y}(t) = \mathbf{h}\big(\mathbf{x}(t), \mathbf{u}(t)\big) \tag{3.3b}$$

where **x**(t) is a vector of state-variables and **u**(t) is the input vector.

$$\mathbf{x}(t) = \begin{bmatrix} \dot{\mathbf{d}}_s(t) \\ \mathbf{d}_s(t) \\ \mathbf{d}_f(t) \end{bmatrix}_{(2s+f)x1} \quad ; \qquad u(t) = \begin{bmatrix} \mathbf{F}_1(t) \\ \mathbf{v}\ (t) \end{bmatrix}_{mx1} \tag{3.4a,b}$$

For the linear case and assuming zero initial conditions Eq 3.3 can be rewritten as

$$\dot{\mathbf{x}}(t) = \mathbf{A} \cdot \mathbf{x}(t) + \mathbf{B} \cdot \mathbf{u}(t) \tag{3.5a}$$

$$\mathbf{y}(t) = \mathbf{C} \cdot \mathbf{x}(t) + \mathbf{D} \cdot \mathbf{u}(t) \tag{3.5b}$$

where matrix **A** is referred to as the evolution matrix, **B** is called the control matrix, **C** -the output matrix and **D** -the direct transmission matrix. Constant matrices **A** and **B** are expressed in terms of **m**, **c**, **k**, **e**, **g**, **h**, **p** and **q** as

$$A=\begin{bmatrix} \mathbf{I}_{sxs} & \mathbf{0}_{sxs} & \mathbf{0}_{sxf} \\ -\mathbf{m}^{-1}\mathbf{k} & -\mathbf{m}^{-1}\mathbf{c} & -\mathbf{m}^{-1}\mathbf{e} \\ -\mathbf{g}^{-1}\mathbf{h} & -\mathbf{g}^{-1}\mathbf{p} & -\mathbf{g}^{-1}\mathbf{q} \end{bmatrix}_{(2s+f)x(2s+f)} \quad ; \quad B=\begin{bmatrix} \mathbf{0}_{sx1} \\ -\mathbf{m}^{-1}\mathbf{b}_1 \\ -\mathbf{g}^{-1}\mathbf{b}_2 \end{bmatrix}_{(2s+f)x(2s+f)} \qquad (3.6a,b)$$

For purely lumped mechanical systems consisting only of masses, springs and dampers the matrices **A**, **B**, **C** and **D** simplify to

$$\mathbf{A}=\begin{bmatrix} \mathbf{0} & \mathbf{I} \\ -\mathbf{k}\cdot\mathbf{m}^{-1} & -\mathbf{c}\cdot\mathbf{m}^{-1} \end{bmatrix}; \quad \mathbf{B}=\begin{bmatrix} \mathbf{0} \\ \mathbf{m}^{-1} \end{bmatrix}; \quad \mathbf{C}=\begin{bmatrix} \mathbf{I} & \mathbf{0} \end{bmatrix}; \quad \mathbf{D}=\mathbf{0} \qquad (3.7a,b,c,d)$$

The solution to equations (3.5a) and (3.5b) results in

$$\mathbf{x}(t)=e^{\mathbf{A}(t-t_0)}\mathbf{x}(t_0)+\int_{t_0}^{t} e^{\mathbf{A}(t-\tau)}\mathbf{B}\ \mathbf{u}(\tau)d\tau \qquad (3.8)$$

A block diagram of the above state-space model is shown in Fig. 3.5. It is customary to summarize the attributes of constants and variables in this model as follows

$\mathbf{x}(t) \in \Re^{r}$ – a vector comprising *r* state variables,

$\mathbf{u}(t) \in \Re^{m}$ – a vector comprising *m* inputs,

$\mathbf{y}(t) \in \Re^{n}$ – a vector comprising *n* outputs,

$\mathbf{A} \in \Re^{rxr}$, $\mathbf{B} \in \Re^{m}$, $\mathbf{C} \in \Re^{nxr}$, $\mathbf{D} \in \Re^{nxm}$ [5]

where $n=2s+f$ and $\Re^{r}$ denotes a real-valued *r*-dimensional space.

[5] It is also common, particularly on the West Coast, to use the notation **F**, **G**, **H** and **J** in place of **A**, **B**, **C** and **D**.

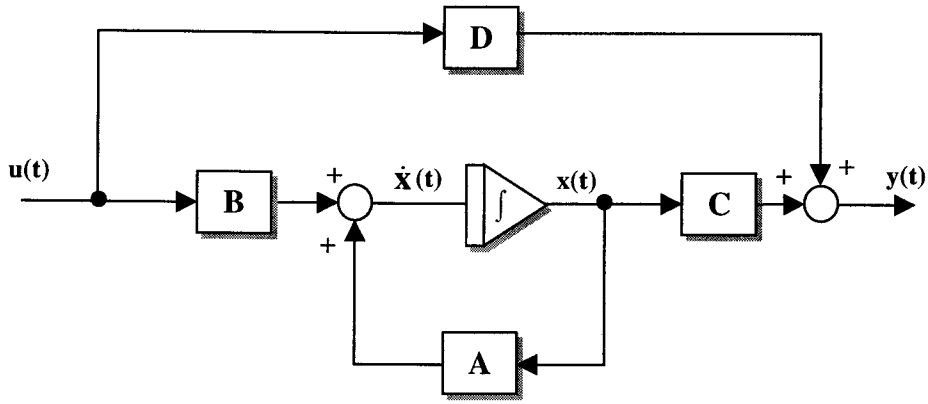

Fig. 3.5: State-space model of a continuous-time system.

Discrete Time-Domain: Implementing models on computers necessitates the transformation of continuous systems into discrete time-domain. The discrete state-space representation can be obtained from Eq. (3.8) by passing the input **u**(t) through a *Zero-Order-Hold* (ZOH). Letting $t = kT + T$ and $t_0 = kT$ the discrete time version of Eq. (3.8) becomes, (Franklin and Powell, 1984)

$$\mathbf{x}(kT+T) = e^{\mathbf{A}T}\mathbf{x}(kT) + \left(\int_0^T e^{\mathbf{A}\eta} d\eta\right)\mathbf{B}\,\mathbf{u}(kT) \tag{3.9}$$

where $\eta = kT + T - \tau$ and T is the sampling interval. If $e^{\mathbf{A}T} = \boldsymbol{\Psi}$ and $\left(\int_0^T e^{\mathbf{A}\eta} d\eta\right)\mathbf{B} = \boldsymbol{\Omega}$, Eqs. (3.5b) and (3.8) reduce to the difference equations in standard form:

Discrete state equation: $$\mathbf{x}(k+1) = \boldsymbol{\Psi}\cdot\mathbf{x}(k) + \boldsymbol{\Omega}\cdot\mathbf{u}(k) \tag{3.10a}$$

Discrete output equation: $$\mathbf{y}(k) = \mathbf{C}\cdot\mathbf{x}(k) + \mathbf{D}\cdot\mathbf{u}(k) \tag{3.10b}$$

where k is a shorthand notation for kT and $k+1$ for $kT+T$. The discrete state matrix $\boldsymbol{\Psi}$ can be also expressed in a series expansion

$$\mathbf{\Psi} = e^{\mathbf{A}T} = \mathbf{I} + \mathbf{A}T + \frac{\mathbf{A}^2T^2}{2\,!} + \frac{\mathbf{A}^3T^3}{3\,!} + \frac{\mathbf{A}^4T^4}{4\,!} + \ldots \tag{3.11}$$

The integral in the discrete input matrix $\mathbf{\Omega}$ can be evaluated term by term to give

$$\mathbf{\Omega} = \sum_{k=0}^{\infty} \frac{\mathbf{A}^k T^k}{(k+1)\,!}\, T\,\mathbf{B} \tag{3.12}$$

Once the state-space model is available in continuous or discrete form, it can easily be transformed into the continuous or discrete transfer function or zero-pole model using

$$\mathbf{G}(s) = \frac{\mathbf{Y}(s)}{\mathbf{U}(s)} = \mathbf{C} \cdot (s \cdot \mathbf{I} - \mathbf{A})^{-1} \cdot \mathbf{B} + \mathbf{D} \tag{3.13}$$

for the continuous transformation, and

$$\mathbf{G}(z) = \frac{\mathbf{Y}(z)}{\mathbf{U}(z)} = \mathbf{C} \cdot (z \cdot \mathbf{I} - \mathbf{\Psi})^{-1} \cdot \mathbf{\Omega} + \mathbf{D} \tag{3.14}$$

for the discrete transformation.

Three features of the state-space models deserve particular attention with regard to automatic supervision.

i. A simple model given by Eqs. (3.5a) and (3.5b) describe a broad class of MIMO systems. This is of special importance due to the increasing availability of software systems facilitating symbolic calculations (eg. *Mathematica* or *Maple*). Utilizing the state-space formalism with these packages enables easy handling of equations which, if dealt with by traditional means would require many pages of calculations.

ii. A continuous-time state-space model can be readily converted into the equivalent 'difference equations' model that is needed for the implementation of several standard methods presented below on digital computers.

iii. A large number of algorithmic analysis methods developed in control theory can be utilized to obtain information needed for the system's supervision.

3.2.3 Transfer Function Model

The transfer function (TF) model is often used in controls theory. Linear, time-invariant MIMO systems can be described by this model. It is a rational polynomial in s and can be derived using the Laplace transformation applied to Eq. (3.1) or directly from the state-space model (described above). The transfer function $G_{ij}(s)$ relates one particular output $y_i(t)$ to one particular input $u_j(t)$ (see Fig. 1.2).

$$G_{ij}(s) = \frac{Y_i(s)}{U_j(s)} = \frac{b_p s^p + b_{p-1} s^{p-1} + \ldots + b_2 s^2 + b_1 s + b_0}{s^q + a_{q-1} s^{q-1} + \ldots + a_2 s^2 + a_1 s + a_0} \tag{3.15}$$

A set of model coefficients $\hat{\mathbf{\Lambda}}_\mathbf{p}$ (see Eq. (2.20)) can be estimated from experimental data. There are many methods available (Ljung, 1984; Young, 1981; Astrom, 1971) to obtain an accurate fit of the TF model to the actual system, however this kind of model doesn't provide any direct information about physical parameters of the system. The physical parameters $\mathbf{\Theta}$ are 'hidden' in the model coefficients $\mathbf{\Lambda_p}$ and unless a deterministic and invertible relationship between the TF model (Eq. (3.15)) and a constitutive model based on first principles (Eq. (3.2)) can be built, those physical parameters cannot be found. Nevertheless this purely signal-based model is a useful tool for investigating the system's dynamic behavior due to changes in the physical parameters $\mathbf{\Theta}$. Visual inspection of Bode and Phase plots can aid in determining the resonance frequencies and damping ratios of the system.

3.2.4 Zero Pole Model

The zero-pole (ZP) model is very similar to the transfer function model, only the polynomials are represented in a factored form. The benefit is immediate insight into modal properties (ω_n, ξ), as shown below

$$G(s) = g\frac{(s-z_1)(s-z_2)\cdots(s-z_p)}{(s-p_1)(s-p_2)\cdots(s-p_q)} \tag{3.16}$$

where g - gain of the system,

$z_1 \ldots z_p$ - real or complex valued zeros,

$p_1 \ldots p_q$ - real or complex valued poles.

Zeros and poles can be plotted on the s-plane, as shown in Fig. 3.6 and provide information about the system's dynamic behavior.

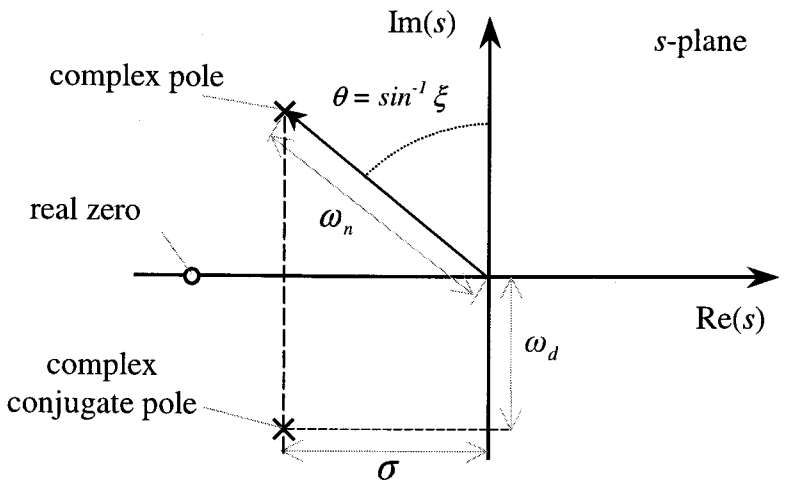

Fig. 3.6: Zero/Pole representation in the s-plane (Franklin and Powell, 1994).

Stability of the system can be readily assessed (unstable if $\mathrm{Re}\{p_i\} > 0$) and natural frequencies and damping ratios can be calculated using the relationships

$$\mathrm{Re}(p_i) = \xi_i \cdot \omega_{n,i} \tag{3.17a}$$

$$\left|\mathrm{Im}(p_i)\right| = \omega_{n,i} \cdot \sqrt{1-\xi_i^2} \tag{3.17b}$$

Similarly to the TF model, the ZP model is a very convenient tool for analyzing system's behavior, especially as a result of changes in physical parameters $\boldsymbol{\Theta}$. However, if the zeros and poles cannot be expressed as a function of $\boldsymbol{\Theta}$, then this model is also not suitable for physical parameter estimation.

3.3 Modeling Methodology

The basic components used in the model derivation described below are Lagrange's energy method, linear algebra, homogenous transformations and state-space formalism. Differential equations of motion can be derived for a free conservative system using Lagrange's method as (Meriam, 1980)

$$\frac{\partial}{\partial t}\frac{\partial L}{\partial \dot{q}_j} - \frac{\partial L}{\partial q_j} = 0; \qquad L = T(\mathbf{q}, \dot{\mathbf{q}}) - U(\mathbf{q}) \tag{3.18a,b}$$

where $T(\mathbf{q}, \dot{\mathbf{q}})$, $U(\mathbf{q})$ - kinetic and potential energy, respectively,

$\mathbf{q}$ - a set of generalized coordinates for the entire modeled system,

q_j - j-th element of $\mathbf{q}$.

Eq. (3.18a) is referred to as Lagrange's equation of the first kind. With the inclusion of the dissipation energy function D and an external force Q_j associated with the j-th generalized coordinate, Eq. (3.18a) becomes Lagrange's equation of the second kind (Meriam, 1980).

$$\frac{\partial}{\partial t}\frac{\partial T}{\partial \dot{q}_j} - \frac{\partial T}{\partial q_j} + \frac{\partial D}{\partial \dot{q}_j} + \frac{\partial U}{\partial q_j} = Q_j \tag{3.19}$$

Newton's method is sometimes used instead of Lagrange's method and is concerned with forces and torques instead of energies (kinetic, potential and dissipative). However, it is generally much easier to define the energies of a particular system than to define the individual forces acting on each body. Definition of the individual forces can become very taxing in some cases, particularly in the structures considered in this research.

Another alternative to Lagrange's energy formalism is Kane's method. Rather than considering all the forces and torques acting on a body, Kane's method deals with *generalized* active and inertia forces (Kane et al, 1983). The primary advantage of this is a simplification of equations needed to describe the system, since some of the forces acting on the bodies contribute nothing to the generalized forces[6]. Equating the sum of respective generalized active and inertia forces to zero produces Kane's dynamical equations of motion. This method in general, will produce the equations in the most compact form, implying that this is the easiest approach. However, one must keep in mind that there is also a set of associated kinematical equations that must be satisfied when using this method (Ginsberg, 1995).

3.4 Automatic Model Generation - General Considerations

Obtaining Eqs. (3.1) for machine tools (three-dimensional systems) is a complicated task. Commonly used computer aided modeling packages can perform this task numerically (e.g., ADAMS (Mechanical Dynamics, 1997), I-DEAS (Spectral Dynamics, 1996), ANSYS (Ansys, 1997) or DADS - SIMULINK (CADSI, 1997), but experience shows that the accuracy of the obtained models is unsatisfactory.

---

[6] Due to force cancellation.

Also, for the purpose of physical parameter estimation, the critical parameters need to be available in symbolic form. An available package capable of symbolic modeling, AUTOLEV (Schaechter and Levinson, 1988), has a cumbersome user interface and for efficient use requires familiarity with Kane's method (Kane et al., 1983) which is less frequently used than the classical Lagrange-Hamilton approach (Meriam, 1980; Ginsberg, 1995). Because of the above reasons, a specialized computer aided package has been developed for deriving symbolic models of modern machine tools. The package implements Lagrange's method (Meriam, 1980) for a class of systems shown in Fig. 3.1 and conveniently links the results with the analytical 'tools' developed in control theory for the analysis of complex dynamic systems (Wolfram, 1992). Once the analytical model is generated in terms of equations of motion for the system, wide range of possibilities for evaluating, testing and characterizing the system are available. This is especially true if the model is transformed into the state-space representation. For example, system characteristics like controllability or observability can be readily tested. The modeling and analysis are performed in the *Mathematica* programming environment (Wolfram, 1991).

For computer implementation it is necessary to develop a structured approach towards calculating the kinetic, potential and dissipative energy needed for computation of Eq. (3.13). Below, three cases of increasing complexity of energy calculations are considered. They differ in the way the general motion of the rigid bodies is modeled. This affects the calculation of the elongations of the *stiffness-damping elements* (SDEs), which are needed for the derivation of the potential and dissipative energies.

3.4.1 CASE 1: SDEs Aligned with Principal Cartesian Directions

A simple sub-system of Fig. 3.1, which comprises one single rigid body supported by a single SDE is considered in Fig. 3.7.

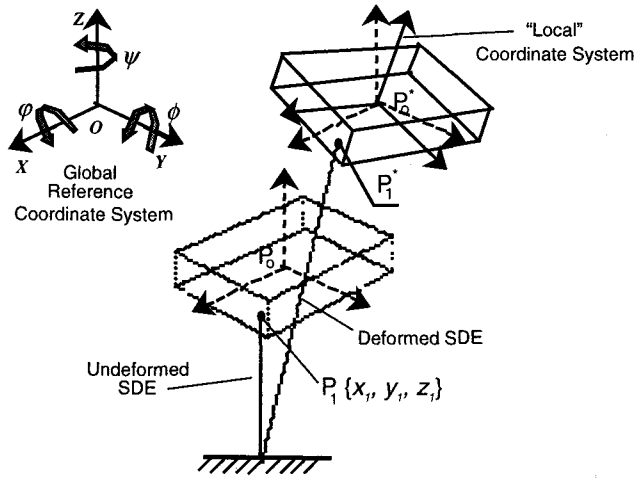

Fig. 3.7: The elongation of a spring-damping element.

The body has six DOFs. Therefore, the generalized coordinates, a set of variables, which completely define the location, and orientation of each component of the system, can be written in vector form as

$$\mathbf{q} = \{x(t), y(t), z(t), \varphi(t), \phi(t), \psi(t)\}^T \tag{3.20}$$

However, it is assumed that the main mode of vibration is in the vertical direction. Then the elongation of the SDE due to the body's displacement can be approximated for small deformations as

$$l = z(t) + y_1\varphi(t) - x_1\phi(t) \tag{3.21}$$

where x_1 and y_1 are the coordinates of the SDE attachment point P_1 to the body.

Eq. (3.21) is obtained intuitively by inspection of Fig. 3.7. This is possible for such a simple case, but for more general deformations (see CASE 2) a rigorous analytical approach is recommended. In general, the elongation of any elastic element between the body and the fixed base can be written in a symbolic form

$$l_k = l_k(\mathbf{q}) \quad ; \qquad k = 1, 2, \ldots, n \tag{3.22}$$

where n is the number of SDEs. The elongations are defined as functions of generalized coordinates. The forces between the body and the base arising from all SDE couplings are directly related to their respective elongations that can be written in the vector form

$$\mathbf{L}(\mathbf{q}) = \{l_1, l_2, \ldots, l_n\}^{\mathrm{T}} \tag{3.23}$$

This vector is a function of the generalized coordinates and can be written as a linear combination

$$\mathbf{L}(\mathbf{q}) = \mathbf{H} \cdot \mathbf{q} \tag{3.24}$$

where $\mathbf{H}$ is a function of geometric dimensions. For the simple case of only one SDE $\mathbf{L}(q)$ is equal to l in Eq. (3.21). Now the potential energy due to deformation of all SDEs between the body and the base can be calculated as

$$U(\mathbf{q}) = \frac{1}{2}\mathbf{L}^{\mathrm{T}}\mathbf{K}_{\mathbf{SDE}}\mathbf{L} = \frac{1}{2}\mathbf{q}^{\mathrm{T}}\mathbf{H}^{\mathrm{T}}\mathbf{K}_{\mathbf{SDE}}\mathbf{H}\mathbf{q} = \frac{1}{2}\mathbf{q}^{\mathrm{T}}\mathbf{K}^{*}_{\mathbf{SDE}}\mathbf{q} \tag{3.25}$$

where $\mathbf{K}_{SDE}$ represents a diagonal matrix of stiffnesses and

$$\mathbf{K}^{*}_{\mathbf{SDE}} = \mathbf{H}^{\mathrm{T}}\mathbf{K}_{\mathbf{SDE}}\mathbf{H} \tag{3.26}$$

$\mathbf{K}^{*}_{\mathbf{SDE}}$ in the above equation is a 'weighted' global stiffness matrix. $\mathbf{H}$ is obtained as

$$\mathbf{H} = [0 \quad 0 \quad 1 \quad y_1 \quad x_1] \tag{3.27}$$

$\mathbf{K}_{\mathbf{SDE}}$ in that case is only a scalar K_{SDE} but $\mathbf{K}^{*}_{\mathbf{SDE}}$ is still a matrix.

$$\mathbf{K}^{*}_{\mathrm{SDE}} = \begin{bmatrix} 0 & 0 & 0 & 0 & 0 \\ 0 & 0 & 0 & 0 & 0 \\ 0 & 0 & 0 & y_1 & x_1 \\ 0 & 0 & y_1 & y_1^2 & x_1 y_1 \\ 0 & 0 & x_1 & x_1 y_1 & x_1^2 \end{bmatrix} \tag{3.28}$$

The energy dissipation due to damping is calculated similarly to the potential energy, only it is proportional to the displacement *velocity.*

$$D(\mathbf{q}) = \frac{1}{2}\dot{\mathbf{q}}^{\mathrm{T}}\mathbf{H}^{\mathrm{T}}\mathbf{B}_{\mathrm{SDE}}\mathbf{H}\dot{\mathbf{q}} = \frac{1}{2}\dot{\mathbf{q}}^{\mathrm{T}}\mathbf{B}^{*}_{\mathrm{SDE}}\dot{\mathbf{q}} \tag{3.29}$$

In Eq. (3.29) $\mathbf{B}_{SDE}$ represents a diagonal matrix of damping of SDEs and $\mathbf{B}^{*}_{SDE}$ is again a 'weighted' damping matrix. The expression for kinetic energy for the rigid body is straightforward and involves the use of a diagonal (global) mass matrix

$$T(\dot{\mathbf{q}}) = \frac{1}{2}\dot{\mathbf{q}}^{\mathrm{T}}\mathbf{M}\ \dot{\mathbf{q}} \tag{3.30}$$

Application of Lagrange's equation of the second kind (Eq. 3.19) then extracts the equations of motion for each generalized coordinate.

3.4.2 CASE 2: Arbitary Directions of SDEs

As in the previous case, a subsystem comprising one single rigid body supported by two spring-damper elements (SDE 1, SDE 2) from a fixed base. The initial, (undeformed) position and the displaced position (dashed line) of the rigid body is shown below.

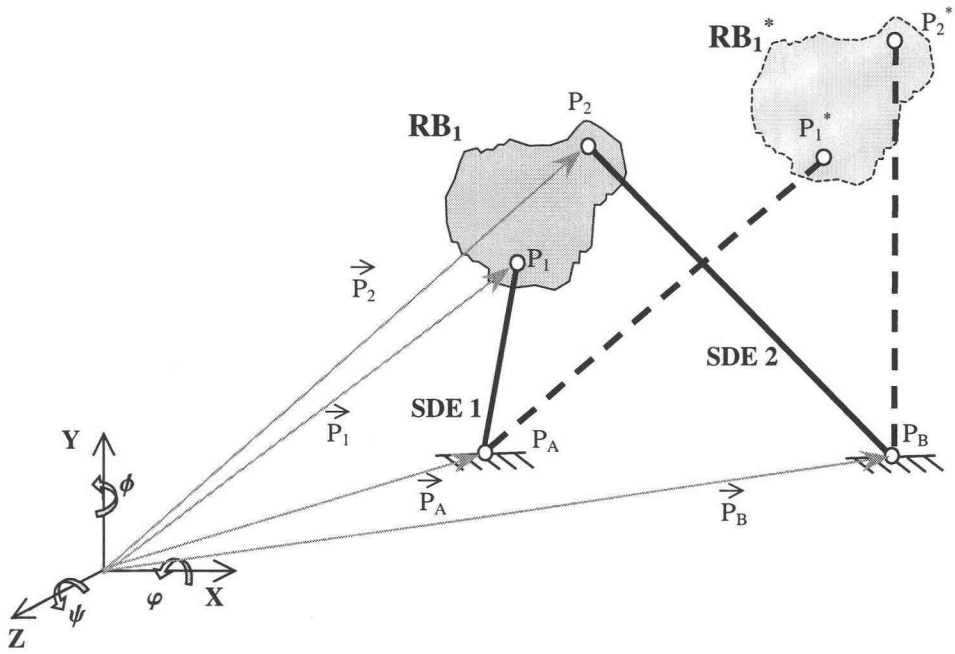

Fig. 3.8: Movement of a single lumped mass supported by two SDEs in three-dimensional space for CASE 2.

The arrangement is similar to CASE 1, except the elongations of the SDEs are calculated using position vectors. This allows the consideration of a general motion of the body and is more accurate than the approximation made in Eq. (3.21). The attachment points of the SDEs are denoted P_1 and P_2 on the body, and P_A, P_B on the fixed base. In the reference coordinate system these points can be identified by position vectors $\vec{P}_1$, $\vec{P}_2$, $\vec{P}_A$ and $\vec{P}_B$ [7] respectively. As in CASE 1, the rigid body can move with six DOF, therefore the vector of generalized coordinates is identical to CASE 1 (Eq. 3.20).

---

[7] $\vec{P}$ - (with arrow) denotes a vector which can be represented graphically and has a certain length and direction.
P - (bold) denotes a data structure, which can have more than three components.
P - (plain) is just a label for a point and does not have any numerical value.

The expression for the total kinetic energy in terms of masses, moments of inertia and generalized coordinates is also the same as in CASE 1, however the calculation of the potential energy of the system (and dissipative forces) differs in the following way:

The elongations of the SDEs are calculated using the above defined position vectors. The initial position the SDE 1 and SDE 2 are assumed in a relaxed state, and their initial lengths l_1 and l_2 can be calculated as

$$l_{0,1} = \left|\vec{P}_1 - \vec{P}_A\right| \quad ; \quad l_{0,2} = \left|\vec{P}_2 - \vec{P}_B\right| \tag{3.31}$$

After the body assumes a displaced position (indicated by dashed lines in Fig. 3.8) the deflected lengths of the SDEs are

$$l_1^* = \left|\vec{P}_1^* - \vec{P}_A\right| \quad ; \quad l_2^* = \left|\vec{P}_2^* - \vec{P}_A\right| \tag{3.32a,b}$$

The new, displaced position vectors $\vec{P}_1^*$ and $\vec{P}_2^*$ are a function of the generalized coordinates and can be calculated using transformation matrices, which describe spatial motions. Transformation matrices have been used extensively in the area of robotics to describe coordinate transformations (Craig, 1955). The following list of explains the use of these matrices:

1) Transformation matrices apply, in general, to points.
2) Two coordinate systems are involved:
   - reference system,
   - "moving body" (local) system.
3) Translations and rotations (x, y, z, φ, ϕ, ψ) pertain to the movement of the local system.
4) Attachment point vectors are created by using points, as explained above.
5) Locations of points (e.g. $\{x_1, y_1, z_1\}$ in CASE 1) on the moving body are defined in local coordinate systems.

6) Because all points on the moving bodies are multiplied by the same transformation matrices, a concise mathematical notation is possible (and it is introduced in this research.

The homogeneous transformation matrix **TM** is a *4x4* matrix and represents simultaneous rotation and translation of a vector $\vec{P}$ to a new vector $\vec{P}^*$ by

$$\mathbf{P}^* = \mathbf{TM} \cdot \mathbf{P} \tag{3.33}$$

where **TM** is calculated as

$$\mathbf{TM} = \mathbf{TM}_t \cdot \mathbf{TM}_{rx} \cdot \mathbf{TM}_{ry} \cdot \mathbf{TM}_{rz} \tag{3.34}$$

The matrices $\mathbf{TM}_t$, $\mathbf{TM}_{rx}$, $\mathbf{TM}_{ry}$ and $\mathbf{TM}_{rz}$ describe translation, rotation around *x*-, *y*- and *z*-axis respectively. They are listed in Appendix A. As an example, a simplified form (small angle approximations[8]) of the transformation matrix **TM** is

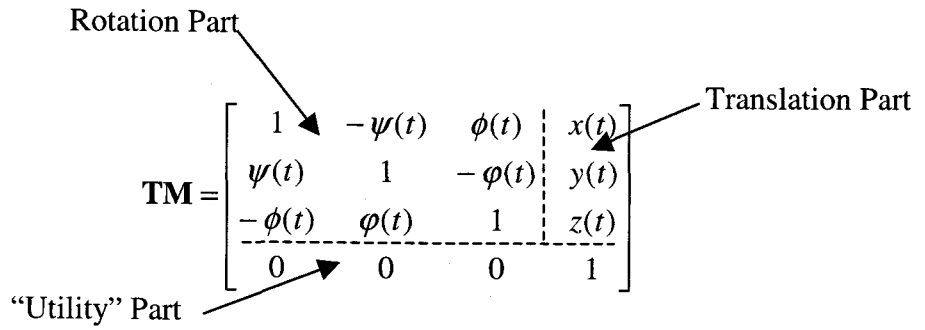

(3.35)

The matrix consists of three parts. The rotation part describes an influence of the generalized angles φ, ϕ and ψ. The translation part represents the translation motions of a vector without any change in its orientation. The utility part facilitates mathematical matrix manipulations. It does not influence the translation or the rotation. To have the matrix and vector dimensions consistent in Eq. (3.33) the three-dimensional position vectors need to have '1' as a fourth utility component as well.

After the new position vectors $\vec{P}^*$ are calculated using Eq. (3.33) the elongations of SDE 1 and SDE 2 are

$$l_1 = l_{0,1} - l_1^* \quad ; \qquad l_1 = l_{0,1} - l_1^* \tag{3.36a,b}$$

This method of calculating the SDE elongations can be extended to n SDEs. For convenience the undeformed and deformed lengths of all SDEs are represented in vector form as

$$\mathbf{L}_0(\mathbf{q}) = \{l_{0,1}, l_{0,2}, ..., l_{0,n}\}^T \quad ; \qquad \mathbf{L}^*(\mathbf{q}) = \{l_1^*, l_2^*, ..., l_n^*\}^T \tag{3.37a,b}$$

The elongations of the SDEs are then simply calculated as

$$\mathbf{L} = \mathbf{L}_0 - \mathbf{L}^* \tag{3.38}$$

The potential and dissipative energies can then be calculated using Eq (3.25) and (3.29). CASE 2 applies if: 1) the bodies do not change their average positions (time invariant moments of inertia in the global reference coordinate system), or 2) variations of the generalized coordinates are expressed in coordinate systems that continuously follow the average positions (translations and rotations) of the bodies. For major reconfigurations of the system a more general CASE 3 needs to be considered.

---

[8] The simplified form is used only to illustrate the general structure of **TM**. However, CASE 2 has been developed primarily to deal with large rotation angles.

3.4.3 CASE 3: Systems with Reconfiguration

If the arrangement of rigid bodies changes significantly, e.g. by repositioning of the main machine tool table, then assumptions made in CASE 2 are not adequate. Small vibrations can not be taken into account when large movements are tracked with the vector method. Therefore CASE 2 is extended in order to accommodate these small but significant vibrations superimposed on large movements.

Motions of model elements are described using right-hand coordinate systems. There are two kinds of systems in this case: A global coordinate system X, Y, Z and the local ones x_i, y_i, z_i. The global coordinate system is arbitrarily situated, and the displacements and loads of the model are described in this system. The local coordinate systems corresponding to the particular rigid bodies and the SDEs are "body fixed". Local coordinate systems, x_i, y_i, z_i, are attached at the center of mass of the RBs. The axes of these systems coincide with principal axes of inertia of the elements in the state of equilibrium and also to the stiffness of the SDE attached to this body. External loads, $u_k(t)$, acting on the RB are also described in the local coordinate system. The axes of the coordinate system coincide with principal axes of stiffness of the k-th SDE: x_e, y_e, z_e.

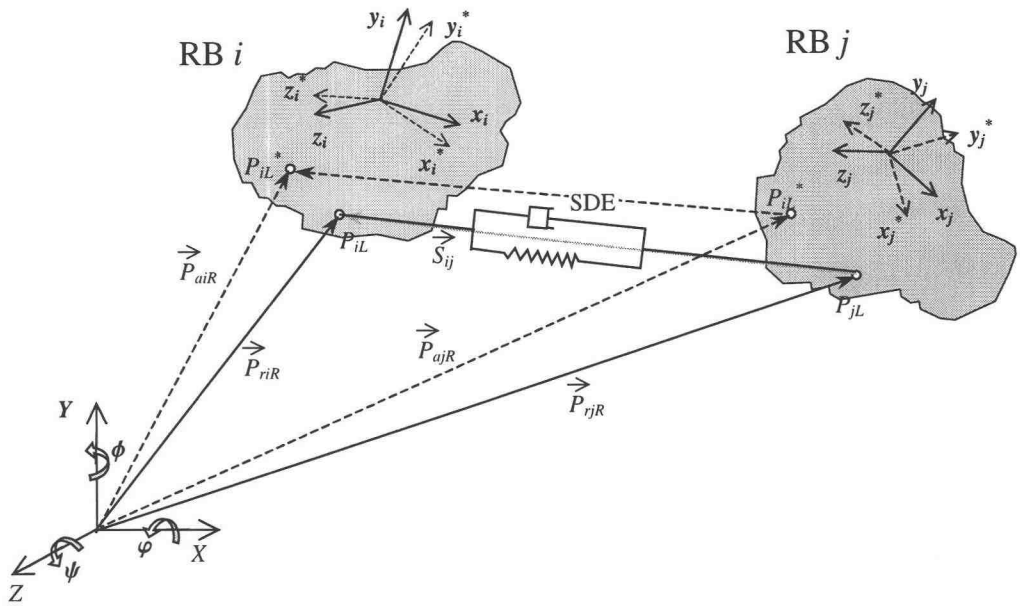

Fig. 3.9: Movement of a lumped mass in space.

A spring-damper element between 2 bodies i and j is considered in Fig. 3.8. This SDE is attached at point P_{iL} to body i, and at point P_{jL} to body j. Both points are defined in local coordinate systems associated with each of the bodies. Coordinates of these points in a stationary reference coordinate system $(XYZ)_R$ are P_{riR} and at point P_{rjR} , respectively. The length and orientation of the SDE under consideration is expressed in vector notation as

$$\vec{S}_{ij} = \vec{P}_{riR} - \vec{P}_{rjR} \tag{3.39}$$

$\vec{S}_{ij}$ changes due to NC programmed motion (e.g., increase of the active leadscrew length due to table translation) or due to vibrations. The latter change is of primary interest from the viewpoint of deriving the equations of motion. The former change is secondary and causes non-stationarity of the system and its model. In the traditional ('serial structure') machine tools only the lengths of $\vec{S}_{ij}$ change while in the 'parallel structure' machines both the lengths and orientations can change significantly.

Changes in the positions of bodies i and j are expressed by six-element sets of generalized coordinates associated with these bodies, $\mathbf{q_i}^*$ and $\mathbf{q_j}^*$. Components of these sets, namely three translations and three rotations, depend upon the NC programmed motion as well as vibrations of the bodies. It is assumed that the programmed motion does affects neither the potential nor the kinetic energy of the spring-dashpot element under consideration[9]. Changes of the $\mathbf{q_i}^*$ and $\mathbf{q_j}^*$ coordinates due to this motion are considered nominal components of instantaneous generalized coordinates and denoted $\mathbf{q_{io}}$ and $\mathbf{q_{jo}}$, respectively. On the other hand, the changes due to vibrations, $\mathbf{q_i}$ and $\mathbf{q_j}$, impact these energies. The following equations apply

$$\mathbf{q_i}^* = \mathbf{q_{io}} + \mathbf{q_i} = \{x_{0i} + x_i,\ y_{0i} + y_i,\ z_{0i} + z_i,\ \varphi_{0i} + \varphi_i,\ \phi_{0i} + \phi_i,\ \psi_{0i} + \psi_i\} \quad (3.40a)$$

$$\mathbf{q_j}^* = \mathbf{q_{jo}} + \mathbf{q_j} = \{x_{0j} + x_j,\ y_{0j} + y_j,\ z_{0j} + z_j,\ \varphi_{0j} + \varphi_j,\ \phi_{0j} + \phi_j,\ \psi_{0j} + \psi_j\} \quad (3.40b)$$

If the bodies i and j assume new positions $\mathbf{q_i}^*$ and $\mathbf{q_j}^*$, the average (nominal) locations of points P_{iL} and P_{jL} in the reference coordinate system become P_{aiR} and P_{ajR}

$$\mathbf{q_i}^* = P_{aiR}(\mathbf{q_{io}}) = \mathbf{TM}(\mathbf{q_{io}})\ P_{iL} \quad (3.41a)$$

$$\mathbf{q_j}^* = P_{ajR}(\mathbf{q_{jo}}) = \mathbf{TM}(\mathbf{q_{jo}})\ P_{jL} \quad (3.41b)$$

where $\mathbf{TM}(\mathbf{q_{i(j)o}})$ is a suitable homogeneous transformation matrix (Craig, 1955). Assuming these new end positions for the SDE, its extension for small increments of $\mathbf{q_i}$ and $\mathbf{q_j}$ can be found as the dot product

$$\Delta s\ (P_{iL}, \mathbf{q_{io}}, \mathbf{q_i}, P_{jL}, \mathbf{q_{jo}}, \mathbf{q_j}) \cong [\Delta\vec{P}(\mathbf{q_{io}}, \mathbf{q_i}) - \Delta\vec{P}(\mathbf{q_{jo}}, \mathbf{q_j})] \cdot \vec{u}_{Sij}(\mathbf{q_{io}}, \mathbf{q_{jo}}) \quad (3.42)$$

where $\vec{u}_{Sij}(\cdot)$ is the unit vector of $\vec{S}_{ij}$ and "()" abreviates "($\mathbf{q_{io}}$, $\mathbf{q_{jo}}$)".

---

[9] This assumption is made here to simplify discussion of the proposed modeling approach and is exactly fulfilled when the machine is at rest. It can still be acceptable at slow feeds.

$$\Delta\vec{P}_i(\mathbf{q}_{io},\mathbf{q}_i)=\mathbf{T}_t(\mathbf{q}_i)\ P_{aiR}(\mathbf{q}_{io})\ \ ;\ \ \Delta\vec{P}_j(\mathbf{q}_{jo},\mathbf{q}_j)=\mathbf{T}_t(\mathbf{q}_j)\ P_{aiR}(\mathbf{q}_{jo}) \qquad (3.43a,b)$$

The potential energy of the spring in the SDE under consideration is calculated as

$$U_{SDE}(P_{iL},\mathbf{q}_{io},\mathbf{q}_i,P_{jL},\mathbf{q}_{jo},\mathbf{q}_j)=0.5\ K_{ij}\ (\Delta s\ (\cdot))^2 \qquad (3.44)$$

The total potential energy is obtained by summing energies of all SDEs. Similarly, the dissipative force in each SDE is calculated as

$$D_{SDE}(P_{iL},\mathbf{q}_{io},\mathbf{q}_i,P_{jL},\mathbf{q}_{jo},\mathbf{q}_j)=0.5\ B_{ij}\left(\frac{\partial}{\partial t}\Delta s\ (\cdot)\right)^2 \qquad (3.45)$$

Since the SDEs are assumed massless, the only contributors to the kinetic energy are the movements of the rigid bodies themselves. Assuming the energy is defined about the center of mass, then the kinetic energy of the *i*-th body in Fig. 3.9 can be conveniently separated into translational and rotational terms

$$T_i=T_{i,trans}+T_{i,rot} \qquad (3.46)$$

The translational kinetic energy is simply written as

$$T_{i,trans}(\dot{\mathbf{q}}_{i,T})=\frac{1}{2}\dot{\mathbf{q}}_{i,T}^{T}\ \mathbf{m}_i\ \dot{\mathbf{q}}_{i,T} \qquad (3.47)$$

where $\mathbf{m}_i$ is the diagonal mass matrix and $\dot{\mathbf{q}}_{i,T}=\{\dot{x}_i,\dot{y}_i,\dot{z}_i\}$ is defined as the vector of generalized translational velocities for the *i*-th rigid body in the global reference frame.

The rotational kinetic energy has a similar form, only it uses the local body inertia tensor and vector of generalized rotational velocities, $\dot{\mathbf{q}}_{i,r}=\{\dot{\varphi}_i,\dot{\phi}_i,\dot{\psi}_i\}$

$$T_{i,rot}(\dot{\mathbf{q}}_{i,r})=\frac{1}{2}\dot{\mathbf{q}}_{i,r}^{T}\ \mathbf{I}_{i,r}\ \dot{\mathbf{q}}_{i,r} \qquad (3.48)$$

Summing kinetic, potential and damping energies over all m rigid bodies in the system (two bodies for this example) produces an expression for the total energy of the multi-degree-of-freedom system under consideration. Application of Lagrange's equation of the second kind then yields the equations of motion for each generalized coordinate

$$\frac{d}{dt}\left(\frac{\partial \sum_i T_i}{\partial\ \dot{\mathbf{q}}_k^g}\right) - \frac{\partial \sum_i T_i}{\partial\ \mathbf{q}_k^g} + \frac{\partial \sum_{ij} D_{ij}}{\partial\ \dot{\mathbf{q}}_k^g} + \frac{\partial \sum_{ij} U_{ij}}{\partial\ \mathbf{q}_k^g} = Q_k$$

$$\text{for } i = 1,2,...n\ ;\ i < j \text{ and } k = 1,2,\ ...,6\,n \qquad (3.49)$$

where Q_k represents the external force associated with the k-th generalized coordinate from the global list of generalized coordinates $\mathbf{q}^g$. The final result is a general vector-matrix equation encapsulating motion of all rigid bodies.

3.4.4 Accounting for Gyroscopic Forces

If the kinetic energy due to spinning of rigid bodies is to be included, the gyroscopic forces need to be taken into account. The gyroscopic effect appears when the orientation of the axis of rotation of a rigid body changes while that body is spinning (Ginsberg, 1995). Assume that the rigid body considered is a spindle rotating with constant speed n_{sp}.

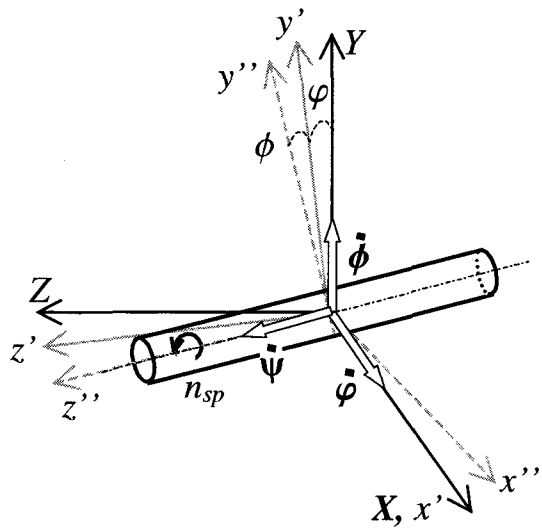

Fig. 3.10: Gyroscopic effect.

Due to vibrations the orientation of the spindle axis changes an angle φ around the x-axis (precession) and an angle ϕ around the y-axis (nutation). This can be mathematically tracked through the transformation of coordinate systems. The standard way of calculating the kinetic energy due to gyroscopic motion is using the Euler angles together with body-fixed transformations. However, since the generalized coordinates of the entire system are defined space-fixed (see Fig. 3.3), the following approach can be used.

The initial coordinate system (X, Y, Z)[10] is first turned an angle φ around the X-axis. Any vector in the XYZ-coordinate system can be transformed into the new $x'y'z'$-coordinate system[11] using the transformation matrix

[10] Indicated with solid lines in Fig. 3.10.
[11] Indicated with gray solid lines in Fig. 3.10.

$$\mathbf{TM}_{\varphi} = \begin{bmatrix} 1 & 0 & 0 \\ 0 & \cos\varphi(t) & \sin\varphi(t) \\ 0 & -\sin\varphi(t) & \cos\varphi(t) \end{bmatrix} \tag{3.50}$$

If the *x'y'z'*-system is rotating with an angular velocity $\dot{\varphi}$ around the *X*-axis, then the vector $\dot{\varphi}$ represented in the *XYZ*-coordinate system is

$$\dot{\varphi} = \begin{bmatrix} \dot{\varphi} \\ 0 \\ 0 \end{bmatrix} \Bigg|_{XYZ} \tag{3.51}$$

Next, a subsequent rotation is applied, which moves the *x'y'z'*-coordinate system an angle ϕ around the initial space-fixed *Y*-axis into the final *x''y''z''*-coordinate system[12]. The transformation matrix $\mathbf{TM}_{\phi}$ needed for this rotation is

$$\mathbf{TM}_{\phi} = \begin{bmatrix} \cos\phi(t) & 0 & -\sin\phi(t) \\ 0 & 1 & 0 \\ \sin\phi(t) & 0 & \cos\phi(t) \end{bmatrix} \tag{3.52}$$

If the *x''y''z''*-system is rotating with an angular velocity $\dot{\phi}$ around the *Y*-axis, then the vector $\dot{\phi}$ represented in the *XYZ*-coordinate system is

$$\dot{\phi} = \begin{bmatrix} 0 \\ \dot{\phi} \\ 0 \end{bmatrix} \Bigg|_{XYZ} \tag{3.53}$$

The spindle itself is spinning with a constant angular velocity $\dot{\psi} = 2\pi\, n_{sp}$ around the *z''*-axis and thus one can calculate the resultant angular velocity vector ω in the final *x''y''z''*-coordinate system as

---

[12] Indicated with gray dashed lines in Fig. 3.10.

$$\omega\big|_{x"y"z"} = \dot{\boldsymbol{\varphi}}\big|_{x"y"z"} + \dot{\phi}\big|_{x"y"z"} + \dot{\psi}\big|_{x"y"z"} \tag{3.54}$$

$\dot{\psi}\big|_{x"y"z"}$ is simply $\dot{\psi} = \begin{bmatrix} 0 \\ 0 \\ \dot{\psi} \end{bmatrix}\Bigg|_{x"y"z"}$ but $\dot{\boldsymbol{\varphi}}\big|_{x"y"z"}$ and $\dot{\phi}\big|_{x"y"z"}$ have to be calculated as

$$\dot{\boldsymbol{\varphi}}\big|_{x"y"z"} = \mathbf{TM}\varphi \cdot \mathbf{TM}\phi \cdot \dot{\boldsymbol{\varphi}}\big|_{XYZ} = \dot{\varphi}\begin{bmatrix} \cos(\phi) \\ \sin(\varphi)\sin(\phi) \\ \cos(\varphi)\sin(\phi) \end{bmatrix}\Bigg|_{x"y"z"} \tag{3.55}$$

$$\dot{\phi}\big|_{x"y"z"} = \mathbf{TM}\varphi \cdot \mathbf{TM}\phi \cdot \dot{\phi}\big|_{XYZ} = \dot{\phi}\begin{bmatrix} 0 \\ \cos(\varphi) \\ -\sin(\varphi) \end{bmatrix}\Bigg|_{x"y"z"} \tag{3.56}$$

The resultant angular velocity $\boldsymbol{\omega}\big|_{x"y"z"}$ becomes

$$\boldsymbol{\omega}\big|_{x"y"z"} = \begin{bmatrix} \omega_{x"} \\ \omega_{y"} \\ \omega_{z"} \end{bmatrix}\Bigg|_{x"y"z"} \begin{bmatrix} \cos(\phi) \\ \sin(\varphi)\sin(\phi)\dot{\varphi} + \cos(\varphi)\dot{\phi} \\ \dot{\psi} + \cos(\varphi)\sin(\phi)\dot{\varphi} - \sin(\varphi)\dot{\phi} \end{bmatrix}\Bigg|_{x"y"z"} \tag{3.57}$$

Now the kinetic energy due to the gyroscopic effect can be readily calculated as

$$T_{Gyro} = \frac{1}{2} I_{zz}\, \omega_{z"}{}^2 = \frac{1}{2} I_{zz} \left(\dot{\psi} + \cos(\varphi)\sin(\phi)\dot{\varphi} - \sin(\varphi)\dot{\phi}\right)^2 \tag{3.58}$$

3.5 Automatic Model Generation for a Spindle Assembly

The analytical modeling methodology described above is applied in this section to a realistic system. It is a spindle assembly, the main entity of any metal cutting machine tool, therefore such a system is considered here. An experimental system dealt with henceforth is described in more detail in Chapter 5. This system is a

good representative of a broader class of devices involving rotating machinery that can be dealt with by the proposed approach.

A purely mechanical, multi-degree-of-freedom (MDOF) model of the spindle assembly is derived. Fig. 3.11 shows a simplified rigid body model of this system. The rigid supports shown in the figure indicate only general constraints for the housing but not the actual locations. The exact connection to the rigid base is shown in Fig. 3.14.

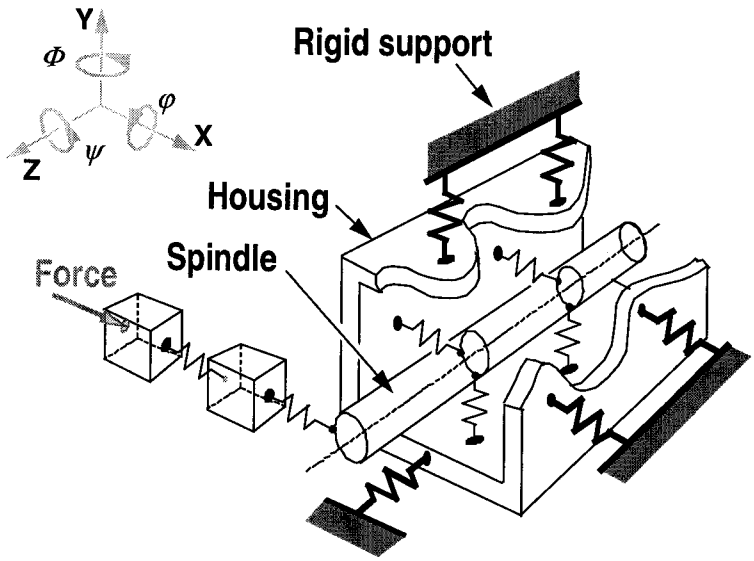

Fig. 3.11: A 'rigid body' model of the spindle.

The spindle shaft is supported in the housing by means of elastic elements with viscous damping[13] which represent rolling element bearings. The housing, in turn, is attached to the rigid base by means of other elastic elements, which represent physical components (e.g. guideways or bolted joints) of the machine tool. The exciting force is applied at the spindle nose through a dynamic system represented in the figure by two masses and elastic elements with damping. This system is introduced to model the impact of the remaining mechanical components of the machine tool (coupled through the cutting process) on the spindle dynamics. The two mass-spring-dashpot systems shown in Fig. 3.11 accurately represents an electro-dynamic shaker used in the tests (see Chapter 5).

The housing has three translational (x, y and z) and three rotational degrees-of-freedom (DOF), (φ, ϕ and ψ). The spindle shaft itself has five DOF. This is one DOF less than the housing, because the spindle rotates freely around the z-axis. Therefore the global vector of generalized coordinates, which comprises the DOF of spindle and housing is defined as

$$\mathbf{q}(t) = \{x_s(t), y_s(t), z_s(t), x_h(t), y_h(t), z_h(t), \varphi_s(t), \phi_s(t), \varphi_h(t), \phi_h(t), \psi_h(t)\}^T \quad (3.59)$$

where $x_s(t)$ denotes a generalized coordinate for the spindle,

$x_h(t)$ denotes a generalized coordinate for the housing.

Their respective time derivatives, the generalized velocities and the generalized accelerations are denoted $\dot{\mathbf{q}}(t)$ and $\ddot{\mathbf{q}}(t)$.

---

[13] These elements are graphically represented by springs. Supporting springs in the Z-direction are omitted for clarity.

In this model, the balls of the angular contact bearings are represented by the *'spindle-housing'* springs, as shown in Fig. 3.12. Ideally each ball is a linear spring-damper system. However, in this simplified model only one vertical and one horizontal ball is considered, for the sake of clarity. In doing so, the number of parameters influencing the behavior of the bearings (like number of balls, inner ring curvature, outer ring curvature etc.) is reduced. There are four parameters for the vertical and horizontal ball (two springs and two dampers) and one spring-damper system at the center of the spindle shaft for the support in *Z*-direction. The *attachment* points in the figure indicate fixed points on the housing and shaft, respectively. These points are needed for the calculation of the spring and damper extensions, as described in the previous sections.

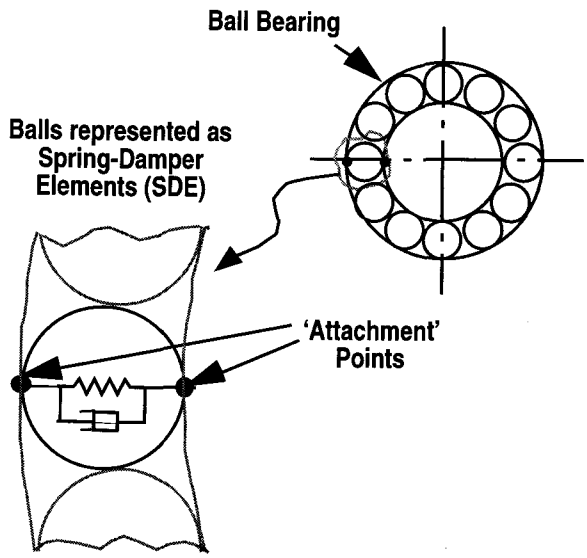

Fig. 3.12: Bearing modeling.

To model this system mathematically according to CASE 2 in Section 3.3.2, position vectors to the attachment points have to be established. They are defined in a

reference (global) coordinate system, which can be chosen arbitrarily. In this case it is chosen to be at the geometric center of the housing. Position vectors determine where the individual rigid bodies are located with respect to the reference coordinate system, and the locations where springs and dampers are connected to the individual rigid bodies. Employing the position vectors and knowledge of how they change the elongations of the springs, the potential energies can be calculated. The investigated set-up has a fixed-free bearing arrangement. The front bearing is fixed and therefore has an axial spindle-housing spring representing the axial bearing stiffness. In addition, the spindle is held in place in the horizontal and vertical direction by two radial spindle-housing springs representing the radial bearing stiffness. It is important to note that those springs are one-dimensional, thus only deflecting in one major direction. Also, in the arrangement under consideration the bearings do not generate moments. This is a purposeful simplification. The spindle-housing springs together with position vectors pointing to their attachment points are shown below.

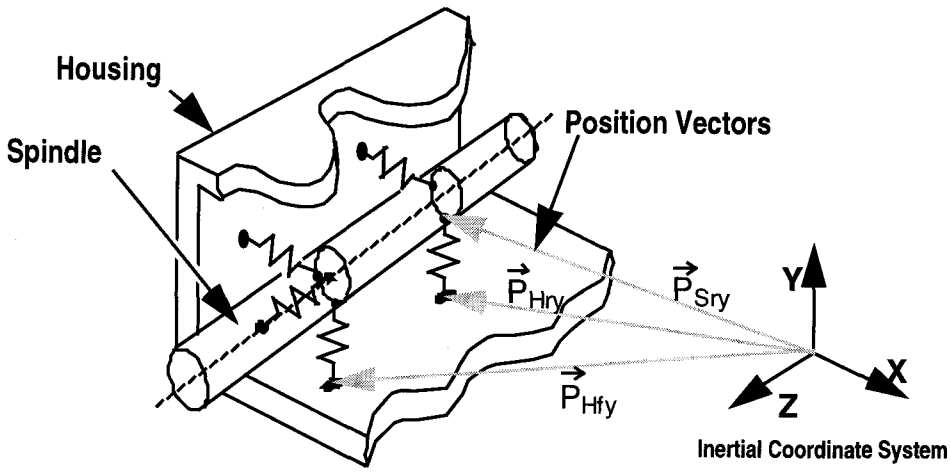

Fig. 3.13: The 'spindle-housing' springs.

The position vectors of the spindle-housing springs to the attachment points on the spindle-side are denoted $\vec{P}_{Sfx}$, $\vec{P}_{Sfy}$, $\vec{P}_{Sfz}$, $\vec{P}_{Srx}$ and $\vec{P}_{Sry}$ [14] and are given below in the initial, non-vibrating state as an example.

$$\mathbf{P}_{\mathbf{Sfx}} = \begin{bmatrix} -x_{sb0} \\ 0 \\ z_{sb0} \\ 1 \end{bmatrix}; \mathbf{P}_{\mathbf{Sfy}} = \begin{bmatrix} 0 \\ -y_{sb0} \\ z_{sb0} \\ 1 \end{bmatrix}; \mathbf{P}_{\mathbf{Sfz}} = \begin{bmatrix} 0 \\ 0 \\ z_{sb0} \\ 1 \end{bmatrix}; \mathbf{P}_{\mathbf{Srx}} = \begin{bmatrix} -x_{sb0} \\ 0 \\ -z_{sb2} \\ 1 \end{bmatrix}; \mathbf{P}_{\mathbf{Sry}} = \begin{bmatrix} 0 \\ -y_{sb0} \\ -z_{sb2} \\ 1 \end{bmatrix} \quad (3.60)$$

where x_{sb0}, y_{sb0}, z_{sb0}, z_{sb1} and z_{sb2} are geometric distances of the relevant bearing locations. The vectors have a fourth row, as mentioned in Section 3.2, which is called the utility part. It facilitates matrix manipulation, but does not influence the coordinates of the vector. The vectors $\vec{P}_{Hfx}$, $\vec{P}_{Hfy}$, $\vec{P}_{Hfz}$, $\vec{P}_{Hrx}$ and $\vec{P}_{Hry}$ define the attachment points for the spindle-housing springs on the housing side. The complete list of all position vectors with their numerical values is shown in Appendix C2.

The length and orientation of these position vectors change as the generalized coordinates change. Putting all position vectors related to one body in one matrix improves the efficiency of calculations. As a result, manipulations do not have to be performed on each individual vector, but rather on the whole matrix. $\boldsymbol{M_{SB,0}}$ is the matrix of all attachment points of the spindle-housing springs on the spindle-side and $\boldsymbol{M_{HB,0}}$ is the matching matrix on the housing-side.

$$\mathbf{M}_{\mathbf{SB,0}} = \left[\mathbf{P}_{\mathbf{Sfx}}\ \mathbf{P}_{\mathbf{Sfy}}\ \mathbf{P}_{\mathbf{Sfz}}\ \mathbf{P}_{\mathbf{Srx}}\ \mathbf{P}_{\mathbf{Sry}}\right] = \begin{bmatrix} -x_{sb0} & 0 & 0 & -x_{sb0} & 0 \\ 0 & -y_{sb0} & 0 & 0 & -y_{sb0} \\ z_{sb0} & z_{sb0} & z_{sb0} & -z_{sb2} & -z_{sb2} \\ 1 & 1 & 1 & 1 & 1 \end{bmatrix} \quad (3.61)$$

[14] The subscripts means: S = Spindle, H = Housing, fx, fy, fz = front in x-, y- or z-direction, rx, ry = rear in x- or y- direction.

$$\mathbf{M}_{\mathbf{HB,0}} = \left[\mathbf{P}_{\mathbf{Hfx}}\ \mathbf{P}_{\mathbf{Hfy}}\ \mathbf{P}_{\mathbf{Hfz}}\ \mathbf{P}_{\mathbf{Hrx}}\ \mathbf{P}_{\mathbf{Hry}}\right] = \begin{bmatrix} -x_{hb0} & 0 & 0 & -x_{hb0} & 0 \\ 0 & -y_{hb0} & 0 & 0 & -y_{hb0} \\ z_{sb0} & z_{sb0} & z_{sb1} & -z_{sb2} & -z_{sb2} \\ 1 & 1 & 1 & 1 & 1 \end{bmatrix} \tag{3.62}$$

In the investigated spindle-bearing system the housing is bolted onto a massive steel base by four screws located on the four corners of the cube shaped housing. In the model this connection of the housing to a rigid base is represented by four 'housing-base' springs shown in Fig. 3.14. In contrast to the one-dimensional spindle-housing springs, these springs are three-dimensional since each screw fixes the housing in all three directions. The attachment points of these springs on the housing-side are defined by four position vectors $\vec{P}_{h1}$, $\vec{P}_{h2}$, $\vec{P}_{h3}$ and $\vec{P}_{h4}$. On the base-side they are denoted by vectors $\vec{P}_{b1}$, $\vec{P}_{b2}$, $\vec{P}_{b3}$ and $\vec{P}_{b4}$.

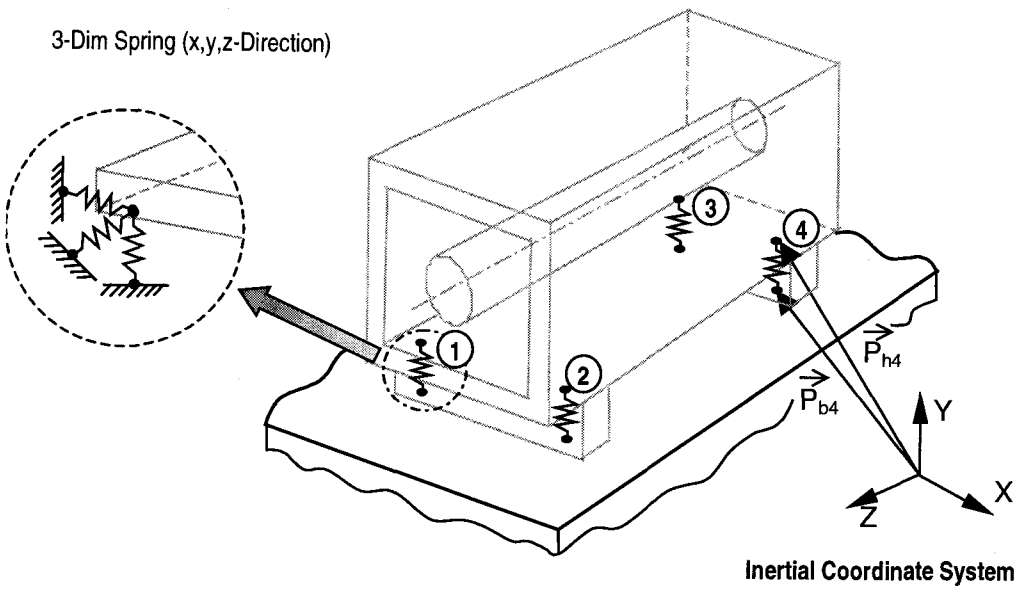

Fig. 3.14: The 'housing-base' springs.

$\boldsymbol{M_{H,0}}$ is the matrix of all attachment points of the housing-base springs on the housing side. $\boldsymbol{M_{B,0}}$ is the matching matrix on the base side.

$$\mathbf{M_{H,0}} = \left[\mathbf{P_{h1}}\ \mathbf{P_{h2}}\ \mathbf{P_{h3}}\ \mathbf{P_{h4}}\right] = \begin{bmatrix} -x_{h0} & x_{h0} & -x_{h0} & x_{h0} \\ -y_{h0} & -y_{h0} & -y_{h0} & -y_{h0} \\ z_{h0} & z_{h0} & -z_{h0} & -z_{h0} \\ 1 & 1 & 1 & 1 \end{bmatrix} \tag{3.63}$$

$$\mathbf{M_{B,0}} = \left[\mathbf{P_{b1}}\ \mathbf{P_{b2}}\ \mathbf{P_{b3}}\ \mathbf{P_{b4}}\right] = \begin{bmatrix} -x_{h0} & x_{h0} & -x_{h0} & x_{h0} \\ -y_{b0} & -y_{b0} & -y_{b0} & -y_{b0} \\ z_{h0} & z_{h0} & -z_{h0} & -z_{h0} \\ 1 & 1 & 1 & 1 \end{bmatrix} \tag{3.64}$$

Additional position vectors needed are the force-input location $\vec{P}_{In}$ and the desired output measurement location $\vec{P}_{Out}$. Their use will be described later, after all the energies and the Lagrangian are derived.

$$\mathbf{P_{In}} = \begin{bmatrix} x_{In} \\ y_{In} \\ z_{In} \end{bmatrix} \quad ; \quad \mathbf{P_{Out}} = \begin{bmatrix} x_{Out} \\ y_{Out} \\ z_{Out} \end{bmatrix} \tag{3.65a,b}$$

After all position vectors are defined and put into convenient matrix forms, the extensions of the SDEs are found using transformation matrices as described in Section 3.4.2 (Eq. 3.33). The transformation matrices needed for the housing, $\mathbf{TM_H}$, and spindle, $\mathbf{TM_S}$, assuming small angle approximations are found as (see Appendix A for derivation)

$$\mathbf{TM_H} = \begin{bmatrix} 1 & -\psi_h(t) & \phi_h(t) & x_h(t) \\ \psi_h(t) & 1 & -\varphi_h(t) & y_h(t) \\ -\phi_h(t) & \varphi_h(t) & 1 & z_h(t) \\ 0 & 0 & 0 & 1 \end{bmatrix} \tag{3.66}$$

$$\mathbf{TM_S} = \begin{bmatrix} 1 & 0 & \phi_s(t) & x_s(t) \\ 0 & 1 & -\varphi_s(t) & y_s(t) \\ -\phi_s(t) & \varphi_s(t) & 1 & z_s(t) \\ 0 & 0 & 0 & 1 \end{bmatrix} \tag{3.67}$$

The deflection of the "housing-base springs" can be found using the equation

$$\mathbf{\Delta d}_{\mathbf{HB}} = [\mathbf{\Delta d}_1\ \mathbf{\Delta d}_2\ \mathbf{\Delta d}_3\ \mathbf{\Delta d}_4] = (\mathbf{TM}_{\mathbf{H}} - \mathbf{I}) \cdot \mathbf{M}_{\mathbf{H,0}} - \mathbf{M}_{\mathbf{B,0}} \tag{3.68}$$

The deflections of the "spindle-housing springs" can be found using the equation

$$\mathbf{\Delta d_{SH}} = [\mathbf{\Delta d_{fx}}\ \mathbf{\Delta d_{fy}}\ \mathbf{\Delta d_{fz}}\ \mathbf{\Delta d_{rx}}\ \mathbf{\Delta d_{ry}}] = (\mathbf{TM_S} - \mathbf{I}) \cdot \mathbf{M_{SB,0}} - (\mathbf{TM_H} - \mathbf{I}) \cdot \mathbf{M_{HB,0}} \tag{3.69}$$

If a vector of housing-base stiffnesses is introduced in the form

$$\mathbf{k_{HBj}} = \{k_{HBxj}, k_{HByj}, k_{HBzj},\ 0\} \qquad ;\ j=1 \ldots 4 \tag{3.70}$$

then the potential energy due to the deflection of these springs can be calculated as

$$U_{HB} = \frac{1}{2}\left(\mathbf{k_{HB,1}} \cdot \mathbf{\Delta d_1}^2 + \mathbf{k_{HB,2}} \cdot \mathbf{\Delta d_2}^2 + \mathbf{k_{HB,3}} \cdot \mathbf{\Delta d_3}^2 + \mathbf{k_{HB,4}} \cdot \mathbf{\Delta d_4}^2\right) \tag{3.71}$$

where $\mathbf{\Delta d_j}^2$ is the square of the components of Eq. (3.68). Similarly the damping energy can be calculated by introducing a vector of housing-base dampings of the form

$$\mathbf{c_{HBj}} = \{c_{HBxj}, c_{HByj}, c_{HBzj},\ 0\} \qquad ;\ j=1 \ldots 4 \tag{3.72}$$

for each 3-dim housing-base spring. The damping energy due to the deflection velocities $\frac{\partial}{\partial t}\mathbf{\Delta d_j}$ of these springs can be calculated as

$$D_{HB} = \frac{1}{2}\left(\mathbf{c_{HB,1}} \cdot \left(\frac{\partial}{\partial t}\mathbf{\Delta d_1}\right)^2 + \mathbf{c_{HB,2}} \cdot \left(\frac{\partial}{\partial t}\mathbf{\Delta d_2}\right)^2 + \mathbf{c_{HB,3}} \cdot \left(\frac{\partial}{\partial t}\mathbf{\Delta d_3}\right)^2 + \mathbf{c_{HB,4}} \cdot \left(\frac{\partial}{\partial t}\mathbf{\Delta d_4}\right)^2\right) \tag{3.73}$$

Since the spindle-housing springs are only one-dimensional, their extensions need to be multiplied by the appropriate unit vector

$$\mathbf{u}_x = [1 \;\; 0 \;\; 0 \;\; 0] \quad ; \; \mathbf{u}_y = [0 \;\; 1 \;\; 0 \;\; 0] \quad ; \; \mathbf{u}_z = [0 \;\; 0 \;\; 1 \;\; 0] \tag{3.74}$$

After introducing bearing stiffnesses k_{fx} , k_{fy} , k_{fz} , k_{rx} and k_{ry} , the potential energy of the spindle-housing springs calculates to

$$U_{SH} = \frac{1}{2}\left(k_{fx}\mathbf{u}_x \cdot \Delta\mathbf{d}_{fx}{}^2 + k_{fy}\mathbf{u}_y \cdot \Delta\mathbf{d}_{fy}{}^2 + k_{fz}\mathbf{u}_z \cdot \Delta\mathbf{d}_{fz}{}^2 \right)$$
$$+ \frac{1}{2}\left(k_{rx}\mathbf{u}_x \cdot \Delta\mathbf{d}_{rx}{}^2 + k_{ry}\mathbf{u}_y \cdot \Delta\mathbf{d}_{ry}{}^2 \right) \tag{3.75}$$

The damping energy calculates to

$$D_{SH} = \frac{1}{2}\left(c_{fx}\mathbf{u}_x\left(\frac{\partial}{\partial t}\Delta\mathbf{d}_{fx}\right)^2 + c_{fy}\mathbf{u}_y\left(\frac{\partial}{\partial t}\Delta\mathbf{d}_{fy}\right)^2 + c_{fz}\mathbf{u}_z\left(\frac{\partial}{\partial t}\Delta\mathbf{d}_{fz}\right)^2 \right)$$
$$+ \frac{1}{2}\left(c_{rx}\mathbf{u}_x\left(\frac{\partial}{\partial t}\Delta\mathbf{d}_{rx}\right)^2 + c_{ry}\mathbf{u}_y\left(\frac{\partial}{\partial t}\Delta\mathbf{d}_{ry}\right)^2 \right) \tag{3.76}$$

The calculation of the kinetic energy T is straightforward. It is the sum of the kinetic energies of the individual masses for each generalized coordinate, which include a translational and rotational portion (Eq. (3.77) through (3.82)). This total kinetic energy (Eq. 3.77) also includes a gyroscopic portion due to the spinning of the shaft with the rotational speed n_{sp}.

$$T = T_{S,rot.} + T_{S,tr.} + T_{Gyro} + T_{H,rot.} + T_{H,tr.} \tag{3.77}$$

$$T_{S,rot.} = \frac{1}{2}\left(J_{Sxx}\dot{\varphi}_s^2 + J_{Syy}\dot{\phi}_s^2 - J_{Sxy}\dot{\varphi}_s\dot{\phi}_s\right) \tag{3.78}$$

$$T_{S,tr.} = \frac{1}{2}m_s(x_s^2 + y_s^2 + z_s^2) \tag{3.79}$$

$$T_{S,rot.} = \frac{1}{2}J_{Szz}(2\pi\, n_{sp} + \cos(\varphi_s)\sin(\phi_s)\dot{\varphi}_s - \sin(\varphi_s)\dot{\phi}_s)^2 \tag{3.80}$$

$$T_{H,tr.} = \frac{1}{2} m_h (x_h^2 + y_h^2 + z_h^2) \tag{3.81}$$

$$T_{H,rot.} = \frac{1}{2}\left(J_{Hxx}\dot{\varphi}_h^2 + J_{Hyy}\dot{\phi}_h^2 + J_{Hzz}\dot{\psi}_h{}^2 - J_{Hxy}\dot{\varphi}_h\dot{\phi}_h - J_{Hxz}\dot{\varphi}_h\dot{\psi}_h - J_{Hyz}\dot{\phi}_h\dot{\psi}_h \right) \tag{3.82}$$

where the subscripts "*rot.*" And "*tr.*" represent the rotational and translational kinetic energy respectively.

The generalized input force **Q**(t) is derived based on the input force vector $\mathbf{F_{In}}(t)$, an input moment $\mathbf{M_{In}}(t)$ and the force application point $\mathbf{P_{In}}$ (Eq. 3.65a).

$$\mathbf{F_{In}}(t) = \begin{bmatrix} F_x(t) \\ F_y(t) \\ F_z(t) \end{bmatrix} \quad ; \quad \mathbf{M_{In}}(t) = \begin{bmatrix} M_x(t) \\ M_y(t) \\ M_z(t) \end{bmatrix} \tag{3.83a,b}$$

$$\mathbf{Q}(t) = \{F_x(t), F_y(t), F_z(t), 0, 0, 0, F_z(t)y_{In} - F_y(t)z_{In}, F_z(t)x_{In} + F_x(t)z_{In}, 0, 0, 0\}^T \tag{3.84}$$

After all the energies and the generalized input forces have been derived, the eleven equations of motion for the 11 DOF system can be calculated using the Lagrange's Equation (Eq. 3.13). The resulting differential equations[15] are too long to be shown here. An equation for the generalized coordinate x_s is shown her as an example.

$$\begin{aligned} & k_{rx}\left(x_s(t) - x_h(t) - z_{s1}\phi_s(t) + z_{s1}\phi_h(t)\right) + k_{fx}\left(x_s(t) - x_h(t) + z_{s1}\phi_s(t) - z_{s1}\phi_h(t)\right) \\ & + c_{rx}\left(\dot{x}_s(t) - \dot{x}_h(t) - z_{s1}\dot{\phi}_s(t) + z_{s1}\dot{\phi}_h(t)\right) + c_{fx}\left(\dot{x}_s(t) - \dot{x}_h(t) + z_{s1}\dot{\phi}_s(t) - z_{s1}\dot{\phi}_h(t)\right) \\ & + m_s\ddot{x}_s(t) = F_x(t) \end{aligned} \tag{3.85}$$

---

[15] Derived by a suitable program performing symbolic computations.

The eleven EOMs can be put in vector matrix form as shown below.

$$\mathbf{m}\,\ddot{\mathbf{q}}(t) + \mathbf{c}\,\dot{\mathbf{q}}(t) + \mathbf{k}\,\mathbf{q}(t) = \mathbf{Q}(t) \tag{3.86}$$

From this equation the **m**, **c** and **k** matrices can be readily extracted. They are shown in Appendix C3. Also the state-space and TF model can be derived according to Sections 3.2.2 and 3.2.3.

3.6 Model Based Estimation

Various methods for estimating physical parameters are investigated in this research. In particular, six methods seem most promising and will therefore be described here in more detail. Since physical parameters only appear in constitutive models, such a model is developed in the previous Section for the system shown in Fig. 3.11. The resulting set of governing equations of motion is derived and one example of this set is shown in Eq. (3.76) above. All six estimation methods use this set of equations as a basis together with experimental data to obtain the physical parameters. These parameters can be found using various optimization algorithms (e.g. simulated annealing (Davis, 1987), adaptive grid refinement (Loehle, 1998) or deepest descent method (Pinter, 1996). The differences between the experimental and the theoretical model are minimized with respect to the unknown physical constants. The six estimation methods described below are referred to as: 1) "direct" method involving Newtonian equations of motion, 2) "two step" identification involving on black box models, 3) "one step" identification based on gray box models, 4) extended Kalman filter, 5) use of functional relationships and 6) "hybrid" method.

3.6.1 "Direct" Method

As outlined in Chapter 2 the differential EOM become algebraic equations if one can measure accelerations, velocities, displacements and forces directly. For the simple MDOF system analyzed in Chapter 5.3 the model can be written in the form (Eq. (5.2) presented in the form of Eq. (2.14)).

$$\begin{bmatrix} m_1 & 0 & c_{11}+c_{12} & -c_{12} & k_{11}+k_{12} & -k_{12} \\ 0 & m_2 & -c_{12} & c_{12}+c_{22} & -k_{12} & k_{12}+k_{22} \end{bmatrix} \begin{pmatrix} \ddot{d}_1 \\ \ddot{d}_2 \\ \dot{d}_1 \\ \dot{d}_2 \\ d_1 \\ d_2 \end{pmatrix} = \begin{pmatrix} F_1 \\ F_2 \end{pmatrix} \tag{3.87}$$

For six sets of measurement data the measurement vector becomes a square matrix and thus can be inverted.

$$[m \quad c \quad k] = \begin{pmatrix} F_{11} & F_{12} & F_{13} & F_{14} & F_{15} & F_{16} \\ F_{21} & F_{22} & F_{23} & F_{24} & F_{25} & F_{26} \end{pmatrix} \begin{pmatrix} \ddot{d}_{11} & \ddot{d}_{12} & \ddot{d}_{13} & \ddot{d}_{14} & \ddot{d}_{15} & \ddot{d}_{16} \\ \ddot{d}_{21} & \ddot{d}_{22} & \ddot{d}_{23} & \ddot{d}_{24} & \ddot{d}_{25} & \ddot{d}_{26} \\ \dot{d}_{11} & \dot{d}_{12} & \dot{d}_{13} & \dot{d}_{14} & \dot{d}_{15} & \dot{d}_{16} \\ \dot{d}_{21} & \dot{d}_{22} & \dot{d}_{23} & \dot{d}_{24} & \dot{d}_{25} & \dot{d}_{26} \\ d_{11} & d_{12} & d_{13} & d_{14} & d_{15} & d_{16} \\ d_{21} & d_{22} & d_{23} & d_{24} & d_{25} & d_{26} \end{pmatrix}^{-1} \tag{3.88}$$

This method presents a closed form solution for the physical parameters in theory. It has not been tested in this research because of the extensive amounts of measurements necessary.

3.6.2 "Two Step" Method

This method is based on the comparison of the transfer functions from the analytical model and from experimental data. Fig. 3.14 illustrates the relationship between the actual system and different models.

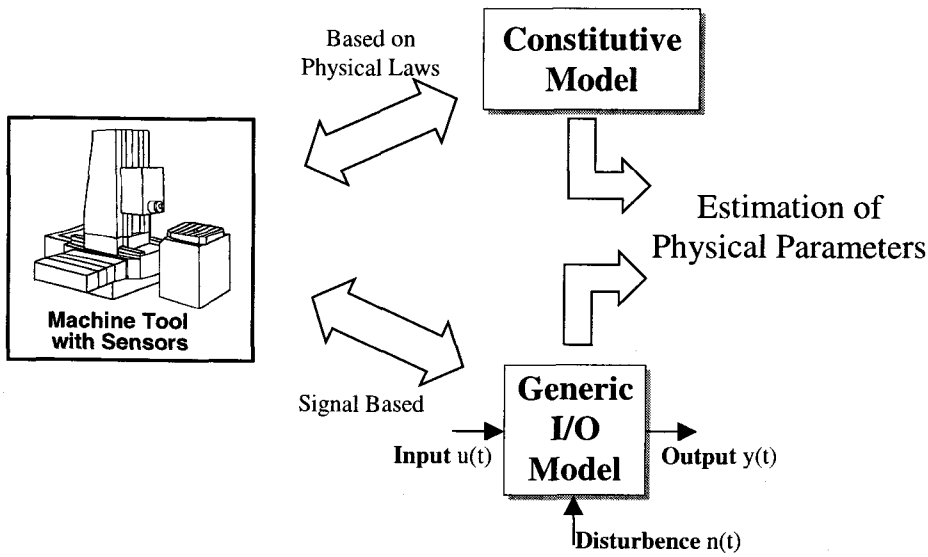

Fig. 3.15: Concept of physical parameter estimation.

From the constitutive equations of motion an analytical transfer function is calculated. For a system shown in Fig. 1.2 and Eq. (1.2), which has n inputs and m outputs, there exist $m \cdot n$ separate transfer functions describing the system. Each of those transfer functions contains information about the system and some or all of its physical parameters. In particular, the coefficients a_i and b_j of Eq. (3.15) are functions of these physical parameters. In this method, those coefficients are used to estimate the physical parameters. It will be shown later that using more than one transfer function is often required to estimate the **m**, **c** and **k** matrices. However, for the sake

of clarity, the method will first be presented using only one transfer function. The method can be easily extended to include more transfer functions.

A single-input single-output system (SISO) shown below is considered. Parametric identification (Ljung, 1987; Young, 1981; Astrom, 1971) applied to experimental input-output data facilitates the estimation of a transfer function $G_e(s)$. This monic transfer function has numerical coefficients $\hat{a}_i$ and $\hat{b}_j$.

$$G_e(s) = \frac{\hat{b}_p s^p + \hat{b}_{p-1} s^{p-1} + \ldots + \hat{b}_2 s^2 + \hat{b}_1 s + \hat{b}_0}{s^q + \hat{a}_{q-1} s^{q-1} + \ldots + \hat{a}_2 s^2 + \hat{a}_1 s + \hat{a}_0} \tag{3.89}$$

The same system is modeled by an analytical transfer function $G_a(s)$, (Eq. 3.4), that is obtained using one of the methods described in Section 3.2. The coefficients a_i and b_j are explicit functions of the physical parameters collectively represented by a set $\Theta = \{m_1, \ldots m_r, c_1, \ldots c_s, k_1, \ldots k_s\}$.

$$G_a(s) = \frac{b_p s^p + b_{p-1} s^{p-1} + \ldots + b_2 s^2 + b_1 s + b_0}{s^q + a_{q-1} s^{q-1} + \ldots + a_2 s^2 + a_1 s + a_0} \tag{3.90}$$

where
$$a_i = f_i(\Theta) \tag{3.91a}$$
$$b_j = g_j(\Theta) \tag{3.91b}$$

Comparison of coefficients in the analytical and empirical transfer function yields *p+q-1* equations involving the physical parameters.

$$a_i(\Theta) = \hat{a}_i \tag{3.92a}$$
$$b_j(\Theta) = \hat{b}_j \tag{3.92b}$$

It is important that the numerator and denominator of Eq. (3.89) and Eq. (3.90) have the same order, otherwise the coefficients can not be compared and Eq. (3.92a) and Eq. (3.92b) are meaningless (see also Fig. 3.16).

The task is to solve this set of equations for the unknown physical parameters. Unfortunately, this turns out to be a difficult task, and usually an analytical closed form solution does not exist. There are several reasons for this. First, the experimentally identified TF coefficients $\hat{a}_i$ and $\hat{b}_j$ are corrupted with random noise, introduced through I/O identification of noisy experimental data. Second, the theoretical TF might not exactly represent all the physical phenomena present in the system, since assumptions and linearizations were probably made. Thirdly, a_i and b_j are usually nonlinear functions of **m**, **c** and **k**, making linear techniques for solving the system of equations not applicable. Table 3.1 illustrates the difficulty of finding a closed form solution of Eq. (3.92).

Table 3.1: Determination of uniqueness of solution of Eq. (3.92).

f_i , g_j linear / $\hat{a}_i$, $\hat{b}_j$ corrupted	**No**	**Yes**
No	Exact solution can be found numerically	Exact closed form solution exists
Yes	Numerical solution, optimal in a statistical sense can be found. This solution might be inaccurate.	Closed form solution, statistically optimal can be found (e.g. "least square" sense optimal. This solution might be inaccurate

Only if the functions f_j and g_j of Eq. (3.91) are linear in the physical parameters, and $\hat{a}_i$ and $\hat{b}_j$ are not corrupted with noise, then a closed form solution is guaranteed. Still, with the system's behavior known and with exact measurements of input and output signals the determination of the physical parameters should be possible. Even if the system does not have an analytical closed form solution, iterative methods can be used to obtain estimates of the physical parameters **m**, **c** and **k**. The determination

of the parameters becomes a statistical estimation problem. It can be shown that this problem can be solved using global minimization methods.

The following methodology was developed as a guideline for setting up these equations (3.92a) and (3.92b) described above, and finding a solution for the physical parameters **m**, **c** and **k**.

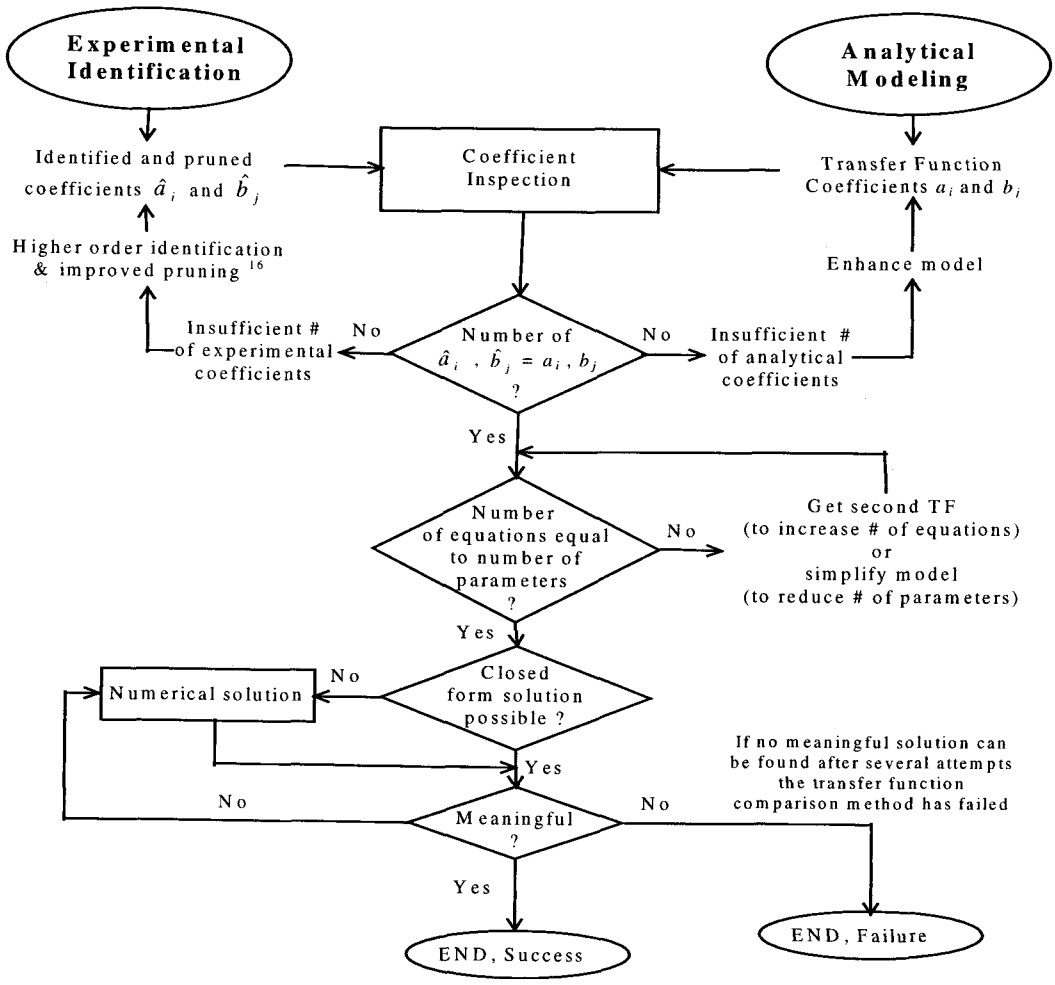

Fig 3.16: Methodology for transfer function coefficients comparison.

[16] see Section 4.7 for more details on 'pruning'.

The first objective within this methodology is to obtain the same order of the theoretical and experimental transfer functions, and as a result, the same number of coefficients a_i and b_j. Typically in experimental parametric identification, the higher order model one chooses, the more accurate the identification is. Unfortunately, high order identification causes so called 'phantom' poles and zeros to appear, which are nonexistent in the real system. In this research 40^{th} order ARMAX (Ljung, 1987; Isermann, 1981) identification is used causing the result to contain 40 poles and 39 zeros, even though from theoretical modeling it was clear that the system should have much fewer zeros and poles. Hence, so-called 'model pruning' (Shyan-Huang, 1994) has to be used to identify and eliminate these 'phantom' poles and zeros (see also Section 4.7).

After the system of equations has been built with equal number of transfer function coefficients, one has to analyze how many equations there are and how many variables are unknown. If there are more unknowns than equations, the problem is under-determined. The number of equations needs to be increased by including another transfer function of the same system. Also, the number of unknowns could be reduced, by lumping physical parameters together. In doing so one could monitor e.g. the sum of two masses instead of each mass individually. If there exist more equations than unknowns, the system is over-determined. This should actually help in the numerical minimization procedure, since more equations means more information about the system which facilitates finding the optimal parameters. However, "least squares" sense solution is possible in the latter case.

The set of equations (3.92a,b) is not only non-linear, but also multi-dimensional. Solving this set of equations is equivalent to finding the roots of

$$\hat{a}_i - a_i(\boldsymbol{\Theta}) = 0 \tag{3.93a}$$

$$\hat{b}_j - b_j(\boldsymbol{\Theta}) = 0 \tag{3.93b}$$

Multidimensional root finding is considered a very difficult problem. It is easier to find a minimum of a function of many variables, which helps here as well. One might collapse all these dimensions into one. Adding up the squares of the individual functions f_i to get a master function Q, which is positive definite and has a global minimum of exactly at zero all the solutions of the original set of nonlinear equations. In order to facilitate computer implementation, equations (3.93a) and (3.93b) are put into vector notation, such that

$$\hat{\mathbf{\Lambda}}_{\mathrm{TF}} = \begin{bmatrix} \hat{a}_1 \\ \vdots \\ \hat{a}_{q-1} \\ \hat{b}_1 \\ \vdots \\ \hat{b}_p \end{bmatrix} \qquad \mathbf{\Lambda}_{\mathrm{TF}} = \begin{bmatrix} a_1 \\ \vdots \\ a_{q-1} \\ b_1 \\ \vdots \\ b_p \end{bmatrix} \tag{3.94a,b}$$

Equations (3.93a,b) then become the total error between the experimental and analytical transfer function coefficients

$$\mathbf{e} = \mathbf{\Lambda}_{\mathrm{TF}}(\mathbf{\Theta}) - \hat{\mathbf{\Lambda}}_{\mathrm{TF}} \tag{3.95}$$

The error vector **e** may not become zero and it might not be possible to solve Eq. (3.95) analytically then numerical methods need to be applied. A performance index can be formed using different norms. The quadratic norm is built as

$$l_q(\mathbf{e}) = \frac{1}{2}\mathbf{e}^{\mathrm{T}} \mathcal{L}\, \mathbf{e} \tag{3.96}$$

where $\mathcal{L}$ is a diagonal matrix weighing the relative importance of the components of **e**. Another norm used often is the euclidian (L_2) norm.

$$l_e(\mathbf{e}) = \|\mathbf{e}\|_2 = \sqrt{e_1^{\,2} + e_2^{\,2} + \cdots + e_n^{\,2}} \tag{3.97}$$

In this research the sum of normalized squares is used as a performance index for physical parameter estimation.

$$Q(\Theta) = l_{ns}(\Theta) = \sum_{i=1}^{n} \left(\frac{\Lambda_i - \hat{\Lambda}_i(\Theta)}{\Lambda_i} \right)^2 \tag{3.98}$$

Applying Eq. (3.98) to the case of transfer function coefficient comparison leads to

$$Q_{TF}(\Theta) = \sum_{i=1}^{p+q-1} \left(\frac{\Lambda_{TF,i} - \hat{\Lambda}_{TF,i}(\Theta)}{\Lambda_{TF,i}} \right)^2 \tag{3.99}$$

Minimizing this performance index $Q_{TF}(\Theta)$ leads to the estimates of the physical parameters as shown in Eq. (3.100) below.

$$\hat{\Theta} = \arg\min_{\Theta \in D} Q_{TF}(\Theta) \tag{3.100}$$

Unfortunately the shape of the function $Q_{TF}(\Theta)$ can be complex and can have multiple minima in addition to the global one. The challenge is to develop search methods, which will not get trapped in local minima, but which will find the global minimum. Details about global minimization are described in Section 4.3. A slight modification of the TF coefficient comparison method is outlined below.

Zero Pole Comparison is an alternative to the method of comparing transfer function coefficients. Instead of using the coefficients a_i and b_i of the analytical and experimental transfer function, the poles and zeros are used directly. Zeros and poles are more meaningful in describing the behavior of the system, since their values represents explicitly the nature of the system. In particular, zeros and poles give direct information on the resonance frequency and damping ratios of the system (see Section 3.2.3).

In order to completely describe a system, the DC-gain has to be known in addition to the zeros and poles of the system. After the zeros and poles and the DC-gain are calculated from the model and from the experimental data, a performance

index can be derived using the error between the model and experimental poles, zeros and DC-gain.

$$\hat{p}_i - p_i(\boldsymbol{\Theta}) = e_{p,i} \tag{3.101a}$$

$$\hat{z}_j - z_j(\boldsymbol{\Theta}) = e_{z,j} \tag{3.101b}$$

$$\hat{g} - g(\boldsymbol{\Theta}) = e_g \tag{3.101c}$$

Similarly to Eq. (3.94a,b) the differences between experimental and analytical poles, zeros and gains can be put into a vector notation such that

$$\hat{\boldsymbol{\Lambda}}_{\mathbf{ZP}} = \begin{bmatrix} \hat{p}_1 \\ \vdots \\ \hat{p}_{\frac{q}{2}} \\ \hat{z}_1 \\ \vdots \\ \hat{z}_{\frac{p}{2}} \\ \hat{g} \end{bmatrix} \qquad \boldsymbol{\Lambda}_{\mathbf{ZP}} = \begin{bmatrix} p_1 \\ \vdots \\ p_{\frac{q}{2}} \\ z_1 \\ \vdots \\ z_{\frac{p}{2}} \\ g \end{bmatrix} \tag{3.102a,b}$$

The performance index is then calculated similarly to Eq. (3.99)

$$Q_{ZP}(\boldsymbol{\Theta}) = \sum_{i=1}^{p+q-1} \left(\frac{\Lambda_{ZP,i} - \hat{\Lambda}_{ZP,i}(\boldsymbol{\Theta})}{\Lambda_{ZP,i}} \right)^2 \tag{3.103}$$

Minimization should again lead to an optimal estimate of the unknown physical parameters Θ.

$$\hat{\boldsymbol{\Theta}} = \arg\min_{\Theta \in D} Q_{ZP}(\boldsymbol{\Theta}) \tag{3.104}$$

The following figure (in the *s*-plane) can illustrate this error minimization process.

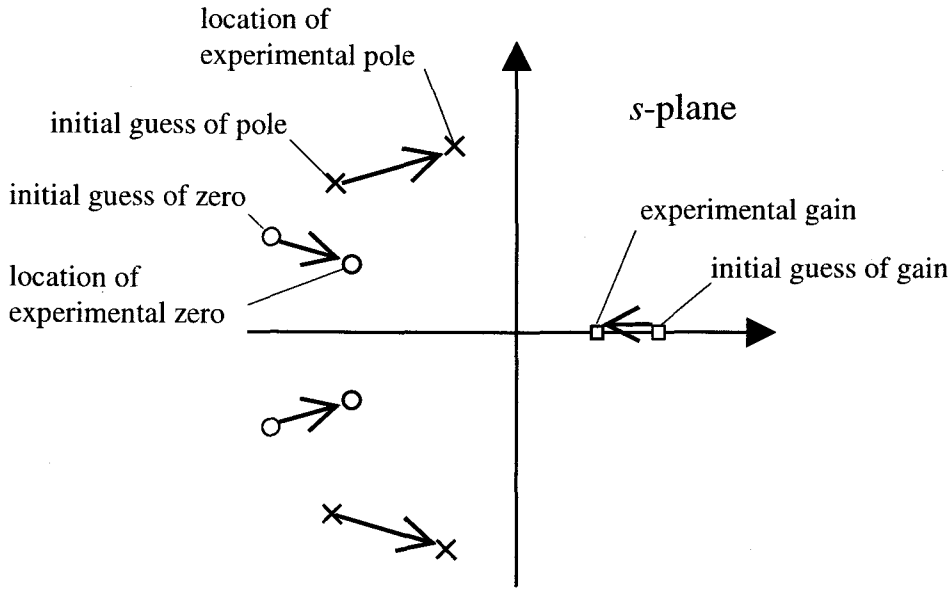

Fig. 3.17: Error minimization in the *s*-plane.

3.6.3 "One Step" Method

In this method the analytical transfer function is used as well. An output signal is simulated from the theoretical model, which is compared with the respective experimental data. In order to estimate the physical parameters **m**, **c** & **k**, the sum of squared errors between the simulated and experimental data has to be minimized with respect to **m**, **c** & **k**. Therefore, the simulated output data has to be a function of the physical parameters. Since the experimental data is in discrete form, the theoretical transfer function of the continuos domain needs to be transformed into the discrete domain using, for example, Tustin's method (DeCarlo, 1989).

$$G_d = \frac{b_{0d} + b_{1d}q + \ldots + b_{md}q^m}{a_{0d} + a_{1d}q + \ldots + a_{nd}q^n} \tag{3.105}$$

From the discrete transfer function of the system, (Eq. 3.105)[17], a recursive formula can be obtained in the form of Eq. (3.106). It shows the theoretical model output $\hat{y}_k$ as a function of past outputs and present and past inputs to the system. a_{jd} and b_{id} are the discrete transfer function coefficients and are a function of the physical parameters **m**, **c** and **k**.

$$\hat{y}_k(\boldsymbol{\Theta}) = \frac{1}{a_{0d}} \left(\sum_{i=0}^{m} b_{id}(\boldsymbol{\Theta}) \cdot u_{k-ir} - \sum_{j=1}^{n} a_{jd}(\boldsymbol{\Theta}) \cdot y_{k-jr} \right) \tag{3.106}$$

The error between the simulated and experimental output is

$$e_k(\boldsymbol{\Theta}) = \hat{y}_k(\boldsymbol{\Theta}) - y_k \tag{3.107}$$

Here the euclidian norm of the output error (Eq. (3.97)) is used for building the performance index.

$$Q_{TD}(\boldsymbol{\Theta}) = \left\| \mathbf{y} - \hat{\mathbf{y}}(\boldsymbol{\Theta}) \right\|_2 \tag{3.108}$$

This can be minimized similarly to Eq.(3.100)

$$\hat{\boldsymbol{\Theta}} = \arg\min_{\Theta \in D} Q_{TD}(\boldsymbol{\Theta}) \tag{3.109}$$

---

[17] The subscript "*d*" in Eq. (3.105) and (3.106) denotes discrete coefficients

3.6.4 Extended Kalman Filter

Physical parameters of a system can also be estimated using an extended Kalman filter (Kalman, 1960). It is essentially an observer, as shown in Fig 3.18.

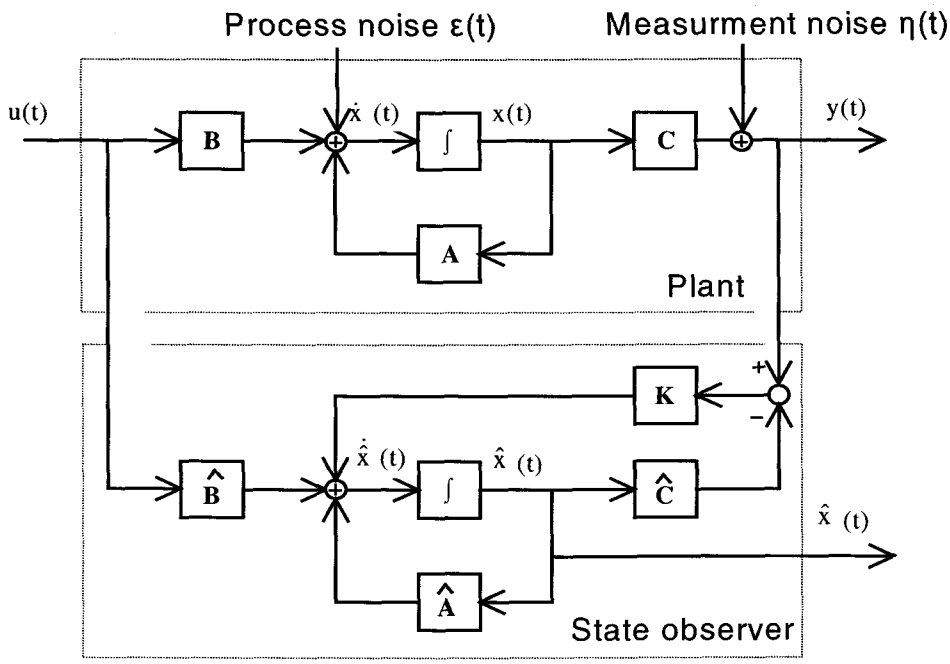

Fig. 3.18: The Kalman filter as an optimal observer.

The Kalman filter gain **K** is calculated to give optimal estimates of the state variables **x(t)** with respect to minimizing process and measurement noise. It is employed for physical parameter estimation in the following way: one can rewrite the state-space formulation of the system (repeated here for clarity but with noise) such that the unknown physical parameters are represented as additional state variables of the system.

$$\dot{\mathbf{x}}(t) = \mathbf{A} \cdot \mathbf{x}(t) + \mathbf{B} \cdot \mathbf{u}(t) + \boldsymbol{\varepsilon}(t) \tag{3.110}$$

Then the Kalman filter can be used to estimate those states and hence find the unknown system constants. Unfortunately, as a result the dimension of the system increases, and the evolution matrix **A** also becomes non-linear. One way to deal with these difficulties is to linearize the model using the Taylor series expansion around some operating state $\mathbf{x}_0$. Eq. (3.110) can be rewritten to separate all non-linear components into **n(x)** leaving the linear components in $\mathbf{\Gamma}$.

$$\dot{\mathbf{x}}(t) = \mathbf{\Gamma}\,\mathbf{x}(t) + \mathbf{n}(\mathbf{x}) + \mathbf{B}\,\mathbf{u}(t) + \boldsymbol{\varepsilon}(t) \tag{3.111}$$

Expanding **n(x)** with a Taylor's expansion about some state $\mathbf{x}_0$ gives

$$\mathbf{n}(\mathbf{x}) = \mathbf{n}(\mathbf{x}_0) + \mathbf{J}(\mathbf{x} - \mathbf{x}_0) \tag{3.112}$$

where **J** represents the Jacobian matrix of **n** evaluated at $\mathbf{x}_0$

$$J_{ij} = \frac{\partial n_i}{\partial x_j} \tag{3.113}$$

Substituting Eq. (3.112) into Eq. (3.111) gives

$$\dot{\mathbf{x}}(t) = (\mathbf{\Gamma} + \mathbf{J})\;\mathbf{x}(t) - \mathbf{n}(\mathbf{x}_0) - \mathbf{J}(\mathbf{x}_0) + \mathbf{B}\;\mathbf{u}(t) + \boldsymbol{\varepsilon}(t) \tag{3.114}$$

Equation (3.114) can then be put into discrete form. One obtains a linearized discrete state-space form.

$$\mathbf{x}_{i+1} = \mathbf{\Psi}_i\,\mathbf{x}_i + \mathbf{\Omega}_i\,\mathbf{u}_i + \boldsymbol{\varepsilon}_i \tag{3.115}$$

$$\mathbf{d}_i = \mathbf{C}_i\mathbf{x}_i + \boldsymbol{\eta}_i \tag{3.116}$$

The optimal estimate of the state vector can be calculated as

$$\hat{\mathbf{x}}_{i+1} = \mathbf{\Psi}_i\hat{\mathbf{x}}_i + \mathbf{\Omega}_i\mathbf{u}_i + \mathbf{K}\left(\mathbf{d}_i - \mathbf{C}_i\hat{\mathbf{x}}_i\right) \tag{3.117}$$

where the gain **K** is calculated by solving the Riccati equation. More detailed information can be found in (Trujillo,1997).

Due to the linearization necessary as described above, there is no guaranty that the states and therefore the physical parameters converge to their actual values. The extended Kalman filter presented by the equations above is applied in this research, to a simple spring mass system described in Section 5.3.4.3.

3.6.5 Use of Functional Relationships

As explained in Chapter 1 (see Fig. 1.1), feature extraction of measured signals is an important component of the monitoring chain. If one can find functional relationships between these features and physical parameters, monitoring would be quick and straightforward. Observation of features would give direct indication of the behavior of physical parameters. These relationships can be analytical or empirical. They might be explored by establishing "feature" maps, which illustrate the change of features due to modification of physical parameters.

Unfortunately there is no guaranty whether such a relationship exists and no rigorous approach is available on how to find it. However, the analytical model developed in this thesis greatly facilitates searching such relationships. Generation of features such as resonance frequency or damping ratio can be done quickly for many different sets of physical parameters. In Chapter 5.4.4 this method is applied to the problem of preload monitoring.

3.6.6 "Hybrid" Method

As a conclusion of the analysis of the five methods above, a combination of two or more of these methods can lead to improved estimation results. For example

the extended Kalman filter can be combined with the "one step" method for fast estimation of varying parameters and multiple estimation of slow changing parameters. This method has to be evaluated and tested in more detail in the future.

3.7 Closure

In this Chapter a methodology of computer aided model derivation and gray box model-based estimation is presented. The concept of analytic model building is discussed and three cases of increasing complexity are analyzed. An analytical model of a MDOF machine tool is developed for the purpose of physical parameter estimation. The model is built in an incremental manner from first principles and allows easy modification by the user. It consists of multiple rigid bodies connected by spring-damper elements. Once position vectors and attachment points to the SDEs have been defined, the program will derive the EOMs automatically using Lagrange's method. Also different physical parameter estimation methods are investigated. The following table summarizes these methods and the circumstances when they can be applied.

Table 3.2: Summary of different estimation methods.

Estimation Method	Comments
1) Direct method involving Newtonian EOMs.	Closed form solution; Has not been tested in depth because excessive requirements of sensors.
2) "Two step" method a) analytical solution	When analytic solution is possible and physically meaningful.
b) numerical solution	When analytical solution is not possible or not physically meaningful.
c) minimization	When analytic solution is not possible or not physically meaningful and numeric methods fail.
3) "One step" method based on gray box I/O models	Computationally intensive, but leads to promising results.
4) Extended Kalman filter	Only feasible for limited physical parameters.
5) Use of functional relationships	If such relationships are found this method is simple.
6) "Hybrid" method	Combination of above methods can take advantage of individual benefits.

4. IMPLEMENTATION AND VALIDATION ISSUES

4.1 Introduction

In order to realize the full potentials of the modeling and estimation methodology developed in Chapter 3 it needs to be implemented on a computer. An inherent feature of physical parameter estimation is its high sensitivity to modeling errors. Therefore computations of the equations in the previous section without any loss of precision is critical otherwise the proposed methodology won't be successful. The working environment for the computer implementation has to be characterized by the following three features. First, the software package used has to allow symbolic calculations since this is the key to tracability of the physical parameters. Second, the ability to perform computations with controlled numerical precision ensures correct calculations of equations, which are very sensitive to inaccuracies. Finally the software has to facilitate mapping of models from the differential equation domain into the system analysis and control theory framework.

Both, *Mathematica*, (Wolfram, 1992) and *Maple*, (Waterloo, 1997) allow symbolic and arbitrary precision calculations. If necessary, infinite precision calculations can be done provided the inputs are entered with infinite precision[18].

[18] In *Mathematica*'s language this means no decimal fractions are used.

In other packages like Matlab (Mathworks, 1995) users have little control on the precision of calculations and therefore those packages are not suited for this research. *Mathematica* has an additional advantage over *Maple* since a package is available, (Wolfram, 1992), which allows the use of functions from controls theory and also can do transformations of models into different representations and domains illustrated in Fig. 3.4.

Since successful estimation hinges on the accurate implementation of computations, the issue of controlled numerical precision is addressed in Section 4.2. Two examples illustrate that modeling of complex mechanical systems necessitates computations with high numerical precision. Section 4.3 presents a discussion of difficulties encountered with the minimization algorithm. The complex shape of the multi-dimensional performance index derived in Section 3.6 causes these difficulties. Next, in Section 4.4 a sensitivity analysis is described to evaluate which parameters are suited for estimation. Rapid changes of sensitivities can indicate potential difficulties with the estimation procedure. Computer simulations are also very helpful in analyzing, evaluating and tuning the estimation procedure and therefore are elaborated on in Section 4.5. Another necessary step before estimation is the validation of the analytical model developed in the previous chapter. One way of comparing the model behavior with the dynamics of the real machine is visualization of its motion, which is dealt with in Section 4.6. A new concept of 'gray box' model based visualization is proposed there. Finally, in Section 4.7 the attempt is made to automate and facilitate different steps of the estimation algorithm through the use of artificial intelligence. For example until recently, the task of experimental identification of transfer functions required significant user input and experience. An intelligent algorithm is proposed which reduces the user involvement.

4.2 Arbitrary Precision Computations

Mechanical systems and machine tools in particular are characterized by quantities, which vary in a wide range. Elements of the stiffness matrix **k** in Eq. (3.86) are very high (of the order 10^8 N/m) whereas elements of the damping matrix **c** can be extremely low (of the order 10^{-2} N/m) (Weck, 1984; Goodwin, 1991). These values appear in the differential equations of motion in matrix form, shown here again for clarity.

$$\mathbf{m}\ \ddot{\mathbf{q}}(t) + \mathbf{c}\ \dot{\mathbf{q}}(t) + \mathbf{k}\ \mathbf{q}(t) = \mathbf{Q}(t) \tag{4.1}$$

Systems of this nature are commonly referred to as being ill conditioned. As a result difficulties arise when dealing with matrices such as Eq. (3.7a), which is shown here again for clarity.

$$\mathbf{A} = \begin{bmatrix} \mathbf{0} & \mathbf{I} \\ -\mathbf{k}\cdot\mathbf{m}^{-1} & -\mathbf{c}\cdot\mathbf{m}^{-1} \end{bmatrix} \tag{4.2}$$

This matrix, called the evolution matrix in state-space theory is used in this research in many ways. One way is for the frequently needed transformation of the state-space model into the TF model. Equation (3.13) is used for this transformation in continuous time,

$$\mathbf{G}(s) = \frac{\mathbf{Y}(s)}{\mathbf{U}(s)} = \mathbf{C}\cdot(s\cdot\mathbf{I} - \mathbf{A})^{-1}\cdot\mathbf{B} + \mathbf{D} \tag{4.3}$$

and Eq. (3.14) for the discrete transformation.

$$\mathbf{G}(z) = \frac{\mathbf{Y}(z)}{\mathbf{U}(z)} = \mathbf{C}\cdot(z\cdot\mathbf{I} - \mathbf{\Psi})^{-1}\cdot\mathbf{\Omega} + \mathbf{D} \tag{4.4}$$

Especially when inverting such ill conditioned matrices computational errors can become large. The severity of the problem will be illustrated below. Since the model of the spindle-assembly is too complex to serve for this purpose a simpler system is used to give insight into the problem.

It will show the user where the errors can manifest themselves and thus is part of the validation of the methodology presented in Chapter 3. Also the user will learn how to deal with those problems, which will almost certainly arise. Two examples from a case well documented in previous research (Chung, 1993) are used to show the class of problems encountered when computing with finite precision. They involve a simple rigid body plate with six DOF moving in space. Its EOMs can be found in any standard dynamics textbook such as Innman (1994). Such a plate actually represents a high performance dynamometer (Model 9257A) manufactured by Kistler. Fig. 4.1 shows the mechanical design of this dynamometer.

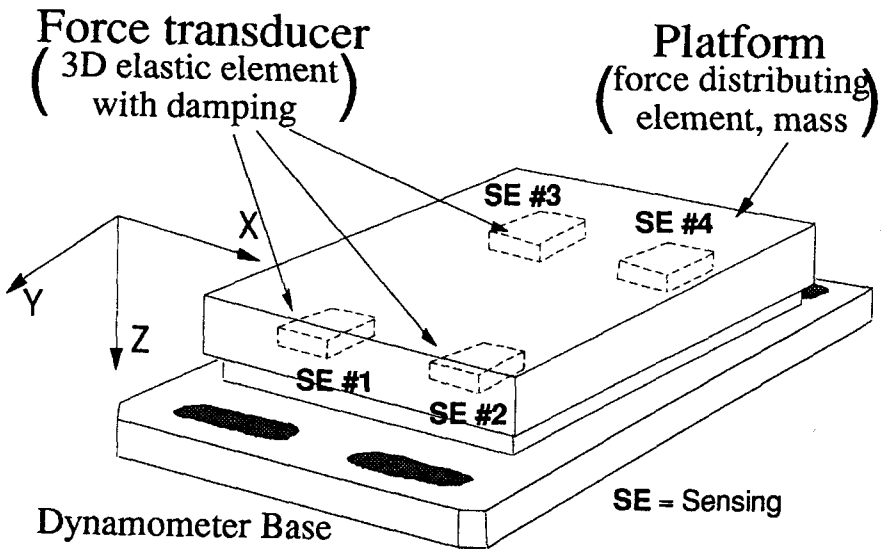

Fig. 4.1: Mechanical design of the *Kistler* dynamometer.

Chung, (1993) investigated and modeled this device in an effort to build an inverse filter to attenuate distortions of the force signals introduced by the vibration modes of the plate. Distorted electrical output signals of the dynamometer are passed through a filter consisting of the inverse transfer function of the system in order to obtain

corrected signals representing the true acting forces on the plate. In the two examples the following problems were encountered:

Example 1: The transfer function (TF) between the input force on the plate and the output displacement in z-direction[19] was derived following the procedure of automatic modeling delineated in Chapter 3. The EOMs in the form of Eq. (4.1) and the state-space model was obtained. Applying Eq. (4.3) in the continuous case or Eq. (4.4) in the discrete case the state-space model can be transformed into the TF model. The structure of the TF model obtained in the continuous domain is shown below

$$G_{XFx}(s) = \frac{b_p s^p + b_{p-1} s^{p-1} + \ldots + b_2 s^2 + b_1 s + b_0}{s^q + a_{q-1} s^{q-1} + \ldots + a_2 s^2 + a_1 s + a_0} \tag{4.5}$$

Finite precision calculations of Eq. (4.5) resulted in $p = 10$ and $q = 12$. Infinite precision calculations however gave $p = 8$ and $q = 10$. Further analysis revealed that the finite precision TF one zero and pole was very close and a zero-pole cancellation should have taken place, which wasn't accomplished due to insufficient precision of calculations. In this case users heuristic knowledge and in depth investigation was needed to correct the result. However in general and in more complex cases such as the spindle assembly it is not possible to check the correctness of computations. Especially in this research it is of utmost importance to obtain the correct model structure. Methods are applied (transfer function coefficient comparison) where the accurate calculation of TF coefficients is critical. As a result infinite precision calculations are needed.

---

[19] The displacement can be used as an output of a model since it is proportional to the electrical output of the actual dynamometer.

Example 2: Before an inverse filter proposed in Chung's research can be developed, it has to be tested whether that inverse exists. According to Sain and Massey (1969) a system is invertable if and only if

$$m \leq r \tag{4.6}$$

and

$$Rank(\mathbf{M}_n) - Rank(\mathbf{M}_{n-1}) = m \tag{4.7}$$

In equations (4.6) and (4.7) m and r are the number of inputs and outputs to the system respectively, and n is the number of state variables. $\mathbf{M}_n$ is referred to as the invertability-matrix and has a similar form as the observability- or controllability-matrix (described in Eq. (6.2) and (6.3)).

$$\mathbf{M}_n = \begin{bmatrix} \mathbf{0} & \mathbf{0} & \mathbf{0} & \cdots & \mathbf{0} \\ \mathbf{CB} & \mathbf{0} & \mathbf{0} & \cdots & \mathbf{0} \\ \mathbf{CAB} & \mathbf{CB} & \mathbf{0} & \cdots & \mathbf{0} \\ \vdots & \vdots & \vdots & \ddots & \vdots \\ \mathbf{CA}^{n-1}\mathbf{B} & \mathbf{CA}^{n-2}\mathbf{B} & \mathbf{CA}^{n-3}\mathbf{B} & \cdots & \mathbf{0} \end{bmatrix} \tag{4.8}$$

The state-space model of the dynamometer has $m = 6$ inputs, $r = 6$ outputs and $n = 12$ state variables. As a result, even for the simple plate moving in 3D-space the matrix $\mathbf{M}_n$ has the size $78x78$ and $\mathbf{M}_{n-1}$ has the size $72x72$. From finite and infinite precision computation of the rank of the invertability matrix the following results were obtained:

Table 4.1: Results of the invertability tests.

	Finite Precision	**Infinite Precision**
Rank ($\mathbf{M}_n$)	12	66
Rank ($\mathbf{M}_{n-1}$)	12	60

Table 4.1 together with Eq. (4.7) shows that finite precision computation lead to the conclusion that the inverse of the dynamometer model does not exist. The proposed inverse filter would be impossible to design. Infinite precision computation however proved these results wrong. User's heuristic knowledge does not help in this case since it is impossible to deal with such large matrices by hand.

The above two examples of previous research among others resulted in the decision to use *Mathematica* for all computations in this research. The work done by Chung does not only serve here as an illustration of the importance of infinite precision, but is also relevant in the research presented here, since this concept can also be applied to the spindle assembly. It would open the possibility of estimating unknown cutting forces by vibration measurement on the spindle housing. An accurate model of the system, such as derived in Chapter 3 is the prerequisite of building this inverse system (Spiewak, 1994).

4.3 Global Minimization

Most of the methods for physical parameter estimation proposed in Chapter 3 relay on the minimization of a performance index. Many minimization algorithms exist and they usually have no difficulties finding minima of well-behaved functions (Pinter, 1996; Press, 1994). However in this research the performance indices built, (Eq. (3.96), (3.106)) have multiple minima and their shape is complex. For example the performance index used for the time domain estimation method derived in Section 3.6.2 is built as follows

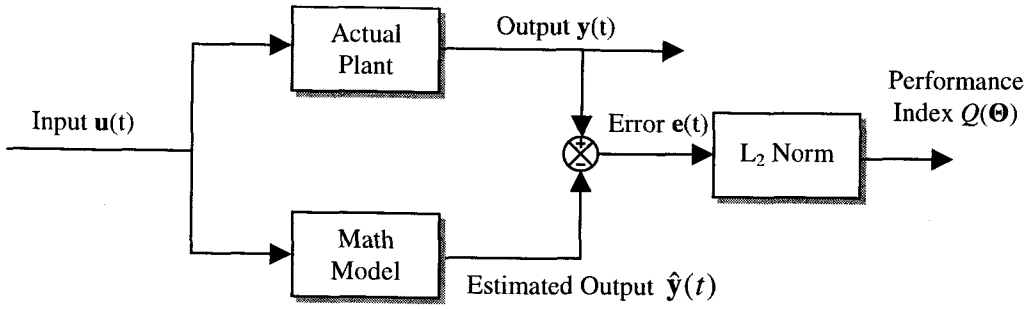

Fig. 4.2: A block diagram for building the performance index.

The system and model output in time-domain are substracted and then the L_2 norm is calculated. The optimal physical parameters are found by minimizing the L_2 norm as done in Eq. (3.95) which is shown here again for clarity

$$\hat{\boldsymbol{\Theta}} = \underset{\Theta \in D}{\arg\min} \left\| \mathbf{y} - \hat{\mathbf{y}}(\boldsymbol{\Theta}) \right\|_2 \tag{4.9}$$

where D is the unconstrained domain of possible mathematical solutions which include negative or complex values. For the spindle assembly this function can have up to twenty variables and therefore a robust method is needed to find its global minima. A minimization algorithm based on the combination of the Brent and the conjugate gradient method is used in this research[20]. However this method like most standard procedures can only find local minima. The user than has to validate whether the found solution is global and meaningful. If not, a new search needs to be conducted starting from different initial conditions. For functions with up to two variables 3D-visualization can aid in analyzing its shape and detect potential difficulties with minimization. Fig. 4.3 shows a 3D-visualization of a 'camelback' function (Loehle, 1998), which can be used to test the robustness of different minimization methods.

The example below illustrates the difficulties encountered when searching for the global minima of the performance index of Eq. (4.9).

Example: The performance index was built for the estimation of the seven physical parameters of the simple MDOF system described in Section 5.2. The unconstrained search of the minimization procedure converged to the following values:

Table 4.2: Unconstrained search results of physical parameter estimates.

Physical Parameter	Numerical Value	Physical Parameter	Numerical Value
m_1, [kg]	-2.54	k_{22}, [10^6 N/m]	5.92
m_2, [kg]	4.43	c_{11}, [Ns/m]	23.56
k_{11}, [10^6 N/m]	3.20	c_{22}, [Ns/m]	12.63
k_{12}, [10^6 N/m]	1.78		

This is mathematically a legitamite solution however, it is physically totally meaningless (negative *Mass_1*). It is common practice to introduce penalty functions in such cases in order to limit the search space. Eq. (4.10) shows how the performance index was modified by the introduction of a penalty function to prevent the algorithm from getting to negative physical parameters.

$$Q^*(\Theta)=\begin{cases} Q(\Theta), & for\ m_1 \geq m_{1,\min} \\ p \cdot Q(\Theta), & for\ m_1 < m_{1,\min} \end{cases} \tag{4.10}$$

---

[20] This method works well in the programming environment chosen in this research.

If the estimated value m_1 becomes smaller than the threshold $m_{1,min}$ the performance index $Q(\Theta)$ is multiplied by the penalty function p.

$$p = 1 + C_p \left(\frac{m_{1,\min} - m_1}{m_{1,\min}} \right)^2 \tag{4.11}$$

The severity of the penalty can be adjusted by the user through modification of the variable C_p. The objective is to select p such, that the shape of the performance index is changed in a smooth way. It should be avoided to introduce ridges in the function or its gradient.

However, in this case the minimization algorithm got 'trapped' at the penalty function. In addition the speed of iteration slowed down significantly. In order to overcome this problem the minimization process was stopped manually and the values modified to move the search away from this obstacle. As a result the procedure became very cumbersome but finally converged to meaningful values.

This example shows the importance of robust minimization algorithms for the successful implementation of this research. New minimization methods have been developed to overcome the above addressed difficulties (e.g. simulated annealing or genetic algorithms (Ingber, 1992)). The genetic algorithm can find multiple minima, but only stochastically and it does not allow constrains to be added. Even that considerable research has been done in this area and some successful applications have been documented (Dietrich, 1998), no generally accepted algorithm has been found which can be readily implemented.

However, recently a new global optimization package became available called *'Adaptive Grid Refinement', (AGR)*, (Loehle, 1998). This minimization algorithm is based on the identification of feasible points at each iteration, which define the solution set. As lower points are found during the grid refinement process, points far

from the current optimum are pruned from the solution set. As a result multiple minima can be found in a single run, if they exist. The algorithm can also find optimal regions, rather than only a single point. These optimal regions might represent an equivalent result or might depict confidence limits for parameter estimation.

The performance of the AGR method compared with traditional gradient approaches is illustrated below through the use of a 'camelback' function.

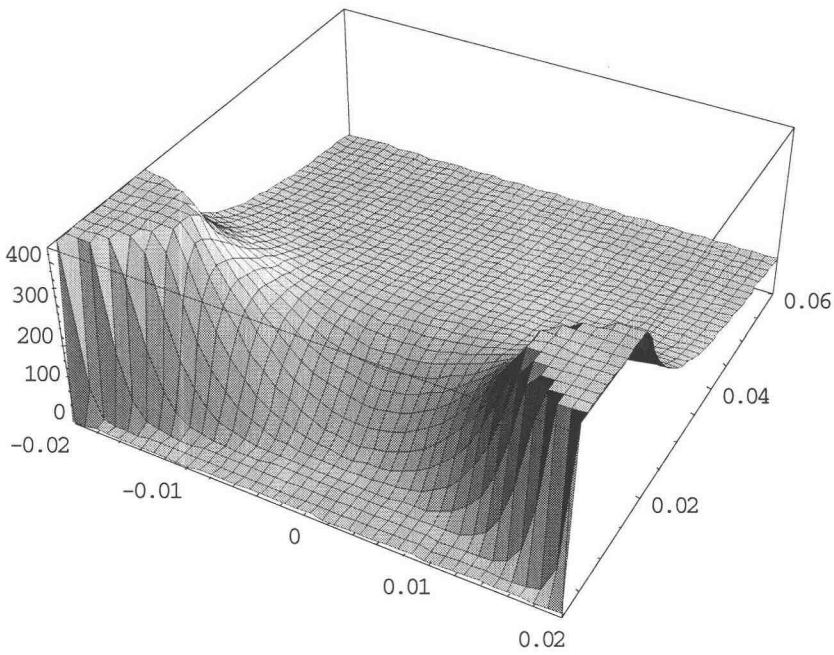

Fig. 4.3: Camelback function.

The traditional minimization method failed to find the correct minimum at (0/0.007). It converges to different values depending what initial conditions are used. The AGR method does not need a special starting point for its search rather it needs bounds for the initial search space. It finds the correct minimum in one single run.

Preliminary tests with the AGR algorithm were also conducted for physical parameter estimation of the simple MDOF system described in Section 5.3. Only five parameters were estimated, but the results were very promising. Convergence to meaningful values was obtained in one single run, without the need to add penalty functions or to aid the algorithm by hand. However the procedure was very time-consuming (it took several days to reach the minimum) and is therefore not suited for practical applications. More in depth investigation is necessary to evaluate this new method including possible implementation on super-computers. This must be left for future research.

4.4 Sensitivity Analysis

As described in the previous section, the complexity of the performance index has a significant influence on the success of the minimization method. The performance index can be built in many different ways and the user benefits from the availability of 'indicators', which evaluate the characteristics of this index. Sensitivity analysis provides such indicators to probe the performance index. Areas of high sensitivity can indicate ridges or instable regions in the performance function. The sensitivity $S_{\alpha}^{Q(\Theta)}$ of a function $Q(\Theta)$, to a change in one of the parameters α is given by (Dorf and Bishop, 1995)

$$S_{\alpha}^{Q(\Theta)} = \frac{1}{Q(\Theta)} \cdot \frac{\partial Q(\Theta)}{\partial \alpha} \tag{4.12}$$

Eq. (4.12) indicates the magnitude of change in the function due to perturbations in the value of the parameter α. Sensitivity analysis should be done before the actual estimation, because it gives hints to which parameters are suited for estimation. This is also of great importance when using functional relationships for estimating physical parameters. It facilitates identification of features in the signals, which are very

sensitive to critical parameters. At the same time these features should not b sensitive to other parameters or to disturbances. Benefits of sensitivity analysis are

- detection of critical parameters and determination of parameter tolerances,
- predictions of solutions in the neighborhood of a known solution by linear interpolation,
- determination of stability boundaries and
- optimization of system parameters in accordance with specified performance criteria using gradient techniques (Eykhoff, 1974).

Having an analytical model available, one can also investigate how changes in physical parameters effect the performance of the model. Calculation of sensitivities is also used to analyze the effect of physical parameters on natural frequencies and damping ratios. However, it is currently impossible to compute natural frequencies and damping ratios symbolically as a function of physical parameters. In such cases one can derive numeric results of how these values change percentage-wise to unit perturbations.

High sensitivity of the performance index is usually desired in order to facilitate locating a minimum. However, in multi-dimensional minimization procedure it is more important that the range of sensitivities of $Q(\boldsymbol{\Theta})$ to different parameters be not too large. If the shape of the performance index looks as in Fig. 4.4a, it is favorable for the minimization algorithm. Different sensitivities to different parameters create a tunnel-like shape for the performance index, which is not particularly good for minimum finding (Fig. 4.4c).

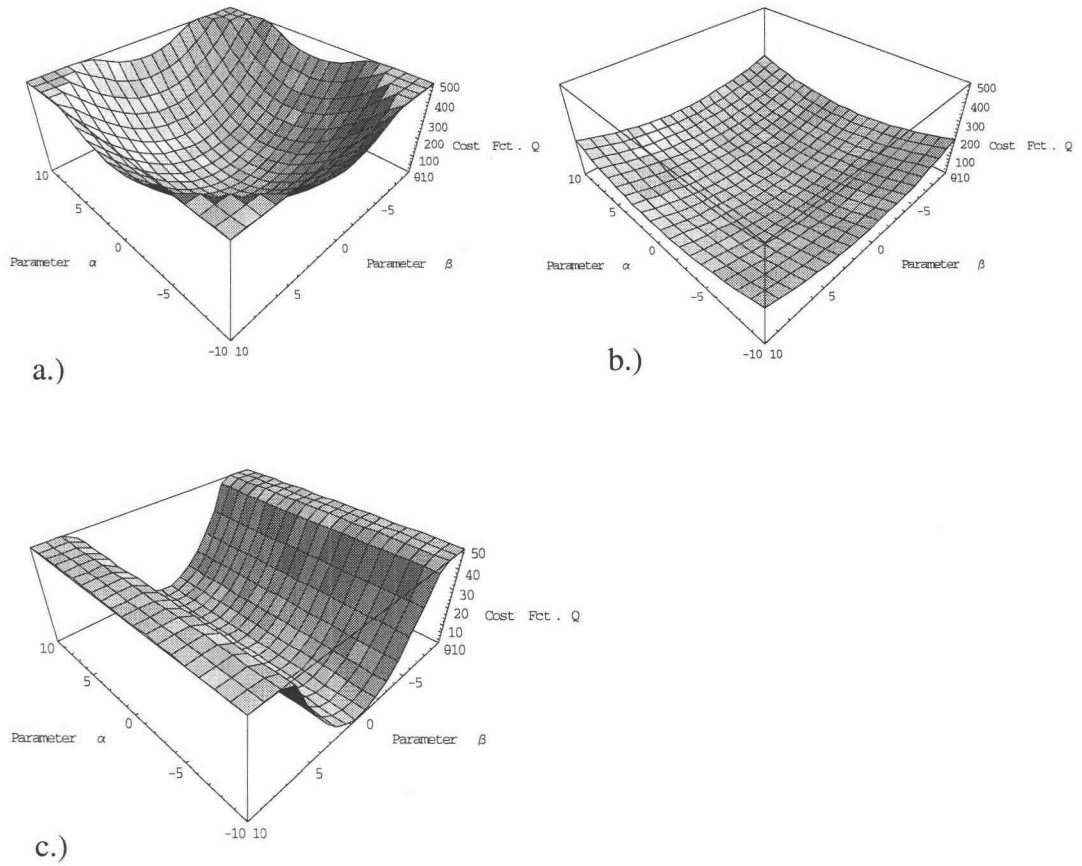

Fig. 4.4: Different shapes of the cost function Q: a.) Favourable sensitivity to parameter a and b, good for minimization. b.) Low sensitivity to parameter a and b, not so good for minimization. c.) Different sensitivity to parameter a and b, bad for minimization.

The shape of the actual performance index of the simple MDOF system analyzed in Chapter 5.2 is shown in Fig. 4.5 as a function of mass m_1 and stiffness k_{11} leaving all other physical parameters fixed at the values listed in Table 5.1. The actual value of m_1 and k_{11} should be approximately 1.39 kg and 1.38 10^6 N/m respectively.

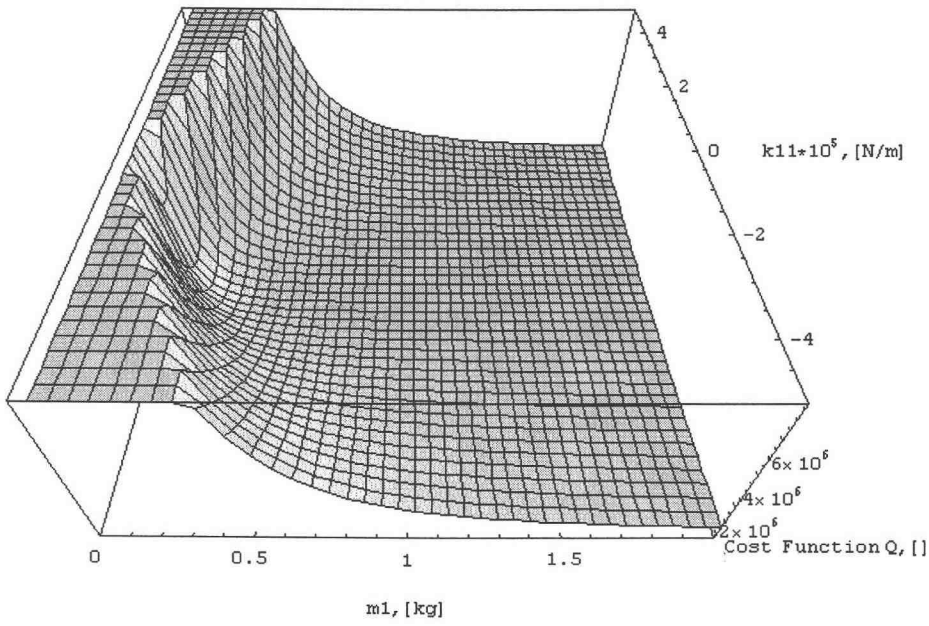

Fig. 4.5: Shape of the cost function $Q(m_1 , k_{11})$ of the simple MDOF system.

The figure illustrates, that in this particular case the performance index naturally prevents the minimization algorithm from converging to a negative *Mass_1*. However, the shape does not change significantly when changing k_{11} to negative values.

4.5 Simulation

In order to be less dependent on actual experimental data, simulations can be used to 1.) eliminate uncertainties of the experimental results, 2.) investigate the influence of signal noise, and 3.) reduce the burden of experimental data collection. Simulations also facilitate the analysis and optimization of various physical parameter estimation methods. Out of the different model based estimation techniques described in Section 3.6, the "two step" method, is investigated more thoroughly. The

experimentally obtained transfer function coefficients $\hat{a}_i$ and $\hat{b}_j$ are simulated by using the analytic transfer function coefficients a_i and b_j (obtained from theoretical modeling), which are functions of physical parameters together with the direct estimations of those parameters referred to as m_{ideal} , c_{ideal} and k_{ideal} (see highlighted values of Table 5.1). Various levels of random noise (see Eq. 4.13 below) is added to the ideal parameters by changing a factor err_{id} (the identification error) in percent (between 5% and 100%) for different runs of simulation.

$$\mathbf{\Lambda_{si}} = \mathbf{\Lambda_{TF}}\Big|_{m,c,k(ideal)} \cdot (1 + err_{id} \cdot R) \tag{4.13}$$

$\mathbf{\Lambda_{si}}$ is a vector of simulated transfer function coefficients, $\mathbf{\Lambda_{TF}}$ is a vector of analytic transfer function coefficients (see Eq. 3.94b) and R is a normally distributed random variable with a mean of zero and standard deviation of 0.3. The performance index $Q(\Theta_s)$, is identical to that initially proposed in Section 3.6, Eq. (3.99) except $\mathbf{\Lambda_{si}}$ is used instead of the experimentally identified $\hat{\mathbf{\Lambda}}$.

$$Q(\mathbf{\Theta}_s) = \sum_{i=0}^{p+q-1} \left(100 \cdot \frac{\Lambda_{si,i} - \Lambda_{TF,i}(\mathbf{\Theta}_s)}{\Lambda_{si,ii}} \right)^2 \tag{4.14}$$

This method of simulation was applied to the simple MDOF system described in Chapter 5.3. The results tabulated below in Table 4.3, show that a global minimum can be found, even when large errors in the transfer function coefficients are present. The estimates of physical parameter are less accurate when more noise is present. However these simulations indicate, that the "two step" method should be capable of estimating physical parameters of the actual system

Table 4.3: Simulation results for the simple MDOF system using the "two step" method.

Ideal Physical Parameters		Noise in transfer function coefficients *a* and *b*					
		5 %		20 %		100 %	
		Estimated Values	St. Dev.	Estimated Values	St. Dev.	Estimated Values	St. Dev.
m_1 [kg]	1.39	1.42	0.002	1.28	0.012	1.44	0.002
m_2 [kg]	1.09	1.09	0.005	1.19	0.009	0.86	0.005
k_{11} [10^6 N/m]	1.38	1.37	0.011	1.31	0.008	1.59	0.011
k_{22} [10^6 N/m]	0.24	0.24	0.006	0.31	0.010	0.37	0.006
k_{121} [10^6 N/m]	0.12	0.12	0.009	0.19	0.003	0.27	0.009
c_{11} [Ns/m]	13.42	13.87	0.014	14.26	0.007	11.18	0.014
c_{22} [Ns/m]	0.47	0.48	0.027	0.33	0.019	0.31	0.027

4.6 Model Validation and Diagnostic Tools

Model validation is the process of confronting the analytical model with various facts about the system and checking whether or not these facts hold true. Once the model is available in state space form, several methods can be applied to verify the model. They include comparison of DC-gains and static responses as well as checking the natural frequencies of the system.

Visualization of machine tool vibrations under controlled (e.g. harmonic) or ambient excitations is also a very powerful element of this validation. Here a new approach especially developed for the research presented in this thesis is described (Jitpraphai, 1997; Jitpraphai et al., 1998). It integrates analytical and experimental

model derivation. A block diagram of the implemented software package is shown in Fig. 4.6.

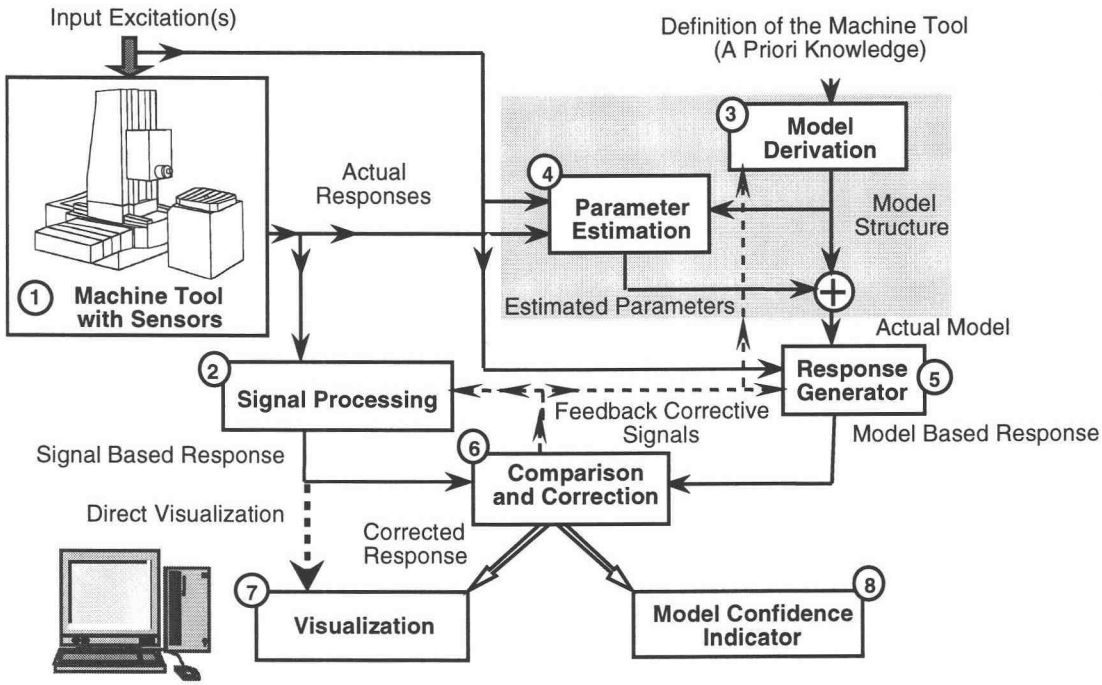

Fig. 4.6: A block diagram of the 'gray box' model based visualization.

The basic entities required for visualization are as follows:

- Definition of the rigid body model representing machine tools,
- Excitation and response signals measured by sensors located on the machine and tested equipment,
- Information about sensors and their locations.

System responses and subsequent visualization are generated along two routes. The left-hand side of the block diagram in Fig. 4.6 represents direct visualization. The input and response signals from the machine tool (Block ①) are processed (Block ②)

to obtain the best estimates of the generalized coordinates for the given type and configuration of sensors. This is accomplished through measurement and display of the locations of rigid bodies. Six variables are necessary and sufficient to completely represent the spatial motion of a rigid body. These variables are referred to as generalized coordinates and include three translations and three rotations.

Once generalized coordinates are known, visualizing pictures of bodies with pre-defined geometry is readily done by employing homogeneous transformation matrices (Craig, 1955). The simplest configuration involves three sensors of linear displacements and three rotation sensors per body. Practically, the measurement of displacements and rotations is cumbersome, so accelerations are measured instead and converted to generalized coordinates by double integration. The most serious drawback of this approach is strong amplification of low frequency disturbances, caused in particular by the thermal drift in accelerometers. To suppress these disturbances, significant signal processing is necessary. One convenient method to measure generalized coordinates involves nine linear accelerometers located on a rigid body as shown in Fig. 4.7 (Padgaonkar et al., 1975).

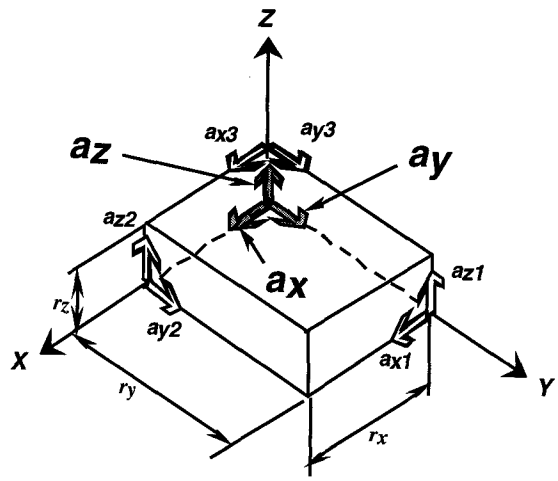

Fig. 4.7: Accelerometer locations on the body.

According to this method, three accelerometers (a_x, a_y, a_z) are mounted at one point of the body and aligned with the body's coordinate system. Double integrated signals from these accelerometers represent linear displacements at this point. If six additional accelerometers are used, represented by the arrows a_{x1}, a_{z1}, a_{y2}, a_{z2}, a_{x3}, a_{y3} in the figure, the angular accelerations can be calculated as

$$\ddot{\varphi} = \frac{a_{z1} - a_z}{2r_y} - \frac{a_{y3} - a_y}{2r_z}, \quad \ddot{\phi} = \frac{a_{z3} - a_x}{2r_z} - \frac{a_{z2} - a_z}{2r_x}, \quad \ddot{\psi} = \frac{a_{y2} - a_y}{2r_x} - \frac{a_{x1} - a_x}{2r_y} \tag{4.15}$$

where r_x, r_y, r_z are defined in the figure. These estimates (function of time) are referred to as *Signal Based Response*. They can be used directly, together with geometric information about the component rigid bodies, to visualize vibrations (heavy dashed line from Block ⑧ to Block ⑦ in Fig. 4.6).

The right side of Fig. 4.6 shows model based visualization. The structure of the analytical model, also referred to as 'gray box' is derived on the basis of physical phenomena and first principles that govern the dynamic behavior of the tested machine (Block ③). Parameters of the model are next estimated from the operational and test data (Block ④). A comparison of the *signal* and *model* based responses, performed in Block ⑥, can immediately indicate a high confidence of visualization if signals from the left and right paths are similar. In such a case, either signal or model based responses can be used for visualization. If not, analysis of the responses often aids in diagnosing and correcting the type of problem. For example, a divergence of spectra at low frequency (< 5 *Hz*) typically indicates the impact of thermal drift in sensors. Once the problem is detected and diagnosed, appropriate corrective action can be applied. One such corrective action involves an additional separation method to be used in the *Signal Processing* Block ② to extract the 'drift-free' generalized coordinates from the signal based responses. As shown in the block diagram, corrective feedback signals are passed to various modules of the algorithm. As the visualization procedure self-tunes to the specific tested machine tool and estimated disturbances are suppressed, differences between the signal and model based responses diminish. A suitable

measure of this similarity, such as the weighted root mean square of residual, serves as a confidence indicator (see Block ⑧) for the model as well as vibration visualization.

At present, only a subsystem of a machine tool (Block ①) comprising the shaft and housing has been investigated. These two units form an eleven DOF, multi-input multi-output (MIMO) system. Its analytical model is derived in Section 3.4. Masses and moments of inertia are the fixed known physical parameters, while the bearing and housing-to-base fixture stiffnesses are adjustable parameters, which represent unknown quantities in actual machine tools. Typical values of these stiffnesses are 20 - 60 $N/\mu m$ (spindle), and 60 - 200 $N/\mu m$ (fixture). The first flexible vibration mode occurs at nearly 730 Hz for the spindle shaft and 2.5 kHz for the housing (Spiewak, 1995). The dampings associated with bearings and fixtures are unknown, uncontrolled variables that have to be estimated experimentally (Bishop, 1955; Nashif, 1985). Based on the developed model and visualization, the dominant 'rigid body' resonances are found in the range of 200-550 Hz. The effect of varying preload and fixture stiffnesses on the frequencies can be readily investigated. As explained in Section 3.5, generalized coordinates of the shaft and housing are measured (by accelerometers), on-line conditioned and recorded. The data acquisition and visualization is implemented under the LabVIEW software package (National Instruments, 1994). Fig. 4.8 shows visualization results using the developed software.

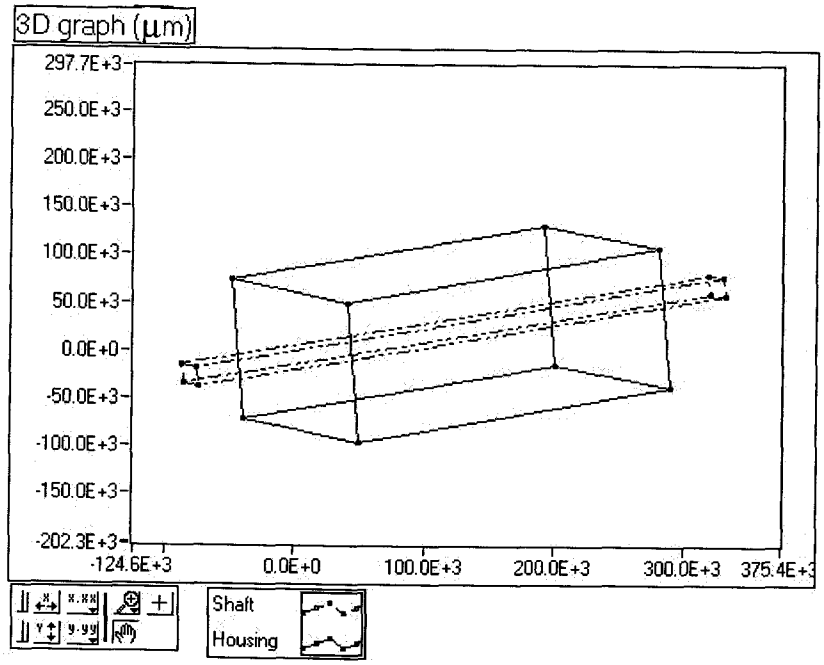

Fig. 4.8: Visualization result of the spindle.

4.7 Use of Artificial Intelligence

Currently the accurate identification of transfer functions from experimental input/output data is a time-consuming and cumbersome task in the physical parameter estimation methodology proposed in Section 3.6. It has been shown in Shyan-Huang (1994) that parametric identification employing high order models such as ARMA models of order 40 yield the most precise estimates of the natural frequencies and damping ratios of systems like the MDOF spindle-assembly. The order selection for the parametric model is not an easy task. Classical identification methodologies attempt to find the smallest number of parameters to best fit the system under consideration. The search begins with a low order model, and the order is then increased iteratively (Pandit and Wu, 1983) until a suitable criterion of fit is satisfied such as Akaike Information Criterion (AIC - Akaike, 1974), BIC, and/or Final

Prediction Error (FPE) Criterion (Akaike, 1969). Since machine tools are MDOF systems and may contain some distributed parameter elements, there is no 'upper bound' limit of the model order. The 'highest order' is determined by: (1) the limitation of the computer's memory that is required to store large data structures used by the identification algorithm, or (2) the limitation imposed by the time required to generate the estimates of model parameters. At the present stage of digital technology, the latter limitation is encountered first. However such 'high order' identification is computationally intensive and generates phantom roots in the numerator and denominator of the transfer function. Obviously high order models have many more roots than the physical model of the spindle-assembly. These 'phantom' roots have no physical counterparts in the investigated real system and therefore need to be recognized and the valid roots extracted. This task is referred to as *Model Pruning*.

At present model order selection and model pruning is done manually. It is based on a human expert's experience and knowledge, which unfortunately is largely of heuristic nature. However some rules and facts discussed below could be used to develop an Artificial Intelligent System for order selection and model pruning (Shyan-Huang, 1994).

Rule 1: If the natural frequency of a root is higher than the cut-off frequency in the data acquisition system, then these roots do not exist in the actual system.

Rule 2: If a pair of zeros and a pair of poles occur very close to each other, then a zero-pole cancellation takes place.

Rule 3: If the damping ratio of a root is very high (more than realistically expected in mechanical systems), it is not a significant peak or null and this root can be omitted.

Artificial intelligence (e.g. pattern recognition through neural networks) could also be used for establishing the frequency-damping map as a function of preload (see Fig 5.34). For many different sets of data the frequency response function has to be

analyzed and the vibration modes identified. Through comparison with the analytic model, changes in certain resonance frequencies can then be used to make statements about the conditions of the bearings.

4.8 Closure

It is the intent to solve the modeling and estimation problem covered in this research with the aid of a standard Desktop PC. Therefore certain compromises and modifications need to be made to keep the computational problems manageable. Calculations would be quicker on large super computers, but the eventual possibility of a shop floor implementation of a monitoring system is considered, and a standard Desktop PC is much more desirable for such an application. The above presented implementation and validation tools significantly help to manage the necessary large models and matrices. *Mathematica* is an ideal software package for this purpose because of its ability to do symbolic calculations and to calculate with arbitrary precision.

Validation is a very important part of examining how well the actual system is represented by the model. Comparing DC-gains and checking natural frequencies of model and actual system are some of the simple tools of validation. Model based visualization of vibrations is one of the more advanced tools and gives intuitive information on how the model and the actual system behave. Based on that knowledge, experiments are conducted in the next section to validate the model and to investigate the estimation methods proposed in Section 3.6.

5. EXPERIMENTAL INVESTIGATION AND ESTIMATION RESULTS

5.1 Introduction

This chapter presents results of experiments conducted to examine the accuracy of the analytical model developed in Chapters 3. Also, the physical parameter estimation methods derived in Chapter 3 are applied and investigated. Experimental investigation provides an insight into the system's properties and the impact of the various parameters on the dynamic performance. This information helps to build an enhanced model of the system, which in turn improves physical parameter estimation. Related issues, such as the use of different sensors, placement concerns and signal processing problems are addressed.

Two different experimental set-ups are used to investigate the methodology of physical parameter estimation. One set-up involves a simple and well defined two degree-of-freedom system described in Section 5.3. A lumped parameter model of the system is formulated and experimental data sets are collected. For comparison a Finite-element model is also developed. Data collected during experiments is a basis for the physical parameter estimation. Estimation procedures developed in Chapters 3 are validated and results are discussed in detail.

The second test set-up represents a shaft-bearing system, described in Section 5.4, which is a common component of rotating machinery. Example applications include machine tools, pumps, compressors, turbines, motors, gearboxes and fans. Thus the investigation of the shaft-bearing system provides knowledge applicable in a broad range of devices. Results of simulations based on a comprehensive lumped-parameter model of such a multi-degree-of-freedom system are analyzed and

compared with experimental results. Particularly, bearing stiffnesses calculated from the model and from experimental data are investigated in depth. The data acquisition system common to both investigated set-ups is presented in Section 5.2. Section 5.5 summarizes the experimental investigation and the estimation results for both systems.

5.2 The Data Acquisition System

The data acquisition system used in this research is shown in Fig. 5.1. Its main components include various sensors, their amplifiers, anti-aliasing filters, analog to digital converters and a desktop computer. A block diagram of the typical configuration is drawn in Fig. 5.2. When using an impact hammer for excitation of the system, the signal of the piezoelectric load cell PCB, type 208B03 (PCB, 1996) at the tip of the instrumented hammer is applied to a signal-conditioning unit (PCB type 408D06). The signal from the load cell is also used as a trigger to initiate the data acquisition. When using continuous excitation, the desired signal is first generated by a digital function-generator Sony/Tektronix, model AFG 2020 (Sony/Tektronix, 1995). Next it is passed through a low-pass filter by Precision®, model 88B (Precision, 1989), to cut off high undesired frequencies and suppress distortions caused by the digital signal generation. The filtered signal is passed through a power amplifier by Bruel & Kjaer, type 2706 (Bruel & Kjaer, 1994). From there it is applied to the electro-magnetic shaker (Bruel & Kjaer, type 4809). The shaker excites the system via a metal stinger through the attached load cell by Kistler, type 9212 (Kistler, 1995). The load cell requires a charge amplifier by Kistler, type 5054A1410.

Output signals of the systems are displacements and accelerations of various mechanical components. Displacements are measured by Bentley&Nevada proximity sensors, type 7200 (Bently&Nevada, 1992). Low impedance piezoelectric accelerometers, (Kistler, type 8702B25M1) are used for acceleration measurements. Signals from the accelerometers are conditioned by an accelerometer coupler (Kistler,

type 5128A) and passed through low-pass anti-aliasing programmable filters by Precision, model 88B (Precision, 1989) and Datel, model FLJ-D6LA2 (Datel, 1987). The filtered and amplified signals are passed through an interface panel and digitized by a National Instruments AT-MIO 16E2 data acquisition card (National Instrument, 1995) installed inside an IBM compatible desktop computer. The DAQ card uses a 12 bit Analog-to-Digital Converter (ADC), a multiplexer and additional amplifiers. Suitable data acquisition, processing and visualization procedures (Jitpraphai, 1998) developed in LabVIEW (National Instrument, 1994) are used for signal collection and analysis. The sensors used in the experiments were calibrated precisely before actual data was taken (see Appendix E).

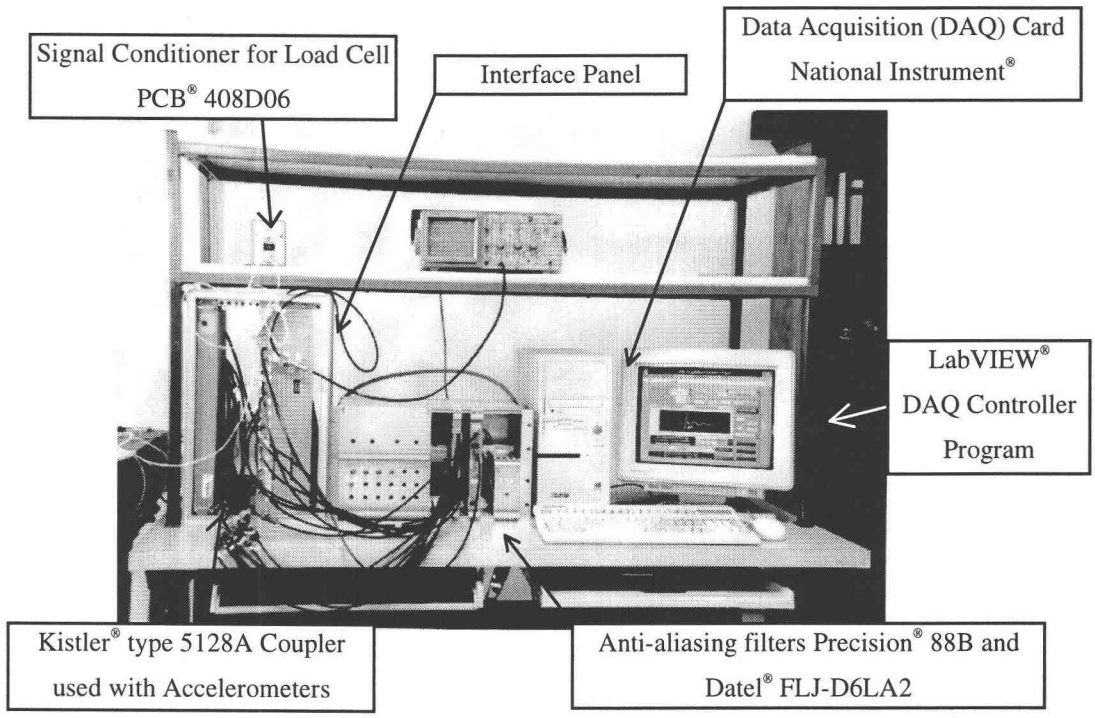

Fig. 5.1: The data acquisition system.

Signals from the system comprise:

- force signals either from the load cell mounted between the tested system and the electro-magnetic shaker, or from the impact hammer,
- acceleration signals from sensors mounted at various locations of the system, and
- displacement signals from proximity sensors.

The LabVIEV data acquisition software allowed selection of the following parameters during data collection:

- Sampling Frequency: ~ 0 – 40,000 Hz,
- Number of recorded signals: 16,
- Number of data: 512 – 16,384 per channel, with 0 – 1024 pre-trigger points,
- Signal acquisition mode: triggered by signal from the force sensor, continuous or one time read.

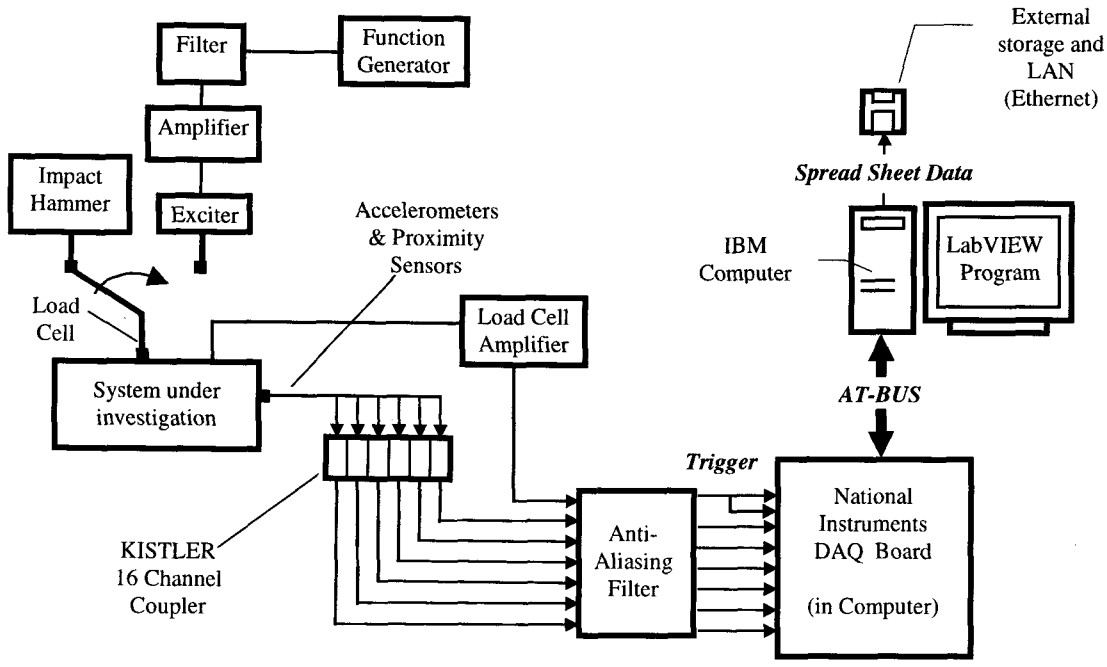

Fig. 5.2: Schematic diagram of the experimental set-up.

5.3 Simple MDOF System

A system consisting of two masses connected by a helical spring (Fig. 5.3) facilitates in-depth investigation and validation of the developed procedures for physical parameter estimation. Its simple structure allows rapid modeling, analysis and structural modification; this facilitates thorough and efficient investigation of the effects caused by parameter variations.

5.3.1 Mechanical Design

The two steel prismatic parts are held by I-beams of different width. The I-beams are bolted to a vertical steel plate, which is welded to a horizontal steel base plate. All the components are manufactured of low carbon 1040 steel. The right mass in Fig. 5.3 is designated *Mass_1* (m_1) and is supported by a thicker I-beam (stiffness k_{11} and damping coefficient c_{11}). The left mass is designated *Mass_2* (m_2) and is supported by a thinner I-beam (stiffness k_{22} and damping coefficient c_{22}). A helical spring (stiffness k_{12} and damping coefficient c_{12}) is located in between the two masses. An additional mass (variable) can be attached to *Mass_1* or *Mass_2* as shown in Fig. 5.4. Transient and continuous excitation can be applied to the system. Fig. 5.3 shows the case of the system being excited through *Mass_1* by the electromagnetic shaker, which provides the input force F_1. However the shaker can be easily removed to facilitate impact hammer excitation. The displacements of *Mass_1* and *Mass_2* represent possible output signals and are measured by proximity sensors. Accelerations of *Mass_1* and/or *Mass_2* can also be measured.

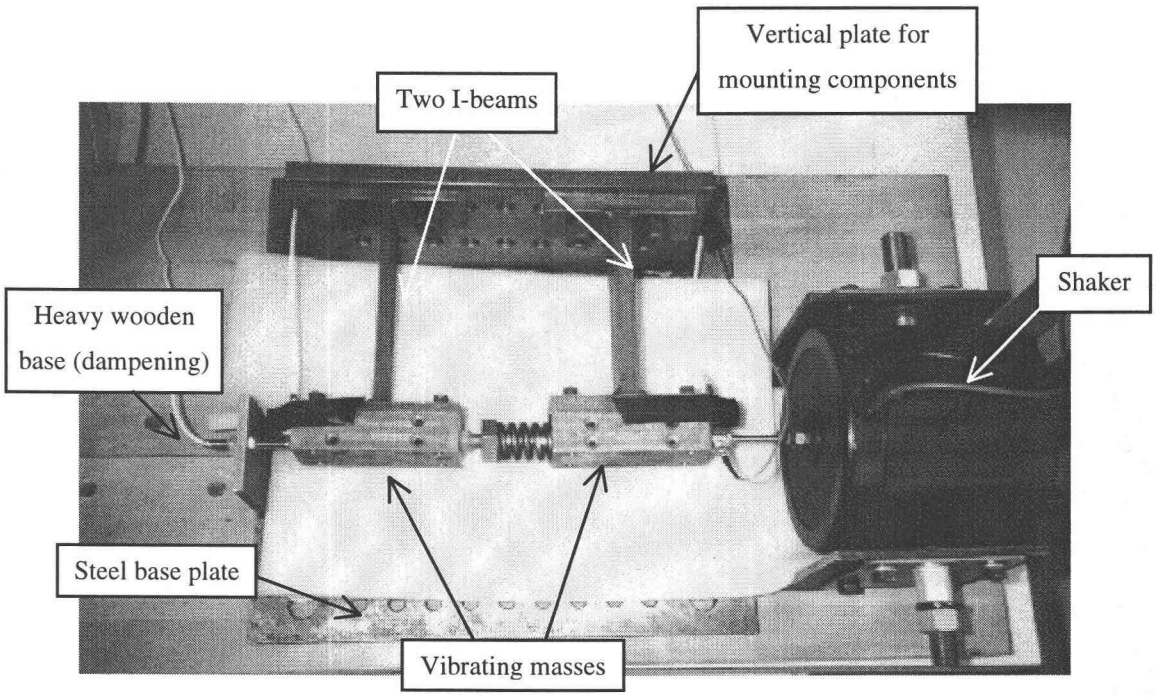

Fig. 5.3: The experimental set-up for the simple MDOF system.

The major direction of vibration of the two masses is horizontal, while the remaining motion of each mass in the other five 'degrees of freedom' have not been taken into account in this research. Simplicity of this set-up is the key factor facilitating rapid and comprehensive testing and validation of various parameter estimation methods. The masses and stiffnesses can be varied. Individual mechanical components can be investigated and characterized (e.g., weighing masses, measuring stiffness of I-beams) separately and their influence on the behavior of the entire system can be modeled with high fidelity. Notwithstanding, the set-up poses considerable challenges due to unmodeled phenomena. Some components, like the back wall and the I-beams, have been idealized in this research for the sake of model simplicity. Specifically, the wall is considered perfectly rigid and the distributed mass of I-beams is neglected. Therefore the lumped parameter model of this set-up only approximates its actual behavior. Additional challenge comes from the considerable noise present in the signals, which makes the estimation difficult.

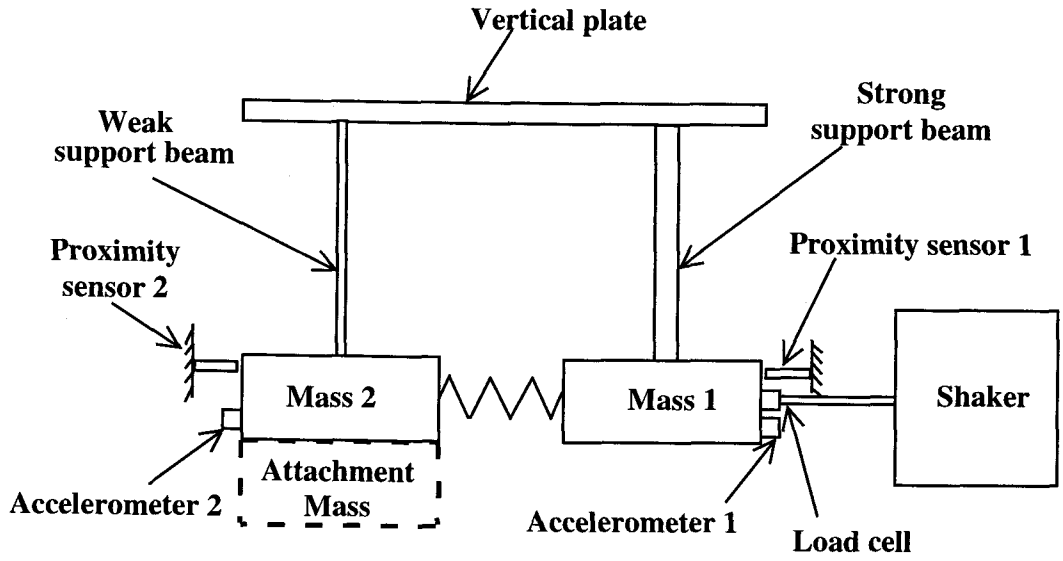

Fig. 5.4: Simplified mechanical diagram of the simple MDOF system.

Obtaining reliable results hinges upon the robustness of the algorithm with respect to the estimation of the required physical parameters. Data compression and extraction of the right features from the recorded signal is essential for accomplishing this goal.

5.3.2 Lumped Parameter Model

Although the experimental set-up described above has distributed parameters, it is modeled as a two degree-of-freedom lumped-parameter system. This simplification is possible since the parameters of concern in this research (prismatic masses mounted at the end of each I-beam, high stiffnesses of the I-beams and their low damping coefficients) have the dominant effect on the system's dynamics.

5.3.2.1 *Model Structure*

In this model the masses are attached to fixed boundaries, as shown in Fig. 5.5. One exciting force, F_1, acts on *Mass_1*. Only the motion along the X-axis is considered. Variables d_1 and d_2 denote the displacements of *Mass_1* and *Mass_2*, respectively.

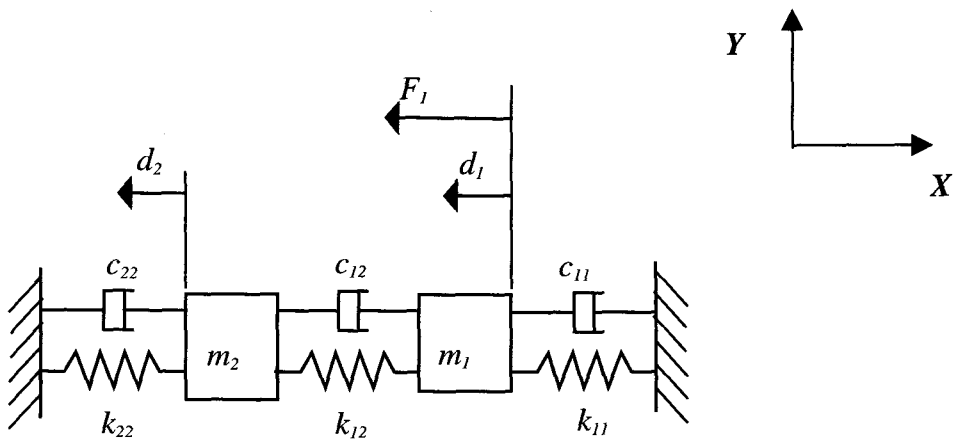

Fig. 5.5: Model of the simple MDOF system.

Eight physical parameters given by Eq. (5.1) are of interest in this research.

$$\Theta_S = \{ m_1, m_2, k_{11}, k_{12}, k_{22}, c_{11}, c_{12}, c_{22} \} \tag{5.1}$$

Based on the two DOF, lumped-parameter model, the equations of motion are

$$\begin{bmatrix} m_1 & 0 \\ 0 & m_2 \end{bmatrix} \begin{pmatrix} \ddot{d}_1 \\ \ddot{d}_2 \end{pmatrix} + \begin{bmatrix} c_{11}+c_{12} & -c_{12} \\ -c_{12} & c_{12}+c_{22} \end{bmatrix} \begin{pmatrix} \dot{d}_1 \\ \dot{d}_2 \end{pmatrix} + \begin{bmatrix} k_{11}+k_{12} & -k_{12} \\ -k_{12} & k_{12}+k_{22} \end{bmatrix} \begin{pmatrix} d_1 \\ d_2 \end{pmatrix} = \begin{pmatrix} F_1 \\ 0 \end{pmatrix} \tag{5.2}$$

or in vector-matrix form

$$\mathbf{m}\,\ddot{\mathbf{d}} + \mathbf{c}\,\dot{\mathbf{d}} + \mathbf{k}\,\mathbf{d} = \mathbf{F} \tag{5.3}$$

Equation (5.3) can be readily transformed into the state-space representation (Section 3.2.2) by forming a state vector as follows

$$\mathbf{x} = [d_1 \; d_2 \; \dot{d}_1 \; \dot{d}_2]^T \tag{5.4}$$

The state-space matrices **A**, **B**, **C** and **D** are

$$\mathbf{A} = \begin{bmatrix} 0 & 0 & 1 & 0 \\ 0 & 0 & 0 & 1 \\ \dfrac{-k_{11}-k_{12}}{m_1} & \dfrac{k_{12}}{m_1} & \dfrac{-c_{11}-c_{12}}{m_1} & \dfrac{c_{12}}{m_1} \\ \dfrac{k_{12}}{m_2} & \dfrac{-k_{12}-k_{22}}{m_2} & \dfrac{c_{12}}{m_2} & \dfrac{-c_{12}-c_{22}}{m_2} \end{bmatrix} \tag{5.5a}$$

$$\mathbf{B} = \begin{bmatrix} 0 & 0 \\ 0 & 0 \\ \dfrac{1}{m_1} & 0 \\ 0 & \dfrac{1}{m_2} \end{bmatrix} \qquad \mathbf{C} = \begin{bmatrix} 1 & 0 & 0 & 0 \\ 0 & 1 & 0 & 0 \end{bmatrix} \qquad \mathbf{D} = \begin{bmatrix} 0 & 0 \\ 0 & 0 \end{bmatrix} \tag{5.5b,c,d}$$

The transfer function model of the system is

$$\begin{pmatrix} d_1(s) \\ d_2(s) \end{pmatrix} = \begin{bmatrix} G_{11}(s) & G_{12}(s) \\ G_{21}(s) & G_{22}(s) \end{bmatrix} \cdot \begin{pmatrix} F_1(s) \\ 0 \end{pmatrix} \tag{5.6}$$

Specifically, the monic transfer function between the input force F_1 and the output displacement d_1 is

$$G_{11}(s) = \frac{d_1(s)}{F_1(s)} = \frac{b_2 \cdot s^2 + b_1 \cdot s + b_0}{s^4 + a_3 \cdot s^3 + a_2 \cdot s^2 + a_1 \cdot s + a_0} \tag{5.7}$$

where

$$b_0 = \frac{k_{12} + k_{22}}{m_1 \cdot m_2}; \qquad b_1 = \frac{c_{12} + c_{22}}{m_1 \cdot m_2}; \qquad b_2 = \frac{1}{m_2} \tag{5.8a,b,c}$$

and

$$a_0 = \frac{k_{11} \cdot k_{12} + k_{11} \cdot k_{22} + k_{12} \cdot k_{22}}{m_1 \cdot m_2} \tag{5.9a}$$

$$a_1 = \frac{c_{12} \cdot k_{11} + c_{22} \cdot k_{11} + c_{11} \cdot k_{12} + c_{22} \cdot k_{12} + c_{11} \cdot k_{22} + c_{12} \cdot k_{22}}{m_1 \cdot m_2} \tag{5.9b}$$

$$a_2 = \frac{c_{11} \cdot c_{12} + c_{11} \cdot c_{22} + c_{12} \cdot c_{22} + k_{12} \cdot m_1 + k_{22} \cdot m_1 + k_{11} \cdot m_2 + k_{12} \cdot m_2}{m_1 \cdot m_2} \tag{5.9c}$$

$$a_3 = \frac{c_{12} \cdot m_1 + c_{22} \cdot m_1 + c_{11} \cdot m_2 + c_{12} \cdot m_2}{m_1 \cdot m_2} \tag{5.9d}$$

The monic transfer function between F_1 and d_2 is

$$G_{21}(s) = \frac{d_2(s)}{F_1(s)} = \frac{b_1^* \cdot s + b_0^*}{s^4 + a_3 \cdot s^3 + a_2 \cdot s^2 + a_1 \cdot s + a_0} \tag{5.10}$$

where

$$b_0^* = \frac{k_{12}}{m_1 \cdot m_2}; \qquad b_1^* = \frac{c_{12}}{m_1 \cdot m_2} \tag{5.11a,b}$$

The transfer functions under considerations have the same denominator and, consequently, the same characteristic equation.

The DC-gain of a transfer function represents the static "stiffness" of the mechanical system at masses m_1 and m_2 and can be calculated by setting the Laplace operator to zero. These static stiffnesses are

$$k_{S11} = G_{11}(0) = \frac{b_0}{a_0} = \frac{k_{12} + k_{22}}{k_{11} \cdot k_{12} + k_{11} \cdot k_{22} + k_{12} \cdot k_{22}} \tag{5.12a}$$

$$k_{S21} = G_{21}(0) = \frac{b_0^*}{a_0} = \frac{k_{12}}{k_{11} \cdot k_{12} + k_{11} \cdot k_{22} + k_{12} \cdot k_{22}} \tag{5.12b}$$

In Section 5.3.4 (Estimation Results), this model will be used for physical parameter estimation.

5.3.2.2 *Experimental Measurement of Parameters*

The purpose of the experimental analysis is verification of the estimation methods developed in Chapter 3. The physical parameters **m, c** and **k** appearing in the analytical model need to be estimated using experimental data. Having the model structure derived in Section 5.3.2.1, any of the procedures proposed in Chapter 3 can be used to estimate the values of physical parameters defined in the list given by Eq. (5.1). To compare the estimation results with a reliable reference, conventional procedures are also used to obtain the unknown masses, stiffnesses and dampings. They are tabulated in Table 5.1.

Table 5.1: Measured and calculated values of the physical parameters.

Physical Parameters	Numerical Values
Mass m_1 [kg]	1.14 [1]
	1.39 [2]
Mass m_2 [kg]	0.95 [1]
	1.09 [2]
Stiffness k_{11} [10^6 N/m]	1.88 [3]
	1.36 [4]
	1.37 [5]
	1.40 [6]
	1.38 [7]
Stiffness k_{22} [10^6 N/m]	0.16 [3]
	0.27 [4]
	0.24 [5]
	0.23 [6]
	0.24 [7]

Physical Parameters	Numerical Values
Stiffness k_{12} [10^6 N/m]	0.04 [8]
	0.19 [9]
	0.17 [9]
	0.10 [9]
	0.12 [9]
Damping c_{11} [Ns/m]	13.42 [10]
Damping c_{22} [Ns/m]	0.47 [10]
Damping c_{12} [Ns/m]	0 [11]

The index numbers in the table above refer to the itemized list below indicating the method of calculation of each specific physical parameter. Traditional methods for determining the respective numerical values that were employed in this research included the following:

For the masses m_1 and m_2:

(1) Calculation as the product of volume V and density ρ.

(2) Partial disassembly and weighing of the components.

For the beam stiffnesses k_{11} and k_{22}:

(3) Theoretical calculation from the formula,

$$k = \frac{3EI}{l^3} \tag{5.13}$$

which approximates the lumped end stiffness of a distributed cantilever beam (Thomson, 1981). E is the modulus of elasticity, l is the length of the beam and I is the area moment of inertia. All geometric dimensions and moments of inertia of the simple MDOF system are listed in Appendix B 1.

(4) Evaluation based on the measurement of static deflection caused by a known force of the respective partially disassembled beam-mass component using mechanical sensing devices, in this case a ring dynamometer and a dial gage.

(5) As above, except using a proximity sensor instead of the dial gage.

(6) Evaluation based upon the measurement of deflection caused by a known periodical force generated by an exciter. The force was generated by the B&K shaker as a 5 Hz sinusoidal waveform, while the displacement was measured by a proximity sensor.

(7) As above, except for the use of random signal and subsequent input/output identification on the partial disassembled beam-mass component using load cell and proximity sensor signals. The DC-gain was calculated to obtain the stiffness of the beam.

For the helical spring stiffnesses k_{12} between the two masses:

(8) Calculation according to the formula (Thomson, 1981).

$$k = \frac{Gd^4}{64nR^3} \tag{5.14}$$

where G is the modulus of shear, n the number of coils, d the diameter of the steel wire forming the spring and R the outer radius of the entire spring.

(9) Calculation using Eq. (B.3) in Appendix B3 together with k_{11} & k_{22} evaluated with methods (4), (5), (6) and (7), respectively and the gain from 5 Hz measurements.

For the dampings c_{11} and c_{22}:

(10) Calculation from impulse response data involving the Log-Decrement method. Each beam-mass system was tested separately (see Appendix B4).

For the damping c_{12} of the helical spring between the two masses:

(11) The dampings c_{12} for the helical spring is difficult to measure, but from the literature (Bishop, 1956; Myklestad, 1952) it was found to be negligible compared to c_{11} and c_{22}; therefore assumed zero.

The results, compared in Table 5.1, show significant discrepancies (up to 30 %) between the values of some parameters obtained by different methods. This can be due to such factors as the measurement errors, inadequate knowledge of material properties or simplifications in mathematical approximation. The level of discrepancy is even higher for the damping values as they are usually very difficult to assess. Furthermore, the rotation of the prismatic masses can be a source of measurement error when assessed by a dial gage or proximity sensor. The method of on-line parameter estimation proposed in this research provides yet another set of values that can resolve some ambiguities in the data compiled in Table 5.1. The most likely values are highlighted in the table. Directly measured values are treated in this research as more reliable than the values estimated indirectly, and electronic sensors are deemed more accurate than mechanical devices (e.g. dial gages).

5.3.3 Validation of the Model

After the model is built it must be verified through experiment or through comparison with reference models. Here frequency and FE analysis is used to validate the lumped parameter model.

5.3.3.1 Transfer Function Analysis

First low frequency sine wave experiments are performed to check the DC-gain and the linearity of the system. The input force recorded by the *Kistler* load cell and the output displacement of *Mass_1* and *Mass_2* are shown below.

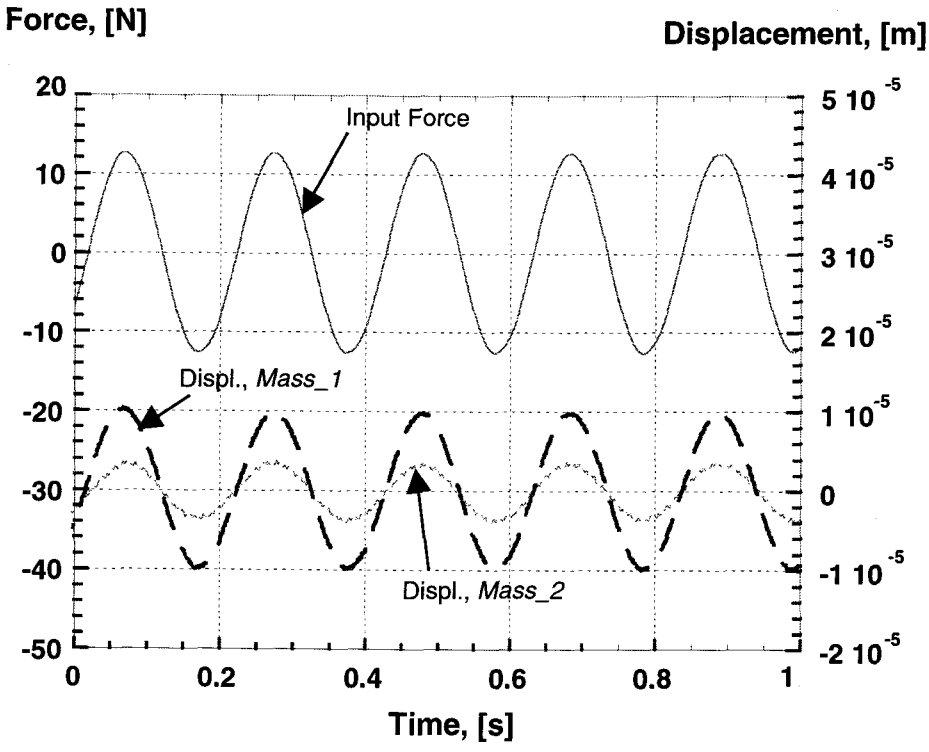

Fig. 5.6: Force input and proximity sensor output of *Mass_1* and *Mass_2* for low frequency sine wave excitation.

Magnitudes of the input force above 20 N cause distortions in the output displacement of *Mass_2* which indicate non-linear regime of operation. An approximate 50 % increase of *Mass_2* [21] does not cause any significant change in the waveforms at this low frequency. As expected, the calculated stiffness is independent of the mass variation.

The theoretical DC-gain of the transfer functions G_{11} and G_{21} can be calculated using Equations (5.12a and b) and the highlighted physical parameters of Table 5.1. The results are compared with experimental DC-gains from the sine wave and white noise measurements as tabulated below.

Table 5.2: DC-gain values of the simple MDOF system.

	Theoretical Gain	**Experimental Gain (5 Hz Test)**	**Experimental Gain (White Noise Test)**
DC-Gain of G_{11} [10^{-8} m/N]	49.1	68.0	63.0
DC-Gain of G_{21} [10^{-8} m/N]	8.1	28.6 (no add. mass) 28.0 (with add. mass)	22.0

The frequency behavior of the transfer function G_{11} using the analytical model of Section 5.3.2 together with the highlighted physical parameters from Table 5.1 is shown in Figure 5.7 and 5.8. The model (solid line), the experimental (dashed) and the pruned experimental (gray dashed) transfer functions are compared. The importance of pruning is explained in detail in Section 4.7.

[21] for change in the experimental set-up see Fig. 5.4 and see a signal comparison in Appendix B2.

The magnitude graphs (Fig. 5.7) have qualitative similarities (similar DC-gains, two distinct resonance peaks, similar shapes) but considerable quantitative differences. Originally, the rigid body model of the system using physical reference parameters from Table 5.1 has two resonance frequencies and their respective damping ratios at

$$f_{1,a} = 192.9 \ Hz \qquad \xi_{1,a} = 0.0030 \tag{5.15}$$

$$f_{2,a} = 74.5 \ Hz \qquad \xi_{2,a} = 0.0005 \tag{5.16}$$

where as the experimental analysis shows $f_{1,e}$ much lower. From Fig 5.7 the experimental resonance frequencies are

$$f_{1,e} = 138 \ Hz \qquad \xi_{1,e} = 0.0124 \tag{5.17}$$

$$f_{2,e} = 77 \ Hz \qquad \xi_{2,e} = 0.0056 \tag{5.18}$$

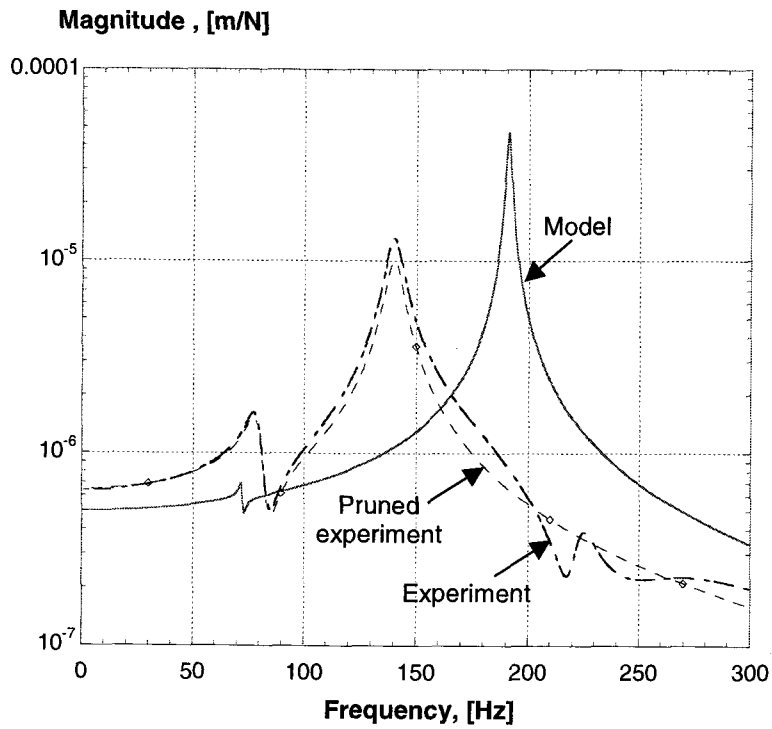

Fig. 5.7: Magnitude comparison of transfer function G_{11}.

The phase graph in Fig. 5.8 below shows an expected 90° phase shift at the first resonance frequency, which gets immediately cancelled by a closely following zero (see also the pole/zero graph in Fig. 5.10). Then there is another drop of the phase down to–180° at the second resonance frequency. The 'unpruned' experimental phase shows another phase shift at 220 *Hz* caused by a 'phantom' pole. However, this disappears after pruning. The frequency behavior of the transfer function G_{21} is shown in Fig. 5.9. The phase plot is omitted since important features are shown and described in Fig. 5.9.

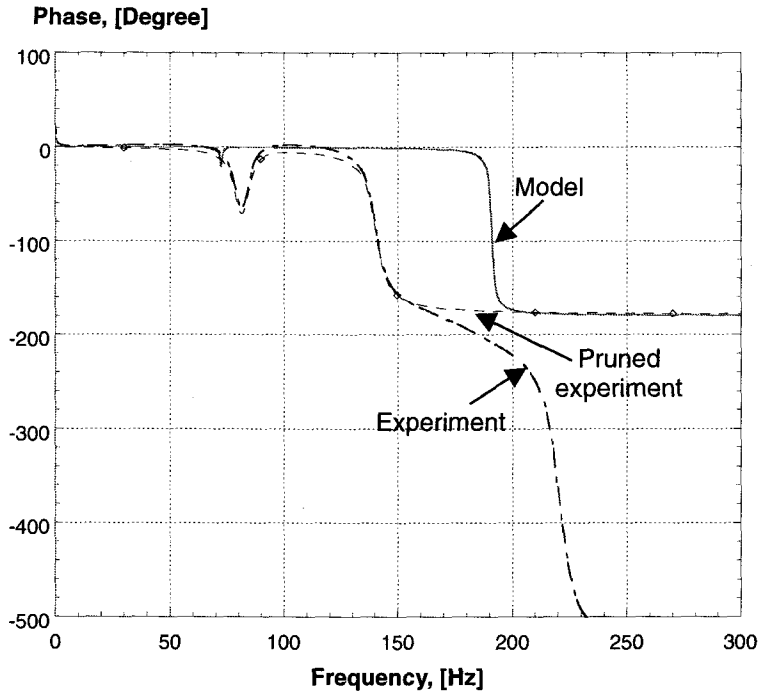

Fig. 5.8: Phase comparison of transfer function G_{11}.

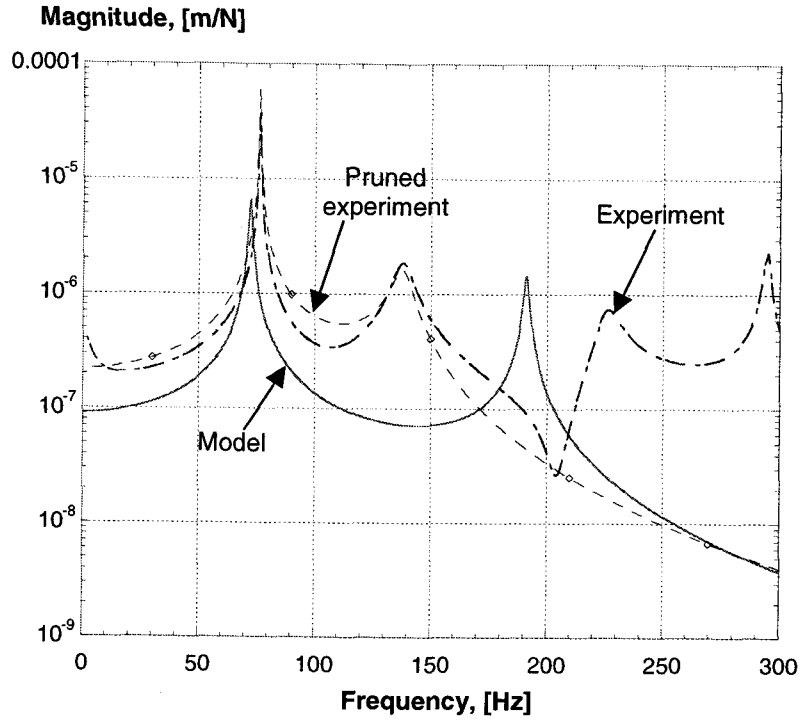

Fig. 5.9: Magnitude comparison of transfer function G_{21}.

The differences in the transfer function graphs are due to the numerical values of the physical parameters **m**, **c** and **k** being only approximations. Using the parameters from Table 5.1, assuming the damping of the helical spring is negligible, an analytical transfer function G_{11} can be calculated. It equates to

$$G_{11,a}(s) = \frac{0.72 \cdot s^2 + 5.28 \cdot s + 158405.39}{s^4 + 20.29 \cdot s^3 + 1687904.43 \cdot s^2 + 1.36 \cdot 10^7 \cdot s + 3.22 \cdot 10^{11}} \tag{5.19}$$

From experimental identification and after subsequent pruning of the high order transfer function one obtains

$$G_{11,e}(s) = \frac{0.11 \cdot s^2 + 0.71 \cdot s + 775.35}{s^4 + 142.37 \cdot s^3 + 2.52 \cdot 10^5 \cdot s^2 + 1.81 \cdot 10^6 \cdot s + 1.20 \cdot 10^7} \tag{5.20}$$

The coefficients of $G_{11,a}$ and $G_{11,e}$ are very different. However, it is more meaningful to compare the zeros and poles of the two transfer functions before making any conclusions.

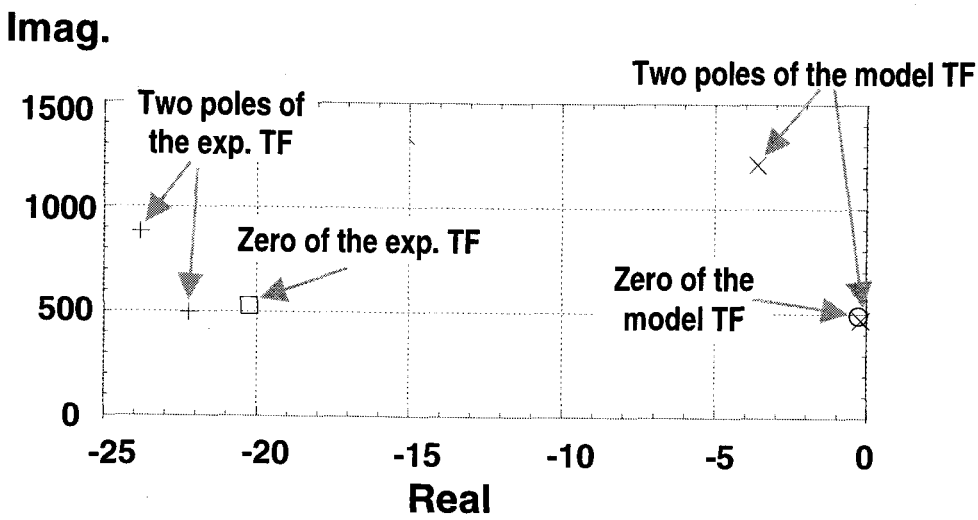

Fig. 5.10: Pole & Zero comparison of G_{11}.

Fig. 5.10 shows that the experimental as well as the analytical transfer functions have two complex conjugate poles and one complex conjugate zero. Fig. 5.10 can be interpreted by comparing it to the standard zero-pole plot (Fig.3.11).

5.3.3.2 Finite Element Analysis

One method of validating the lumped parameter model is through comparison with a finite element model. Finite element analysis (FEA) is often used as an alternative of rigid body (RB) modeling, to get an accurate picture of deflections of mechanical systems, especially if the analyzed systems have significant flexible modes. As already described in Section 2.2, FEA is not as convenient for physical

parameter estimation problems, because physical parameters do not remain in a symbolic form during the FEA process. FEA was performed using *Ansys V 5.3* (Ansys, 1997) for the simple MDOF system. The structure of this model can be seen below.

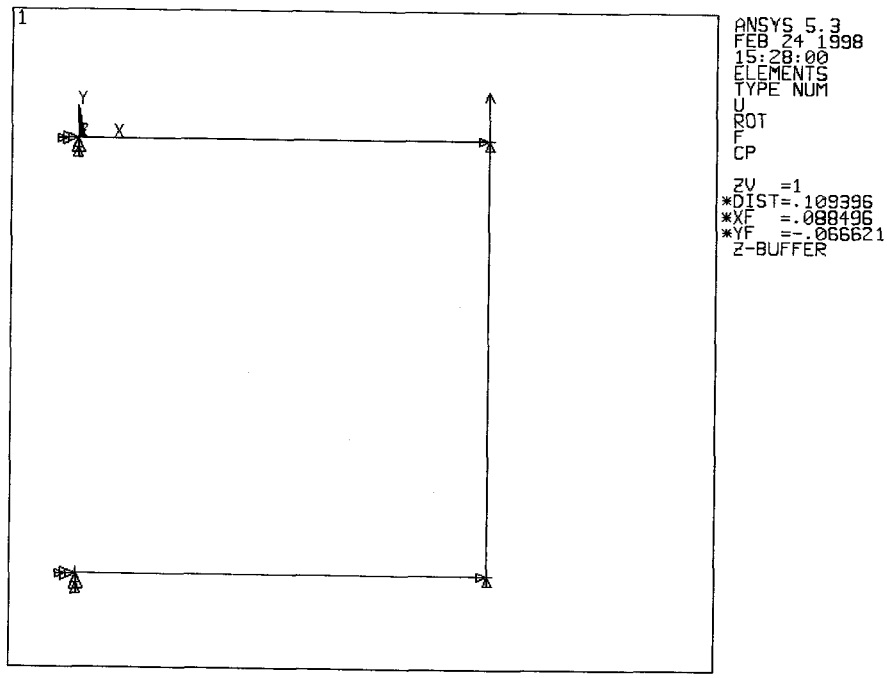

Fig. 5.11: FE model of the simple MDOF system.

The physical parameters used for this model are again taken from Table 5.1. A frequency analysis is performed on the FE model and the resonance frequencies are evaluated. Two different cases are compared, to investigate the change in resonance frequencies and the change in estimation results caused by the additional attached mass.

CASE 1: No additional mass is attached on either *Mass_1* or *Mass_2*.

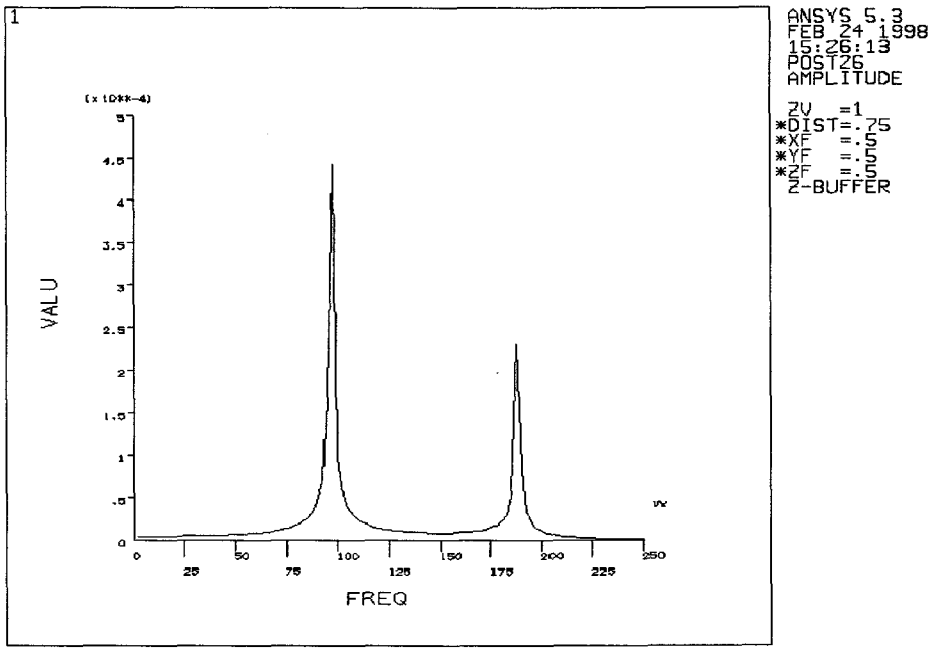

Fig. 5.12: Frequency characteristic of a point placed on *Mass_2*.

As can be seen from the figure, the two resonance frequencies are at

$$f_{1,FEA} = 190\ Hz \tag{5.21}$$

$$f_{2,FEA} = 95\ Hz \tag{5.22}$$

Comparing these frequencies with those obtained from the RB model of Eq. (5.15) and Eq. (5.16), one can see differences, but the values are reasonable close. In fact, the FE model agrees much better with the RB model than with the experimental analysis of Eq. (5.17) and (5.18). The higher resonance frequency in particular shows significant discrepancy when comparing the FE model with the experiment.

CASE 2: An additional mass of 0.75 *kg* is attached on *Mass_1*.

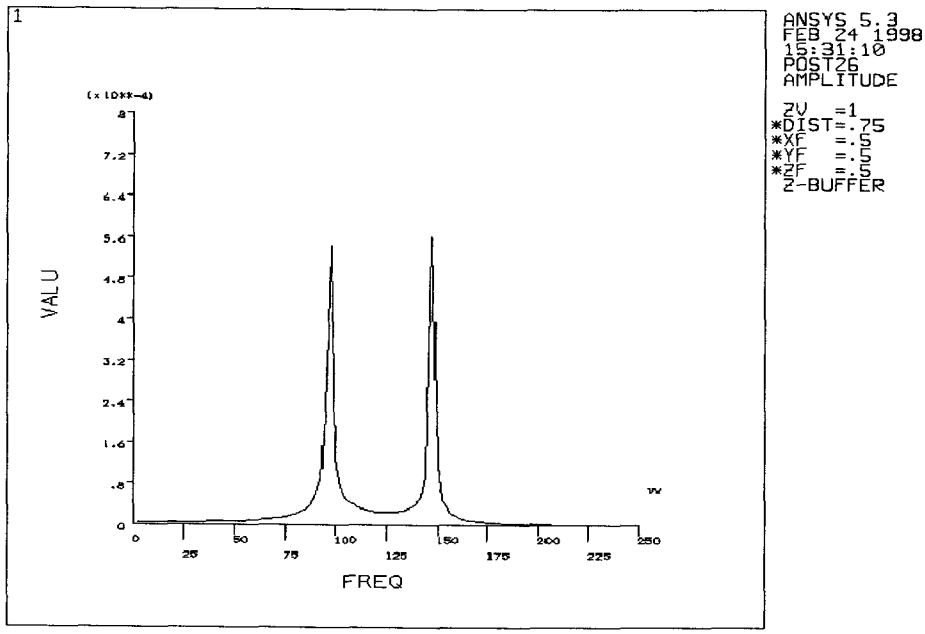

Fig. 5.13: Frequency characteristic when additional mass is added to *Mass_1*.

As can be seen from Fig. 5.13, the two resonance frequencies for the case with an additional mass attached to *Mass_1* are at

$$f_{1,FEA} = 145\ Hz \tag{5.23}$$

$$f_{2,FEA} = 95\ Hz \tag{5.24}$$

Obviously, the lower resonance frequency does not change but the higher resonance frequency drops accordingly. The results of case 2 can be compared to the resonance frequencies of the respective rigid body model and to experimental analysis. They are documented in Appendix B2. From the FE analysis it can be concluded that the RB model built in Section 5.3.1 is a good representation of the simple MDOF system. In particular the agreement of resonance frequencies shows that the model structure is

appropriate and therefore tuning the model coefficients should suffice to build an accurate representation of the experimental system.

5.3.4 Model Based Parameter Estimation

To meaningfully analyze and interpret the following estimation results it is advisable to do a sensitivity analysis as described in Section 4.4. Since the sensitivity S for the resonance frequency and damping ratio cannot be calculated explicitly as a function of the physical parameters, a percentage change is tabulated below in Table 5.3.

Table 5.3: Sensitivities of resonance frequencies and damping ratios.

Physical Parameters Changes, [%]		**Resonance Frequency Changes, [%]**		**Damping Ratio Changes, [%]**	
		f_1	f_2	ξ_1	ξ_2
m_1	+10 %	-4.7	~ 0	-4.7	~ 0
	-10 %	+5.4	~ 0	+5.4	~ 0
m_2	+10 %	~ 0	-4.7	~ 0	-4.7
	-10 %	~ 0	+5.4	~ 0	+5.4
k_{11}	+10 %	+4.8	~ 0	-4.6	~ 0
	-10 %	-5.0	~ 0	+5.3	~ 0
k_{22}	+10 %	~ 0	+4.1	~ 0	-3.9
	-10 %	~ 0	-4.3	~ 0	4.4
k_{12}	+10 %	+0.8	+0.1	-0.6	-0.1
	-10 %	+0.8	+0.1	-0.6	-0.1
c_{11}	+10 %	~ 0	~ 0	+10.0	~ 0
	-10 %	~ 0	~ 0	-10.0	~ 0
c_{22}	+10 %	~ 0	~ 0	~ 0	+9.9
	-10 %	~ 0	~ 0	~ 0	-9.9

Originally the RB model has resonance frequencies and damping ratios as listed in Eq. (5.15) and (5.16). Table 5.3 shows that the parameters m_1 and k_{11} influence the resonance frequency f_1 and the damping ratio ξ_1, where as the parameters m_2 and k_{22} influence the resonance frequency f_2 and the damping ratio ξ_2. k_{12} has little effect on the characteristic of the system which indicates weak coupling of the two masses. c_{11} and c_{22} naturally have a very direct influence on the damping of the system.

There are different methods to estimate the optimal physical parameters as described in Section 3.6. The "direct" method involving Newtonian EOM is not applied because of the extensive number of sensors necessary. The "two step" method involving Black Box models is most promising and is also straightforward, since only transfer function coefficients need to be compared. The "one step" method based on Gray Box models is computationally intensive, but is applied for this system. Another method tested is based on the extended Kalman filter.

5.3.4.1 Estimation Using "Two Step" Method

The methodology described in Section 3.6.2 and illustrated in Fig. 3.15 is applied to estimate the physical parameters of the simple MDOF system. Using the TF coefficients of G_{11} and G_{21} as shown in Eq. (5.7) and (5.10) 9 equations in the form of Eq. (3.91a,b) are formulated. Since c_{12} is assumed negligible seven unknown parameters remain to be estimated.

$$\boldsymbol{\Theta}_{s1} = \left\{ m_1, m_1, k_{11}, k_{12}, k_{22}, c_{11}, c_{22} \right\} \tag{5.25}$$

A performance index $Q_{TF}(\boldsymbol{\Theta}_{s1})$ is built according to Eq. (3.97). Ten minimization runs are documented here, beginning from different starting values $m_{1(0)}$ through $c_{22(0)}$. The starting values were statistically varied 100% from the approximations in Table 5.1. The ten sets of starting values are shown below in Table 5.4.

Table 5.4: Seven sets of starting values for the minimization procedure.

Parameters	1. Set	2. Set	3. Set	4. Set	5. Set	6. Set	7. Set
$m_{1(0)}$, [kg]	1.11	2.62	1.87	2.43	1.02	2.15	1.08
$m_{2(0)}$, [kg]	1.78	1.94	0.90	1.22	0.70	0.59	2.03
$k_{11(0)}$, [10^6 N/m]	2.24	1.17	1.26	2.79	3.00	2.31	1.85
$k_{22(0)}$, [10^6 N/m]	0.75	0.32	0.36	0.25	0.62	0.93	1.55
$k_{12(0)}$, [10^6 N/m]	0.20	0.22	0.19	0.96	0.69	0.91	0.58
$c_{11(0)}$, [Ns/m]	16.02	22.82	15.49	11.81	8.37	30.61	21.93
$c_{22(0)}$, [Ns/m]	0.79	0.76	0.84	0.33	0.41	0.36	0.48

The minimization results tabulated in Table 5.5 show that for a wide range of different starting values the minimization procedure finds one global minimum with high repeatability. However, the resulting numerical values of the parameters are not satisfactory.

Table 5.5: Solutions from the minimization procedure.

Physical Parameters	Average Value at Minimum	Standard Deviation
m_1, [kg]	2.471	0.0004
m_2, [kg]	2.521	0.096
k_{11},[10^6 N/m]	0.9422	0.0050
k_{22}, [10^6 N/m]	4.3045	0.0164
k_{12}, [10^6 N/m]	0.154	0.0606
c_{11}, [Ns/m]	27.156	0.00015
c_{22}, [Ns/m]	1.865	0.0709

Comparison with the expected parameters (highlighted in Table 5.1) show large discrapencies. This is not caused by a poor minimization procedure, but rather by the fact that transfer function coefficients have no physical meaning and can carry a significant error as seen from the transfer function comparison in Eq. (5.19) and (5.20). Even when the physical parameters minimize to a wrong value, the shape of the resulting transfer function looks promising as can be seen from Fig. 5.14 and 5.15. Fig. 5.14 shows experimental and model transfer function G_{11} before the minimization, and Fig. 5.15 after minimization. Figures 5.16 and 5.17 show the same for G_{21}. The estimation results for the case of an additional mass attached on *Mass_1* are shown in Appendix B2.

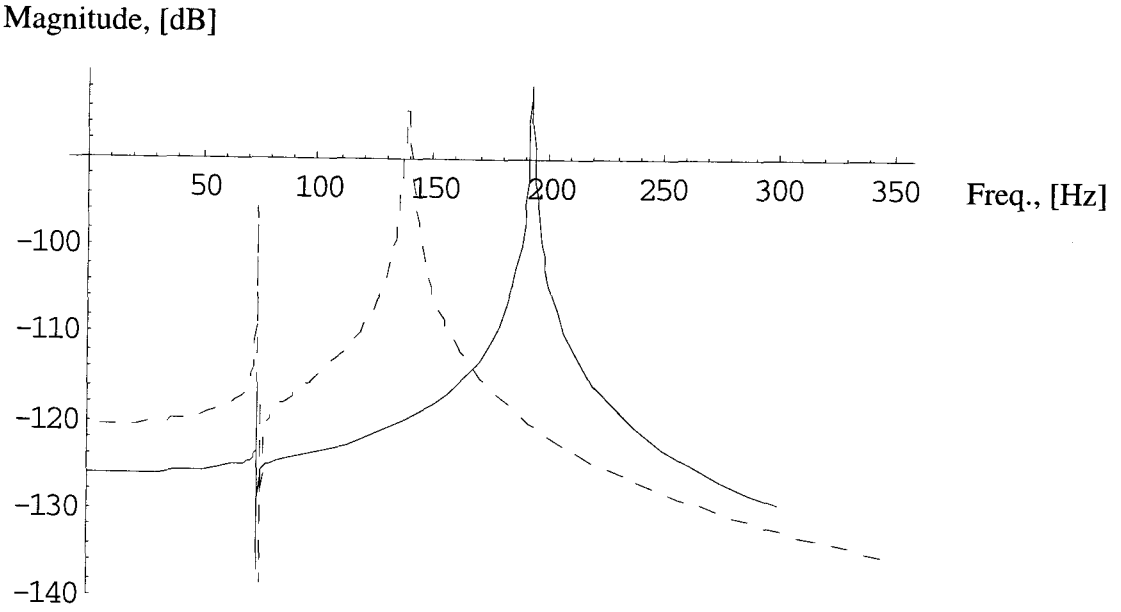

Fig. 5.14: Experimental (dashed) and model (solid) magnitude plot of G_{11} in *m/N* before minimization (small mass).

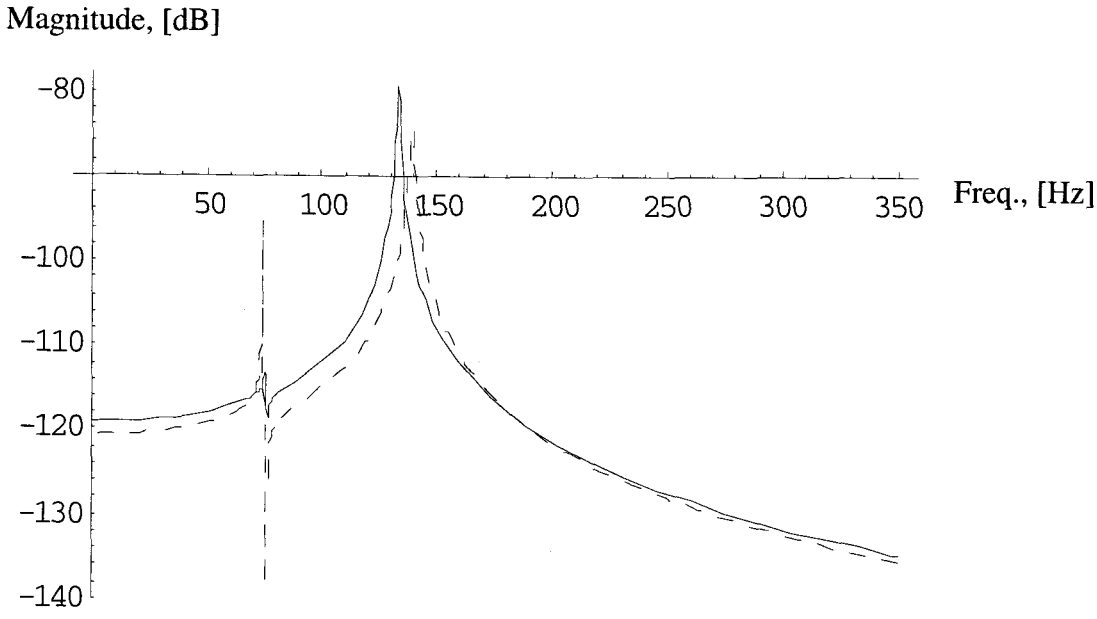

Fig. 5.15: Experimental (dashed) and model (solid) magnitude plot of G_{11} in *m/N* after minimization (small mass).

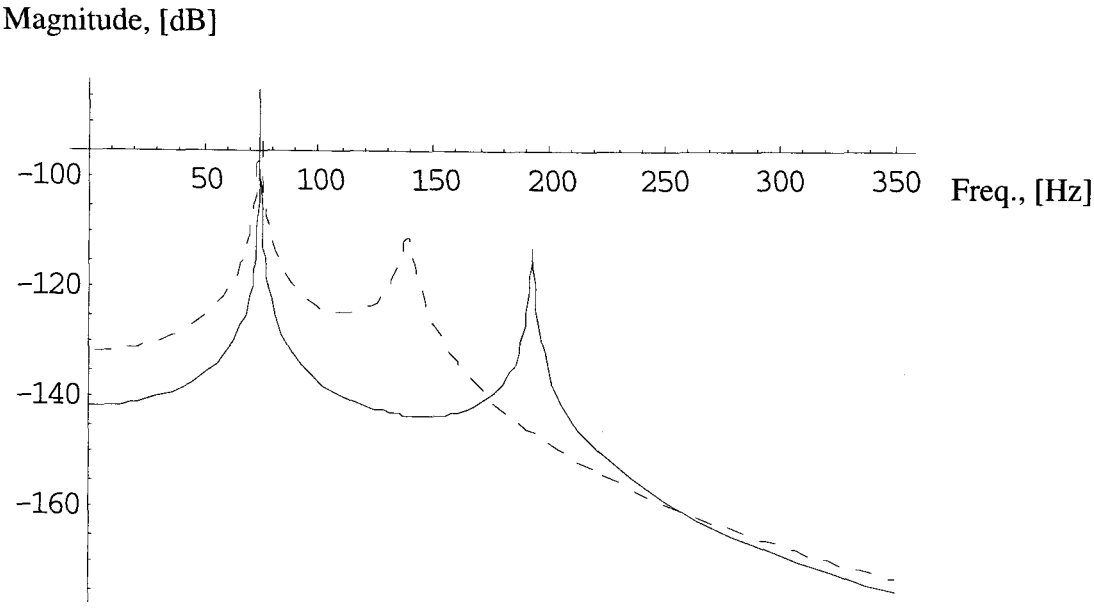

Fig. 5.16: Experimental (dashed) and model (solid) magnitude plot of G_{21} in *m/N* before minimization (small mass).

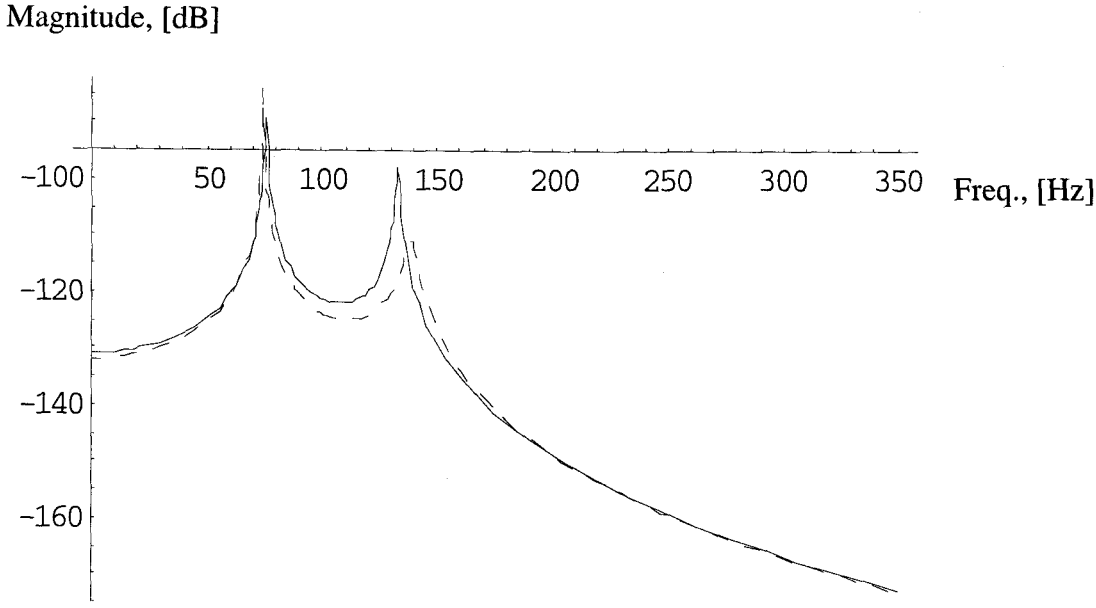

Fig. 5.17: Experimental (dashed) and model (solid) magnitude plot of G_{21} in *m/N* after minimization (small mass).

When looking at the bode plots above a good agreement between the shape of the experimental and analytical TF can be observed. The numerical results of the estimated physical parameters (Table 5.5), however were not at all close to the parameters expected (from direct estimation). It can be concluded that the estimation in Laplace-domain does not lead to satisfactory results. One reason might be that the experimental identification procedure of the TF is not accurate enough to allow using these few TF coefficients as a base for estimating physical parameters. Also the search for the global minimum cannot be limited in its bounds since it is not known in which range the TF coefficients vary. As can be seen from Eq. (5.19) and (5.20) they can vary between 10^{-1} to 10^{11}. The values do not have any physical meaning, therefore intuitive assessment is difficult.

5.3.4.2 Estimation Using "One Step" Method

In the time-domain a performance index like Eq. (3.108) in Section 3.5.2 is used. Since there were slight uncertainties about the zero level and phase shift of the signals collected, the phase and level were included as variables in the performance index in addition to the physical parameters Θ_s. The data used for the estimation was a 10 *Hz* square wave output signal from the proximity sensor on *Mass_2*. First tests showed that certain physical parameters tend to become negative during the minimization process. Therefore a penalty function was incorporated into the performance index for m_1, k_{11} and c_{11} as described in Chapter 4.3 Several minimization runs were computed with the following result being only an example. The number of iterations and the resulting error level depend on the tolerance set for reaching the required accuracy. The result illustrated in the figure below was reached with the following parameters:

Table 5.6: Estimation results in the time-domain.

Parameter	**Estimation Result**	**Parameter**	**Estimation Result**
m_1, **[kg]**	1.349	c_{11}, **[Ns/m]**	5353.59
m_2, **[kg]**	0.556	c_{12}, **[Ns/m]**	10.2092
k_{11}, **[10^6 N/m]**	1.518	c_{22}, **[Ns/m]**	2.2892
k_{12}, **[10^6 N/m]**	0.0538	***Phase shift*, [deg]**	13.887
k_{22}, **[10^6 N/m]**	0.0843	***Off-set*, [m]**	0.000486

The minimization procedure converged very slowly since each collected datapoint is used for estimation. The penalty function introduced new problems as described in Section 4.3 such that the procedure had to be guided manually. The final estimated

values show good agreement with parameters obtained by conventional methods for the first I-beam. The parameters m_1, k_{11} and c_{11} show good results. The values for the second I-beam give rather poor results. The set-up has to be modified for more accurate estimation of the second I-beam (e.g. putting an additional force sensor in front of Mass_2 and off-setting the filtering effect of the first I-beam by an 'inverse' filter). This must be left for future research. The experimentally obtained output signal and the model output after optimization are shown in Fig. 5.18.

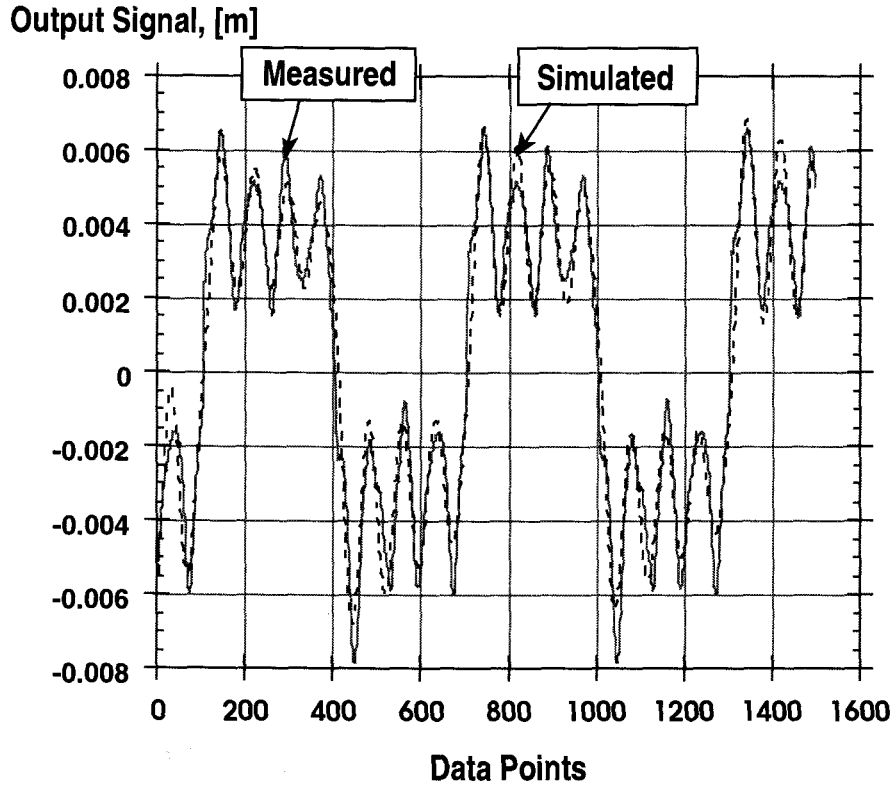

Fig. 5.18: Measured and simulated output signal from the proximity sensor on *Mass_2*.

Since the minimization algorithm used, caused some difficulties in finding a good minimum quickly a different algorithm called AGR was tested. The AGR method is

described in more detail in Section 4.3 and promises faster convergence and the ability to find multiple minima in one single run. The result is shown in Fig. 5.19 below

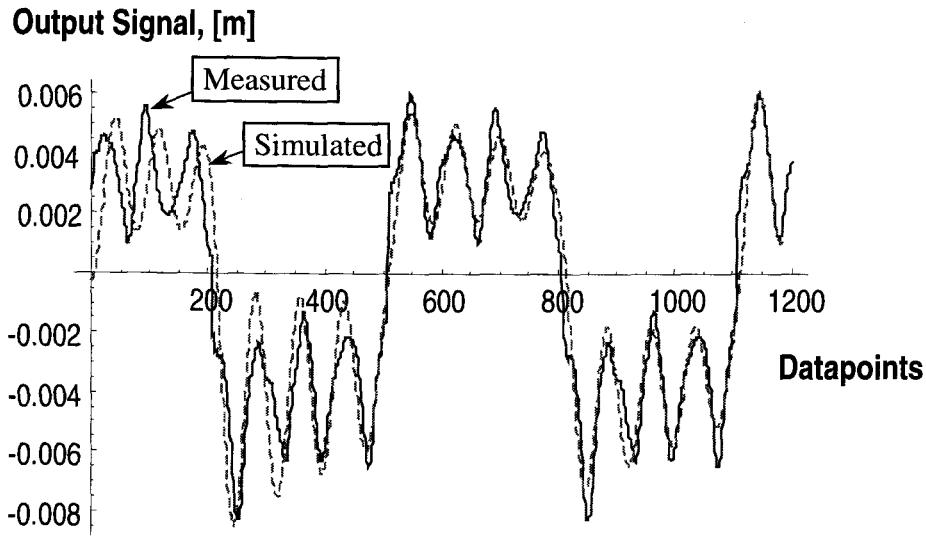

Fig. 5.19: Measured and simulated output signal from the proximity sensor on *Mass_2* using the AGR method.

It can be concluded that estimation in time-domain gives reasonably good results, where as the Laplace-domain method did not meet expectations. In both cases the need for more robust minimization methods is obvious. Additional research is necessary to explore the full potential of the proposed methods.

5.3.4.3 Estimation Using the Extended Kalman Filter

In order to apply the concept of the extended Kalman filter to physical parameter estimation, the dynamic system needs to be enhanced to include the unknown parameters in the state vector. This concept is illustrated and tested below.

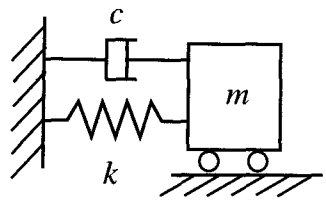

Fig. 5.20: A simple spring-mass system.

Considered is simple spring mass system shown in Fig. 5.20 and given by

$$\ddot{x} + 2\ \xi\ \omega\ \dot{x} + \omega^2 x = 0 \tag{5.26}$$

where ξ and ω are considered constants to be determined from measurements of the displacement. In order to use the Kalman filter equations derived in Section 3.6.3, the constants must be considered variables. One has to define the following state vector **x**

$$x = \begin{bmatrix} x_1 \\ x_2 \\ x_3 \\ x_4 \end{bmatrix} = \begin{bmatrix} x \\ \dot{x} \\ \xi \\ \omega \end{bmatrix} \tag{5.27}$$

The complete state-space description of this dynamic system is given by

$$\dot{\mathbf{x}} = \begin{bmatrix} 0 & 1 & 0 & 0 \\ 0 & -2x_3x_4 & 0 & -x_3x_4 \\ 0 & 0 & 0 & 0 \\ 0 & 0 & 0 & 0 \end{bmatrix} \mathbf{x} \tag{5.28}$$

The matrices $\mathbf{\Gamma}$ and **n** from Eq. (3.111) are now filled with the appropriate terms to separate the linear from the non-linear parts.

$$\mathbf{\Gamma} = \begin{bmatrix} 0 & 1 & 0 & 0 \\ 0 & 0 & 0 & 0 \\ 0 & 0 & 0 & 0 \\ 0 & 0 & 0 & 0 \end{bmatrix} \tag{5.29}$$

$$\mathbf{n}(\mathbf{x}) = \begin{bmatrix} 0 \\ -2x_2x_3x_4 - x_1x_4^2 \\ 0 \\ 0 \end{bmatrix} \tag{5.30}$$

The Jacobian matrix $\mathbf{J}(\mathbf{x_0})$ evaluated at $\mathbf{x_0}$ calculates to

$$\mathbf{J}(\mathbf{x}_0) = \begin{bmatrix} 0 & 0 & 0 & 0 \\ -x_{04}^2 & -2x_{03}x_{04} & -2x_{02}x_{04} & -2x_{02}x_{03} - 2x_{01}x_{04} \\ 0 & 0 & 0 & 0 \\ 0 & 0 & 0 & 0 \end{bmatrix} \tag{5.31}$$

The state variables are now estimated with the generated displacement data. The procedure outlined in Section 3.6.3 is used to update the state variables using the measured data. The initial values used were $x_1 = 1.0\ m$, $x_2 = 0.0\ m/s$, $x_3 = 0.05$ and $x_4 = 1000\ Hz$. An integration step of 2.5 10^{-5} seconds was used for a total time of 0.01 seconds. The tracking of the state x_1, which represents the displacement of the spring-mass system, is shown below.

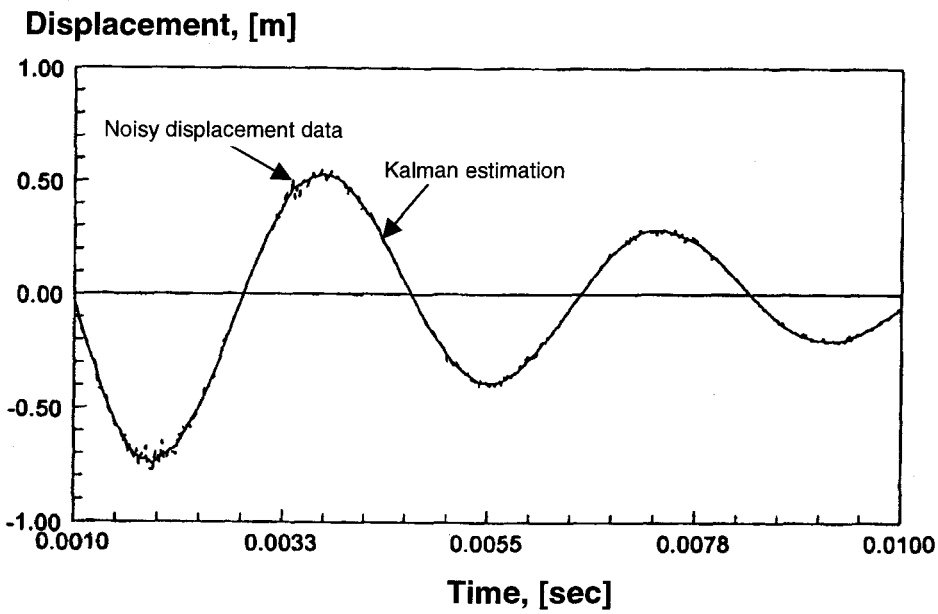

Fig. 5.21: Estimation of the state x_1 with the extended Kalman filter.

The constant damping coefficient ξ and the natural frequency ω were also estimated within 0.0015 seconds to their correct initial values of 0.1 and 1715 *Hz*. Fig. 5.22 and 5.23 show the fast convergence of these values.

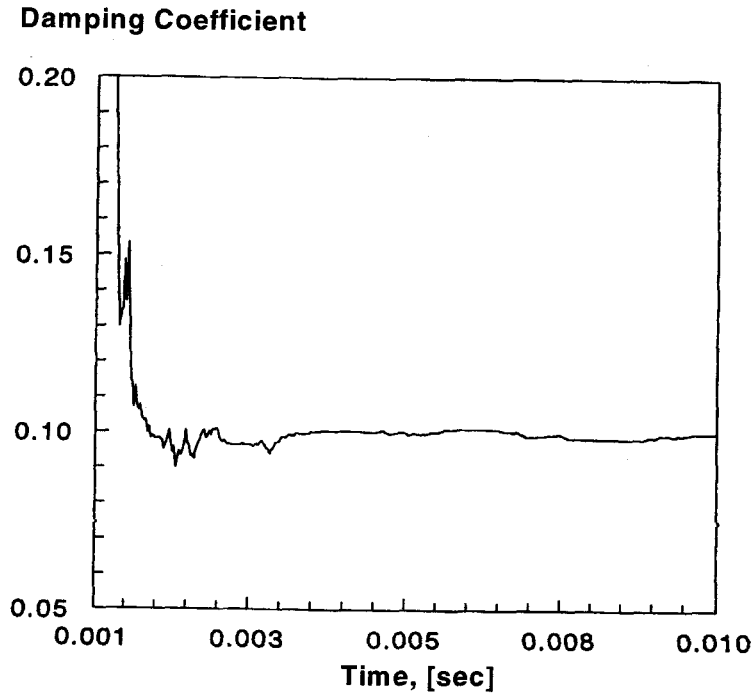

Fig. 5.22: Estimation of the state x_3, (ξ).

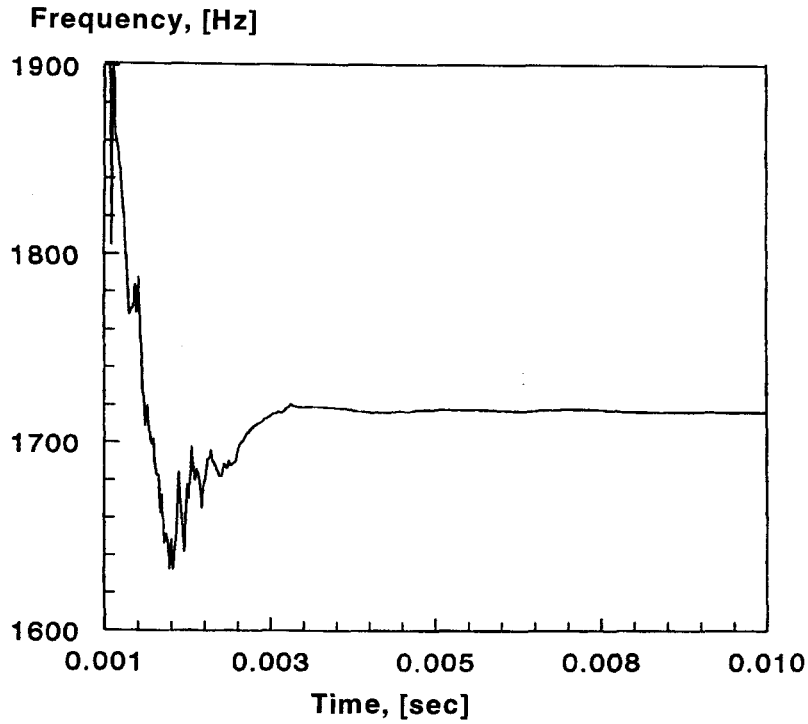

Fig. 5.23: Estimation of the state x_4, (ω).

The same procedure was applied to the simple MDOF system described in Section 5.3.2, but without success. Assuming c_{12} to be zero, seven additional states have to be established, to accommodate all physical parameters present in this system. The modified state vector **x** becomes

$$\mathbf{x} = \begin{bmatrix} x_1 \\ x_2 \\ x_3 \\ x_4 \\ x_5 \\ x_6 \\ x_7 \\ x_8 \\ x_9 \\ x_{10} \\ x_{11} \end{bmatrix} = \begin{bmatrix} d_1 \\ d_2 \\ \dot{d}_1 \\ \dot{d}_2 \\ m_1 \\ m_2 \\ k_{11} \\ k_{12} \\ k_{22} \\ c_{11} \\ c_{22} \end{bmatrix} \tag{5.32}$$

In this case the evolution matrix $\mathbf{A}_1$ of the state-space description is given by

$$\mathbf{A}_1 = \begin{bmatrix} 0 & 0 & 1 & 0 & 0 & 0 & 0 & 0 & 0 & 0 & 0 \\ 0 & 0 & 0 & 1 & 0 & 0 & 0 & 0 & 0 & 0 & 0 \\ -\frac{x_7 x_8}{x_5} & \frac{x_8}{x_5} & -\frac{x_{10}}{x_5} & 0 & 0 & 0 & 0 & 0 & 0 & 0 & 0 \\ \frac{x_8}{x_6} & -\frac{x_8 x_9}{x_6} & 0 & -\frac{x_{11}}{x_5} & 0 & 0 & 0 & 0 & 0 & 0 & 0 \\ 0 & 0 & 0 & 0 & 0 & 0 & 0 & 0 & 0 & 0 & 0 \\ 0 & 0 & 0 & 0 & 0 & 0 & 0 & 0 & 0 & 0 & 0 \\ 0 & 0 & 0 & 0 & 0 & 0 & 0 & 0 & 0 & 0 & 0 \\ 0 & 0 & 0 & 0 & 0 & 0 & 0 & 0 & 0 & 0 & 0 \\ 0 & 0 & 0 & 0 & 0 & 0 & 0 & 0 & 0 & 0 & 0 \\ 0 & 0 & 0 & 0 & 0 & 0 & 0 & 0 & 0 & 0 & 0 \\ 0 & 0 & 0 & 0 & 0 & 0 & 0 & 0 & 0 & 0 & 0 \end{bmatrix} \tag{5.33}$$

The only non-zero elements of the *11x11* $\mathbf{\Gamma}$ matrix are $\Gamma_{13} = 1$ and $\Gamma_{24} = 1$. The vector $\mathbf{n}(\mathbf{x})$ of non-linear components is

$$\mathbf{n}(\mathbf{x}) = \begin{bmatrix} 0 \\ 0 \\ -\frac{x_3 x_{10}}{x_5} + \frac{x_2 x_8}{x_5} - \frac{x_1(x_7 + x_8)}{x_5} \\ -\frac{x_{11} x_4}{x_5} + \frac{x_1 x_8}{x_6} - \frac{x_2(x_8 + x_9)}{x_6} \\ 0 \\ 0 \\ 0 \\ 0 \\ 0 \\ 0 \\ 0 \end{bmatrix} \tag{5.34}$$

In this case the estimation algorithm did not converge to meaningful values. The analysis of causes is difficult. The number of unknown states in this system might be too large for their accurate estimation based on just two state measurements. No further investigation was done on this method.

5.4 Spindle-Bearing System

The second, more realistic system used to investigate the concept of physical parameter estimation is the following spindle-bearing set-up. It consists of a medium-speed machine tool spindle, suspended by two sets of angular contact bearings. Fig. 5.24 shows the experimental test rig.

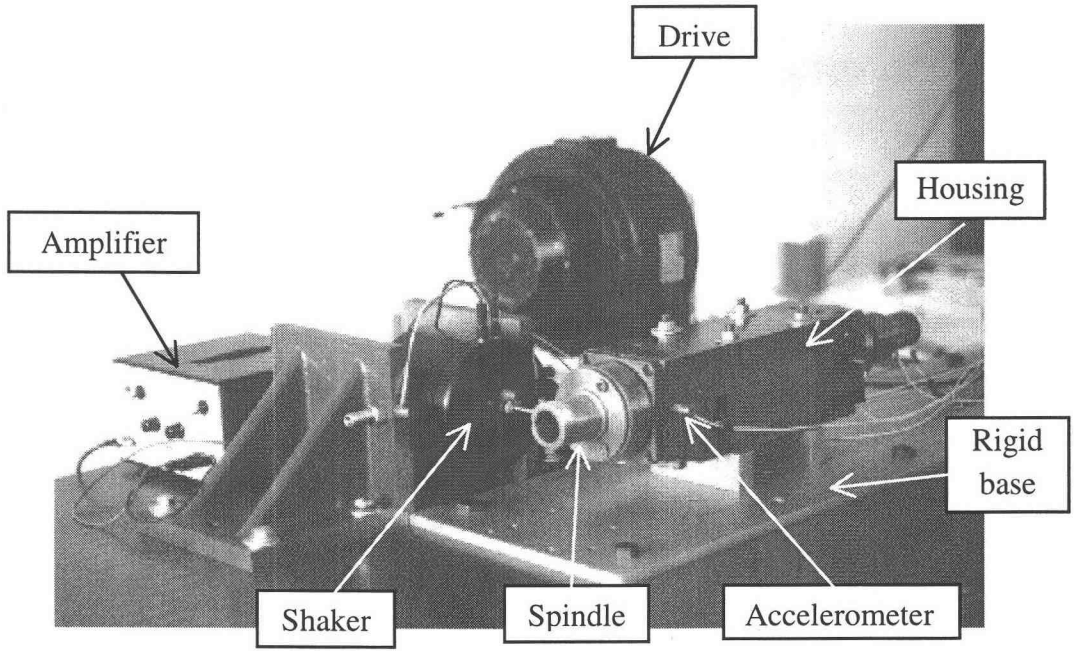

Fig.5.24: The experimental set-up of the spindle-bearing system.

The spindle housing is attached to the rigid base via four screws. An electromagnetic shaker (Bruel & Kjaer) excites the system by generating an input force F. An electric motor can rotate the spindle to speeds of up to 2000 *rpm*.

5.4.1 Mechanical Design

Main geometric dimensions characterizing the experimental set-up are shown in Table 5.7. *Barden* angular contact bearings, type #110H, with a contact angle of 15° (Barden, 1996) are used in this set-up. Detailed information about the bearing characteristic is found in Appendix D.

Table 5.7: Geometric dimensions characterizing the spindle-bearing system.

	Housing	Spindle		Bearings
Length, [m]:	0.340	0.612	**Type:**	Barden 110H
Width, [m]:	0.105		**# of Balls:**	18
Height, [m]:	0.125		**Outer Dia., [m]:**	0.08
Outer Diameter, [m]:		0.05	**Inner Dia., [m]:**	0.05
Inner Diameter, [m]:		0.026	**Dist. between Bearings, [m]**	0.275

A technical drawing of the spindle-bearing set-up is shown below.

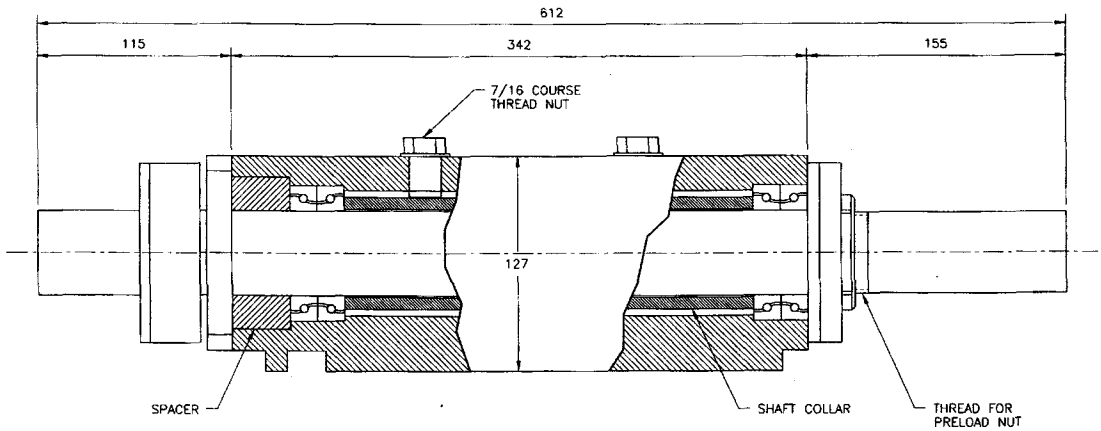

Fig. 5.25: Technical drawing of the spindle-bearing system.

5.4.2 Lumped Parameter Model

A purely mechanical, multi-degree-of-freedom (MDOF) model of this spindle assembly is built in Section 3.5. Fig. 3.11 shows a 'rigid body' model of the spindle. The system is modeled as an eleven DOF system. The housing has three translational (x, y and z) and three rotational DOF, (φ, ϕ and ψ). The spindle itself has five DOF.

5.4.2.1 Model Structure

The system is modeled according to CASE 2 in Section 3.4.3. Only small vibrations are considered around some fixed reference position. Large system reconfigurations e.g. by repositioning of the main machine tool table (CASE 3) are not taken into account here. Also gyroscopic effects are neglected for the sake of brevity. The spindle and housing are assumed to have symmetric mass distribution, so that the global inertia matrix is diagonal (see Appendix C3).

5.4.2.2 Experimental Measurement of Parameters

Estimates (not using physical parameter estimation methods as of Section 3.6, but traditional methods) of the physical parameters are tabulated below in Table 5.8.

Table 5.8: Reference physical parameters of the spindle-bearing system.

Physical Parameters (housing)	Numerical Values (housing)	Physical Parameters (spindle)	Numerical Values (spindle)
m_h	24.61 *kg*	m_s	10.67 *kg*
$k_{H1X} = k_{H2X} = k_{H3X} = k_{H4X}$	65 10^6 *N/m*	$k_{FX} = k_{RX}$	60 10^6 *N/m*
$k_{H1Y} = k_{H2Y} = k_{H3Y} = k_{H4Y}$	130 10^6 *N/m*	$k_{FY} = k_{RY}$	60 10^6 *N/m*
$k_{H1Z} = k_{H2Z} = k_{H3Z} = k_{H4Z}$	65 10^6 *N/m*	k_{FZ}	30 10^6 *N/m*
$c_{H1X} = c_{H2X} = c_{H3X} = c_{H4X}$	1000 *Ns/m*	$c_{FX} = c_{RX}$	1000 *Ns/m*
$c_{H1Y} = c_{H2Y} = c_{H3Y} = c_{H4Y}$	1000 *Ns/m*	$c_{FY} = c_{RY}$	1000 *Ns/m*
$c_{H1Z} = c_{H2Z} = c_{H3Z} = c_{H4Z}$	1000 *Ns/m*	c_{FZ}	1000 *Ns/m*

The stiffnesses of the housing-base screws in the *y*-direction are approximated with the formula

$$k_{HBY} = \frac{EA_{Screw}}{l_{Screw}} = 129.9 \cdot 10^6 \frac{N}{m} \tag{5.35}$$

The stiffnesses in the *x*- and *z*-direction are estimated at 50 % of k_{HBY}. The bearing stiffnesses are obtained from low frequency force & displacement measurements. Dampings are difficult to estimate and are somewhat arbitrarily assumed to be 1000 *Ns/m*.

5.4.3 Validation of the Model

In order to compare the model with the actual system, vibration measurements were performed on the spindle-bearing set-up described above. Forces, deflections and accelerations were recorded at various locations. The location of sensors is shown in Fig. 5.24. The data acquisition equipment used for signal collection was the same

as for the simple MDOF system (see Section 5.2). Fig. 5.26 shows a force vs. displacement graph resulting from a sinusoidal force input through the electro-magnetic shaker connected to the front of the spindle.

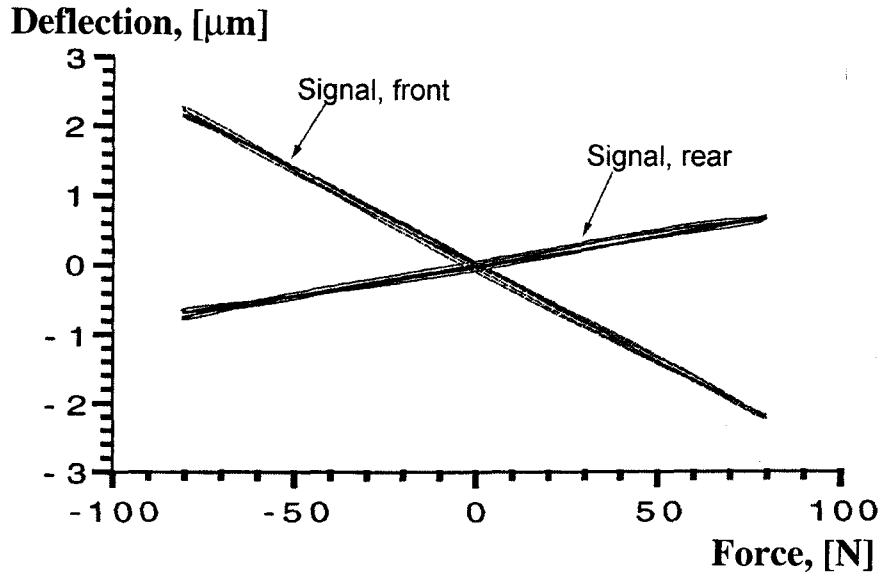

Fig. 5.26: Linearity of the spindle-bearing system.

These initial simple tests allow visual inspection of the quality of the signals ('hazy' or 'crisp') and also reveal information about the linearity of the system. It can be concluded that for low input forces (<100 *N*), the system behaves almost perfectly linear and therefore a linearized model is a good representation of this system. The graph in Fig. 5.26, labeled (Signal front) is obtained from a load cell mounted at the shaker and a proximity sensor in front of the spindle. The graph labeled (Signal rear) is obtained from the same load cell but from a proximity sensor mounted at the rear of the spindle.

The slope of the graphs gives some indication of the stiffness of the spindle, however the evaluation of the correct spindle stiffness requires a closer look at the entire system (see Section 5.4.4).

The model can also be validated in the frequency domain. Experimental I/O identification was applied to the signals (load cell and proximity sensor at the front) and the resulting transfer function is shown in Fig. 5.27.

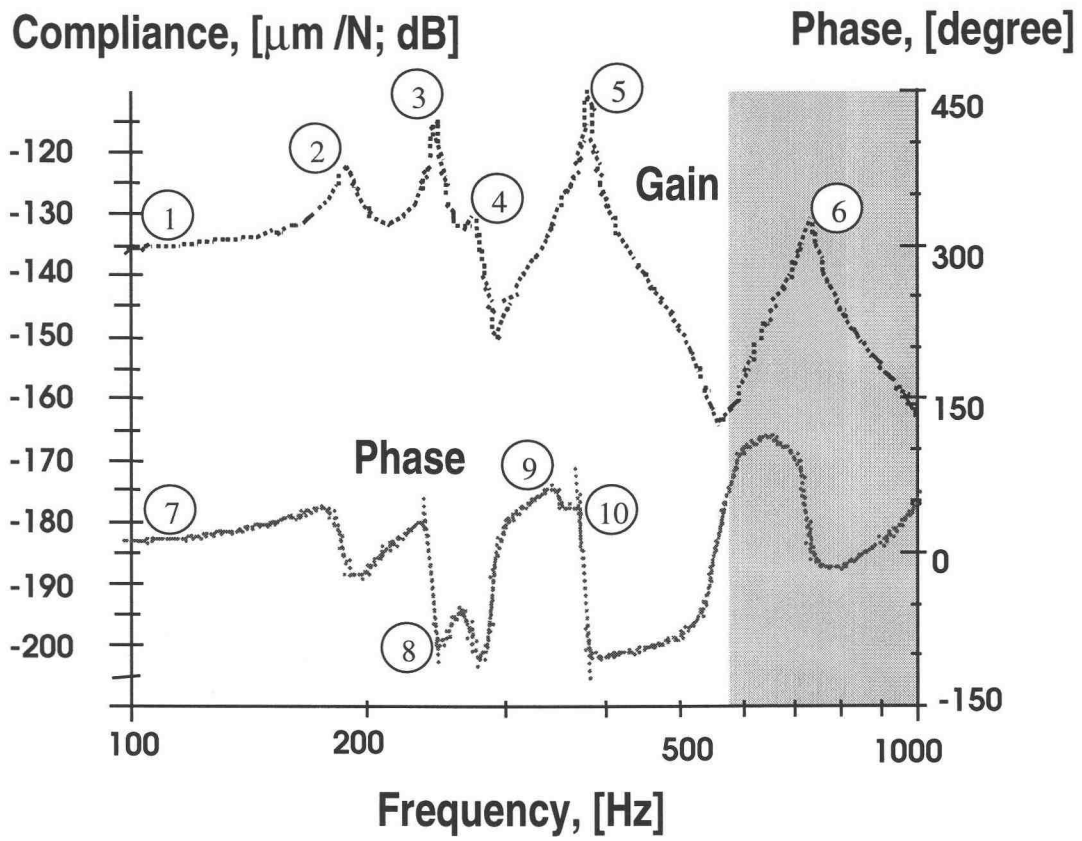

Fig. 5.27: Experimental transfer function characteristic of the spindle-bearing system.

The shaded area is not considered here. The features of the experimental transfer function in Fig 5.27 labeled (1) through (10) are described below:

① The intersection of the magnitude graph with the *Y*-axis represents the DC-gain of the system. Even though Fig. 5.28 doesn't show the entire frequency range down to 0 *Hz* it can be approximated that the experimental DC-gain is ~ 135 *dB*. This is in good agreement with the model DC-gain (see Fig. 5.29).

② The first resonance peak appears at approx. 190 *Hz*. This cannot be attributed to any feature in the model. It is currently unknown what this resonance frequency is caused by. It is possible that the experiment table, which acts as the base of the system, causes this resonance. Since the rigid body model assumes a motionless base this resonance doesn't appear in Fig. 5.29.

③ This strong resonance peak at approx. 220 *Hz* is one of the rigid body modes of the spindle. It agrees well with the model resonance frequency at 215 *Hz*.

④ This smaller resonance peak cannot be found in the model. It is considered insignificant, since its magnitude is ~20 *dB* or 10 times lower than the previous resonance peak (feature 3).

⑤ At ~ 390 *Hz*, there is another significant resonance peak, which coincides with the second peak in the model (at 310 *Hz*). This represents another rigid body mode.

⑥ This resonance peak is not existent in the RB model, but it agrees with the resonance found in Comparin's research (see Table 5.10). Therefore this is the first flexible mode of the spindle. In this research flexible modes are not of concern and therefore are not modeled.

⑦ The experimental phase agrees well with the model phase in that it starts with zero phase shift at low frequencies.

⑧ Not considering the unknown resonance at 190 *Hz*, the first significant phase drop occurs at 220 *Hz*.

⑨ After the drop, the phase recovers quickly due to the anti-resonance (zero) at 290 *Hz*.

⑩ Another significant phase drop exists because of the second strong resonance peak at 390 *Hz*. The region above 550 *Hz* is not discussed here.

The natural frequencies revealed through experimental analysis can be compared with frequencies of the model, which are calculated from the **A** matrix. Using all geometric dimensions and physical parameters from Table 5.6, 5.7 and Appendix C1, all eleven natural frequencies and damping ratios of the model are calculated as follows:

Table 5.9: Natural frequencies and damping ratios of the spindle-bearing model.

Natural Frequency, [Hz]	Damping Ratio
214.705	0.0201
235.532	0.0237
288.883	0.0250
310.671	0.0204
336.537	0.0430
510.146	0.0368
552.928	0.0259
553.565	0.0399
903.223	0.0316
1145.304	0.0199
1248.862	0.0327

Fig. 5.28 shows the model transfer function between the input force in the *x*-direction on the front of the spindle and the output displacement on the front of the spindle shaft. Not all natural frequencies shown in Table 5.9 can be observed in the figure because only the vibrations along the x-axis are evaluated. Two very strong resonance frequencies can be observed at 1350 *rad/sec* (215 *Hz*) and at 1940 *rad/sec* (310 *Hz*) (highlighted in Table 5.9). They are caused by rigid body motion of the spindle and housing.

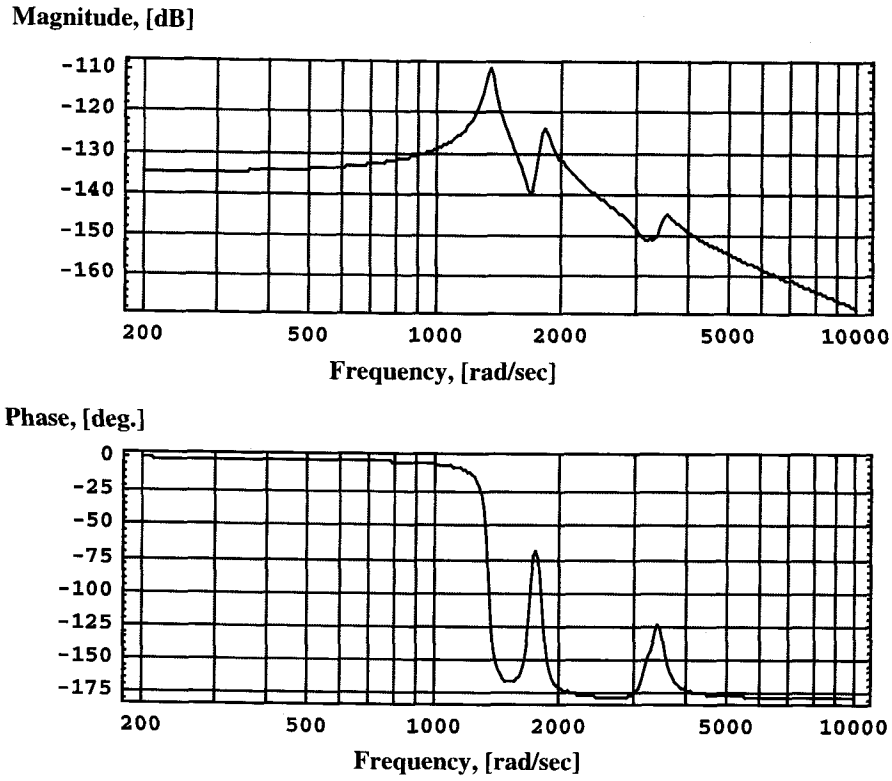

Fig.5.28: Magnitude and Phase characteristic of the spindle-bearing model.

Detailed information pertaining to the flexible mode vibrations of the considered spindle[22] has been available from previous studies (Comparin, 1983; Spiewak, 1995). In particular, essential flexible modes have been defined. That research showed that the combined spindle-housing flexible modes are above 800 Hz, significantly higher than the rigid body modes. Table 5.10 shows the principle results in terms of resonance frequencies and damping ratios (Comparin, 1983).

[22] The spindle-bearing set-up shown in Fig. 5.24 was obtained from Mr. Comparin after he finished his research.

Comparin's calculated flexible modes of Table 5.10 were obtained by FE analysis of the spindle-bearing system and show a reasonable agreement with his experimental results. Comparin also investigated the housing and shaft as separate components. The shaft itself has resonances found experimentally at 692 *Hz*, 1898 *Hz* and 3442 *Hz* (calculated with FEA: 681 *Hz*, 1879 *Hz* and 3448 *Hz* respectively). The housing has even higher natural frequencies because of its short and stocky shape (experimental: 3582 *Hz* and 3823 *Hz*; FEA: 4765 *Hz* and 4880 *Hz*). The fact that the rigid body modes appear in a quite different frequency range (~200-400 *Hz*) than the flexible body modes (> 700 *Hz*) is very important in this research. It justifies that the developed RB model, neglecting flexible motion is a good representation of the system below 600 *Hz*.

Table 5.10: Flexible modes of the investigated spindle-assembly (Comparin, 1983).

Natural Frequency [Hz]	Damping Ratio	Comment
892	0.008	1st flexible mode, experimental
900	-	1st flexible mode, calculated
1301	-	2nd flexible mode, calculated
1444	0.023	2nd flexible mode, experimental
1802	0.018	3rd flexible mode, experimental
2050	-	3rd flexible mode, calculated

5.4.4 Estimation of Key Physical Properties

Due to computer limitations and difficulties with the minimization procedure, no estimation method involving the minimization of a performance index was applied to the spindle-bearing system. However all necessary prerequisites are fulfilled to

perform this task. Optimization of the minimization procedure must be left for future research. It was found in Section 5.3.4.2 that time domain estimation leads to promising results. In particular low frequency square wave excitation results in desirable signals for estimation because intuitive evaluation of the final fit is possible. Nevertheless, the optimization of the performance index is demanding since there will be many more variables than in the case of the simple MDOF system. This must also be left for future research. Still, signals are collected for square wave excitation to show the feasibility of the method (see Fig. 5.29 below).

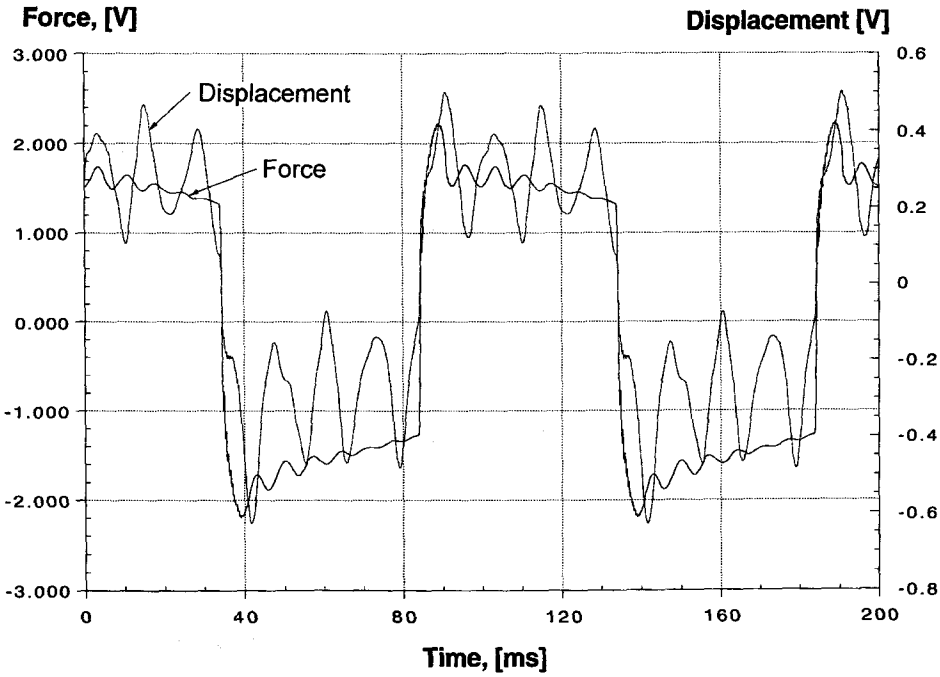

Fig. 5.29: Square wave characteristic of the spindle.

For the application of preload monitoring the analytical spindle model developed in Chapter 3 was used to search functional relationships between the features in the measured signals and the bearing stiffness.

The spindle model derived in Section 3.5 has eleven vibration modes characterized by natural frequencies f_{ni}, and damping ratios ζ_{ni}, (i = 1, 2,...11). They are readily calculated from the eigenvalues of the evolution matrix $\mathbf{A}(\Theta)$ (Eq. (3.7a). This matrix depends upon the system properties including the stiffnesses of bearings. As these stiffnesses depend in turn upon the preload, F_p, the pattern of $f_{ni}[\Theta(F_p)]$ and $\zeta_{ni}[\Theta(F_p)]$ can be used to establish this preload. It should be remembered, however, that this pattern is also strongly affected by other stiffnesses in the system, which may significantly vary in the realistic working conditions. To resolve this difficulty, the proposed analytical model is of utmost importance.

The above concept can be implemented in several ways, e.g., pattern recognition by artificial neural networks, discriminant functions, or fuzzy logic. Since the analytical model is available, a 'deep knowledge' expert system is an attractive alternative. Specifically, the inherent complexity of the frequency-damping-preload relationship can be efficiently dealt with by establishing 'maps', such as shown below

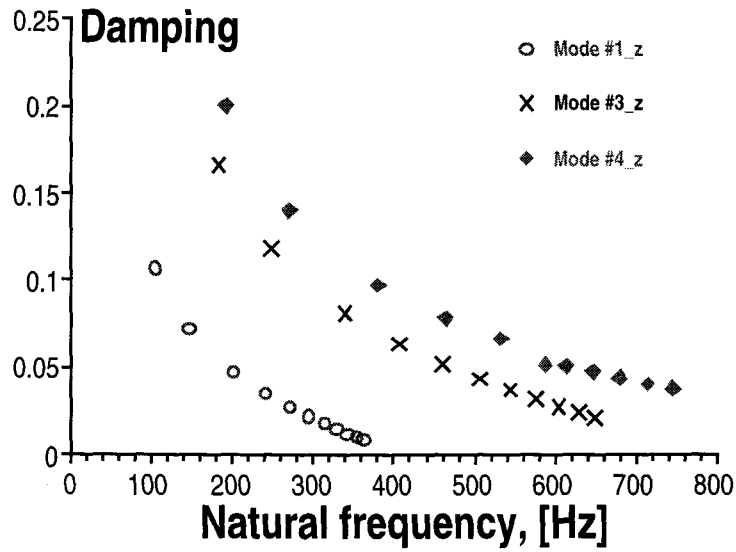

Fig. 5.30: Frequencies and damping ratios calculated for the first five modes. Preload (%, left to right): 5, 15, 25, 40, 55, 70, 85, 100, 115, 130, 150.

Based on the proposed model (automatically generated in Section 3.5 together with coefficients established in Section 5.4.2.2), distinctive traces are plotted for the damping-frequency relationships for varying preload and for chosen vibration modes of the investigated spindle (see Section 5.4). While building these maps, it is advisable to start with a weakly coupled system (low bearing stiffness), so the vibration modes of the shaft and the housing can be easily distinguished.

A systematic development of the system for practical application should start with identifying these modal properties which are the most sensitive to the bearing preload, F_p. Computing the sensitivity coefficients (see Eq. 4.12) readily does this. Based on the results, a list of candidate modal properties for consideration (see Fig. 5.30) is established. In the next step, different sensor types (e.g., accelerometers, displacement sensors) and locations are examined. The analysis indicates which sensor types and locations are favorable for the estimation of the modal properties. This is illustrated by way of the following example.

Considered is a proximity sensor measuring displacements of the front end of the spindle shaft in the x-direction (Fig. 5.22). The output matrix, $\mathbf{C}(\Theta)$, accounts for an impact of two generalized shaft coordinates on the measured output signal. These coordinates are: 1) translational motion along the x-axis and 2) rotational motion about the y-axis. The other matrices in the state-variable model are not affected by the sensor selection. The Bode plots shown in Fig. 5.31 represent a scalar transfer function of the system obtained according to Eq. (3.15).

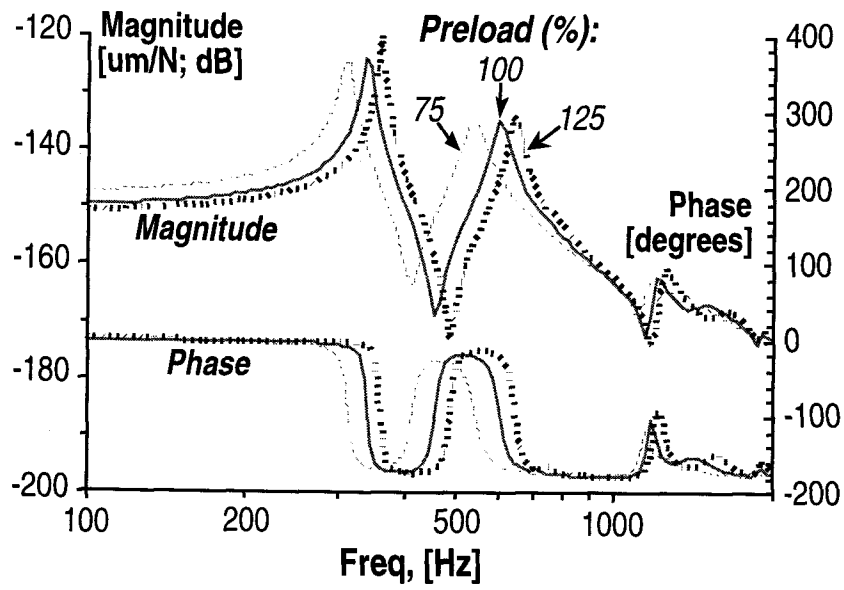

Fig. 5.31: Bode plots of the transfer function $G_{sxFx}(\Theta,s)$ obtained analytically for different preloads F_p.

The plots are generated for the nominal preload (solid), a lower preload (75% of nominal - dashed thin line) and an increased preload (125% - dashed heavy line). A shift of the resonance frequencies is clearly visible. The sensitivity of frequency shift due to preload change, $S_{F_p}^{f_{ni}}$, is approximately the same for both pronounced resonance peaks (345 *Hz* and 595 *Hz*). The third resonance at 1100 *Hz* is 45 *dB* below the first one, so it not suitable for detection using the proximity sensor under consideration. It should be noted, however, that the measurement of acceleration instead of displacement would 'lift' the magnitude plot at higher frequencies (proportionally to the frequency squared). This could be a reason for using an accelerometer in place of a proximity sensor.

It is worthwhile to investigate if the preload can be estimated by measuring the spindle housing vibrations. By modifying the output matrix, $\mathbf{C}(\Theta)$, a new transfer function is generated. Its magnitude plot is compared in Fig. 5.32 with the transfer

function discussed above. The most significant difference is the lower gain (about 15 *dB*) of the plot corresponding to the housing measurement. However, the two strongest resonance peaks occur at the same frequencies as in the transfer function representing the measurement of the shaft vibrations. It is an interesting conclusion, since the measurement of housing vibrations is significantly easier and suitable acceleration sensors are widely available.

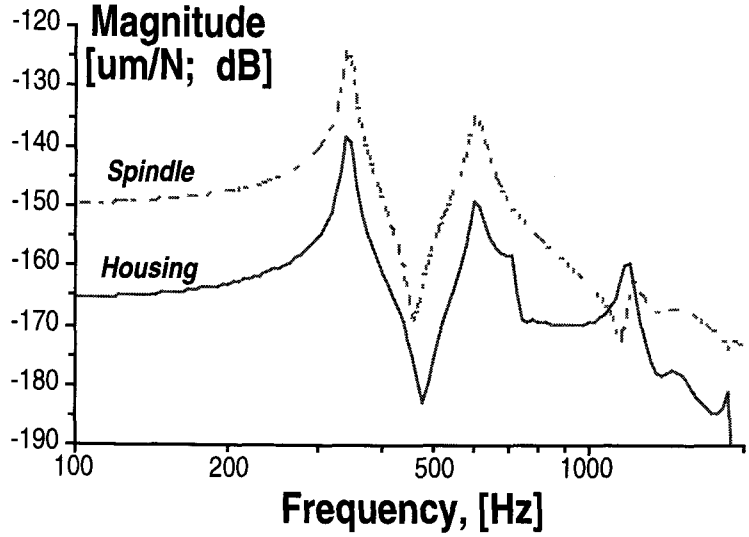

Fig. 5.32: Magnitude plots of transfer functions of the shaft and housing.

The proposed location of the sensor close to the end of the shaft or housing (far away from the shaft's center of gravity) is also established by analyzing the derived MDOF model. The analysis (omitted here for the sake of brevity) reveals that the rotational motion of the shaft about the Y axis is featured by the lowest modal frequency (345 *Hz*), while the second lowest frequency (595 *Hz*) represents the translational shaft motion in the *x*-direction. Placing the proximity (or acceleration) sensor away from the center of gravity allows the monitoring of both peaks. Indeed,

for the system under consideration it is possible to find such a location that both peaks have approximately the same magnitude.

Experimental veryfication of the bearing stiffness is difficult. One reason is that the total stiffness of the spindle is built up from a number of contributory elements, as shown in Fig. 5.33. These elements are the spindle flexure element, the bearing flexure element, and the contact flexure element.

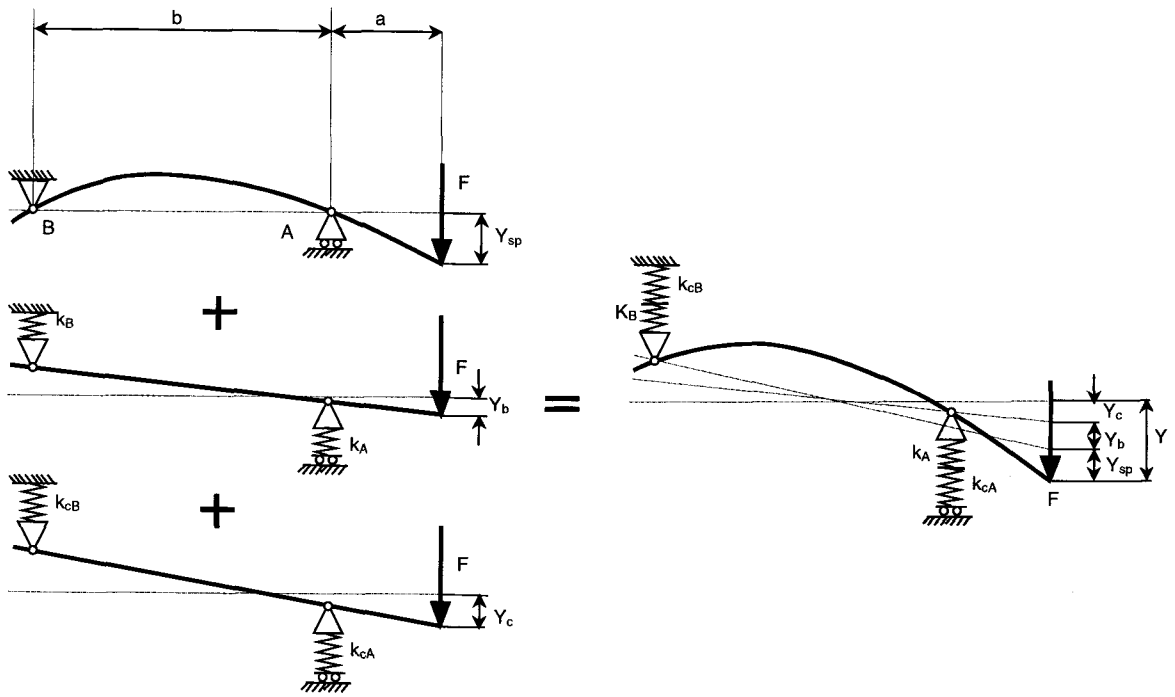

Fig. 5.33: Deflections of a main spindle.

The deflection contribution of the spindle is due to the flexible nature of the material. The contribution of the bearing is due to the bearing stiffness. In addition there is a contact stiffness due to the various interfaces (e.g. rings and spacers) between the bearing and the housing. Because of the serial connection of the

individual contributions to the total flexure, the total flexibility at the point-of-force application is given by

$$\frac{1}{k} = \frac{1}{k_{sp}} + \frac{1}{k_b} + \frac{1}{k_c} = \frac{Y_{sp}}{F} + \frac{Y_b}{F} + \frac{Y_c}{F} \tag{5.36}$$

The combination of what is measured in the following experiments equates to the total stiffness k. A direct comparison with the bearing stiffness information supplied by the manufacturer is difficult, because even if the flexible stiffness of the spindle is negligible (very high), the contact stiffness due to some 'looseness' at several interfaces is rather low. Since Eq. (5.36) shows an inverse relationship for the stiffness, high component siffnesses hardly contribute to the total stiffness. This is actually a positive finding, since on-line monitoring of the stiffness would reveal any looseness in the system immediately. To evaluate this total stiffness at the bearings, the spindle-bearing system is excited with a 5 Hz sinusoidal wave. Stiffness changes at higher frequencies are thus avoided. Taking into account the different sensor locations, Equations (5.37) and (5.38)[23] solve for the stiffness at the front and rear bearings respectively.

$$k_f = \frac{1.397 \cdot U_f}{0.840 \cdot d_{Sf} - 0.160 \cdot d_{Sr}} \tag{5.37}$$

$$k_r = \frac{0.397 \cdot U_f}{0.160 \cdot d_{Sf} - 0.840 \cdot d_{Sr}} \tag{5.38}$$

The manner in which the stiffness is evaluated differs from the approach taken for the simple MDOF system (where only a simple ratio of magnitudes is calculated, see Fig (5.6). Equations (5.37) and (5.38) are applied to each data point collected in the experiment and thus statistical variations become existent.

---

[23] See Appendix C4 for derivation.

Fig 5.34 shows example stiffness evaluations for the 'no shim' configuration (the purpose of inserting different shims will be explained further below). The stiffness varies in the range indicated by the figure. The spikes are due to a zero crossover of the input signal and the resulting sudden increase in the ratio of Eq. (5.37) and (5.38).

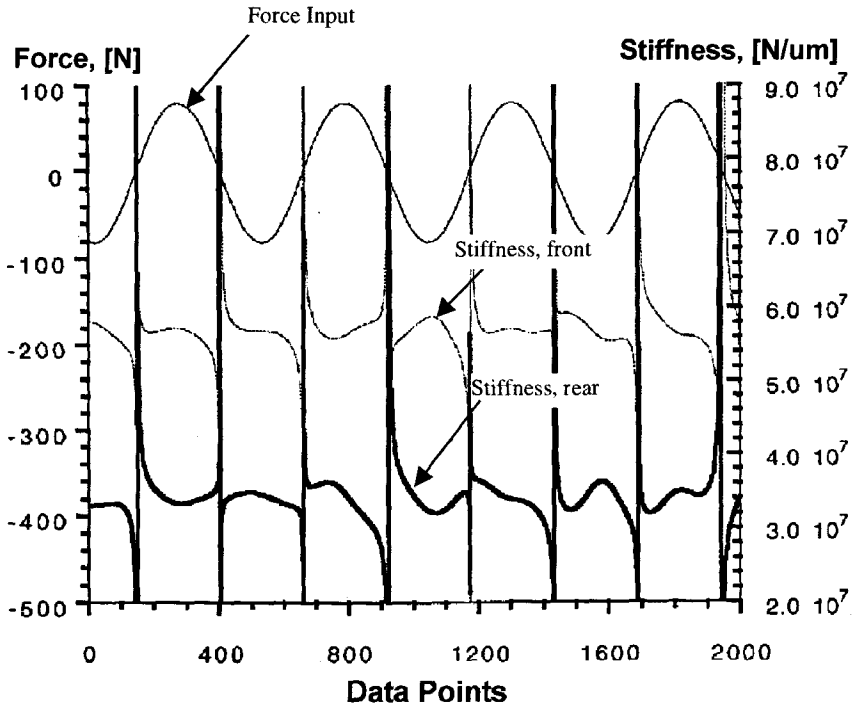

Fig. 5.34: Evaluating the stiffness at 5 *Hz*.

As described above, a relationship exists between the increase in preload, the increase in bearing stiffness and the change in natural frequencies. But these relationships have to be verified experimentally. Therefore the total stiffness is evaluated for each different preload configuration.

To change the preload, shims of various thicknesses were inserted between the two outer bearing races of the front and rear bearing (Fig. 5.35). The bearings were manufactured for a medium standard preload of 85 *lb*. The thickness variation of the shims was 13 μm, 38 μm and 76 μm.

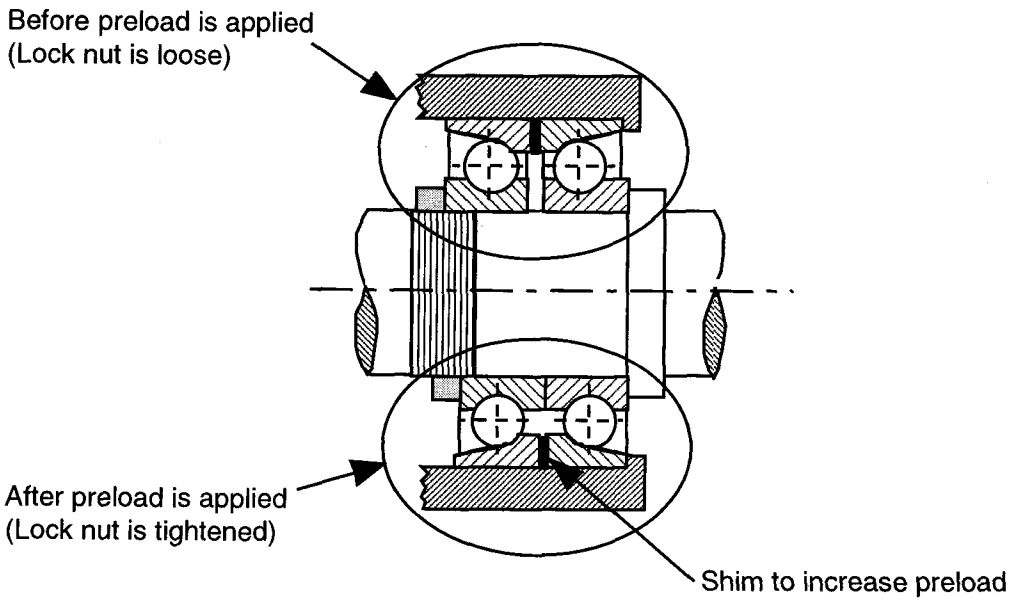

Fig. 5.35: Preload increase through use of additional shim.

A summary of the stiffness calculation results for the front and rear stiffnesses of the spindle-bearing system is shown in Fig. 5.36 and 5.37 respectively. It can be seen that increasing the shim thickness, which raises the preload applied to the bearings, increases the stiffness of the bearings. Each mark in Fig. 5.36 and 5.37 represents a separate experiment and the length of the mark represents the level of statistical variation. Repeatable levels of stiffnesses were difficult to accomplish since for a preload change the spindle had to be dissassembled. Also, note that the rear stiffness increases at a similar rate as the front stiffness, although starting from a lower level.

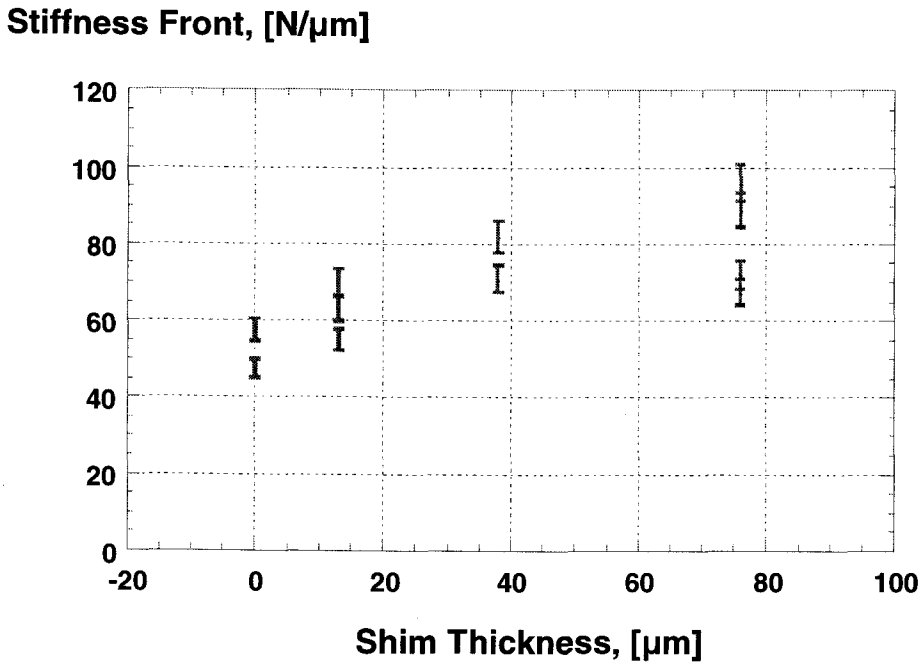

Fig. 5.36: Front bearing stiffness change with increasing preload.

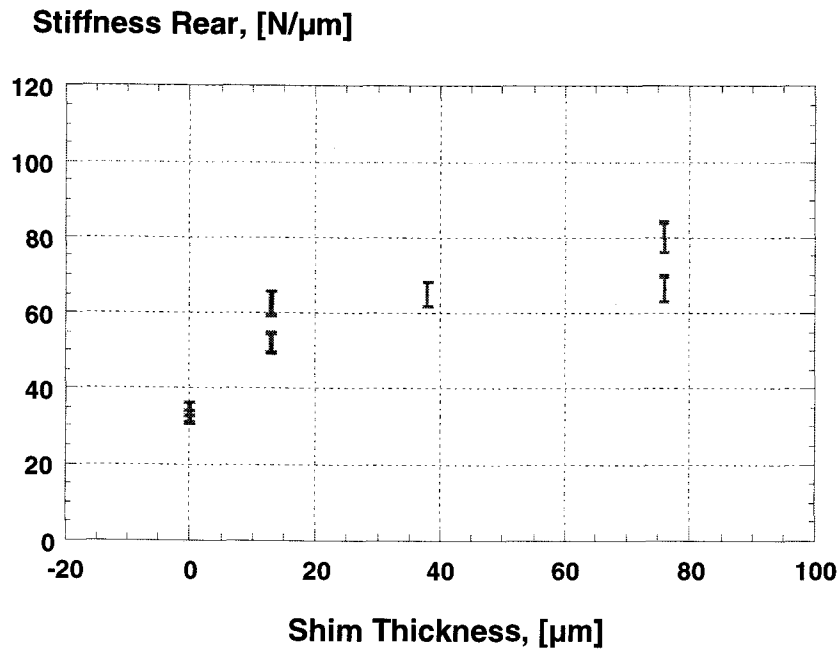

Fig. 5.37: Rear bearing stiffness change with increasing preload.

Frequency changes due to variations in the preload are shown for the model in Fig. 5.38. Showing these changes from actual data is essential for proving the theory of the proposed preload monitoring method. The experimental results should not be expected to be as clear as those from the model. This is because variations caused by disassembly and re-assembly as well as effects of other components (e.g. table, various rings and spacers) cause resonances (feature 2 in Fig. 5.27) that blur the result. Nevertheless, Fig. 5.38 shows how the natural frequencies clearly change with the preload variation.

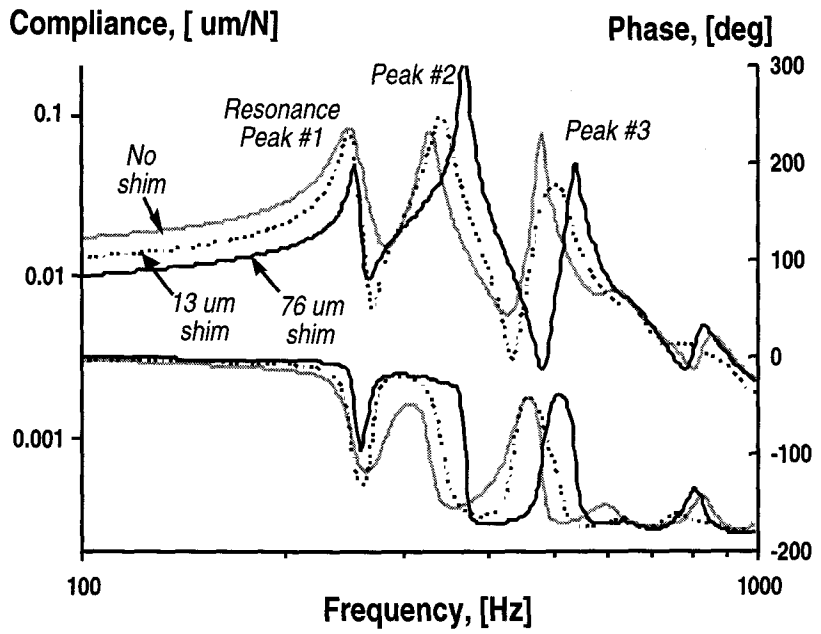

Fig. 5.38: Bode plots of the transfer function $G_{sxFx}(\Theta,s)$ obtained experimentally for different preloads F_p.

5.5 Closure

This chapter presented experimental analysis to examine the accuracy of the analytical model developed in Chapters 3, and to analyze the physical parameter estimation methodology. Two different experimental set-ups were used for investigation. One set-up involves a simple and well defined two degree-of-freedom system described in Section 5.3. A lumped parameter model of the system was formulated and experimental data was collected. The analysis revealed that the "two step" method did not lead to satisfactory results. The "one step" method has a significant better performance.

The second test set-up represented a shaft-bearing system. In depth model and experimental analysis showed that the concept of physical parameter estimation is applicable and realistic for shop floor environments. Due to computer limitations and difficulties with the minimization procedure, no estimation method based on minimizing the performance index was applied to the spindle-bearing system. However all necessary prerequisites are fulfilled to perform this task. Optimizing the minimization procedure must be left for future research. A functional relationship was found between resonance frequencies, damping ratios and the bearing stiffness. Based on this relationship a empirical "feature" map was constructed which is used for monitoring the bearing preload.

6. CONCLUSIONS AND RECOMMENDATIONS

6.1 Conclusions

A methodology of physical parameter estimation for monitoring and diagnosis of mechanical systems is presented. It integrates two important components: (1) computer aided model generation and (2) estimation of physical parameters. The development of the entire methodology was done in a programming environment of *Mathematica*, which allows symbolic as well as arbitrary precision computations.

A class of lumped parameter models is generated automatically using Lagrange's energy method, linear algebra and homogenous transformations. The proposed modeling approach is particularly suitable for parallel kinematics machines, in which the impact of bending moments can be made negligible by suitable design and rigid body approximation is sufficiently accurate.

The models built for a simple MDOF system and for the spindle-assembly are validated through comparison with FE models and through experimental analysis. In particular for the spindle-assembly a frequency region is established (<800 *Hz*) where the rigid body model is a good representation of the system. A comparison with earlier research on the same set-up (Comparin, 1983) shows that flexible modes do not appear in this region. Transfer functions are also compared (see Fig. 5.38 and 5.39). They show significant similarities in the above frequency range.

With regard to the estimation of physical parameters the research has lead to the formulation of six methods. They are:

(1) "Direct" method – Its main advantage is a closed form solution. The disadvantage is a number of sensors that are necessary, which makes this method not practical for industrial applications because of increased equipment and installation costs, and deterioration of reliability.

(2) "Two step" method – The partitioning in this method has a drawback of errors being less traceable through the two steps. It was found that small errors in the identified model coefficients obtained in the first step cause large errors in the estimation results of the second step. Specifically the appearance of multiple solutions in the second step, which was not predicted by simulations, necessitates the use of robust algorithms that can find global minima instead of being trapped locally.

(3) "One step" method – This method is computationally very intensive, since no information compression is applied as in the "two step" method.

(4) Extended Kalman filter – The validity of this approach has been demonstrated in a simple one DOF example. The method works well and is very fast for the estimation of few parameters.

(5) Functional relationships – This is the simplest method, but it relays on the existence of functional relationships between features in measured signals and physical parameters.

(6) "Hybrid" method – Combination of two or more of the above methods has the potential to significantly improve the accuracy and robustness of physical parameter estimation.

6.2 Recommendations for Future Research

The research presented in this thesis has revealed several obstacles that have to be overcome before an efficient, fast and robust method for physical parameter estimation can be implemented. The major areas recommended for future research are as follows:

Model Enhancement: Currently the proposed methodology applies to systems that can be approximated by lumped parameter models. However it is possible to account for flexible modes by applying techniques well documented in the literature. In particular two methods are straightforward in their application: (1) "rigid body" approximation (Schmitz, 1985) and (2) component mode synthesis (Zhang, 1991). Accuracy and robustness of these extended models have to be tested. The major tasks for research are as follows:

- The spindle dynamic behavior and in particular the bearing stiffness can vary substantially as the rotational speed increases due to the bearing gyroscopic moment and centrifugal force (Shin et al., 1994). This has not been taken into account in this research. Therefore it is recommended to include this effect in the spindle model.
- The current models are built using Lagrange's energy method. Implementation of alternative approaches such as Kane's method (Kane et al., 1983) will provide additional validation of the existing models.
- Experimental evaluation of the proposed methodology necessitates extension of the model to represent the test rig under investigation more accurately. This can be done by including additional components such as the base, exciter, or V-belt pulley.
- Knowledge of the actual physical parameters is indispensable for the evaluation of different estimation algorithms. In particular the fixture of the spindle housing to the base changes after every assembly and disassembly. Accurate and rapid methods for experimental determination of these parameters need to be developed.

Enhancement of Non-Linear Minimization: The difficulties encountered with minimization require additional research in two areas:

(1) Search for more efficient minimization algorithms. Current minimization techniques proved insufficient in this research for finding global minima of complex shaped functions. New, more robust methods such as simulated annealing, genetic algorithms and adaptive grid refinement need to be investigated.

(2) Speed of computations. The proposed methodology has been developed on and for generally available desktop computers such as a standard 200 *MHz* Pentium PC. It was found in this research that their speed is not adequate. Some computations, in particular for the "one step" method, run for several days. The methodology or parts of it should be ported to more powerful computers (e.g. workstations or supercomputers). Another possibility is to implement specialized hardware using DSP processors for a fast computation of model responses (needed to evaluate performance indices).

Improvement of Estimation: Improvements in the model as described above will automatically lead to better results in all proposed estimation methods.

- The proposed "hybrid" method (see Section 3.6.6) has the best potential of accurate and fast estimation of multiple parameters. It is therefore recommended to focus future research on this method.
- There are many different ways of building the performance index as indicated in Eq. (3.98) and (3.99). They greatly affect the efficiency of minimization and thus are critical for fast parameter estimation. It is recommended for future research to define guidelines for optimization of the performance index structure.

Improvement of the Experimental Set-Up: The conducted research has indicated the need for enhancement of the experimental set-up in two ways:

- Additional sensors to measure internal forces of the system (e.g. a force between the two masses of the simple MDOF system) will allow building a more robust performance index.
- Experimental measurement of flexible vibration modes of the complete spindle assembly will provide better insight on the validity of the RB model and indicates necessary extensions.

Implementation in the Shop-Floor Environment: High-speed estimation of bearing preload based on a functional relationship proved feasible in this research. This method should be applied in the shop-floor conditions. The same method should be investigated for monitoring the stiffness of housing-base fixture. These fasteners are easily accessible (no disassembly necessary as with the bearing preload variation) and can be accurately set. Monitoring the housing-base fixture could immediately detect any looseness or failure.

The optimal environment for continuation of this research involves collaboration with machine tool designers. Their experience in design and FE modeling is crucial in the effort of implementing a monitoring and diagnosis system based on physical parameter estimation for the next generation of machine tools.

BIBLIOGRAPHY

Aini, R., Rahnejat, H., and Gohar, R., "A Five Degrees of Freedom Analysis of Vibrations in Precision Spindles.", Int. Journal of Machine Tool and Manufacturing, Vol. 30, No. 1, pp. 1-18, 1990.

Akaike, H., " Power Spectrum Estimation through Autoregression Model Fitting.", Ann. Inst. Stat. Math., Vol. 21, pp. 407-419, 1969.

Akaike, H., "A New Look at the Statistical Model Identification.", IEEE Trans. Autom. Control, Vol. AC-19, pp. 716-723, 1974.

Allemag, R. J., Brown, D. L., "A Correlation Coefficient for Modal Vector Analysis.", 1st International Modal Analysis Conference, Orlando, Florida, pp 110-116, 1982.

Ansys, *Ansys* Version V 5.3, Ansys, Inc., Canonsburg, PA, 1997.

Astrom, K. J., Eykhoff, P., "System Identification - A Survey.", Automatica 7, pp 123-162, 1971.

Astrom, K.J., "Maximum Likelihood and Prediction Error Methods.", Automatica 16, pp 551-574, 1980.

Barden, Bearing Catalog C-20, Barden Corporation, Danbury, CT, 1996.

Bendat, J. S., Piersol, A. G., Random Data, Analysis and Measurement Procedures, 2nd. Ed., John Wiley & Sons, New York, 1986.

Bendat, J. S., Piersol, A. G., Engineering Applications of Correlation and Spectral Analysis, John Wiley & Sons, New York, 1986.

Bently & Nevada, Transducer Systems Catalog, Bently & Nevada, Inc., 1992.

Bianchi, G., Paolucci, C. F., Van den Braembusche, P., Van Brussel, H., "Towards Virtual Engineering in Machine Tool Design.", Annals of the CIRP, Vol. 45, No. 1, pp. 381-384, 1996.

Billings, S. A., "Identification of Nonlinear Systems - A Survey.", IEE Proc. D, Vol. 127, pp 272-285, 1980.

Bishop, R. E. D., "The Treatment of Damping Forces in Vibration Theory.", Journal of the Royal Aeronautics Society, Vol 59, p 738, 1955.

Bishop, R. E. D., "The General Theory of Hysteretic Damping.", Aero. Quart., Vol 7, 1956.

Bohlin, T. "A Case Study of Gray Box Identification." Automatica, Vol. 33, pp. 307-318, 1994.

Box, G. E. P., Jenkins, G. M., Time Series Analysis: Forecasting and Control, Holden-Day, San Francisco, 1976.

Brisbine, B., Personal Communications, University of Stuttgart, 1999.

Bruel & Kjaer, User Guide, Bruel & Kjaer, Corp., 1994.

CADSI, *DADS – SIMULINK*, CADSI, Inc., Coralville, IA, 1997.

Carne, T. G. et al., "Finite Element Analysis and Modal Testing of a Rotating Wind Turbine.", International Journal of Analytic and Experimental Modal Analysis, Vol. 3, p 33, 1988.

Chen, B., "Computer-Aided Derivation of State Space Models for Linear Dynamic Systems.", M.S. Thesis, Oregon State University, 1996.

Cheung, Y. K., Leung, A. Y. T., Finite Element Methods in Dynamics, Science Press, Kluwer Academic Publishers, Beijing, 1991.

Chung, Y., "Model Based Adaptive Compensation of Dynamic Characteristics of In-Process Sensors.", Ph.D. Thesis, University of Wisconsin-Madison, 1993.

Comparin, R. J., "The Dynamic Analysis of a Machine Tool Spindle.", M.S. Thesis, Ohio State University, 1983.

Craig, G., John, J., Introduction to Robotics: Mechanics and Control., Addison-Wesley Publishing Company, Inc., 1955.

Dasgupta, S., Anderson, B. D. O., and Kaye, R. I. "Identification of Physical Parameters in Structured Systems." Automatica, Vol. 24, No. 2, pp. 217-225, 1988.

Davis, L., Genetic Algorithms and Simulated Annealing, Morgan Kaufmann Publishers, Los Altos, CA, 1987.

DeCarlo, R. A., Linear Systems, Prentice-Hall, Inc. 1989.

Dietrich, T. G., Personal Communications, CS Department, Oregon State University, 1998.

Dixon, L. C. W., Optimization in Action, Academic Press, London, 1976.

Doeblin, O. E., System Modelling and Response: Theoretical and Experimental Approaches, John Wiley & Sons, New York, 1980.

Dorf, C. D., Bishop, R. H., Modern Control Systems, 7th. Ed., Addison-Wesley, New York, 1995.

Eckert, L., Freund, H., Schilling, "Identification von Strukturmatrizen aus Dynamischen Nachgiebigkeiten.", VDI Bericht 536, pp255-272, 1984.

Ewins, D. J., Modal Testing: Theory and Practice, John Wiley & Sons, Inc., 1984.

Eykhoff, P., System Identification, John Wiley, London, 1974.

Fagan, M. J., Finite Element Analysis: Theory and Practice, Longman Scientific & Technical, Wiley Harlow, Essex, England, 1992.

Franklin G. F., Powell, J. D., Feedback Control of Dynamic Systems, Addison-Wesley, 1994.

Friswell, M.I., Mottershead, J.E.,"Model Updating in Structural Dynamics: A Survey.", J. of Sound and Vibr., 167(2), 1993.

Friswell, M. I., Mottershead, J. E., Finite Model Updating in Structural Mechanics, Kluwer Academic Publishers, Dordrecht, The Netherlands, 1995.

Fritzen, C. P., "Identification of Mass, Damping and Stiffness Matrices of Mechanical Systems.", ASME Journal of Vibrations, Acoustics, Stress and Reliability in Design, Vol. 108, pp 9-16, 1986.

Gelb, A., Applied Optimal Estimation, MIT Press, Cambridge, MA, 1988.

Ginsberg, J. H., Advanced Engineering Dynamics, Cambridge University Press, 1995.

Goodwin, M. J., "Experimental Techniques for Bearing Impedance Measurement.", Journal of Engineering for Industry, Vol. 113, pp. 335-342 1991.

Harris, T.A., Rolling Bearing Analysis, J. Wiley, New York, 1991.

He, J., Ewins, D. J., "Compatability of Measured and Predicted Vibration Modes in Model Improvement Studies.", AIAA Journal, 29(5), 1991.

Hebsacker, M., "Statistische Auslegung und Optionen von Hexaglide-Maschinen.", M.S. Thesis, IWF-ETHZ, 1995

Hewlett Packard, Operator's Guide: Spectrum Analyzer HP 3576A, Palo Alto, CA, 1997.

Hsia, H. C., Identification: Least Square Methods, Lexington Books, Lexington, Mass., 1977.

Imregun, M., Visser, W. J., "A Review of Model Updating Techniques.", Shock and Vibration Digest, Vol 23, pp 9-20, 1991.

Ingber, L., Rosen, B., "Genetic Algorithms and Very Fast Simulated Annealing: A Comparison.", Mathematical and Computer Modeling, Vol. 16, pp 87-100, 1992.

Inman, D. J., Engineering Vibration, Prentice-Hall Inc. New Jersey, 1994.

Isermann, R., Digital Control Systems, Springer-Verlag, New York, 1981.

Isermann, R., "Process Fault Detection Based on Modeling and Estimation Methods – A Survey." Automatica, Vol. 20, No. 4, pp. 387-404, 1984.

Isermann, R., Freyermuth, B., "Process Fault Diagnosis Based on Process Model Knowledge-Part 1: Principles for Fault Diagnosis with Parameter Estimation.", Journal of Dynamic Systems, Measurement, and Control, Vol. 113, pp. 620-626, Dec. 1991.

Isermann, R., Freyermuth, B., "Process Fault Diagnosis Based on Process Model Knowledge-Part 2: Case Study Experiments.", Journal of Dynamic Systems, Measurement, and Control, Vol. 113, pp. 627-633, Dec. 1991.

Isermann, R., "Estimation of Physical Parameters for Dynamic Processes with Application to an Industrial Robot.", International Journal of Control, Vol. 55, No. 6, pp. 1287-1298, 1992.

Jitpraphai, T., "Model Based Visualization of Vibrations in Mechanical Systems.", M.S. Thesis, Oregon State University, 1997.

Jitpraphai, T., Nickel, T., Spiewak, S. A., "'Gray Box' Model Based Visualization of Vibrations in Mechanical Systems.", International Conference on Monitoring and Automatic Supervision in Manufacturing, Warsaw, Poland 1998.

Kalman, R. E., "A New Approach to Linear Filtering.", Trans. ASME j. of Basic Engineering Vol. 82, pp. 35-45, 1960.

Kane, T. R., Likins, P. W., Levinson, D. A., Spacecraft Dynamics., McGraw-Hill, Inc., 1983.

Kistler, Piezo Instrumentation Catalog, Kistler Instrument, Corp., 1995.

Knowledge Revolution, *Working Model 2D*, Knowledge Revolution, Inc., San Mateo, CA, 1997.

Kuo, B. C., Automatic Control Systems, Prentice-Hall, Inc., Englewood Cliffs, New Jersey, 1995.

Lacey, S.J., Wardle, F.P., Poon, S.Y., "High Speed Bearing for CNC Machine Tool Spindles.", Chartered Mechanical Engineering, Vol. 30, No. 12, pp. 51-56, 1983.

Leuridan, J. M., "Direct System Parameter Identification of Mechanical Structures with Application to Modal Analysis.", M. S. Thesis, University of Cincinnati, 1981.

Link, M., "Theory of a Method for Identifying Incomplete System Matrices from Vibration Test Data.", Zeitschrift fuer Flugwissenschaft und Weltraumforschung, Vol. 9, pp 76-82, 1985.

Ljung, L., System Identification: Theory for the User, Prentice-Hall Inc., 1987.

Ljung, L., "System Identification in a MIC Perspective.", Modeling, Identification and Control, Vol. 15, No. 3, pp. 153-159, 1994.

Loehle, A., Global Optimization Software Package, Loehle Enterprises, Naperville, IL, 1998.

MathWorks, *Matlab 4.0*, The Mathworks, Inc., Natick, MA, 1995.

Matsubara, M. et al., "Computational Modeling of Precision Spindles Supported by Ball Bearings.", Int. Journal of Machine Tool and Manufacturing, Vol. 28, No. 4, pp. 429-442, 1988.

Mechanical Dynamics, *Adams* Version 9.01, Mechanical Dynamics, Inc., Ann Arbor, MI, 1997.

Meriam, J. L., Engineering Mechanics Volume 2, Dynamics, John Wiley & Sons, Inc., 1980.

Mitchell, J. S., An Introduction to Machinery Analysis and Monitoring, Pen Well Publishing Co., 1981.

Myklestad, N. O., "The Concept of Complex Damping.", Journal of Applied Mechanics, Vol 19, p 284, 1952.

Nashif, A. D., Jones, D. I., Henderson, J., Vibration Damping, John Wiley & Sons, 1985.

National Instruments, *Lab VIEW® for Windows*, National Instruments, Corp., Austin, TX, 1994.

National Instruments, AT-MIO 16E2 DAQ-card Manual, National Instruments, Corp., Austin, TX, 1995

Natke, H. J., "Updating Computational Models in the Frequency Domain Based on Measured Data: A Survey.", Probablistic Engineering Mechanics, Vol 3, pp 8-35, 1988.

Nickel, T., "Physical Parameter Estimation for Mechanical Systems.", M.S. Thesis, University of Wisconsin-Madison, 1994.

Norton, J. P., An Introduction to Identification, Academic Press, 1986.

Ogata, K., Discrete-Time Control Systems, Prentice-Hall Inc., 1987.

O'Reilly, J., Observers for Linear Systems, Springer-Verlag, London, 1994.

Padgaonkar, A. J., Krieger, K. W., King, A. I., "Measurement of Angular Acceleration of a Rigid Body Using Linear Accelerometers.", Journal of Applied Mechanics, Transactions of the ASME, Vol. 42, pp. 552-556, 1975.

Pandit, S. M., Wu, S. M., Time Series Analysis, System Analysis with Applications, John Wiley & Sons, Inc., 1983.

PCB, Transducer Catalog, PCB, Corp., 1996.

Pinter, J. D., Global Optimization in Action., Kluwer Academic Publishers, Boston, 1996.

Precision, 88 Series, 8 Pole, 8 Zero Programmable Filter Modules, Precision Filters, Inc., 1989.

Press, W.H, Teukolsky, S.A., Vetterling, W.T., Flannery, B.P., Numerical Recipies in C, Cambridge University Press, 1994.

Rake, H., "Step Response and Frequency Response Methods.", Automatica, Vol.16,No.2, pp.519-526, 1980.

Reddy, V. R.. and Sharan, A. M., "The Finite Element Modeled Design of Lathe Spindles: The Static and Dynamic Analysis.", ASME Journal of Vibrations, Acoustics, Stress and Reliability in Design, Vol. 109, pp407-415, 1987.

Schaechter, D. A., Levinson, D. B., "Interactive Computerized Symbolic Dynamics for the Dynamicist.", Jornal of the Astronautical Sciences, Vol. 36, No. 4, pp. 365-388, 1988

Schmitz, E., "Robotic Arm Control.", Ph.D. Thesis, Dept. of Aero / Astro, Stanford University, Stanford, CA, 1985.

Segalman, D. J., Dohrmann, C. R., "A Method for Calculating the Dynamics of Rotating Flexible Structures, Part 1: Derivation.", Journal of Vibrations and Acoustics, Vol. 118, pp 313-317, 1996.

Shabana, A. A., Theory of Vibration, Volume 1: An Introduction., Springer Verlag, London, 1995.

Shin, Y. C., Wang, K. W. and Chen, C. H., "Dynamic Analysis and Modeling of a High Speed Spindle System.", Transactions of NAMRI/SME, pp 298-304, 1990.

Shin, Y. C., Wang, K. W. and Chen, C. H., "An Integrated Approach Toward the Dynamic Analysis of High-Speed Spindles, Part 1: System Model.", Transactions of ASME, Vol. 116, pp 506-513, 1994.

Shyan-Huang, M., "High Speed Model-Based Identification of Dynamic Systems.", Ph.D Thesis, University of Wisconsin-Madison, 1994.

Sony/Tektronix, User Manual, Sony, Corp., 1995.

Spectral Dynamics Research Corp., I-DEAS Model™ , Structural Dynamics Research Corp., 1996.

Spiewak, S.A., Di Corpo, J., "Adaptive Compensation of Dynamic Characteristics for In-Process Sensors.", ASME Journal of Engineering for Industry, Vol 113, pp 198-206, 1991.

Spiewak, S.A., "Acceleration Based Indirect Force Measurement in Metal Cutting Processes.", International Journal of Machine Tools and Manufacturing, Vol.35,No.1, pp.1-17, 1995.

Stark, H., Woods, J. W., Probability, Random Processes, and Estimation Theory for Engineers, Prentice-Hall, Englewood Cliffs, NJ, 1994.

Szafarczyk, C., "Automated Supervision in Manufacturing Systems. Principles, Classification and Terminology.", Proceedings of the 3rd International Conference on Automatic Supervision, Monitoring and Adaptive Control in Manufacturing, pp. 7 – 22, 1990.

Takata, S., Sata, T., Model Referenced Monitoring and Diagnosis – Application to the Manufacturing System, Computers in Industry, 1986.

Techno-Science Inc., TSI Software Package, Techno Science Inc., 1998.

Thomson, W. T., Theory of Vibration with Applications, 2nd ed., Prentice-Hall, Englewood Cliffs, NJ, 1981.

Timoshenko, S., Young, D. H. and Weaver, W., Vibration Problems in Engineering., 4th Ed., John Wiley, New York, 1974.

Tlusty, J., Livingston IV, R., Teng, J.B., "Nonlinearities in Spindle Bearings and their Effects." Annals of the CIRP, Vol. 35, No. 1, pp. 269-273, 1986.

Tosatti, L., Bianchi, G., Fassi, I., Boer, C. R., Jovane, F., "An Integrated Methodology for the Design of Parallel Kinematic Machines (PKM).", Annals of the CIRP, Vol. 47, No. 1, 1998.

Trujillo, D. M., Busby, H. R., Practical Inverse Analysis in Engineering., CRC Press, New York, 1997.

Tu, J.F., "On-line Preload Monitoring for High-speed Anti-friction Spindle Bearings Using Robust State Observers.", Ph.D. Thesis, University of Michigan, 1991.

Unbehauen, H. and Rao, G.P., "Continuous-time Approach to System Identification – A Survey.", Automatica, Vol. 26, No. 1, pp. 84-96, 1990.

Van Brussel H., et. al., "Comparative Assesment of Harmonic, Random, Swept Sine and Shock Excitation Methods for the Identification of Machine Tool Structures with Rotating Spindles.", Annals of CIRP, Vol.24, pp.291-296, 1975.

Verhaegen, M., Chou, C. T., Johansson, R., "Continuous Time Identification of SISI Systems Using Laguerre Functions.", submitted to I.E.E.E. Trans. On Signal Proc., July 1996.

Warnecke, H., Neugebauer, R., Wieland, F., "Development of Hexapod Based Machine Tool.", Annals of the CIRP, Vol. 47, No. 1, 1998.

Waterloo Maple, *Maple*, Version V 5.1, Waterloo Maple, Inc., Waterloo, Ontario, 1997.

Weaver, W. Jr., Johnston, P. R., Structural Dynamics by Finite Elements, Prentice-Hall, Englewood Cliffs, N. J., 1987.

Weck, M., Handbook of Machine Tools, J. Wiley, Chicester, 1984.

Weikert, S., Rehsteiner, F., Brisbine, B., Spiewak, S. A., "Model Based Minimization of Dynamic Tool Path Errors.", Proc. of the 2nd SAE Aerospace Manufacturing Technology Conference, Long Beach, CA, 1998.

Wellstead, P. E., "Non Parametric Methods of System Identification.", Automatica 17, No.1, pp.53-69, 1981.

Willsky, A. S., "A Survey of Design Methods for Failure Detection in Dynamic Systems.", Automatica, Vol. 12, pp 601-611, 1976.

Wolfram Research, *Mathematica*, Wolfram Research, Inc., 1991.

Wolfram, S., Mathematica – A System for Doing Mathematics by Computer, Addison – Wesley, Redwood City, CA, 1991.

Wolfram Research, *Mathematica – Controls Professional Tool Box*, Wolfram Research, Inc., 1992.

Wong, K. Y., Polak, E., "Identification of Linear Discrete System Using the Instrumental Variable Approach.", Institution of Electronic and Electrical Engineers, Vol. AC-12, pp 707-718, 1967.

Young, P. C., "An Instrumental Variable Method for Real-Time Identification of Noisy Processes.", Automatica, Vol. 6, pp 271-287, 1970.

Young, P.C., "Parameter Estimation for Continuous-time Models – A Survey.", Automatica, Vol. 17, pp. 23-39, 1981.

Young, P. C., Recursive Estimation and Time-Series Analysis, Springer Verlag, 1984.

Zhang, J. H., Natke, H. G., "A two-level updating procedure of the component mode synthesis model.", Mechanical Systems in Signal Processing, Vol. 5, pp. 501-514, 1991.

Ziaei-Rad, S., Imregun, M., "On the Accuracy Required of Experimental Data for Finite Element Model Updating.", J. of Sound and Vibr., 196(3), pp 323-336, 1996.

Ziegler, J.G., Nichols, N.B., "Optimum Settings for Automatic Controllers.", Trans. ASME, Vol. 64 pp.759-768, 1942.

APPENDICES

Appendix A: Matrix Calculations

A1: Transformation Matrices

The derivation of the transformation matrices $\mathbf{TM_{rx}}$, $\mathbf{TM_{ry}}$ and $\mathbf{TM_{rz}}$ for rotation φ, ϕ and ψ around the x, y and z-axis respectively can be found in Craig, (1955). They are shown below:

$$\mathbf{TM}_{\mathrm{rx}}(\varphi,t)=\begin{bmatrix}1 & 0 & 0 & 0\\ 0 & \cos\varphi(t) & -\sin\varphi(t) & 0\\ 0 & \sin\varphi(t) & \cos\varphi(t) & 0\\ 0 & 0 & 0 & 1\end{bmatrix} \tag{A1}$$

$$\mathbf{TM}_{\mathrm{ry}}(\phi,t)=\begin{bmatrix}\cos\phi(t) & 0 & \sin\phi(t) & 0\\ 0 & 1 & 0 & 0\\ -\sin\phi(t) & 0 & \cos\phi(t) & 0\\ 0 & 0 & 0 & 1\end{bmatrix} \tag{A2}$$

$$\mathbf{TM}_{\mathrm{rz}}(\psi,t)=\begin{bmatrix}\cos\psi(t) & -\sin\psi(t) & 0 & 0\\ \sin\psi(t) & \cos\psi(t) & 0 & 0\\ 0 & 0 & 1 & 0\\ 0 & 0 & 0 & 1\end{bmatrix} \tag{A3}$$

The matrix for translational transformation $\mathbf{TM_t}$ is

$$\mathbf{TM}_{\mathrm{t}}(x,y,z,t)=\begin{bmatrix}1 & 0 & 0 & x(t)\\ 0 & 1 & 0 & y(t)\\ 0 & 0 & 1 & z(t)\\ 0 & 0 & 0 & 1\end{bmatrix} \tag{A4}$$

The transformation matrix of the individual rigid bodies can be calculated through the combination of Eq. (A1) to (A4). The transformation matrix for the general motion of the spindle is a combination of the matrices $\mathbf{TM_{rx}}$, $\mathbf{TM_{rz}}$ and $\mathbf{TM_t}$. The matrix $\mathbf{TM_{rz}}$ is not included, since the spindle can rotate freely around the z-axis. The subscripts

"*s*" and "*h*" in the following matrices express that these general coordinates belong to the spindle and housing respectively.

$$\mathbf{TM}_S = \mathbf{TM}_t(x_s, y_s, z_s, t) \cdot \mathbf{TM}_{rx}(\varphi_s, t) \cdot \mathbf{TM}_{ry}(\phi_s, t) \tag{A5}$$

The simplified (for small angles) spindle transformation matrix calculates to

$$\mathbf{TM_S} = \begin{bmatrix} 1 & 0 & \phi_s(t) & x_s(t) \\ 0 & 1 & -\varphi_s(t) & y_s(t) \\ -\phi_s(t) & \varphi_s(t) & 1 & z_s(t) \\ 0 & 0 & 0 & 1 \end{bmatrix} \tag{A6}$$

The housing transformation matrix can be calculated through

$$\mathbf{TM_H} = \mathbf{TM}_t(x_h, y_h, z_h, t) \cdot \mathbf{TM}_{rx}(\varphi_h, t) \cdot \mathbf{TM}_{ry}(\phi_h, t) \cdot \mathbf{TM}_{rz}(\psi_h, t) \tag{A7}$$

The simplified (for small angles) housing transformation matrix equates to

$$\mathbf{TM_H} = \begin{bmatrix} 1 & -\psi_h(t) & \phi_h(t) & x_h(t) \\ \psi_h(t) & 1 & -\varphi_h(t) & y_h(t) \\ -\phi_h(t) & \varphi_h(t) & 1 & z_h(t) \\ 0 & 0 & 0 & 1 \end{bmatrix} \tag{A8}$$

A2: Inversion of Large Matrices

The derivation of models for machine tools like the ones presented in Section 3.2 involves dealing with high dimensioned matrices. For example, the model of the spindle-bearing system described above has 11 degrees-of-freedom. In the state space model derivation the dimension of the system matrix **A** is always twice the number of degrees-of-freedom (see Section 3.2.2). Therefore the size of the **A** matrix for the spindle model is *22x22*. When dealing with these kinds of large matrices, it is necessary to use all the mathematical 'tricks' in order to simplify them and to avoid lengthy, unnecessary computer calculations. Consider a matrix multiplication of two *22x22* matrices. More than 20,000 additions and multiplications are needed for such an operation.

In order to derive a transfer function from the **A**, **B** and **C** matrices of the state space formulation, it is necessary to compute the inverse of a matrix of the form (*s* **I** - **A**). If it is intended to use this model for the purpose of physical parameter estimation then the **A** matrix will not be numerical, but will have up to 50 symbolic variables in it. Investigations done here showed that a PC with a Pentium 150 *MHz* processor is not capable of inverting a matrix of that size symbolically in a reasonable amount of time. Fortunately, there are mathematical tools to simplify such large matrices. Using the matrix inversion lemma (Ogata, 1987) one can simplify the inversion of a large matrix as follows:

If the matrices **A**, **B**, **C** and **D** are, respectively, an *n* x *n*, an *n* x *m*, an *m* x *n*, and an *m* x *m* matrix, then

$$\begin{bmatrix} \mathbf{A} & \mathbf{B} \\ \mathbf{C} & \mathbf{D} \end{bmatrix}^{-1} = \begin{bmatrix} \left(\mathbf{A}-\mathbf{B}\mathbf{D}^{-1}\mathbf{C}\right)^{-1} & -\left(\mathbf{A}-\mathbf{B}\mathbf{D}^{-1}\mathbf{C}\right)^{-1}\mathbf{B}\mathbf{D}^{-1} \\ -\mathbf{D}^{-1}\mathbf{C}\left(\mathbf{A}-\mathbf{B}\mathbf{D}^{-1}\mathbf{C}\right)^{-1} & \mathbf{D}^{-1}\mathbf{C}\left(\mathbf{A}-\mathbf{B}\mathbf{D}^{-1}\mathbf{C}\right)^{-1}\mathbf{B}\mathbf{D}^{-1}+\mathbf{D}^{-1} \end{bmatrix} \tag{A9}$$

provided $|\mathbf{D}| \neq 0$ and $\left|\mathbf{A}-\mathbf{B}\mathbf{D}^{-1}\mathbf{C}\right| \neq 0$. The matrix (*s* **I** - **A**) therefore can be inverted using Eq. (A9). If the *22x22* matrix to be inverted is reduced in this manner to an *11x11* matrix, and the computation will be much easier and faster. For larger matrices this lemma can be applied several times consecutively, and thus the dimension reduced considerably.

A3: Pseudo-Inverse of Matrices

The concept of pseudo-inverses of a matrix is a generalization of the notion of an inverse. Consider the vector-matrix equation

$$\mathbf{A}\ \mathbf{x} = \mathbf{b} \tag{A10}$$

where **A** is an n x *m* matrix, **x** is an *m*-vector and **b** is an *n*-vector. Depending on whether $m > n$ or $m < n$, the concept of right pseudo-inverse or left pseudo-inverse can

be introduced to find the minimum norm solution x^o that satisfies the condition $\mathbf{A}\ \mathbf{x}^o = \mathbf{b}$ and $\|\mathbf{x}^o\| \leq \|\mathbf{x}\|$ for all x that satisfy $\mathbf{A}\ \mathbf{x} = \mathbf{b}$.

If **A** has the Rank *m*, then the solution is

$$\mathbf{x}^o = \mathbf{A}^{\mathbf{RM}}\mathbf{b} \tag{A11}$$

where $\mathbf{A}^{\mathbf{RM}}$ is the right pseudo-inverse and is calculated as

$$\mathbf{A}^{\mathbf{RM}} = \mathbf{A}^{\mathbf{T}}\left(\mathbf{A}\mathbf{A}^{\mathbf{T}}\right)^{-1} \tag{A12}$$

If **A** has the Rank *n*, then the solution is

$$\mathbf{x}^o = \mathbf{A}^{\mathbf{LM}}\mathbf{b} \tag{A13}$$

where $\mathbf{A}^{\mathbf{LM}}$ is the left pseudo-inverse and is calculated as

$$\mathbf{A}^{\mathbf{LM}} = \left(\mathbf{A}^{\mathbf{T}}\mathbf{A}\right)^{-1}\mathbf{A}^{\mathbf{T}} \tag{A14}$$

The detailed mathematical proof can be found in Ogata (1987).

Appendix B: Additional Information about the simple MDOF System

B1: Geometric Dimensions

Table B1: Geometric Dimensions of the simple MDOF System.

Geometric Dimension	Numerical Value
Mass 1: width w_{m1}, [mm]	38.0
height h_{m1}, [mm]	38.0
length l_{m1}, [mm]	101.0
Mass 2: width w_{m2}, [mm]	31.5
height h_{m2}, [mm]	38.0
length l_{m2}, [mm]	101.0
I- beam 1: width w_{beam1}, [mm]	12.5
height h_{beam1}, [mm]	38.0
length l_{beam1}, [mm]	127.5
I-beam 2: width w_{beam2}, [mm]	6.0
height h_{beam2}, [mm]	38.0
length l_{beam2}, [mm]	139.0
Helical spring: No. of turns n_{hs}	5
Diameter of steel wire d_{sw}, [mm]	4.5
Radius of total spring r_{hs}, [mm]	13.2
Distance between the two masses l_{m1m2}, [mm]	60.0

The area moments of inertia of the two I-beams are:

$$I_{beam1} = \frac{h_{beam1} \cdot w_{beam1}^{3}}{12} \tag{B1}$$

$$I_{beam2} = \frac{h_{beam2} \cdot w_{beam2}^{3}}{12} \tag{B2}$$

B2: Signal Change for Additional Mass

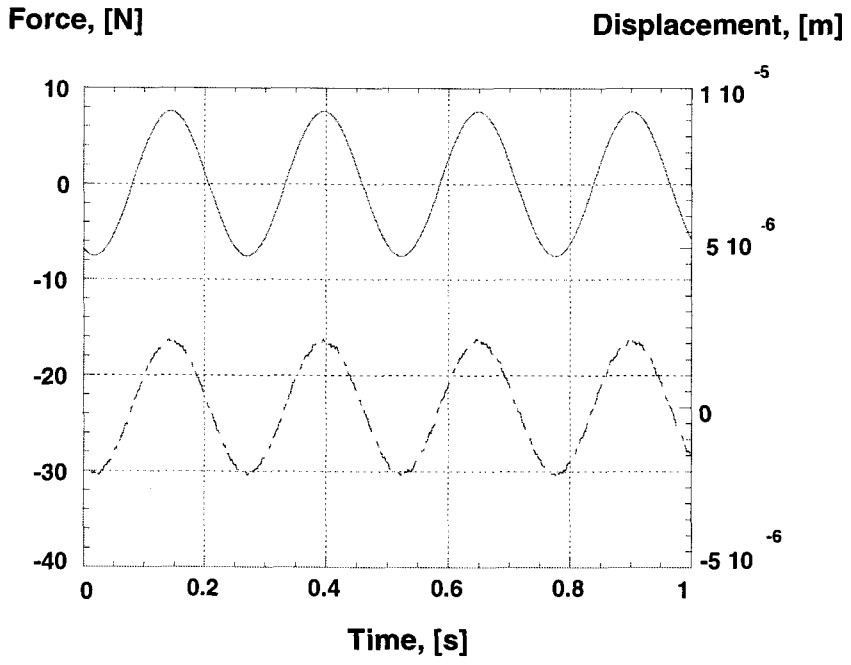

Fig. B1: Force and proximity signal on *Mass_2* with additional mass for low frequency sine wave excitation.

Transfer function analysis and physical parameter estimation was also done on simple MDOF system modified through attachment of an additional mass of 0.75 *kg* on *Mass_1*. Graphical results are presented below:

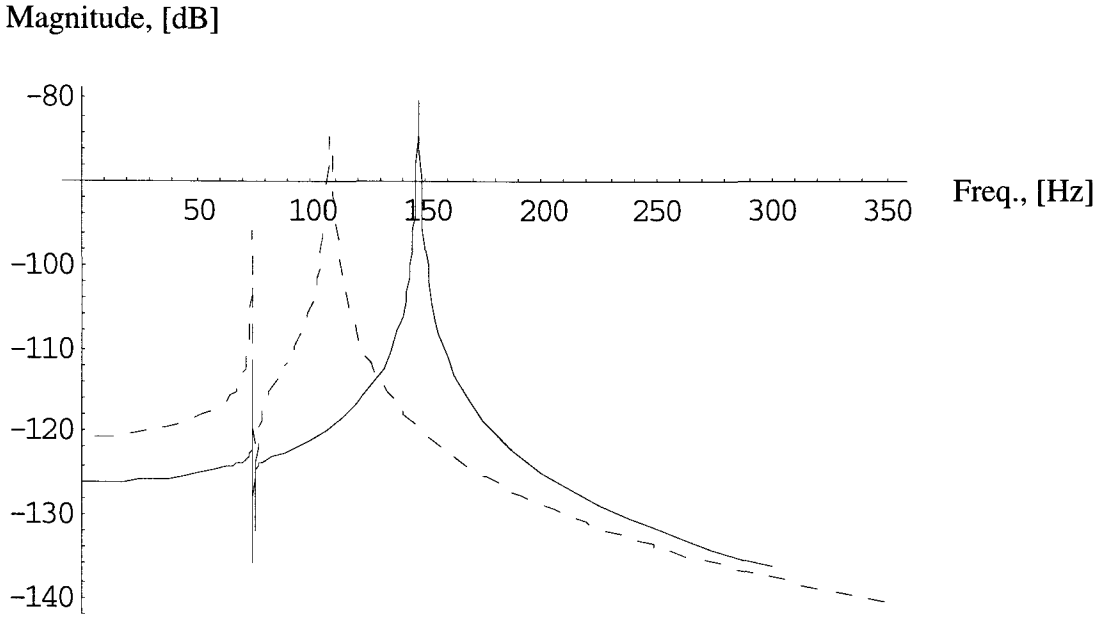

Fig. B2: Experimental (dashed) and model (solid) magnitude plot of G_{11} in *m/N* before minimization (large mass).

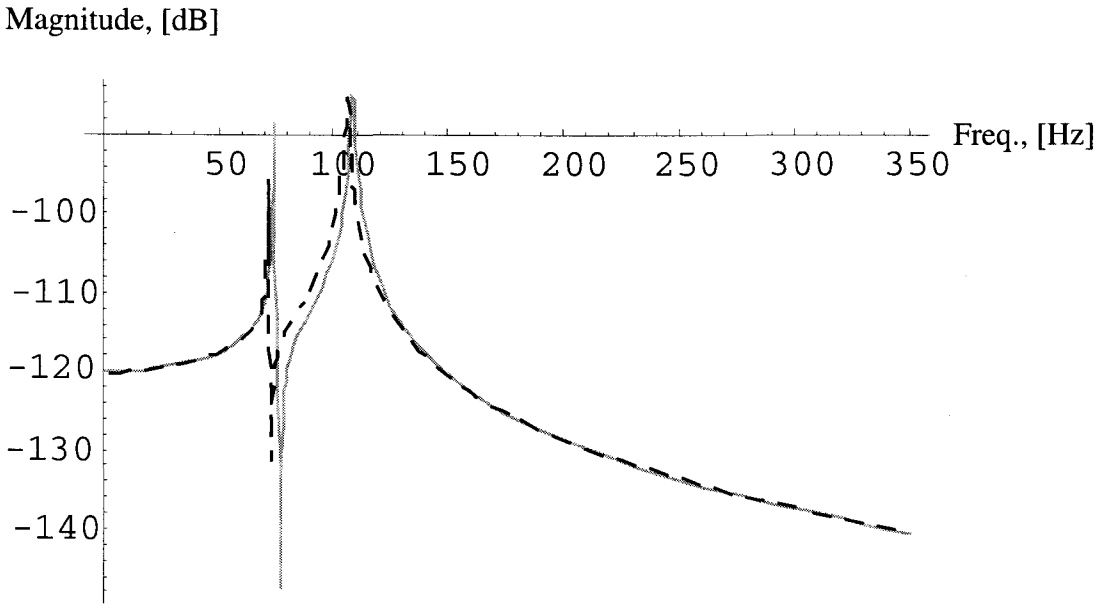

Fig. B3: Experimental (dashed) and model (solid) magnitude plot of G_{11} in *m/N* after minimization (large mass).

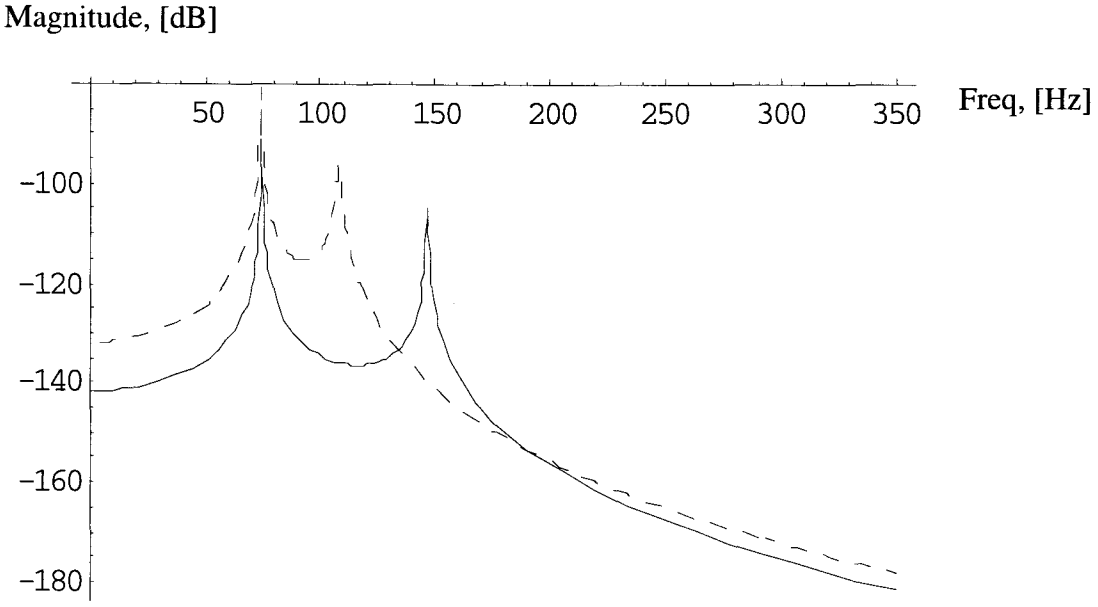

Fig. B4: Experimental (dashed) and model (solid) magnitude plot of G_{21} in *m/N* before minimization (large mass).

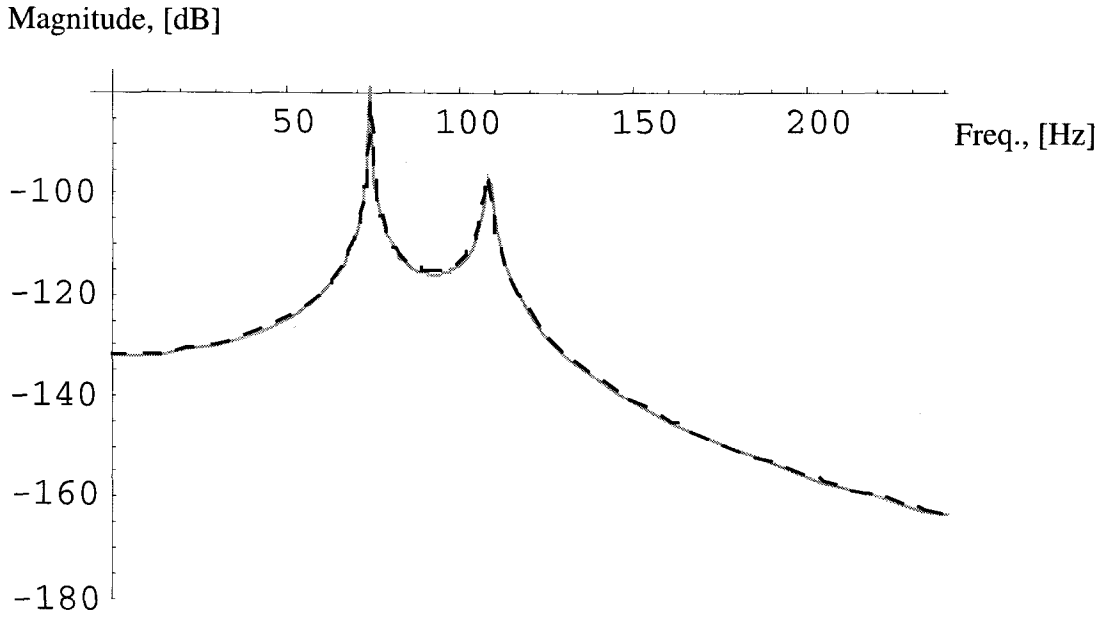

Fig. B5: Experimental (dashed) and model (solid) magnitude plot of G_{21} in *m/N* after minimization (large mass).

B3: Stiffness Calculation for Helical Spring

From the transfer function G_{11} and G_{21}, Eq's (5.7) and (5.10) the DC-gain can be calculated by setting $s = 0$ as done in Eq. (5.12). If the gain is determined experimentally as shown in Table 5.2, then k_{12} can be determined.

From Eq. (5.12a):

$$k_{12} = \frac{k_{22} - g_{11} \cdot k_{11} \cdot k_{22}}{g_{11} \cdot k_{11} + g_{11} \cdot k_{22} - 1} \tag{B3}$$

From Eq. (5.12b):

$$k_{12} = \frac{g_{21} \cdot k_{11} \cdot k_{22}}{1 - g_{21} \cdot k_{11} - g_{11} \cdot k_{22}} \tag{B4}$$

B4: Damping Calculation Using the Log-Decrement Method

The logarithmic decrement method is the simplest and most frequently used technique to experimentally determine the damping coefficients since equipment and instrumentation requirements are minimal. In this technique the free vibration of a single DOF system can be initiated and the ratio between successive or non-successive displacement amplitudes can be measured. From which the logarithmic decrement δ can be defined as (Shabana, 1995)

$$\delta = \frac{1}{n} \ln\left(\frac{x_i}{x_{i+n}}\right) \tag{B5}$$

where x_i and x_{i+n} are two displacement amplitudes n cycles apart. Once δ has been determined, the damping factor ξ can be determined according to

$$\xi = \frac{\delta}{\sqrt{(2\pi)^2 + \delta^2}} \tag{B6}$$

The equivalent viscous damping coefficient c can then be determined as

$$c = 2\xi\, m\omega \tag{B7}$$

where m is the mass and ω the natural frequency of the system. Results from impact tests, which were used for the damping calculations of the two masses are shown below.

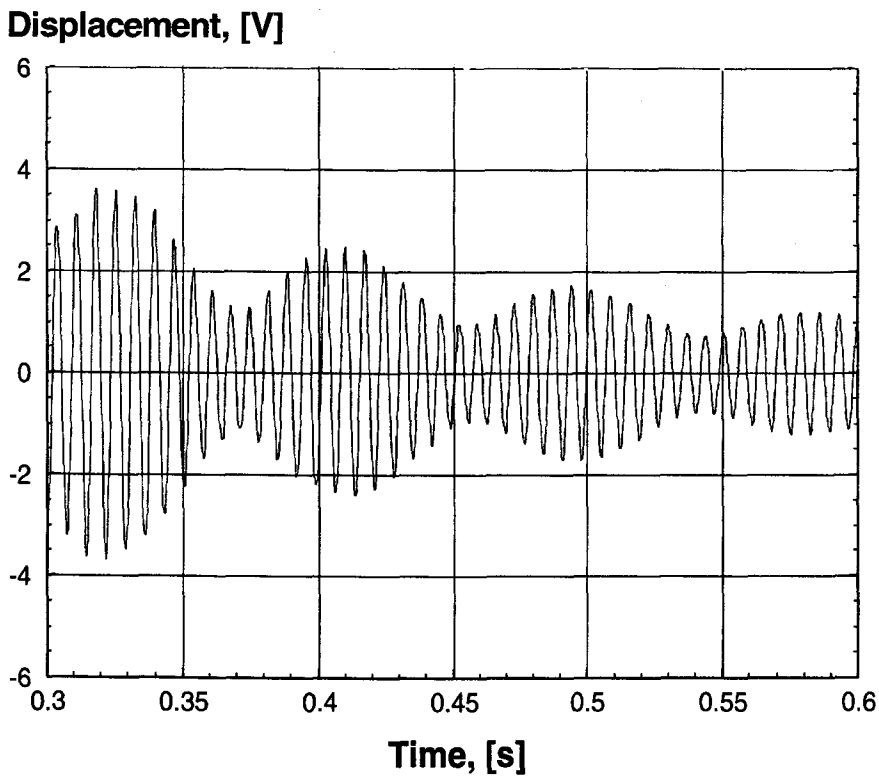

Fig. B6: Impact test result from *Mass_1*.

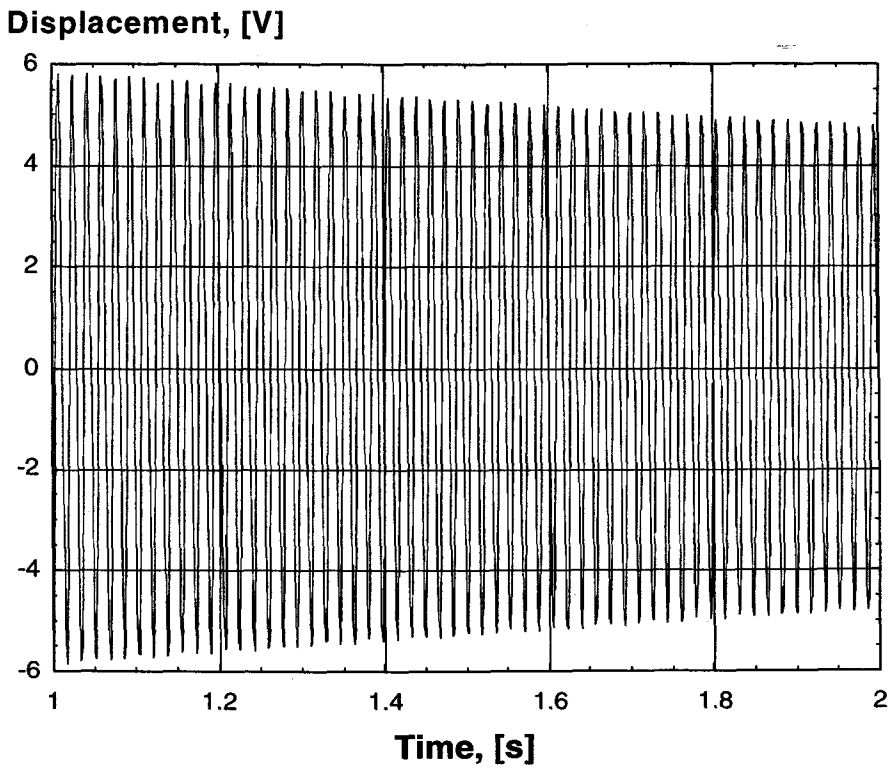

Fig. B7: Impact test result from *Mass_2*.

Appendix C: Additional Information about the Spindle-Bearing System

C1: Geometric Dimensions

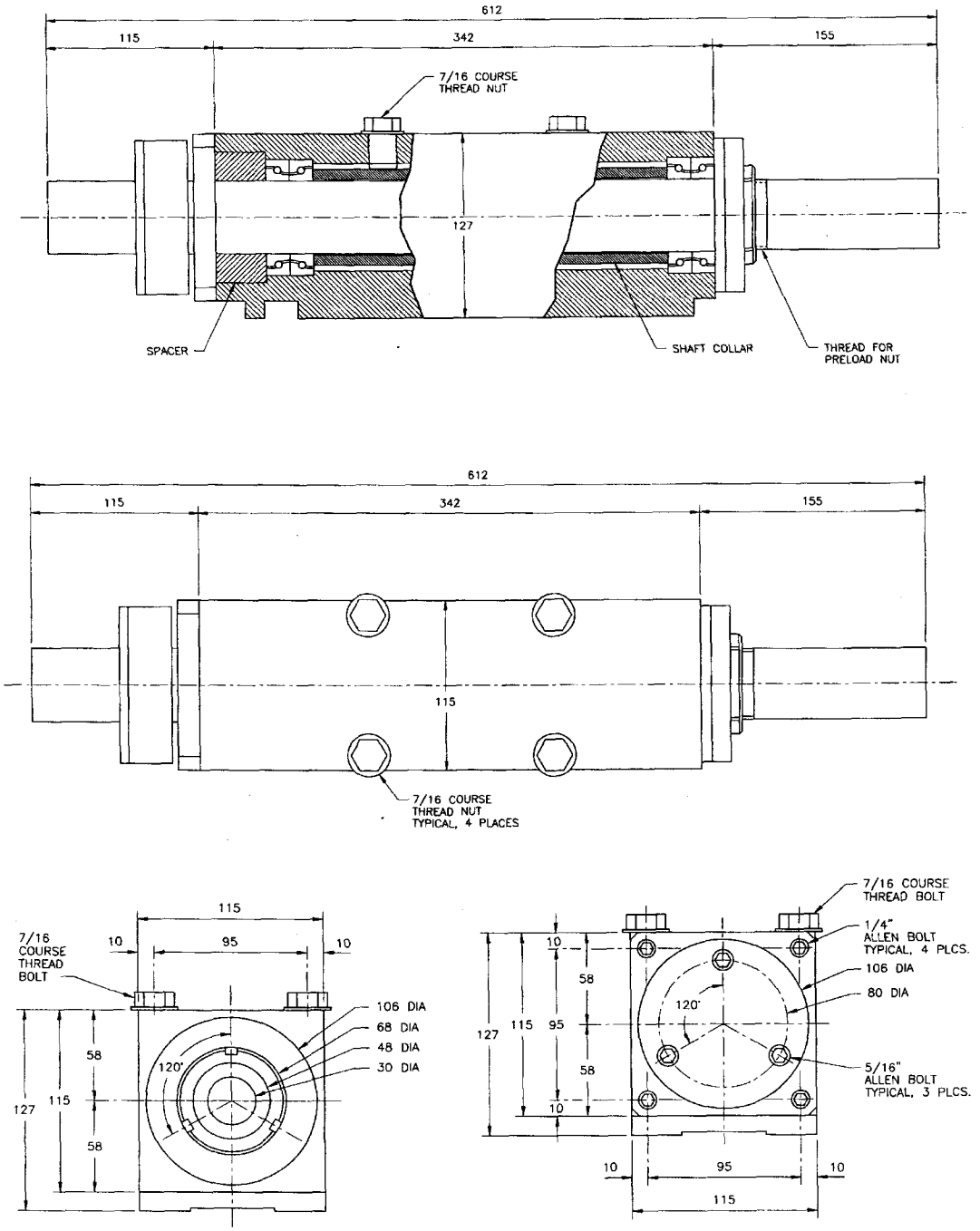

Fig. C1: Technical drawing of the spindle assembly.

C2: Initial Position Vectors

a) Bearing Vectors (spindle side)

$$\mathbf{M_{SB,0}} = \begin{bmatrix} \mathbf{P_{Sfx}} & \mathbf{P_{Sfy}} & \mathbf{P_{Sfz}} & \mathbf{P_{Srx}} & \mathbf{P_{Sry}} \end{bmatrix} = \begin{bmatrix} -x_{sb0} & 0 & 0 & -x_{sb0} & 0 \\ 0 & -y_{sb0} & 0 & 0 & -y_{sb0} \\ z_{sb0} & z_{sb0} & z_{sb0} & -z_{sb2} & -z_{sb2} \\ 1 & 1 & 1 & 1 & 1 \end{bmatrix} \tag{C1}$$

$$\mathbf{M_{SB,0}} = \begin{bmatrix} -0.025 & 0 & 0 & -0.025 & 0 \\ 0 & -0.025 & 0 & 0 & -0.025 \\ 0.127 & 0.127 & 0.127 & -0.162 & -0.162 \\ 1 & 1 & 1 & 1 & 1 \end{bmatrix} \tag{C2}$$

b) Bearing Vectors (housing side)

$$\mathbf{M_{HB,0}} = \begin{bmatrix} \mathbf{P_{Hfx}} & \mathbf{P_{Hfy}} & \mathbf{P_{Hfz}} & \mathbf{P_{Hrx}} & \mathbf{P_{Hry}} \end{bmatrix} = \begin{bmatrix} -x_{hb0} & 0 & 0 & -x_{hb0} & 0 \\ 0 & -y_{hb0} & 0 & 0 & -y_{hb0} \\ z_{sb0} & z_{sb0} & z_{sb1} & -z_{sb2} & -z_{sb2} \\ 1 & 1 & 1 & 1 & 1 \end{bmatrix} \tag{C3}$$

$$\mathbf{M_{HB,0}} = \begin{bmatrix} -0.04 & 0 & 0 & -0.04 & 0 \\ 0 & -0.04 & 0 & 0 & -0.04 \\ 0.127 & 0.127 & 0.2 & -0.162 & -0.162 \\ 1 & 1 & 1 & 1 & 1 \end{bmatrix} \tag{C4}$$

c) Housing-Base Vectors (housing side):

$$\mathbf{M_{H,0}} = \begin{bmatrix} \mathbf{P_{h1}} & \mathbf{P_{h2}} & \mathbf{P_{h3}} & \mathbf{P_{h4}} \end{bmatrix} = \begin{bmatrix} -x_{h0} & x_{h0} & -x_{h0} & x_{h0} \\ -y_{h0} & -y_{h0} & -y_{h0} & -y_{h0} \\ z_{h0} & z_{h0} & -z_{h0} & -z_{h0} \\ 1 & 1 & 1 & 1 \end{bmatrix} \tag{C5}$$

$$\mathbf{M}_{\mathbf{H,0}} = \begin{bmatrix} -0.048 & 0.048 & -0.048 & 0.048 \\ -0.064 & -0.064 & -0.064 & -0.064 \\ 0.06 & 0.06 & -0.06 & -0.06 \\ 1 & 1 & 1 & 1 \end{bmatrix} \tag{C6}$$

d) Housing-Base Vectors (Base side):

$$\mathbf{M}_{\mathbf{B,0}} = \begin{bmatrix} \mathbf{P}_{\mathbf{b1}} & \mathbf{P}_{\mathbf{b2}} & \mathbf{P}_{\mathbf{b3}} & \mathbf{P}_{\mathbf{b4}} \end{bmatrix} = \begin{bmatrix} -x_{h0} & x_{h0} & -x_{h0} & x_{h0} \\ -y_{b0} & -y_{b0} & -y_{b0} & -y_{b0} \\ z_{h0} & z_{h0} & -z_{h0} & -z_{h0} \\ 1 & 1 & 1 & 1 \end{bmatrix} \tag{C7}$$

$$\mathbf{M}_{\mathbf{B,0}} = \begin{bmatrix} -0.048 & 0.048 & -0.048 & 0.048 \\ -0.08 & -0.08 & -0.08 & -0.08 \\ 0.06 & 0.06 & -0.06 & -0.06 \\ 1 & 1 & 1 & 1 \end{bmatrix} \tag{C8}$$

C3: Spindle Arrangement m, c, and k Matrices

$$\mathbf{m}=\begin{bmatrix} m_S & 0 & 0 & 0 & 0 & 0 & 0 & 0 & 0 & 0 & 0 \\ 0 & m_S & 0 & 0 & 0 & 0 & 0 & 0 & 0 & 0 & 0 \\ 0 & 0 & m_S & 0 & 0 & 0 & 0 & 0 & 0 & 0 & 0 \\ 0 & 0 & 0 & m_h & 0 & 0 & 0 & 0 & 0 & 0 & 0 \\ 0 & 0 & 0 & 0 & m_h & 0 & 0 & 0 & 0 & 0 & 0 \\ 0 & 0 & 0 & 0 & 0 & m_h & 0 & 0 & 0 & 0 & 0 \\ 0 & 0 & 0 & 0 & 0 & 0 & J_{Sxx} & -J_{Sxy} & 0 & 0 & 0 \\ 0 & 0 & 0 & 0 & 0 & 0 & -J_{Sxy} & J_{Syy} & 0 & 0 & 0 \\ 0 & 0 & 0 & 0 & 0 & 0 & 0 & 0 & J_{hxx} & -J_{hxy} & -J_{hxz} \\ 0 & 0 & 0 & 0 & 0 & 0 & 0 & 0 & -J_{hxy} & J_{hyy} & -J_{hyz} \\ 0 & 0 & 0 & 0 & 0 & 0 & 0 & 0 & -J_{hxz} & -J_{hyz} & J_{hzz} \end{bmatrix} \tag{C9}$$

If one assumes the housing and spindle being symmetric, then all the off-diagonal elements of matrix **m** become zero.

Due to the large size of the **k** matrix it is split up here as follows

$$\mathbf{k}=[\mathbf{k}_1 \quad \mathbf{k}_2 \quad \mathbf{k}_3] \tag{C10}$$

where $\mathbf{k}_1$, $\mathbf{k}_2$ and $\mathbf{k}_3$ are as shown below.

$$\mathbf{k}_1 = \begin{bmatrix} 2\ k_{FX} & 0 & 0 & -2\ k_{FX} \\ 0 & 2\ k_{FY} & 0 & 0 \\ 0 & 0 & k_{FZ} & 0 \\ -2\ k_{FX} & 0 & 0 & 4\ k_{H1X} + 2\ k_{FX} \\ 0 & -2\ k_{FY} & 0 & 0 \\ 0 & 0 & -k_{FZ} & 0 \\ 0 & -k_{FY} \cdot z_{sb0} + k_{FY} \cdot z_{sb2} & 0 & 0 \\ k_{FX} \cdot z_{sb0} - k_{FX} \cdot z_{sb2} & 0 & 0 & -k_{FX} \cdot z_{sb0} + k_{FX} \cdot z_{sb2} \\ 0 & k_{FY} \cdot z_{sb0} - k_{FY} \cdot z_{sb2} & 0 & 0 \\ -k_{FX} \cdot z_{sb0} + k_{FX} \cdot z_{sb2} & 0 & 0 & k_{FX} \cdot z_{sb0} - k_{FX} \cdot z_{sb2} \\ 0 & 0 & 0 & 4\ k_{H1X} \cdot y_{h0} \end{bmatrix} \tag{C11}$$

$$\mathbf{k}_2 = \begin{bmatrix} 0 & 0 & 0 & -k_{FX} \cdot z_{sb0} + k_{FX} \cdot z_{sb2} \\ -2\ k_{FY} & 0 & -k_{FY} \cdot z_{sb0} + k_{FY} \cdot z_{sb2} & 0 \\ 0 & -k_{FZ} & 0 & 0 \\ 0 & 0 & 0 & k_{FX} \cdot z_{sb0} - k_{FX} \cdot z_{sb2} \\ 4\ k_{H1Y} + 2\ k_{FY} & 0 & k_{FY} \cdot z_{sb0} - k_{FY} \cdot z_{sb2} & 0 \\ 0 & k_{FZ} + 4\ k_{H1Z} & 0 & 0 \\ k_{FY} \cdot z_{sb0} - k_{FY} \cdot z_{sb2} & 0 & k_{FY} \cdot z_{sb0}^{\ 2} + k_{FY} \cdot z_{sb2}^{\ 2} & 0 \\ 0 & 0 & 0 & k_{FX} \cdot z_{sb0}^{\ 2} + k_{FX} \cdot z_{sb2}^{\ 2} \\ -k_{FY} \cdot z_{sb0} + k_{FY} \cdot z_{sb2} & -4\ k_{H1Z} \cdot y_{h0} & -k_{FY} \cdot z_{sb0}^{\ 2} - k_{FY} \cdot z_{sb2}^{\ 2} & 0 \\ 0 & 0 & 0 & -k_{FX} \cdot z_{sb0}^{\ 2} - k_{FX} \cdot z_{sb2}^{\ 2} \\ 0 & 0 & 0 & 0 \end{bmatrix} \tag{C12}$$

$$\mathbf{k}_3 = \begin{bmatrix} 0 & k_{FX}\cdot z_{sb01} - k_{FX}\cdot z_{sb2} & 0 \\ k_{FY}\cdot z_{sb01} - k_{FY}\cdot z_{sb2} & 0 & 0 \\ 0 & 0 & 0 \\ 0 & -k_{FX}\cdot z_{sb01} + k_{FX}\cdot z_{sb2} & 4\ k_{H1X}\cdot y_{h0} \\ -k_{FY}\cdot z_{sb01} + k_{FY}\cdot z_{sb2} & 0 & 0 \\ -4\ k_{H1Z}\cdot y_{h0} & 0 & 0 \\ -k_{FY}\cdot z_{sb0}{}^2 - k_{FY}\cdot z_{sb2}{}^2 & 0 & 0 \\ 0 & -k_{FX}\cdot z_{sb01}{}^2 - k_{FX}\cdot z_{sb2}{}^2 & 0 \\ 4\ k_{H1Z}\cdot y_{h0}{}^2 + 2\ k_{H1Y}\cdot z_{h0}{}^2 + 2\ k_{FY}\cdot z_{sb0}{}^2 + 2\ k_{FY}\cdot z_{sb2}{}^2 & 0 & 0 \\ 0 & 4\ k_{H1Z}\cdot x_{h0}{}^2 + 4\ k_{H1X}\cdot z_{h0}{}^2 + k_{FX}\cdot z_{sb0}{}^2 + 2\ k_{FX}\cdot z_{sb2}{}^2 & 0 \\ 0 & 0 & 4\ k_{H1Y}\cdot x_{h0}{}^2 + 4\ k_{H1X}\cdot y_{h0}{}^2 \end{bmatrix} \tag{C13}$$

Similarly, due to the large size of the **c** matrix it is split up here as follows

$$\mathbf{c} = [\mathbf{c}_1 \quad \mathbf{c}_2 \quad \mathbf{c}_3] \tag{C14}$$

where $\mathbf{c}_1$, $\mathbf{c}_2$ and $\mathbf{c}_3$ are as shown below.

$$\mathbf{c_1} = \begin{bmatrix} 2\ c_{FX} & 0 & 0 & -2\ c_{FX} \\ 0 & 2\ c_{FY} & 0 & 0 \\ 0 & 0 & c_{FZ} & 0 \\ -2\ c_{FX} & 0 & 0 & 4\ c_{H1X} + 2\ c_{FX} \\ 0 & -2\ c_{FY} & 0 & 0 \\ 0 & 0 & -c_{FZ} & 0 \\ 0 & -c_{FY} \cdot z_{sb0} + c_{FY} \cdot z_{sb2} & 0 & 0 \\ c_{FX} \cdot z_{sb0} - c_{FX} \cdot z_{sb2} & 0 & 0 & -c_{FX} \cdot z_{sb0} + c_{FX} \cdot z_{sb2} \\ 0 & c_{FY} \cdot z_{sb0} - c_{FY} \cdot z_{sb2} & 0 & 0 \\ -c_{FX} \cdot z_{sb0} + c_{FX} \cdot z_{sb2} & 0 & 0 & c_{FX} \cdot z_{sb0} - c_{FX} \cdot z_{sb2} \\ 0 & 0 & 0 & 4\ c_{H1X} \cdot y_{h0} \end{bmatrix} \tag{C15}$$

$$\mathbf{c_2} = \begin{bmatrix} 0 & 0 & 0 & -c_{FX} \cdot z_{sb0} + c_{FX} \cdot z_{sb2} \\ -2\ c_{FY} & 0 & -c_{FY} \cdot z_{sb0} + c_{FY} \cdot z_{sb2} & 0 \\ 0 & -c_{FZ} & 0 & 0 \\ 0 & 0 & 0 & c_{FX} \cdot z_{sb0} - c_{FX} \cdot z_{sb2} \\ 4\ c_{H1Y} + 2\ c_{FY} & 0 & c_{FY} \cdot z_{sb0} - c_{FY} \cdot z_{sb2} & 0 \\ 0 & c_{FZ} + 4\ c_{H1Z} & 0 & 0 \\ c_{FY} \cdot z_{sb0} - c_{FY} \cdot z_{sb2} & 0 & c_{FY} \cdot z_{sb0}^{\ 2} + c_{FY} \cdot z_{sb2}^{\ 2} & -2\ J_{Szz} \cdot n_{Sp} \cdot \pi \\ 0 & 0 & -2\ J_{Szz} \cdot n_{Sp} \cdot \pi & c_{FX} \cdot z_{sb0}^{\ 2} + c_{FX} \cdot z_{sb2}^{\ 2} \\ -c_{FY} \cdot z_{sb0} + c_{FY} \cdot z_{sb2} & -4\ c_{H1Z} \cdot y_{h0} & -c_{FY} \cdot z_{sb0}^{\ 2} - c_{FY} \cdot z_{sb2}^{\ 2} & 0 \\ 0 & 0 & 0 & -c_{FX} \cdot z_{sb0}^{\ 2} - c_{FX} \cdot z_{sb2}^{\ 2} \\ 0 & 0 & 0 & 0 \end{bmatrix} \tag{C16}$$

$$\mathbf{c}_3 = \begin{bmatrix} 0 & c_{FX} \cdot z_{sb01} - c_{FX} \cdot z_{sb2} & 0 \\ c_{FY} \cdot z_{sb01} - c_{FY} \cdot z_{sb2} & 0 & 0 \\ 0 & 0 & 0 \\ 0 & -c_{FX} \cdot z_{sb01} + c_{FX} \cdot z_{sb2} & 4\ c_{H1X} \cdot y_{h0} \\ -c_{FY} \cdot z_{sb01} + c_{FY} \cdot z_{sb2} & 0 & 0 \\ -4\ c_{H1Z} \cdot y_{h0} & 0 & 0 \\ -c_{FY} \cdot z_{sb0}{}^2 - c_{FY} \cdot z_{sb2}{}^2 & 0 & 0 \\ 0 & -c_{FX} \cdot z_{sb01}{}^2 - c_{FX} \cdot z_{sb2}{}^2 & 0 \\ 4\ c_{H1Z} \cdot y_{h0}{}^2 + 2\ c_{H1Y} \cdot z_{h0}{}^2 + 2\ c_{FY} \cdot z_{sb0}{}^2 + 2\ c_{FY} \cdot z_{sb2}{}^2 & 0 & 0 \\ 0 & 4\ c_{H1Z} \cdot x_{h0}{}^2 + 4\ c_{H1X} \cdot z_{h0}{}^2 + c_{FX} \cdot z_{sb0}{}^2 + 2\ c_{FX} \cdot z_{sb2}{}^2 & 0 \\ 0 & 0 & 4\ c_{H1Y} \cdot x_{h0}{}^2 + 4\ c_{H1X} \cdot y_{h0}{}^2 \end{bmatrix}$$

(C17)

C4: Bearing Stiffness Calculations

A simplified free-body-diagram of the spindle-bearing system is shown in Fig. C2. It shows the input force U_f and the two resulting radial bearing forces F_{Bf} and F_{Br}. The spindle is seen as a rigid shaft, which can rotate around a pivot point, which is not necessarily the center of gravity.

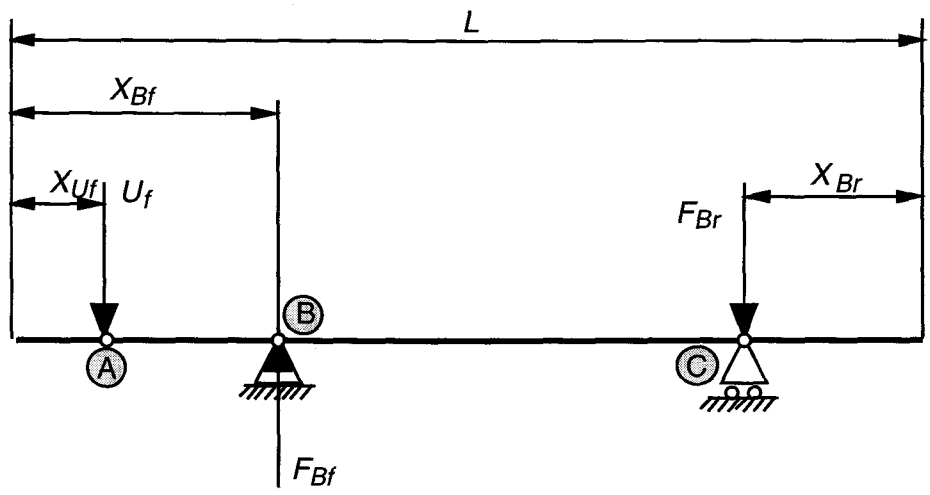

Fig. C2: Simplified free-body-diagram of the spindle.

The rigid-body deflection of the spindle-bearing system under the load U_f can be seen in Fig. C3. The locations of the deflection sensors are also shown with the necessary dimensions.

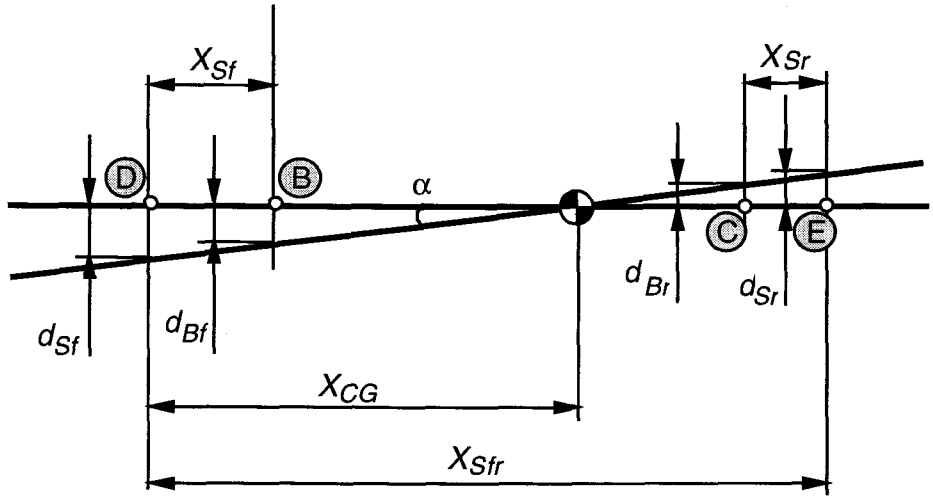

Fig. C3: Spindle in deflected position.

In Fig. C2 and Fig. C3

- (A) denotes the force application point,
- (B) denotes the location of the front bearing,
- (C) denotes the location of the back bearing,
- (D) denotes the front sensor measuring point and
- (E) denotes the rear sensor measuring point.

In order to calculate bearing stiffness from force and deflection measurements, some adjustment calculations need to be done. The radial bearing stiffness k_f is calculated with the formula

$$k_f = \frac{F_{Bf}}{d_{Bf}} \tag{C18}$$

for the front bearing. F_{Bf} denotes the radial force at the front bearing and d_{Bf} denotes the radial deflection at the front bearing. For the rear bearing the formula is as similar.

$$k_r = \frac{F_{Br}}{d_{Br}} \tag{C19}$$

Formulas C12 and C13 only apply for low frequency measurements. Since the actual force and displacement measurements are recorded at different locations on the spindle, than where the actual bearing is positioned, the following formulas need to be used to get the radial bearing stiffnesses. From the balance of forces and moments, one obtains

$$F_{Br} = \frac{U_f (X_{Bf} - X_{Uf})}{(L - X_{Br} - X_{Bf})} \tag{C20}$$

$$F_{Bf} = U_f + F_{Br} \tag{C21}$$

From geometric relations (see Fig. C3) one obtains the pivot point X_P and the radial bearing deflections as a function of the deflection measurements at the sensor locations.

$$X_P = \frac{X_{Sfr} \cdot d_{Sf}}{d_{Sf} + d_{Sr}} \tag{C22}$$

$$d_{Bf} = d_{Sf}\left(1 - \frac{X_{Sf}}{X_P}\right) \tag{C23}$$

$$d_{Br} = d_{Sf}\left(1 - \frac{X_{Sfr} - X_{Sf}}{X_P}\right) \tag{C24}$$

Using equations (C20) through (C24) together with the numerical dimensions of Fig C2 and C3 the radial bearing stiffnesses k_f and k_r in the front and rear calculate to

$$k_r = \frac{0.397 \cdot U_f}{0.160 \cdot d_{Sf} - 0.840 \cdot d_{Sr}} \tag{C25}$$

$$k_f = \frac{1.397 \cdot U_f}{0.840 \cdot d_{Sf} - 0.160 \cdot d_{Sr}} \tag{C26}$$

Appendix D: *Barden* Bearing Manufacturers Information

The *Barden* Corporation provided detailed information about the behavior of the angular contact bearings used in this research. The deflection and stiffness characteristic of the chosen bearings are shown below.

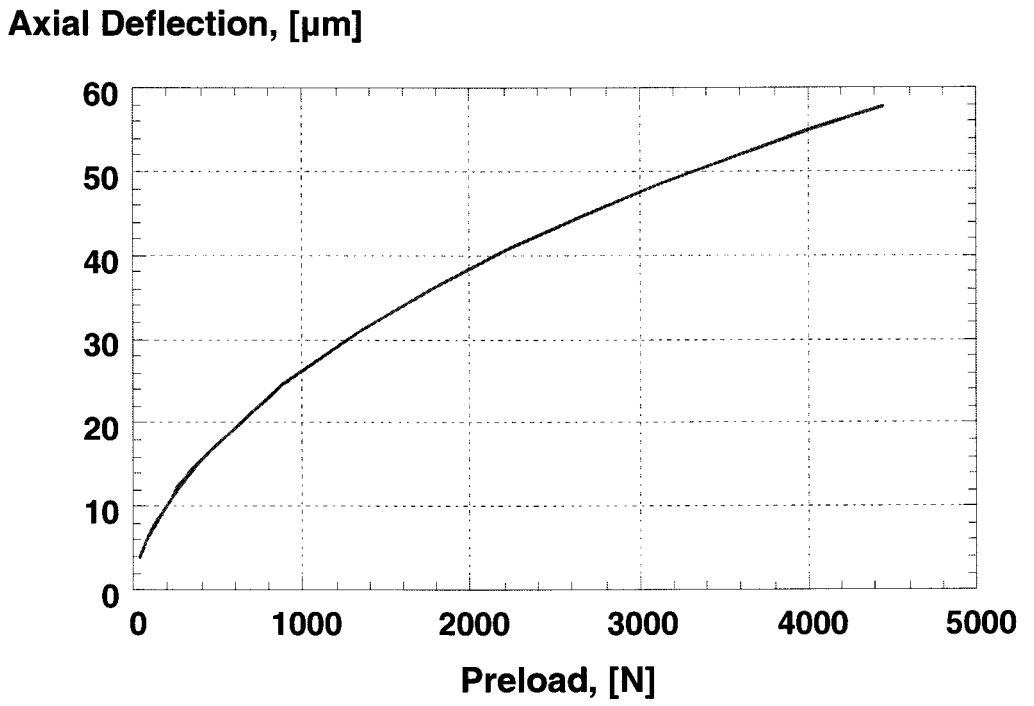

Fig. D1: Preload generated through axial deflection.

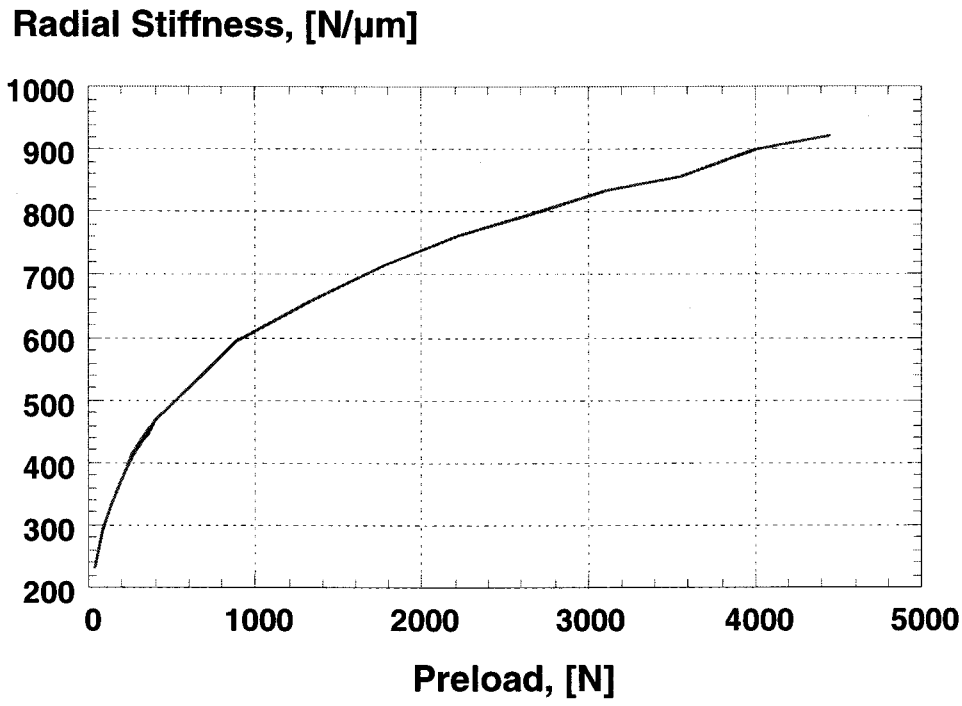

Fig. D2: Radial stiffness change of duplex *Barden* 110H bearings.

Appendix E: Sensor Calibration

a) Kistler Load Cell

A *Kistler* load cell (Model 9212) was used for all force measurements in my experiments. It is a high impedance unit with high rigidity and high sensitivity. The factory specifications are as follows:

Table E1: Technical specifications of the *Kistler* load cell (Model 9212).

Measuring Range:	
Compression	0 to 5000 *lb*
Tension	0 to 500 *lb*
Threshold	0.001 *lb*
Impedance	high
Sensitivity (nominal)	-50 *pC/lb*
Linearity	< +/- 1 % *FSO*
Natural Frequency	70 *kHz*

This load cell was used together with a *Kistler* charge amplifier (Model 5054A1410), which is a special PC board mounted amplifier for converting electrical charge signals from quartz transducers into proportional voltages. It's factory specifications are as follows (Kistler Instruments, 1995):

Table E2: Technical specifications of the *Kistler* charge amplifier (Model 5054A1410).

Range (for +/- 10 V output)	+/- 10 to 1.1 10^6
Frequency Response (-3dB)	~ 0 to 10 *kHz*
Maximum Drift (leakage current)	< +/- 0.03 *pC/s*
Accuracy	< +/- 1 %
Noise	< 2 mV_{rms}
Operating Temperature	0 to 60 °*C*

Also, as part of the data acquisition system programmable filters were used for high frequency cut-off and for anti-ailiasing. These filters were low pass filters from the 66/88 series of Precision Filters Inc. (Model# 88-B-LP8, SN# 36285-35). They are digitally programmable 8 pole, 8 zero active filter modules. The LP8 are elliptic

(Kauer) low-pass filters with 0,044 *dB p-p* pass-band ripple and a 130 *dB/octave* attenuation slope. The cutoff frequency of that particular model can be set between 100 Hz and 102,400 Hz in 100 Hz steps. The amplitude accuracy is +/- 0.2 dB; DC to 0.75 F_c (cutoff frequency). The filters were programmed to 300 Hz cut-off and a gain of 10. (Precision Filters, 1994)

The whole system including load cell, charge amplifier and programmable filter with gain 10 was calibrated before the experiments using static weights. The weights were chosen between 10 and 900 grams. Three test series were performed and the average values were calculated and are plotted below.

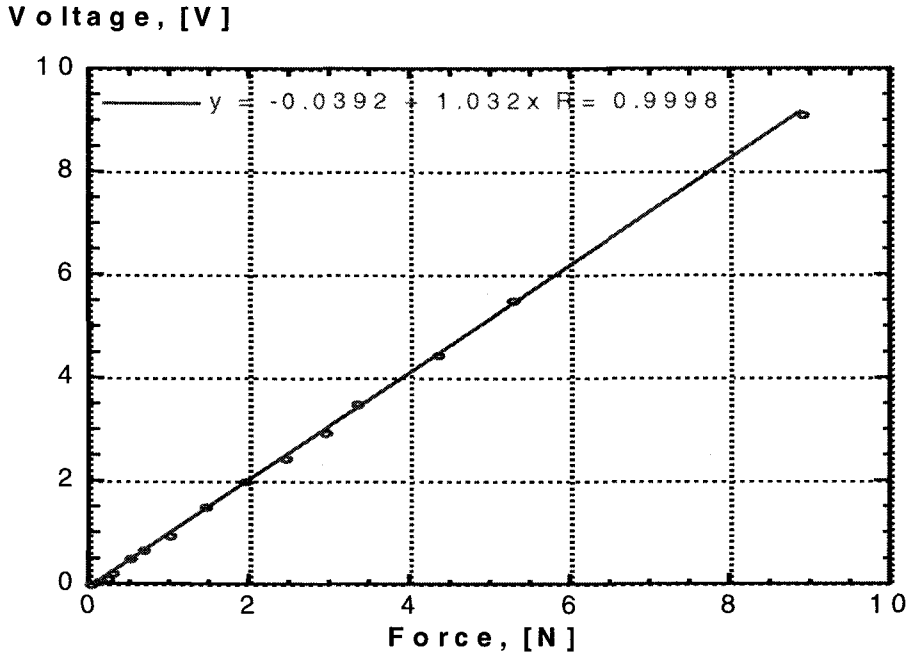

Fig. E1: Load cell calibration curve (*Kistler*, Model 9212).

b) Bently Nevada Proximity Sensor

The *Bently & Nevada* Proximity System (Type 7200 (5 mm) series) was used for all displacement measurements in the experiments. This transducer is a non-contacting, gap to voltage system that measures static as well as dynamic distances between the probe tip and the observed target. The factory specifications are as follows (Bently & Nevada catalog, 1992):

Table E3: Technical specifications of the *Bently & Nevada* proximity system (Type7200).

Calibrated Measuring Range:	0.25 to 2 *mm*
Scale Factor	7.87 *V/mm* +/- 4%
Linearity	0.02 *mm*
Frequency Response	0 to 10 *kHz*
Temperature Sensitivity	-3% at +65°*C*

This system was also used with the above described programmable filter with gain 10 and was calibrated before the experiments using a feeler gage. Three test series were performed and the average values were calculated and are plotted below.

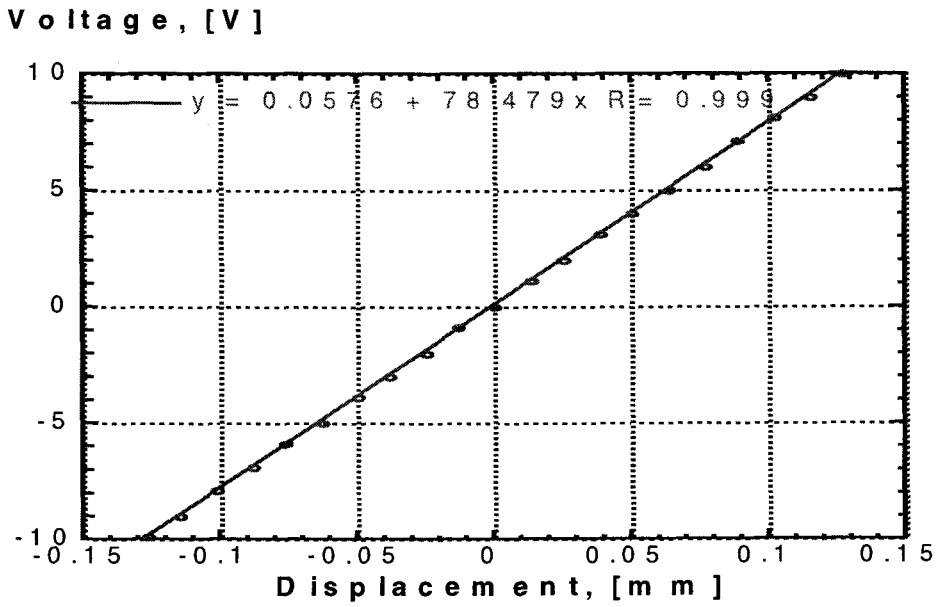

Fig. E2: Proximity sensor calibration curve (*Bently & Nevada*, Type 7200).